ADVANCED THERMAL ANALYSIS OF ReBCO SUPERCONDUCTOR PRECURSOR FILMS AND FUNCTIONAL OXIDES

Silvia Rasi

Universitat de Girona

CSIC
Consejo Superior de Investigaciones Científicas

ICMAB Institut de Ciència de Materials de Barcelona (ICMAB)

DOCTORAL THESIS

ADVANCED THERMAL ANALYSIS OF REBCO SUPERCONDUCTOR PRECURSOR FILMS AND FUNCTIONAL OXIDES

Silvia Rasi

2019

DOCTORATE IN TECHNOLOGY

Directed by: Jordi Farjas, Teresa Puig

Tutor: Jordi Farjas

Thesis submitted to qualify for the PhD degree from the University of Girona

Acknowledgements

First and foremost, I would like to thank the following for the economic support that made this PhD possible: the University of Girona (UdG) for the FI-UdG doctoral grant, and for its support in conferences and work trips; to the ICMAB, for all their resources that made my PhD a stimulating collaboration between them and the UdG; and to the DiffAbs team of the SOLEIL Synchrotron, for providing time and facilities. At a national level, this PhD was supported by the Spanish Programa Nacional de Materiales with the COACHSUPENERGY project (MAT2014-51778-C2-1-R and MAT2014-51778-C2-2-R); by the Ministerio de Ciencia, Innovación y Universidades (RTI2018-095853-B-C21 and RTI2018-095853-B-C22), by the Center of Excellence Severo Ochoa (SEV-2015-0496) and by the Generalitat de Catalunya (2017-SGR-1519). Last but not least, it was funded by the European projects Eurotapes (EU-FP7 NMP-LA-2012-280432), and Ultrasupertape (ERC ADG-2014-669504).

Next, I would like to express my gratitude to my astoundingly supportive tutor, Jordi, for his extraordinary encouragement and availability. Many thanks to Pere, for continuously stimulating me intellectually. To my thesis co-director, Teresa, who I truly thank for giving me plenty of opportunities to build from. To Susagna and Xavier, and to the SUMAN group, I would like to express my great appreciation for our valuable meetings.

Special thanks to my colleagues in Girona; to Anna, for sparing me all the paper-works. To Joan Pere, for the brilliant and (sometimes only) company in the lab. To Quico and Marc, for creatively building the furnaces. To Flavio and Juri, for their undisputable and crucial help in coordinating between the UdG and the ICMAB. I am particularly grateful to Lavinia, Diana, Adrià and Max, for their collaboration towards the end.

Many thanks to the scientific services of the University of Girona (STR-UdG) and of the ICMAB; especially Anna and Xavier were critical for their energy and assistance with the XRD analysis; For his technical assistance and the knowledge developed at SOLEIL, a special thank goes to Cristian M.

Thanks to my family and to my friends, which surprisingly became an important part pf this PhD: in particular to Fabrizio, for his computational assistance, and to Laura, for carrying my samples to ICMAB.

Finally, the most special thanks to Dan, for his constant and crucial support.

LIST OF PUBLICATIONS

- S. Rasi, S. Ricart, X. Obradors, T. Puig, P. Roura-Grabulosa, J. Farjas, Thermal decomposition of Yttrium propionate: film and powder, Journal of Analytical and Applied Pyrolysis (2018), 133, 225-233, https://doi.org/10.1016/j.jaap.2018.03.021
- S. Rasi, F. Silveri, S. Ricart, X. Obradors, T. Puig, P. Roura-Grabulosa, J. Farjas, Thermal decomposition of $CuProp_2$: in-situ analysis of film and powder pyrolysis, Journal of Analytical and Applied Pyrolysis (2019), 140, 312-320, https://doi.org/10.1016/j.jaap.2019.04.008
- S. Rasi, S. Ricart, X. Obradors, T. Puig, P. Roura-Grabulosa, J. Farjas, Radical and oxidative pathways in the pyrolysis of a mixed Barium propionate-acetate, Journal of Analytical and Applied Pyrolysis (2019), 141, 104640, https://doi.org/10.1016/j.jaap.2019.104640
- S. Rasi, S. Ricart, X. Obradors, T. Puig, P. Roura-Grabulosa, J. Farjas, Effect of triethanolamine on the pyrolysis of metal-propionate-based solutions, Journal of Analytical and Applied Pyrolysis (2019), https://doi.org/10.1016/j.jaap.2019.104685
- L. Soler, J. Jareño, J. Banchewski, S. Rasi, N. Chamorro, R. Guzman, R. Yáñez, C. Mocuta, S. Ricart, J. Farjas, P. Roura-Grabulosa, X. Obradors, T. Puig·Ultrafast transient liquid assisted growth of high current density superconducting films: Submitted

LIST OF ABBREVIATIONS

1G	1st generation of HTS
2G	2nd generation of HTS
2-3	2BaO-3CuO composition of the melt
3-7	3BaO-7CuO composition of the melt
CC	Coated conductors
CSD	Chemical solution deposition
EGA	Evolved gas analysis
EGA-FTIR	Evolved gas analysis by infrared detection
EGA-MS	Evolved gas analysis by mass spectrometry detection
FTIR	Fourier Transform Infrared Spectroscopy
H_c	Critical magnetic field

HTS	High Temperature Superconductors
J_c	Critical current density
LAO	$LaAlO_3$
LTS	Low Temperature Superconductors
MS-Q	Mass spectrometry with quadrupole analyzer
ReBCO	$ReBa_2Cu_3O_{7-\partial}$, with Re=rare earth element
SC	Superconductors
Sol.T	Ternary FF-YBCO solution (MAc_x in prop.acid/MeOH)
Sol.t'	Ternary FF-YBCO solution of MAc_x in acetic acid/H_2O
Sol.t''	Ternary FF-YBCO solution of in $YProp_3$, $CuAc_2$ and $BaAc_2$ H_2O
Sol.t'''	Ternary FF-YBCO solution of $BaProp_2$, YAc_3, $CuAc_2$ in H_2O
Sol.TC	Binary FF solution of $CuAc_2$+TEA in prop.acid/MeOH
Sol.TC'	Binary FF solution of $CuProp_2$+TEA in MeOH
Sol.TB	Binary FF solution of $BaAc_2$+TEA in prop.acid/MeOH
Sol.TY	Binary FF solution of YAc_3+TEA in prop.acid/MeOH
Sol.TY'	Binary FF solution of $YProp_3$+TEA in MeOH
TA	Thermal analysis
T_c	Critical temperature
TEA	Triethanolamine
TFA	Trifuoroacetate
TG-DSC	Thermogravimetry coupled with differential scanning calorimetry
TG-FTIR	Thermogravimetry coupled with gas Infrared spectroscopy
TG-MS	Thermogravimetry coupled with mass spectrometry
TLAG	Transient liquid assisted growth
XRD	X-ray diffraction
YBCO	$YBa_2Cu_3O_{7-\partial}$

LIST OF FIGURES

Chapter 1

Chapter 2

Chapter 3

Chapter 4

Chapter 5

LIST OF TABLES

Chapter 3

Chapter 4

Table of Contents

SUMMARY

The energy-use transition towards a drastic reduction of CO_2 emissions is one of the most important challenges that humanity faces; by 2050 the use of renewable energy should account for 80 to 100% of electric energy consumption. To this end, high temperature superconductivity (HTS) has been identified as a crucial technology. In particular $YBaCu_2O_{7-\partial}$ (YBCO) coated conductors (CCs) are on the cutting edge of reducing CO_2 emissions. However, as of now, YBCO CCs are not competitive economically, so it is of the utmost importance to reduce manufacturing costs while achieving high current densities. Chemical solution deposition methods (CSD) have therefore arisen as a cost-effective alternative fabrication route to speed up their introduction into the market.

In this dissertation, we highlight the connection between advanced thermal analysis (TA) techniques and the CSD approach, which is based upon the dependence of YBCO performance on its chemical history. Historically, for instrumental reasons, TA have been usually applied to samples in the form of powder. This dissertation will focus on the need to apply TA to films in order to understand their behavior, as films behave differently than powder due to faster local atmosphere renewal and heat dissipation. Attention is given to a metalorganic propionate-based fluorine-free (FF) solution, because the FF route constitutes a more environmentally friendly alternative to the well-known trifluoroacetate (TFA) route, but without the intrinsic limitation of slow YBCO growth rates (≤1nm/s) characteristic of fluorine-based precursors.

Firstly, thermogravimetry coupled with complementary evolved gas analysis (EGA) techniques (infrared, IR, and mass spectroscopy, MS) is applied to understand the decomposition mechanism of the single-salt precursor solutions. The main tunable parameters during pyrolysis, namely temperature, pressure, furnace atmosphere, flow and sample geometry, will be explored. The difference between film and powder decomposition will be highlighted. This dissertation will show that the thermal behavior is driven by the nature of the metal cation. We will explain why a humid atmosphere is preferred during the pyrolysis stage and why $BaCO_3$ cannot be avoided in favor of an oxide. Finally, the effect of additives to improve rheological properties of the film during the heat treatment will be investigated. Chemical characterization techniques (X-ray diffraction, elemental analysis and infrared spectroscopy) will be applied and the decomposition mechanism revealed and confirmed with the aid of computational chemistry.

Secondly, we will apply this knowledge to the study of the ternary solution, and we will demonstrate that its behavior is more complex than the simple sum of its components. The detrimental effect of water on this metal carboxylate-based solution will be analyzed by TA, and alternative solutions will be proposed within the framework of a cost-effective methodology.

Finally, we will lay out the fundamental principles of the growth route of epitaxial YBCO assisted by a transient liquid (TLAG). TLAG is based on the capability of the ternary system $BaCuO_2$, CuO and Y_2O_3 to achieve ultrafast growth of YBCO; the eutectic reaction between the first two oxides is able to form a transient liquid in the region of the phase diagram where solid YBCO is the equilibrium phase. The stage limiting YBCO growth is the $BaCO_3$ decomposition to yield $BaCuO_2$. For this reason, the limiting parameters for $BaCO_3$ decomposition, such as pressure, CO_2 out-diffusion and film thickness will be explored.

In-situ XRD will reveal the phase evolution during the TLAG which permits the achievement of very high YBCO growth rates, up to 100 nm/s. Finally, the main parameters of the growth process will be analyzed, namely temperature, pressure, solution composition and heating ramps to obtain epitaxial films with high throughput, able to compete with other CSD established routes such as the TFA route.

RESUM

La transició energètica cap a una reducció dràstica de les emissions de CO_2 és un dels reptes més importants als quals s'enfronta la humanitat. Abans del 2050 l'ús de les energies renovables hauria de suposar entre un 80 i un 100% de l'ús total de l'energia elèctrica. Per assolir aquesta fita, la superconductivitat d'alta temperatura (HTS) ha estat identificada com una tecnologia crucial. En particular, els conductors en forma de capes (CCs) de $YBaCu_2O_{7-\partial}$ (YBCO) són capdavanters per reduir les emissions de CO2. No obstant això, fins ara, els CCs de YBCO no són rendibles, així que és molt important reduir els costos de producció tot mantenint una densitat de corrent elevat. En aquest sentit, els mètodes de deposició química (CSD) han sorgit llavors com una ruta de fabricació econòmica que pot per accelerar la seva introducció en el mercat.

En aquesta tesi s'aprofundirà en la relació entre les tècniques d'anàlisis tèrmica avançades (TA) i el mètode de CSD, que al seu torn, es basa en la relació entre les propietats del YBCO i la seva història química.

Històricament i per raons instrumentals, la TA s'aplica a mostres en forma de pólvores. En aquesta tesi es farà èmfasi en la necessitat d'aplicar la TA a les capes per entendre com es comporten quan es tracten tèrmicament, atès que les capes responen de manera diferent a les pólvores per la rapidesa amb la qual l'atmosfera local es renova i amb la qual la calor es dissipa. L'estudi es centrarà en una solució metalorgànica sense fluor (FF) a base de propionats, ja que la ruta FF és una alternativa més respectuosa amb el medi ambient que la més coneguda ruta dels trifluoroacetats (TFA) i a més, no està limitada per la velocitat lenta (≤1nm/s) de creixement del YBCO típica dels precursors fluorats.

Primerament, s'aplicarà la termogravimetria acoblada a les tècniques complementàries (infraroig, IR i espectrometria de massa, MS) d'anàlisi dels gasos formats (EGA) per estudiar el mecanisme de descomposició de les solucions de les sals d'un sol metall. S'exploraran els paràmetres de control de la piròlisi, en concret: la temperatura, la pressió, l'atmosfera del forn, el flux i la geometria de la mostra. Es farà èmfasi en la diferència entre la descomposició de les capes i la de les pólvores. En aquesta tesi es posarà en evidència que el comportament durante el tractament tèrmic depèn de la naturalesa del catió metàl·lic; es justificarà que és millor utilitzar una atmosfera humida durant la fase de la piròlisi, i també es raonarà perquè no es pot evitar la formació de $BaCO_3$ en detriment per a la formació d'un òxid. Finalment, s'investigarà l'efecte dels additius emprats per millorar les propietats reològiques de les capes durant el tractament tèrmic. S'utilitzaran tècniques de caracterització química (difracció de raigs-X, anàlisi elemental i espectroscòpia infraroja) i el mecanisme de descomposició serà identificat i verificat amb l'ajuda de la química computacional.

En segon lloc s'aplicarà aquest coneixement a l'estudi de la solució ternària, i es demostrarà que el seu comportament és més complex que la simple suma de les seves parts. S'analitzarà mitjançant TA l'efecte perjudicial de l'aigua sobre a aquesta solució basada en carboxilats metàl·lics, i es proposaran solucions alteratives i econòmiques.

Així mateix, es descriuran els fonaments de la ruta de creixement de l'YBCO epitaxial assistit per un líquid transitori (TLAG). TLAG es basa en la capacitat del sistema ternari $BaCuO_2$, CuO i Y_2O_3 d'aconseguir velocitats ultra ràpides de creixement de YBCO; la reacció eutèctica entre els primers dos òxids permet formar un líquid transitori a la regió del diagrama de fases on el YBCO sòlid és la fase d'equilibri. L'etapa limitant per al creixement del YBCO és doncs la descomposició del $BaCO_3$ per formar $BaCuO_2$. Per això, s'exploraran els paràmetres que controlen la cinètica de descomposició del $BaCO_3$: la pressió, la difusió del CO_2 i el gruix de les capes.

La difracció in-situ de raigs-X permetrà monitoritzar l'evolució de les fases cristal·lines durant el TLAG, el qual permet assolir velocitats de creixements molt grans, de fins a 100 nm/s. Finalment, s'analitzaran els paràmetres principals del procés de creixement, en concret la temperatura, la pressió, la composició de la solució i la velocitats d'escalfament, per tal d'obtenir capes epitaxials d'alt rendiment i competitives respecte d'altre rutes CSD ja consolidades com la ruta TFA.

RESUMEN

La transición energética hacía una reducción drástica de las emisiones de CO_2 es uno de los retos más importantes a los que se enfrenta la humanidad; antes del 2050 el uso de las energías renovables debería suponer entre un 80 y un 100% del consumo total de la energía eléctrica. Con este fin, se ha identificado a la superconductividad de alta temperatura (HTS) como una tecnología crucial. En particular, los conductores en forma de capas (CCs) de $YBaCu_2O_{7-\partial}$ (YBCO) están a la vanguardia para reducir las emisiones de CO_2. Sin embargo, hasta ahora, los CCs de YBCO no son competitivos económicamente, así que es muy importante reducir los costes de producción manteniendo una densidad de corriente elevada. En este sentido, los métodos de deposición química (CSD) han surgido como una ruta de fabricación alternativa rentable en vistas a acelerar su introducción en el mercado.

En esta tesis se profundizará en la relación entre las técnicas de análisis térmicos avanzados (TA) y la síntesis vía CSD, que se fundamenta en la conexión entre las propiedades del YBCO y su historia química. Históricamente y por razones instrumentales, el TA se ha aplicado a muestras en forma de polvos. Esta tesis enfatizará en la necesidad de aplicar el TA directamente a las capas para así entender su comportamiento durante un tratamiento térmico, dado que las capas se comportan de manera diferente a los polvos por la mayor facilidad con la que la atmosfera local se renueva y el calor se disipa. Se prestará especial atención a una solución metal-orgánica sin flúor (FF) a base de propionatos, dado que es bien sabido que la ruta FF es una alternativa más respetuosa con el medio ambiente que la ruta más conocida de los trifluoroacetatos (TFA), además no adolece del límite intrínseco de una velocidad lenta (≤1nm/s) de crecimiento de YBCO característica de los precursores fluorados.

Primeramente, se usará la termogravimetría acoplada a las técnicas complementarias (infrarrojo, IR y espectrometría de masa, MS) de análisis de los gases formados (EGA) para estudiar el mecanismo de descomposición de las soluciones de las sales de un solo metal. Se explorarán los parámetros de control de la pirolisis, a saber: la temperatura, la presión, la atmosfera del horno, el flujo y la geometría de la muestra. Se enfatizará la diferencia entre la descomposición de las capas y la de los polvos. En este trabajo se demostrará que el comportamiento durante el tratamiento térmico depende de la naturaleza del catión metálico; se mostrará porque es preferible una atmosfera húmeda durante la fase de pirolisis, y porque no se puede evitar la formación de $BaCO_3$ a cambio de obtener un oxido. Finalmente, se investigará el efecto de los aditivos utilizados para mejorar las propiedades reológicas de las capas durante el tratamiento térmico. Se utilizarán técnicas de caracterización química (difracción de rayos-X, análisis elemental y espectroscopia infrarroja) para establecer el mecanismo de descomposición, el cual será confirmado con la ayuda de la química computacional.

En segundo lugar, los resultados obtenidos se aplicarán al estudio de la solución ternaria, y se demostrará que su comportamiento es más complejo que la simple suma de sus partes. Se analizará por TA el efecto perjudicial del agua sobre la solución basada en carboxilatos metálicos, y se propondrán soluciones alternativas y económicas.

Además, se establecerán los principios fundamentales de la ruta de crecimiento de YBCO epitaxial asistida por un líquido transitorio (TLAG). El TLAG se basa en la capacidad del sistema ternario $BaCuO_2$, CuO y Y_2O_3 para conseguir velocidades de crecimiento de YBCO ultra rápidas; la reacción eutéctica entre los dos primeros óxidos forma un líquido transitorio en la región del diagrama de fase donde el YBCO sólido es la fase de equilibrio. La etapa limitante para el crecimiento del YBCO es la descomposición del $BaCO_3$ para formar $BaCuO_2$. Por eso, se explorarán los parámetros que controlan la descomposición del $BaCO_3$, como la presión, la difusión del CO_2 y el grueso de las capas.

La difracción in-situ de rayos-X nos permitirá monitorizar la evolución de las fases cristalinas durante el TLAG, el cual permite conseguir velocidades de crecimientos muy grandes, de hasta 100 nm/s. Finalmente, se analizarán los parámetros principales del proceso de crecimiento, en concreto la temperatura, la presión, la composición de la solución y la velocidad de calentamiento, para obtener capas epitaxiales de alto rendimiento y capaces de competir con otras rutas CSD ya consolidadas como la ruta TFA.

INTRODUCTION

Chapter 1

1.1 YBCO: a High-Temperature Superconductor

Since Onnes' unexpected discovery of superconductivity in a metal in 1911, 75 years passed before, in 1986, it was discovered that ceramic materials as well could be superconductors at temperatures as low as 30K.

A year later, $YBa_2Cu_3O_{7-\partial}$ [1,2], a rare earth (RE) cuprate and ceramic material, raised the upper limit superconductive temperature (T_c) above that of liquid nitrogen (77), paving the way for a whole new class of superconductors, the High Temperature Superconductors (HTS) [3,4]. This breakthrough is one of the reasons that still makes them interesting for applications over the already well-established Low Temperature Superconductors (LTS), whose lower cooling temperatures (~4K) require higher costs, limiting LTS market to mainly medical MRI machines. Conversely, within the market of electric power devices, two types of HTS have developed over the past years: the first generation (1G) [5] of superconductors (SC), due to the highly anisotropic superconducting properties of the materials used (BSCCO: Bi-2212 and Bi-2223) are manufactured as wires, through the "powder-in-tube" method, and so they rely on the filament principle. On the other hand, the 2G SC, to which YBCO belongs, adopt a tape structure, due to their smaller anisotropy in superconducting properties and their good mechanical properties [3,6]. The final product, displayed in Fig. 1.1, constitutes a Coated Conductor (CC) [7,8] where the HTS is typically only ~1 μm thick, grown epitaxially on a substrate and protected by buffer and coating layers (typically the HTS represent a 1% of the total thickness of the tape).

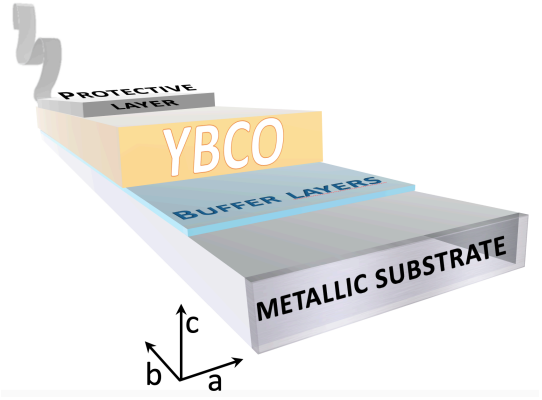

Fig. 1.1: Structure of a Coated-Conductor (CC) layered architecture.

The big advance in the field of energy led by Superconductivity is due to the fact that superconductors are a class of materials with two specific characteristics when cooled down below a characteristic critical temperature (Tc):

- the *zero electrical resistance*
- and the *Meissner effect*

The *zero electrical resistance* is a phenomenon according to which, when current flows through the superconductor below Tc, no dissipation of the energy carried by the current occurs. In a normal conductor the current is always disrupted by electrical resistance, which can be seen as the collisions between the electrons making up the current and the vibrating ionic lattice across which they are moving; in these collisions their energy is absorbed by the lattice and converted into kinetic energy, or heat. This energy dissipation is known as Joule Effect. Although lowering the temperature causes electrical resistivity to decrease, in a normal conductor it never falls to zero. Conversely, in superconductors, it drops to zero below T_c although the crystal pattern is still vibrating, because the electrons combine into a new quantum state (which can be described by a wave function) that is insensitive to collisions.

The other fundamental signature of superconductivity is the *Meissner effect*, which consists of the expulsion of the magnetic field from the bulk of the SC, below T_c, when the material is exposed to an external magnetic field **H**. This perfect diamagnetism comes from the fact that the application of the external magnetic field causes magnetization of the material, creating an induced magnetic field **B** in the material through the generation of screening currents, $B = \mu_0 H$. If H is lower than a critical value, $H<H_c$, B is expelled. For higher values of H, $H>H_c$, B is no longer expelled. The screening current is called persistent current, because thanks to the zero resistivity the magnetic field produced by it has a decay time of $\sim 10^5$ years.

If the temperature or the external field are independently increased, the superconductor loses its state of superconductivity, as shown in Fig. 1.2. These critical values are the boundary between the SC state and the normal state.

Based on their response to the external magnetic field, the Ginzburg-Landau theory of superconductivity [9,10] describes the existence of two types of SC, type I and type II (Fig. 1.3a).

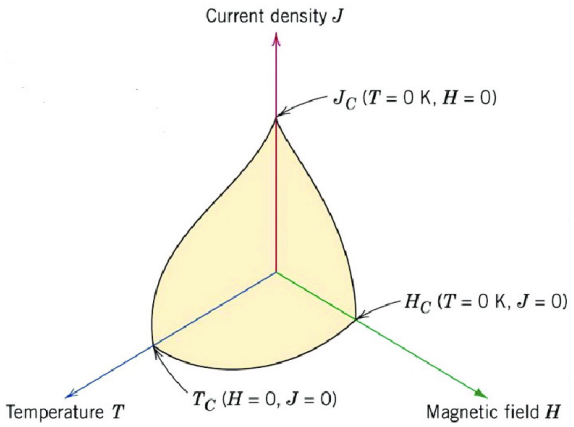

***Fig. 1.2**:* The superconducting state. *Dependence of superconductivity on temperature, current density and external magnetic field.*

The difference is the existence, for type II, of a mixed state which is a transition state between the normal one and the superconducting state. In this state, between H_{c1} and H_{c2} (Fig. 1.3a), the magnetic flux exists in quantized vortices in the bulk of the SC. Regardless of the detailed physical discussion, which can be found elsewhere [11], the main obstacle is that these vortices may move upon the application of a Lorentz-like force. Their displacement is accompanied by dissipation of energy. We define the critical current density, J_c, as the maximum current density before vortices move and thus before dissipation occurs. Within the mixed state, J_c vanishes below H_{c2}, defining another magnetic field, the irreversibility field (H_{IL}, Fig. 1.3b). Small defects in the structure of the order of nanometers, such as dislocations or nanoparticles can be effectively used for pinning the vortices so that they become static. Effective pinning is very beneficial for application as it causes J_c to decrease more slowly with increasing H, stretching the region of H_{IL}.

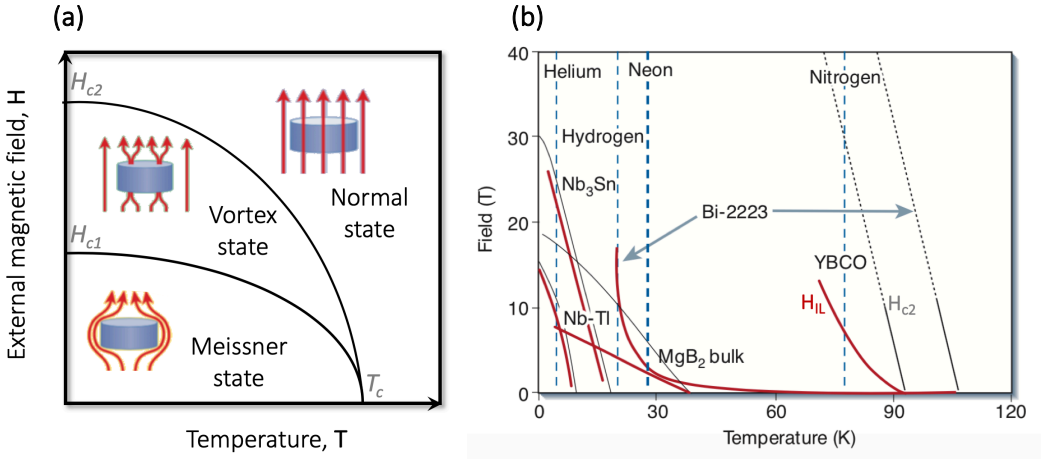

Fig. 1.3: Type II superconductors. ***(a)*** *Phase diagram of type II superconductors;* ***(b)*** *Irreversibility lines (H_{IL}, in red) at which J_c goes to zero and upper critical field lines (H_{c2}, in black) where the bulk superconductivity disappears. Readapted from [12].*

One of the reasons for which YBCO is so promising is that, as a type II SC, its reversibility line (IL) is the highest, as shown in Fig. 1.3b. It displays a T_c of 93K and the highest field current carrying capacity at 77K.

$YB_2Cu_3O_{7-\partial}$ (or alternatively $YB_2Cu_3O_{6+x}$) is characterized by a complex oxygen-deficient perovskite structure, depicted in Fig. 1.4. This structure shifts from the insulating tetragonal phase to the superconductive orthorhombic phase ($\partial \leq 0.5$) where the SC current flows along the a-b plane. Even though there are others SC materials with higher T_c and H_{c2}, YBCO is very promising because it meets all the technical requirements for its use in power transmission cables and high field magnets, thanks to the high IL, which is the real discriminating parameter and not H_{c2}.

One of the main challenges that results in a drop of J_c in HTS, is the problem of the grain boundaries [13–15]. In fact, although there is not yet a complete theory to explain superconductivity at high temperatures, it is thought that the electronic *d*-wave function used to describe the superconducting current is responsible for lowering J_c at the grain boundary, due to

the harder overlapping of two *d*-waves with respect to two s-wave functions as a consequence of their symmetry. S-functions are used to explain superconductivity in LTS by the Bardeen–Cooper–Schrieffer (or BCS) theory [16], which works very well at low temperatures (≤20K). As a consequence, J_c in each YBCO grain is higher than the percolative current in the entire film; thus, a key point in the synthetic strategies developed is to avoid high-angle grain boundaries and phase segregation between grains for the percolation of the superconducting current. These physical-morphological properties, as it will be explained in the next paragraphs, depend strictly on the growth method applied.

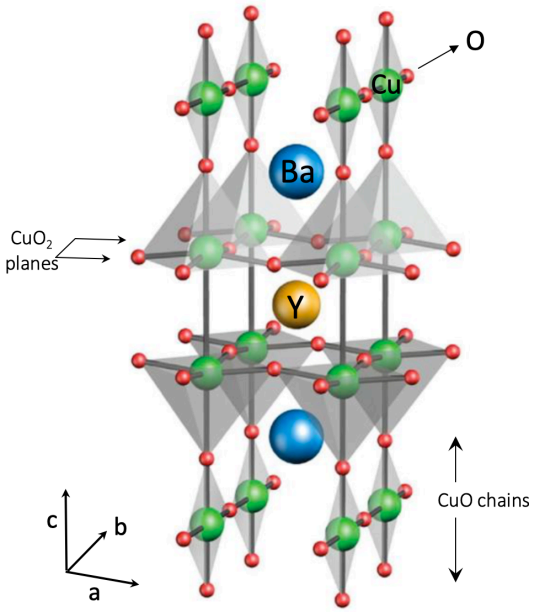

Fig. 1.4: $YB_2Cu_3O_{7-\partial}$ (YBCO) triple structure. *The CuO chains and the CuO_2 planes where the superconducting current flows are indicated.*

1.2 Chemical Solution Deposition methods (CSD)

One of the greatest challenges to HTS tapes industrial synthesis is that nowadays it mostly relies on physical methodologies, such as Pulsed Laser Deposition (PLD), Metalorganic Chemical Vapor Depositions (MOCVD) [7,8] and the recent Reactive Co-Evaporation-Deposition and Reaction (RCE-DR) [17]. These techniques have the advantage to be able to provide exceptional control over the physical structure, since they are based on high-vacuum processes for the deposition of the material on a substrate heated at the oxide growth temperature (Fig. 1.5).

But the major drawback is that vapor deposition techniques require ultra-high vacuum and equipment complexity that are responsible for their high fabrication costs. For these reasons, ex-situ chemical methods like chemical solution deposition (CSD) [18] have arisen as a potential alternative.

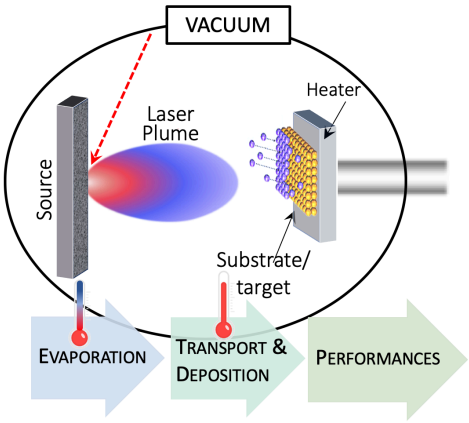

Fig. 1.5: Example of physical YBCO growth methodology. *Schematics of PLD technique, based on the evaporation of a solid source (metals) into a plasma which is directed to a target substrate where the oxide is grown.*

Therefore, optimizing CSD methods is of the outmost importance for YBCO to spread into the market. CSD methods are based on the idea that a homogeneous solution can be deposited on a substrate and a complex oxide can be grown after a thermal treatment. Overall, it involves 4 main steps: solution preparation, deposition, pyrolysis and crystal growth.

The precursor solution usually consists of short-chain metalorganic salts, since it is important that their decomposition is complete without the need to reach high temperatures (>500°C). The solvents and rheological properties such as viscosity, surface tension and contact angle are optimized for the deposition step on a substrate. Deposition can be performed with several techniques, but the one used in this work was spin coating. The solution is injected through a syringe on a substrate which then starts to spin. The initial balance between the viscous shear drag and rotational accelerations causes the film to spread as the thinning behavior is dominated by viscosity. When viscosity does not longer change fluid flow, solvent evaporation will become the dominant process of the thinning behavior.

During pyrolysis all the possible organic material is removed as the dry film undergoes a thermal treatment, normally at temperatures between 100 and 500°C. During this stage important physical transformations occur as the precursors decompose: shrinkage of the film upon gas out-diffusion and crystallization of the inorganic material; if the physical stress becomes too high, also buckling and cracking can take place [19]. In fact, the porosity has to be minimized to avoid phase segregation that could induce low current percolation after YBCO growth, thus leading to a drop of the final film properties [20,21]. Several parameters can so be tuned to reach homogenous films, such as furnace gas composition and flow, temperature program and use of additives as stabilizers [22]. The latter help reducing stress and improve rheological properties, by increasing the viscosity of the initial solution.

Pyrolysis is followed by a crystallization stage. During this step the pyrolyzed film is annealed to temperatures between 600 and 1100°C in specific conditions of total pressure, PO_2, temperature program and gas flow, which represent the main tunable parameters during the growth stage of the final complex oxide. Epitaxial growth here takes place through hetero-epitaxy above a substrate of a different material.

CSD processing steps are schematically represented in Fig. 1.6.

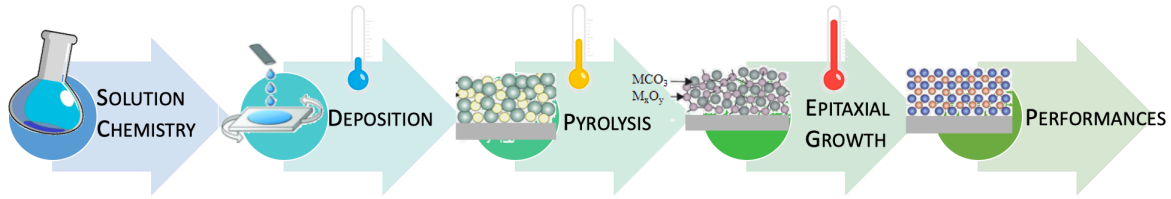

Fig. 1.6: Schematic representation of the CSD process.

1.3 Thermal analysis of metalorganic precursors

To get the final desired properties of the superconducting tapes, each stage of the CSD process needs to be understood and optimized. In this perspective, thermal analyses (TA) are a set of techniques which enable to monitor the evolution of a certain property as a function of temperature. Thus, they are especially suited to analyze structural transformations that take place during pyrolysis of metal-organic precursors: solvent evaporation, precursor pyrolysis, oxidation and decomposition of intermediate compounds that take place during pyrolysis of metal-organic precursors.

One of the key points is that historically thermal analyses are optimized for their application to powders rather than to the corresponding films, and many manufacturers have developed TA equipment around this demand. The use of TA in films is quite limited because the signal-to-noise ratio depends on the sample mass, and sample mass for films is typically one order of magnitude smaller than the sample mass used in TA experiments. Fig. 1.7 shows how some TA techniques such as differential scanning calorimetry (DSC) are at their detection limit when applied to films; it is still possible to study film thermal behavior by combining the information from all TA techniques to reveal the thermal behavior trend when going from film to powder. Only in the last decade, some works of thermogravimetry (TG) analysis focused on films after several studies raised the awareness that films are expected to behave differently than powders [23–28], when the thermal process is controlled by the transport of reactive gases or of evolved volatiles, or by the heat transport in and out of the sample. Therefore, an in-situ study of the thermal processes that lead to YBCO tape synthesis is of fundamental interest to reveal the actual kinetics and mechanism occurring in films.

In fact, there have been an increasing number of publications regarding the thermal decomposition of YBCO precursor powders such as Yttrium acetate (YAc_3) and Yttrium propionate ($YProp_3$) and the corresponding barium and copper salts [29–31]. By EGA-FTIR and EGA-MS, it was shown that the decomposition of propionates in inert atmospheres involves formation of radicals $C_2H_5\cdot$ and $C_2H_5CO\cdot$ (along with CO_2) and their recombination to form a symmetrical ketone [32–34].

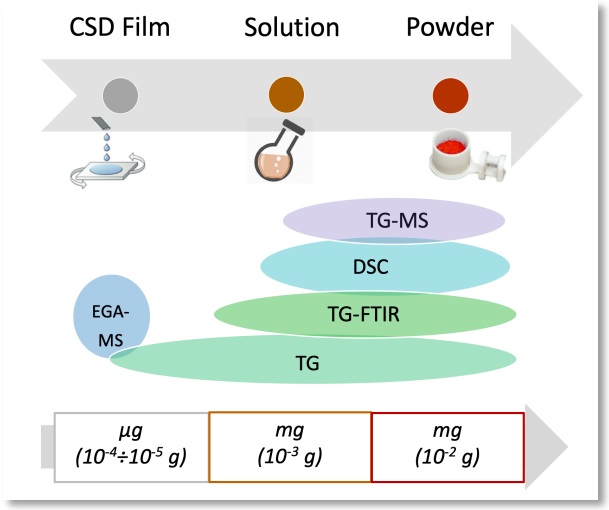

Fig. 1.7: Thermal analysis techniques and their corresponding mass-limitation ranges.

However, so far, the thermal decomposition of $YProp_3$ has been studied only in the form of powder [32,35–37]. In situ evolved gas analysis (EGA) was performed by means of quadrupole mass spectrometry (EGA-MS/Q) by [36,37] in air and in nitrogen, and with Fourier-transform infrared spectroscopy (EGA-FTIR) in argon by [32]. The reported volatiles, even in inert atmosphere, are different, so that, a univocal and general mechanism has not been established yet. Besides, despite the fact that water vapor is commonly used in the synthesis of YBCO FF tapes, none of the published papers analyze the effect of the presence of water vapor in the thermal decomposition of the metalorganic precursor [38,39].

Regarding the thermal decomposition of Copper propionate ($CuProp_2$), for odd chain length of Cu(II)carboxylates like Cu(II)propionate, only MS has been used for the in-situ EGA analysis and 2-pentanone (asymmetrical ketone) was reported to be the main decomposition product [31]. Conversely, no ketones at all were observed for even chain carboxylates of copper(II) [40], mercury(II) [41] and silver(I) [42]. In fact, references [40,41] report on the decomposition of even chain length of Hg(II) and Cu(II) carboxylates as involving formation of ethylene and propionic acid along with CO_2. Clearly, there is no univocal decomposition pathway for metal carboxylates, on the contrary it depends on the surrounding atmosphere, the length of the carboxylate chain and the type of metal ion [43].

Concerning decomposition of barium carboxylates, according to [29], the salt obtained from the acetate precursor in propionic acid and methanol results in a mixed acetate-propionate complex. By coupling mass spectrometry to thermogravimetry (TG-MS) it is shown that during decomposition in air it releases CO_2 in a first small mass loss (≈3%), followed by 3-pentanone, CO_2 and acetone to yield $BaCO_3$. Previously, it was also reported that barium propionate synthesized from the corresponding carbonate in excess of propionic acid, decomposes in inert atmosphere in two steps [44] of similar mass loss, yielding 3-pentanone and traces of acetone, but no CO_2, in accordance with the stoichiometry of the reaction mechanism. Similarly, $BaAc_2$ [45] was shown to decompose to $BaCO_3$, passing through an intermediate barium oxalate stable until 330°C. However, so far, also the thermal decomposition of barium propionate ($BaProp_2$) and barium

acetate ($BaAc_2$) has been studied only for samples in the form of powder and the volatiles observed only through EGA-MS.

Finally, among the additives used as CSD stabilizers, triethanolamine (TEA) is especially common. In particular, TEA is of special interest because of its chelating properties [46,47]; in fact, as an aminoalcohol, its properties lie between those of amines and alcohols, acting as both N-donor and O-donor thanks to the three OH groups. Therefore, while increasing viscosity, TEA is expected to form complexes and increase the stability of the metal carboxylate salts in solution. In fact, it is known that, especially copper, can form stable complexes with nitrogen and oxygen donors [48–50]; similarly, Y^{3+} has been reported to form complexes with TEA [47] while Ba^{2+} is not expected to coordinate with TEA [51,52].

Regarding TEA thermal decomposition during pyrolysis [53,54], the aspect ratio is expected to play a role [55]: in fact, when in the form of films, TEA is likely to evaporate before reaching its decomposition temperature (250-300°C) thanks to the high surface to volume ratio. When it is placed inside a crucible, evaporation is significantly delayed so it can be heated to higher temperature (above 300°C) where it decomposes releasing acetaldehyde (CH_3CHO), CO_2, ammonia (NH_3) and ethylene oxide (CH_2OCH_2) [53,55]. On the other hand, metalorganic complexes of TEA are expected to decompose following several decomposition steps [56] that start with the loss of small TEA units and end with the metal salt decomposition.

1.4 About Growth Routes of ReBCO

So far, chemical methods have relied on the well-established TFA (tri-fluoroacetate) MOD route introduced in 1998 by Gupta et al [57]. The advantage of fluorinated precursors is that the undesired $BaCO_3$ pyrolysis product can be avoided in favor of BaF_2, and thus YBCO grows from oxyfluoride precursors [58]. Nevertheless, this route requires difficult furnace design to remove the dangerous hydrofluoric acid (HF) produced by the BaF_2 decomposition (see Fig. 1.8). Although the TFA route is now well-understood in terms of the main parameters governing YBCO growth [19] and high Jc can be obtained, its limitations have not been fully addressed yet. One way was to switch to low-fluorine routes [59,60] to reduce the amount of HF. But independently of the fluorine content, since YBCO grows from a gas-solid reaction (water interaction with the Barium-fluoride precursor), its crystallization is very slow [24,61–63] and this constitutes a general limit of fluorinated precursors.

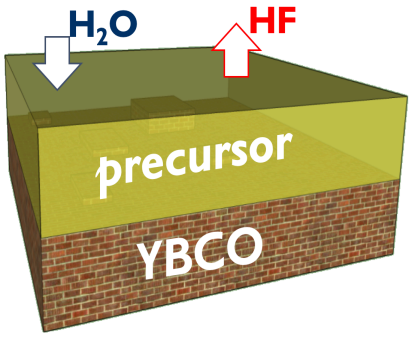

***Fig. 1.8**:* Diagram of the TFA route. *The growth of YBCO depends on a solid - gas reaction.*

In fact, YBCO use in power systems is under the constraint of not only high J_c, but ultra-fast growth rates to reduce time and thus fabrication costs; additionally, thick films are also crucial as they can carry more overall current and they reduce the physical amount of tape bundled-up. If production costs are defined as cost/performance ratio, the requirement for CCs technologies to be feasible should drop to 5-10 €·kA^{-1}·m^{-1}, corresponding to a yearly production capacity of more than 1000 km. Present capacities for coated conductor (CC) production are around 500 km/year with a cost of 100-300 €/(kA·m) [64]. Therefore, a condition is that 2-3 μm films should grow in the time lapse of a few seconds.

Even though chemical methods carry the promise of large-scale applications with low-cost production, they are limited to maximum growth rates of ~1nm/s with the TFA route. Conversely, vapor deposition methods such as PLD [65] and MOCVD [66] are limited by the material flux to ReBCO growth rates ≤10 nm/s. Liquid assisted growth have therefore arisen as an alternative route. Indeed, solid-liquid reactions are faster since atomic diffusion through a liquid is much faster than through a solid. For example, Y (and Ba) cation diffusion coefficient (D) into a solid matrix of polycrystalline YBCO is of the order of $8 \cdot 10^{-12}$ cm^{2}s^{-1} at temperatures as high as 990°C [67], almost two orders of magnitude smaller than Y cation diffusion in the 3BaO-5CuO melt which is approximately $4 \cdot 10^{-10}$ cm^{2}s^{-1} [68]. Overall, growth techniques through a liquid can involve REBCO growth from a congruent melting or from a high temperature solution. The advantage of the congruent melting is that the composition of the liquid is the same as that of the solid.

Although YBCO does not melt congruently, Y-Ba-Cu phase diagrams published in the '90s span over a huge amount of phases and interactions [69–71], thus the possibilities are diverse; very complicated thermodynamic diagrams arise from the fact that this ternary system becomes a multi-parameter system whose phase stabilities are strictly influenced by composition, temperature, P_{O2} and P_{CO2}. Hence, since no congruent YBCO melting exists, liquid assisted techniques involve crystallization of YBCO from a stable Ba-Cu melt in which Y atoms are dissolved. The first reported method was that of Melted Textured Growth (MTG) applied for bulk ceramics [72–74]. In this route, the system consists of YBCO and Y_2BaCuO_5 (211 phase): upon tuning supersaturation of the 211-liquid mixture, the system is very slowly cooled down to crystallize a YBCO single-crystal bulk, exploiting the YBCO peritectic melting [75]. In films this technique gives rise to Liquid Phase Epitaxy (LPE) [68,76,77], schematically represented by Fig. 1.9. In fact, the YBCO phase diagram allows for the existence of many liquid phase interactions, all involving stable melts. None has reported so far YBCO growth from a transient liquid, and never using low-cost commercial chemical precursors, as we present in this work. Finally, one of the main challenges is that the melted oxides require rather high temperatures (600-800°C) and that this type of melt is normally highly reactive and corrosive.

In this thesis, fluorine-free (F-F) precursors are investigated because of their many potentialities to solve some of the issues discussed above; first of all, there is no BaF_2 formation after pyrolysis. In this sense, FF routes are more environmentally friendly and help reduce furnace design costs. At the beginning FF routes were abandoned because of the presence of $BaCO_3$, which brought to light the related decomposition difficulties due to the presence of retained carbon in the final YBCO [78], ascribed to be responsible for the severe deterioration of J_c. Even though the high $BaCO_3$ decomposition temperature, above 1000°C [79], can be lowered in the presence of CuO and Y_2O_3 [80], this issue casted a shadow on FF-route and up to now there is still little understanding about F-F routes mechanisms [80,81].

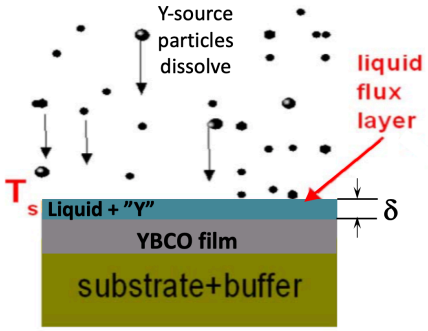

Fig. 1.9: Schematic representation of a type of liquid phase epitaxy. *Readapted from* [82].

1.5 Objectives

108 years down the line since the discovery of superconductivity, and magnetic levitation (which exploits the lift created by magnetic repulsion) is maybe the most sensational application superconductors are recognized for, although the farthest from the near-future applications of HTS.

In fact, thanks to its physical characteristics, such as high T_c and high H_{IL}, promising applications of YBCO are predicted in the field of electrical power (transmission cables, generators, fault current limiters..) and high-field magnets (MRI, NMR, accelerator or even compact fusion), Fig. 1.10, but they are nowadays limited by the production costs. This work will be driven by the need to scale up HTS tape production to large-scale manufacturing, combining the advantages of CSD methods with ultrafast liquid assisted growth.

Since, for fabrication costs to drop, chemical methods are a valid cost-effective candidate, the third chapter of this dissertation is aimed at understanding the thermal decomposition of the isolated metalorganic precursors with the aid of thermal analysis combined with structural characterization techniques; their decomposition is discussed with respect to the difference between film and powder samples. This understanding will lay the basis for the interpretation of the ternary precursor solution in the fourth chapter, which is essential to optimize the YBCO pyrolysis step.

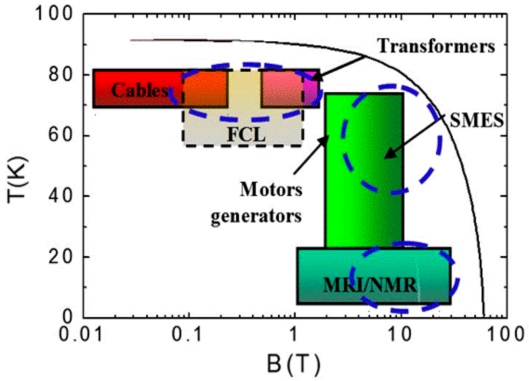

Fig. 1.10: Applications of HTS. *Application range as a function of field and temperature, reproduced from* [8].

Given the fact that for an affordable CCs production, fast growth rates are needed with high throughputs and thick films are required, as they can carry more current, in the last chapter, a novel Transient Liquid Assisted Growth, TLAG-CSD approach, is introduced based on fluorine-free precursors, F-F precursors. The objectives will be multiple: to understand the TLAG-CSD growth methods; to tune growth parameters in order to reach epitaxial films with competitive J_c; to address the thickness problem through an analysis of the $BaCO_3$ decomposition and finally, to reach ultrafast growth rates, 100 times faster than other established routes.

MATERIALS AND METHODS

Chapter 2

2.1 Fabrication of YBCO films

2.1.1 Solution preparation and deposition

Commercial powders of Copper acetate ($CuAc_2$, Alfa Aesar, 99.99%), Barium acetate ($BaAc_2$, Sigma Aldrich, 99.99%) and Yttrium acetate (YAc_3, Alfa Aesar, 99.99%) whose FTIR analysis is shown in Fig. 2.1 were dehydrated at 55°C overnight in a thermostatic vacuum dryer, to remove crystallization water (determined with thermal analysis experiments). Once dried, they were then dissolved in propionic acid (Merck, ≥99%). Anhydrous methanol (MeOH, Sharlau, 99.9%) was added to reach a solvent ratio of 1/1. Two different types of solutions were prepared based on the Cu/Ba ratio: a Y/Ba/Cu=1/2/4.66 (1.5 M) solution for the 3BaO-7CuO melt (3-7 composition), and a Y/Ba/Cu=1/2/3 (1 M) for the 2BaO-3CuO melt (2-3 composition); to the latter typically a 5% v/v of triethanolamine (TEA) was added. Such additives are used to ensure homogeneous coatings of the substrate, and to reduce cracking (Fig. 2.2). The solution was filtered through a 2.2µm membrane and the water amount was measured through a Karl-Fisher apparatus. Water was kept lower than 2%. To ensure epitaxial growth, single-crystal substrate with a low lattice mismatch with respect to YBCO, such as $LaAlO_3$ (LAO) and $SrTiO_3$ (STO), were used. Prior to solution deposition, the substrates were annealed at 900°C in a dry O_2 flux, as shown in Fig. 2.3. Deposition was performed by means of a spin coater from Laurell, model WS-650MZ 23 NPP, with acceleration and speed of 6000 rpm and holding time of 2 minutes. The film was then dried on a hot plate kept at 70°C to remove the remaining solvent.

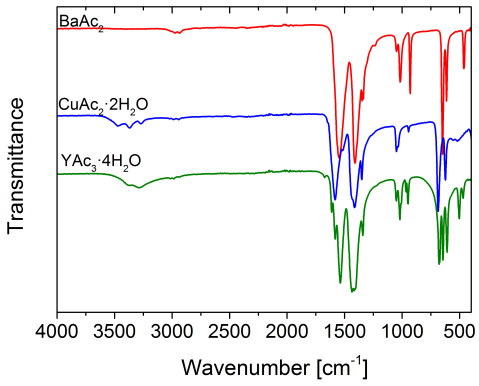

***Fig. 2.1**:* FTIR of the metal acetate precursors. *As-received, prior dehydration and solution preparation.*

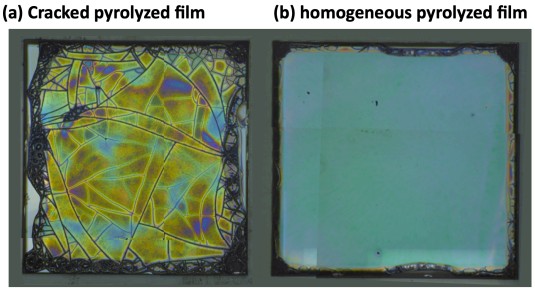

Fig. 2.2: Film morphology after pyrolysis. *Comparison between **(a)** cracked and **(b)** homogenous films*

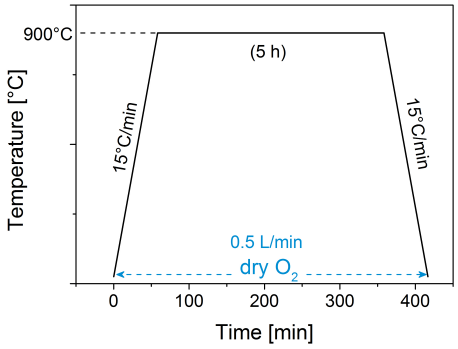

Fig. 2.3: Thermal profile for the substrate oxygenation step.

2.1.2 Pyrolysis

Deposition was followed by pyrolysis, during which films were decomposed to 500°C to remove all organic materials. The thermal profile is shown in figure 2.4a. The final θ-2θ XRD scan (Fig. 2.4b) shows the presence of Y_2O_3, CuO and $BaCO_3$ particles of nanometric size. Anhydrous conditions of deposition and initial stage of pyrolysis (applying dry O_2 until 110° to reduce water uptake from the film, Fig. 2.4a) were chosen to obtain a standard initial condition, because $BaCO_3$ monoclinic was found to form for a H_2O content in solution, superior to 2%.

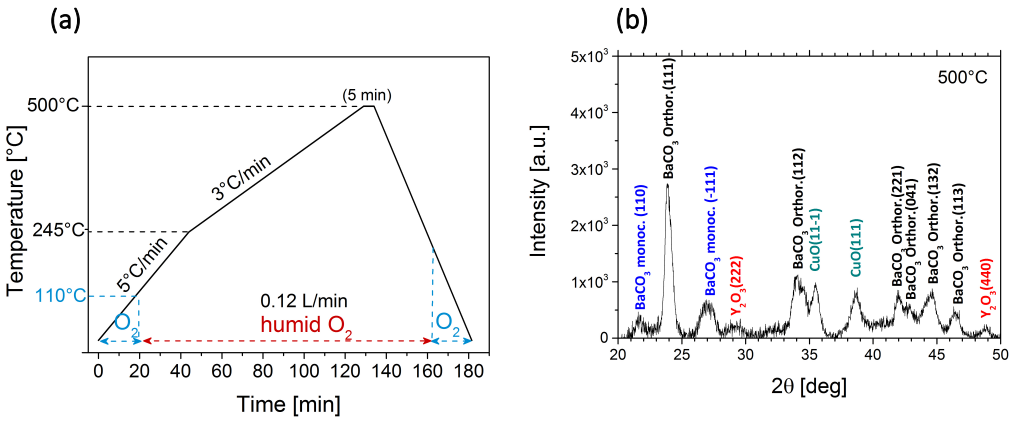

Fig. 2.4: Characterization of the pyrolysis step. ***(a)** Thermal profile and **(b)** XRD scan of a pyrolyzed sample deposited without controlling the humidity conditions.*

2.1.3 Growth from vacuum

YBCO growth was performed in two different furnaces:

- Growth at slow heating rates (10-25°C/min) was carried out in a quartz tube (Fig. 2.5a) where the sample was placed on top of an alumina holder at the close end of the tube; the sample holder contained a thermocouple for the temperature control; a small low-resistance furnace was placed around the close end of the quart tube, while the other end is connected to a turbomolecular pump in series with a rotatory pump. Mixed heating ramps (1200°C/min to 600°C and 25°C/min from 600°C) were also carried out in this furnace by preheating the furnace at the maximum temperature (850°C); once this temperature was reached the furnace was moved in place around the quartz tube with the sample inside and the thermal contact permitted to quickly (~1200°C/min) reach 600°C; then ramps of 25°C/min were applied by controlling with the internal thermocouple.
- Growth at fast heating rates (~100-300°C/min) were carried out in a similar system but with a quartz tube open at both ends allowing for an improved gas flow, as depicted in Fig. 2.5b. One end of the tube is for the gas entrance while the other end is connected to the vacuum system.

In both furnaces, the growth approach involves two stages: one at low pressure followed by a sudden jump to higher pressure. The first stage consists of the heating ramp, where the sample temperature is increased to the selected growth temperature at total pressures of air between 10^{-8} and 10^{-7} bar (P_{O2}~10^{-9}-10^{-8} bar). Just before the pressure jump, in both systems, the turbomolecular pump was switched off and only the rotatory was left on to ensure the proper gas flow. While keeping the sample temperature constant, the pressure jump was carried out either with pure O_2 or Air, with flows of 100 ml/min for the system shown in Fig. 2.5a and of 500 ml/min for Fig. 2.5b. Pressure changes occurred in the range of 1-2 seconds. Both quartz tubes have the same cross section.

After YBCO growth, films are oxygenated at 450°C for 210 minutes. This was the optimal time necessary for the tetragonal to the orthorhombic phase conversion of YBCO; a more detailed discussion on the topic can be found in the thesis of A. Stangl [83].

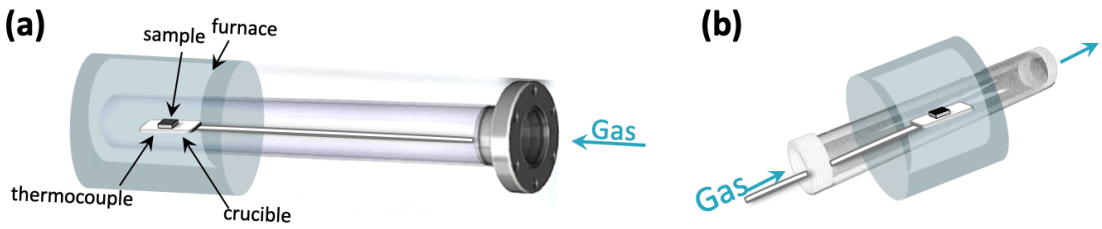

Fig. 2.5: Schematic representation of the furnaces used for the growth from vacuum.

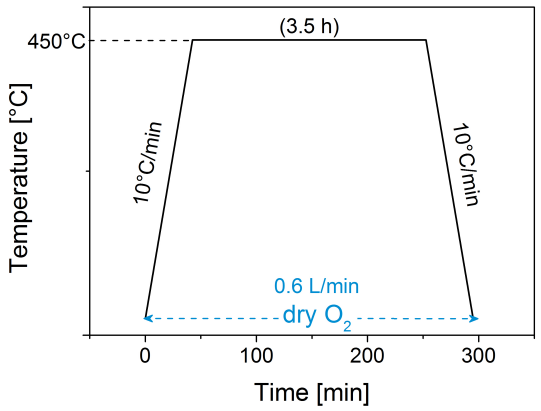

***Fig. 2.6**:* Thermal profile of the YBCO oxygenation step*, where the tetragonal to orthorhombic transformation occurs.*

2.2 Thermal Analysis (TA) techniques and methods

2.2.1 Precursor solution preparation

Single-component solutions were prepared by dissolving the corresponding metal acetates, YAc_3, $BaAc_2$ and $CuAc_2$, in propionic acid (Merck, ≥99%), kept under sonication until complete dissolution of the salt. Then methanol (VWR, ≥99.8%, non-anhydrous) was added in order to obtain a mixture of 1:1 in solvent composition and a metal concentration of $[Y^{3+}]$=0.25M, $[Ba^{2+}]$=0.5M and $[Cu^{2+}]$=0.75M. Film samples were obtained by depositing the initial solution on a $LaAlO_3$ (LAO) substrates and drying them at temperatures between 70-95°C for a few minutes. The film thickness (H) was estimated with the following equation:

$$H = {}^{m}/_{(d \cdot A)} \tag{2.1}$$

where m is the mass of the oxide or carbonate decomposition product at 500°C, d is its particle density, and A is the surface area of the substrate. The powder sample was obtained by drying the corresponding solution at 70-95°C. Single-crystals were also obtained for the Ba and Cu precursor solution over a time of a few months from crystallization from the stored vial at room temperature; they were recovered and dried in low vacuum (635 mmHg) prior to analysis. A powder obtained from an acetate-free solution was also prepared for comparison, dissolving the corresponding metal carbonate ($Y_2(CO_3)_3$, $BaCO_3$, $CuCO_3$, Sigma Aldrich) in propionic acid. Their chemical characterization and the analysis of their thermal behavior can be found in Chapter 3, and throughout this dissertation the above-mentioned solutions will be referred to as the **Cu** (**Y**, or **Ba**) precursor solution.

The study of the effect of triethanolamine (TEA), which can be found in Chapter 4, was based on the following materials. The single component solutions were prepared as previously described in a 1/1 mixture of propionic acid and non-anhydrous MeOH, to keep a stoichiometric ratio of 1/2/3 of, respectively, Y/Ba/Cu (labelled as sol. **TY**, **TB** and **TC**, 2-3 composition). Then, 5% v/v of triethanolamine (TEA, Merck, >99%) was added to each solution so that the final molar

proportions Y/Ba/Cu/TEA were close to 1/2/3/1.5. For comparison, solutions without propionic acid were prepared from the corresponding $MProp_x$ salts (when soluble) dissolved in MeOH with 5% TEA, keeping the same stoichiometric ratio and concentrations: **TY'** ($YProp_3$/TEA in MeOH) and **TC'** ($CuProp_2$/TEA in MeOH). Film samples were prepared from these solutions by drop casting over 10x10 mm $LaAlO_3$ (LAO) substrates; they were dried at ~80°C for a few minutes to remove most of the solvent while avoiding TEA evaporation and then decomposed in humid O_2 for thermal analysis experiments. The corresponding powders were obtained by peeling off the deposited films.

The study of binary solutions that can be found in Chapter 4 was done by mixing single salt solutions prepared in the way previously described. Solutions are referred to as **Cu-Ba** (**Cu-Y** and **Y-Ba**) binary precursor solution with 2-3 composition. Ternary solutions studied by thermal analysis were prepared as explained in section 2.1, with both 2-3 and 3-7 compositions (solution **T**) but with non-anhydrous MeOH.

For comparison, a ternary solution based on the 2-3 composition was also prepared starting from the same metalorganic precursors (metal acetates) but dissolved in a different mixture, a 1:3 of acetic acid and H_2O ($[M_{tot}]$=0.3M, solution **t'**. Finally, solutions **t''** and **t'''** were prepared varying the amount of propionate/acetate ligand in solution: sol. **t'''** is made up of $BaProp_2$, YAc_3, $CuAc_2$ in H_2O ($[M_{TOT}]$=0.5 M), while sol. **t''** consists of $YProp_3$, $CuAc_2$ and $BaAc_2$ in H_2O ($[M_{TOT}$=0.5M). Solutions labelled as **T** and **t** will be discussed in Chapter 4.

2.2.2 Thermogravimetry and Differential thermal analysis (TG-DSC)

Thermogravimetric analysis experiments were performed in a Mettler Toledo thermobalance, with a total flow of 70ml/min of high-purity gases at a total pressure of 1 bar; in inert atmosphere of argon or nitrogen, the total flow corresponds to the protective gas; for experiments run in an oxygen atmosphere, a reactive flow of 55ml/min was applied, with a 15ml/min flow of air as protective gas. Heating rates of 5°C/min were the most used ramps, but sometimes 10 and 25°C/min were also applied. Samples were decomposed in the form of films on 10x10 LAO substrates or as powders in 70-µl open alumina crucibles. A blank curve was previously registered to take into account the change in density of the gas with temperature as well as other systematic artifacts.

2.2.3 Thermogravimetry coupled with infrared evolved gas analysis (TG-FTIR)

TG-FTIR experiments were carried out according to the setup shown in Fig. 2.7, connecting a 30-cm steel tube heated up at 200°C from the gas outlet of the TG equipment to the gas inlet of an infrared spectrometer by Bruker (Alpha II), equipped with a gas cell, also kept at 200°C to minimize condensation. Signal/noise ratio is affected by i) volatiles dilution over time, which is lowered when slow mass stages take place, especially for films where the amount of material is little and ii) by condensation effects, especially for high boiling temperature species like TEA. Spectra were then subtracted by a background and a characteristic wavelength for each volatile is plotted against temperature. Normally the frequencies (cm^{-1}) chosen are: 2355 for CO_2, 1732 or 945 for 3-pentanone, 2820 for TEA, 1145 for propionic acid, 2741 for acetaldehyde; when they overlap with others, a different representation is chosen, and the wavelength does not necessarily correspond to that of the most intense band. FTIR reference spectra are based on the NIST database [84].

2.2.4 Thermogravimetry coupled with mass spectrometry evolved gas analysis (TG-MS)

TG-MS experiments were run connecting a 1-m-long steel capillary tube from the TG to a turbomolecular pump and a quadrupole; this was necessary to adapt the atmospheric pressure of the TG equipment to the vacuum required for the quadrupole to operate ($<10^{-7}$ bar). Given the long path of the volatiles, the sensitivity of this technique is very low and it could be only applied to powder samples.

2.2.5 Evolved gas analysis in vacuum

EGA-MS experiments were run placing the film at one closed end of a quartz tube, on an alumina surface equipped with a thermocouple; a low-resistance furnace was placed around the sample area while a thermocouple in contact with the substrate is used to measure the sample temperature. The furnace is controlled with a proportional-integral-derivative (PID) controller that takes the sample temperature as a control parameter. The other end of the quartz tube was connected to a quadrupole mass spectrometer (MS-Q) analyzer by MKS instruments. The vacuum was reached by pumping the system to $P_{tot} \leq 10^{-7}$ bar with the aid of a turbomolecular pump. MS analysis was based on the NIST database [85].

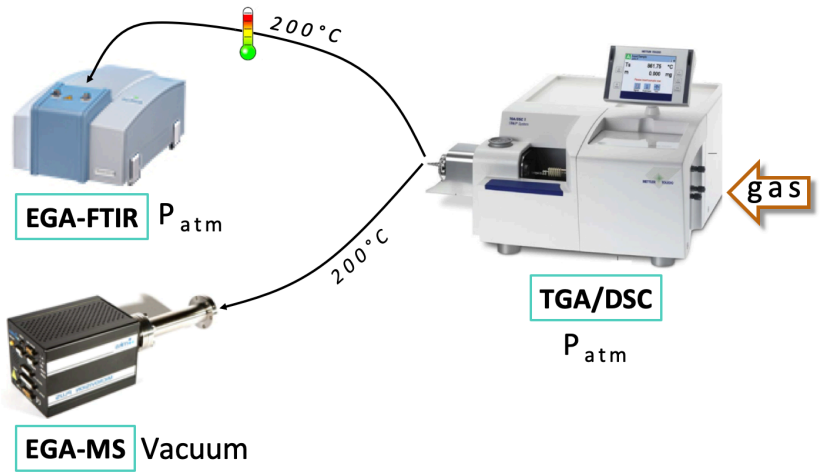

Fig. 2.7: Schematic representation of thermal analysis techniques. *TG-DSC and hyphenated techniques are shown (TG-IR and TG-MS).*

2.2.6 Measurement of the thermal conductivity

Thermal conductivity for $Y(C_2H_5CO_2)_3$ was calculated with a method developed by [86,87], from the slope of the differential scanning calorimetry (DSC) melting peak of a selected metal (indium). The method is based on the principle that the heat flow is influenced by the resistance of the sample in contact with the metal bead. Experiments were conducted in nitrogen flow (40ml/min) with a heating rate of 10K/min in the temperature range 50-200°C; to achieve the desired geometry, an indium bead of 2.0 mm in diameter was set on the top center of a 70µl-alumina crucible filled with the powder sample, without lid.

2.2.7 Measurement of the specific heat capacity

The specific heat capacity, *c,* was determined by DSC. In particular the relationship between the DSC signal and the heat capacity is:

$$DSC = -c\ m\ \frac{dT}{dt} \tag{2.2}$$

DSC experiments were conducted under a 40ml/min nitrogen flow and at a heating rate of 10K/min in the range 50-180°C, with isotherms of 5 minutes at 100°C, 140°C and 180°C. The Al_2O_3 reference signal and the sample signal were both corrected by a blank curve obtained in the same conditions, and with the same aluminum pan as reference crucible (20 µl aluminum pans covered with a pierced lid).

The specific heat capacity was obtained for three different temperatures (100, 140, 180°C). Since it is value is a function of temperature, we chose the closest value to the combustion temperature.

2.2.8 Kinetic analysis

Kinetic methods [88,89] are theoretical models applied to thermal analysis experiments in order to characterize solid state transformations, by deriving kinetic parameters such as the activation energy (E_a) or the pre-exponential constants. Transformations in general can be isothermal and non-isothermal: the latter are the field of thermal analysis techniques, which monitor the evolution of a parameter as a function of the temperature.

Non-isothermal transformation can be studied with model-fitting or model-free methods: the latter are independent of the particular mechanism governing the transformation and are thus called isoconversional methods because they analyze the evolution of a system parameter (temperature, transformation rate..) as a function of the degree of transformation, α. In turn, isoconversional methods can be differential or integral, exact or approximate based on the solution of the following equation:

$$\frac{d\alpha}{dt} = k(T) \cdot f(\alpha) \tag{2.3}$$

Where $k(T)$ is the reaction rate which generally follows an Arrhenius dependence ($k(T) = Ae^{-E/RT}$) for thermally activated processes, while $f(\alpha)$ is the function that describes the degree of transformation for the particular reaction considered. For non-isothermal transformations, in the simplest case of constant heating rate ($\beta = \frac{dT}{dt}$), eq.2.3 becomes:

$$\frac{d\alpha}{dT} = \frac{1}{\beta} \cdot Ae^{-E/RT} \cdot f(\alpha) \tag{2.4}$$

Rearranging the previous equations with the help of logarithmic functions and applying the Friedman isoconversional method, it becomes easy to plot the evolution of a system parameter measured from thermogravimetric experiments, for example $\ln(d\alpha/dt)$, versus $1/T$ in order to obtain E_a from the slope.

The activation energy (E_a) and the pre-exponential constant (A) were obtained performing four TG experiments at 2.5K, 5K, 10K and 20K in the conditions of interest. In the case

of $YProp_3$ (see Chapter 3) the conditions were ~2mg of powder in alumina pan (70µl) decomposed in humid O_2. In the case of $BaCO_3$, films on LAO substrates (10x10 mm, obtained from pyrolysis of 2-3 ternary solution **D** in humid O_2) were decomposed in a 80ml/min-flow of dry N_2. The raw data was elaborated using a free in-house software called "pics", which can run calculations with several kinetic methods. The kinetic values were calculated using the exact differential isoconversional Friedman method [88,89], due to the good accuracy and simplicity of the method. In particular, this choice was led by the fact that the kinetic analysis is applied to thermal decompositions (in the simplest case of constant heating rate), which can be approximated to single-step reactions were the reverse reaction is prevented.

2.2.9 Thermal explosion

In the case of exothermic reactions, in constant heating experiments the sample may undergo a thermal runaway when the time to dissipate the heat generated by the reaction is larger than the characteristic reaction time. In particular, the critical film thickness (H_{cr}) at which a thermal runaway would happen for the sample in the form of film is given by the following relationship [90]:

$$H_{cr} = \frac{R_G T_{Kis}^2}{E_A}\sqrt{\delta_{cr}\frac{ca}{qb}} \tag{2.5}$$

As for powders inside a crucible of radius R filled up to a height H, the critical mass (m_{cr}) is given by [90]:

$$m_{cr} = 5\pi\rho a\frac{t_R}{\theta_T}\frac{0.878R^2+2H^2}{H(1+2\varepsilon)\left\{1-(2+\varepsilon+30\varepsilon^2)\frac{2}{\theta_T}\right\}} \tag{2.6}$$

Where T_{Kis} is the temperature at which the reaction rate is at its maximum, and can be calculated from the Kissinger equation [91–93]:

$$\frac{E_A}{R_G T_{Kis}^2} = \frac{a}{b}e^{-E_A/R_G T_{Kis}} \tag{2.7}$$

R_G is the universal gas constant, E_A is the activation energy, a is the thermal diffusivity ($a \equiv \frac{\lambda}{\rho c}$), c is the specific heat capacity of the sample, q is the heat of reaction (Enthalpy) and b is the heating rate. From these parameters, δ_{cr}, t_R, θ_T and ε were calculated as follows:

$$\delta_{cr}=5C_{TF}[(1+2\varepsilon)(1-(2+\varepsilon+30\varepsilon^2)\frac{2}{\theta_T}]^{-1}$$

$$t_R=(Ae^{-E_A/R_G T_{Kis}})^{-1} \qquad \theta_T=\frac{E_A}{R_G T_{Kis}^2}\frac{q}{c} \qquad \varepsilon = R_G\, T_{Kis}/E_A \tag{2.8}$$

If the radius R is known, Eq. 2.6 can be solved for H if we replace m_{cr} in eq 2.6 by:

$$m_{cr} = \pi\rho R^2 H \tag{2.9}$$

Substituting Eq. 2.9 into Eq. 2.6 we obtain,

$$1 = 5a\frac{t_R}{\theta_T}\frac{0.878/H^2+2/R^2}{(1+2\varepsilon)\left\{1-(2+\varepsilon+30\varepsilon^2)\frac{2}{\theta_T}\right\}} \tag{2.10}$$

Once H is determined from Eq.2.10 , the critical mass m_{cr} can be obtained from Eq. 2.9.

Therefore, from the physical parameters discussed in the previous sections, we were able to calculate, for experiments performed in humid O_2, the critical film thickness, H_{cr}, and the critical mass, m_{cr}, for powders inside a 70-µl alumina pan (finite cylinder geometry, radius R =2.475 mm).

2.3 Thermochemistry calculation with computational methods

Thermochemistry calculations were applied to the study of the thermal decomposition of metal propionates, in particular to $CuProp_2$, in order to understand the degree of degradation of the propionate chain.

Ab-initio theoretical calculations were performed within the framework of Density Functional Theory (DFT) as implemented in the VASP (Vienna Ab-initio Software Package) code [94,95]. All models are periodically replicated through space in all directions, in order to obtain a more accurate description of the solid phases investigated experimentally, as no boundary effects are to be taken into consideration. The theoretical investigation of $CuProp_2$ and CuO was designed to accurately model their electronic structure as a bulk solid. Database structure files for solids were obtained from the American Mineralogist Crystal Structure Database (AMCSD) for CuO (AMCSD code 0018812) and for $CuProp_2$ from the Cambridge Crystallographic Data Centre (CCDC code 1133510). Database structure files were converted into periodic models. The experimental unit cell was relaxed towards the computational minimum energy structure, identified using a built-in DIIS minimization algorithm with a convergence force threshold of 10^{-2} eV/Å. The electronic structure of the investigated molecules and materials was modelled using PAW (Projected Augmented Wave) potentials [96] for the core electrons and plane-wave basis sets with a 850 eV cutoff for valence. Electronic exchange and correlation effects were approximated using the Perdew-Burke-Ernzerhof (PBE) functional [97]. Further corrections for long-range interactions were applied using the semi-empirical Grimme D3 dispersion model [98].

The electronic structure was evaluated differently for gas phase and solid phase systems. For the former, a single K-point was considered sufficient to evaluate the electronic structure, due to the unit cell size having been optimized to minimize the interaction between different replicas of the molecule. For the latter, a K-point grid was obtained using the Monkhorst-pack method and its size was optimized until further increases did not correspond to any change in total energy. Convergence of the electronic self-consistent field (SCF) calculations, set below a 10^{-5} eV threshold, was determined employing Blochl corrected smearing for calculation investigating solid materials, and Gaussian smearing for gas-phase molecules.

The experimental values of enthalpy (Δ_rH exp) were obtained integrating the area of the differential scanning calorimetry (DSC) signal of the TG/DSC experiments with a straight base line in the temperature region corresponding to the decomposition peak. This area was then corrected by the mass (or moles) of the $CuProp_2$ involved in each mass-loss step, obtained from the information retained in the thermogravimetric curves.

Although the experimental values consisted of reaction enthalpies (Δ_rH) at temperatures higher than room temperatures, the theoretical investigation was limited to the calculation of the electronic energy (Δ_rE) of the corresponding reactions. Comparison of theoretical and experimental values is interesting due to the fact that it helps to rule out reaction schemes and to

understand the main contribution of a given reaction to the decomposition path, but a more quantitative analysis was beyond the scope of this work.

2.4 Chemical characterization techniques

2.4.1 Fourier Transform Infrared spectroscopy (FTIR)

Infrared spectra of solid samples were collected with an ALPHA spectrometer from Bruker, in attenuated total reflection (ATR, model Platinum). A background spectrum is recorded prior to any measurement to remove water and CO_2 contribution coming from the atmospheric air. Measurements can be run on both powder and film samples.

2.4.2 X-ray diffraction (XRD)

Several ex-situ XRD measurements were performed based on the type of sample and information required:

- X-ray measurements of powders were carried out with a Cu-Kα X-ray beam of a D8 ADVANCE diffractometer from Bruker AXS, with a voltage of 40 kV and a 40-mA current at the university of Girona.
- Single-crystal XRD measurements were performed with 50 kV and 20 mA in a three-circle diffractometer by Bruker (D8 QUEST ECO) at the university of Girona; the system was equipped with a PHOTON II detector (CPAD) and a doubly curved silicon crystal monochromator, and operated with a Mo Kα (λ= 0.71076 Å) X-ray source.
- YBCO Films were characterized with a General Area Detector Diffraction System (GADDS) from Bruker-AXS (model D8 Advance) which permits the quantitative analysis of crystallinity and orientation of the material thanks to the fact that a large area of the reciprocal space can be observed in one single frame (Fig. 2.8), contrarily to the point detector. In this frame, the presence of diffraction rings signifies that the material is polycrystalline; conversely, single spots indicate texture; intermediate scenarios will be represented by incomplete rings. The diffractometer is equipped with a bidimensional Vantec-500 detector, operating at 40 kV and 20 mA and a Cu-Kα X-ray beam. Usual conditions for a GADDS scan were 2θ=35, ω =10, φ=0, χ=90 and acquisition times of 15 minutes. All measurements were carried out at ICMAB.

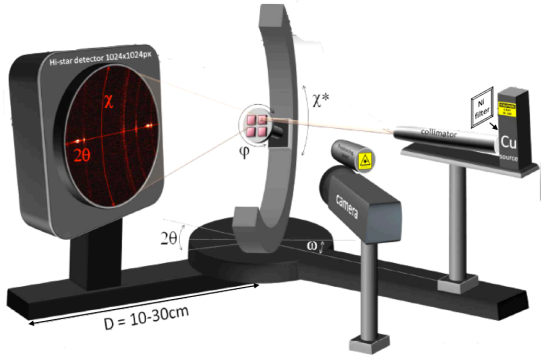

Fig. 2.8: Schematics of XRD analysis on films.

- Non-epitaxial phases in films were characterized with a A25 D8 Discover diffractometer from Bruker-AXS equipped with LinxEye XE-T detector (High-Resolution Position Sensitive Detector with Energy Resolution) in grazing incidence (GIXRD). Conversely, high resolution scans were obtained with the same equipment with 2s time per step, 0.02° stepsize and 1D detector. Rocking curves (or ω scans) were performed on a fixed 2θ position, the YBCO (005) reflection; analysis of the FWHM (Δω) of these peaks provides information about the crystallinity of the sample, which decreases with the broadening of the peak. All above-mentioned measurements were performed at ICMAB.

In situ XRD experiments were performed with a 6-circle diffractometer at the DiffAbs beamline (Fig. 2.9) of SOLEIL Synchrotron, in Paris. All the in-situ data was collected in two runs, during a period of 6 full-day each at SOLEIL. The beamline was equipped with a furnace to follow the XRD phase time-evolution and an area detector (XPAD, X-ray pixel area detector).

The samples were fixed on the heater with a dome screwed in. Two different heaters were used: a DHS 900 (equipped with a peek dome) with maximum heating rate of 30°C/min and a DHS 1100 (equipped with a graphite dome) with maximum ramps of 300°C/min. The heater was connected to a system prepared to achieve different total pressures (P_{TOT}) and oxygen partial pressures (P_{O2}). The system was operated with vacuum pumps and mass flow controllers. Needle valves were used to set the total pressure while electrovalves were used to remotely switch from one system to the other, so that the pressure jump could be operated from the control room. An oxygen sensor was used to pre-set the P_{O2}. For the pressure jump, different combinations of N_2 and air bottles were applied. A schematic diagram of the system can be found in Fig. 2.10.

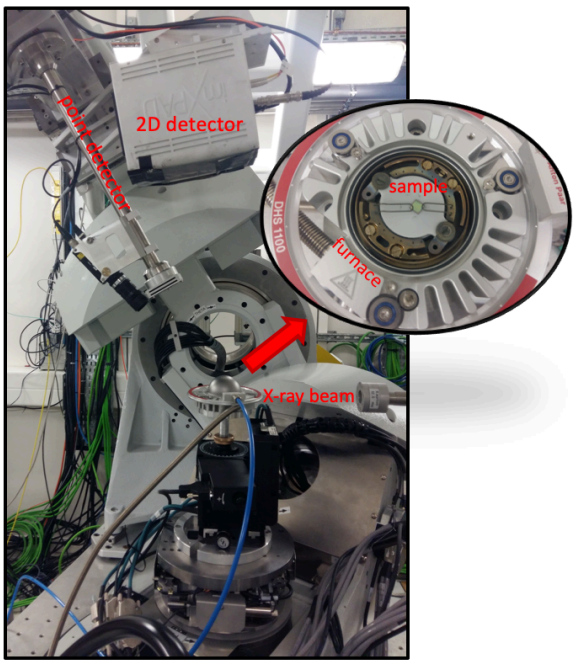

Fig. 2.9: DiffAbs beam-line of SOLEIL synchrotron*, showing the 6-circle diffractometer with the furnace setup*

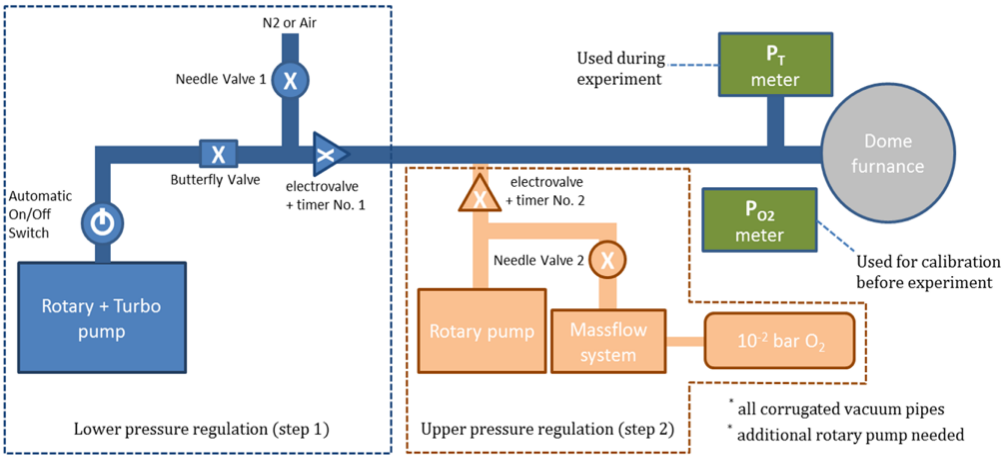

***Fig. 2.10**:* Schematics of the experimental setup at SOLEIL Synchrotron. *To control P_{O2} - T conditions, different pumps and valves were combined.*

Experiments were run with a beam energy of 18 KeV and two different acquisition times: 500 ms (to register the phase evolution before YBCO growth) and 100 ms (to record YBCO growth). To follow the time-evolution of non-epitaxial phases, grazing XRD scans were recorded at angles of ω=4 and δ (=2θ)=-4.5, while to follow YBCO growth ω=7.9-8.1 and δ=-4.5 were used to meet the Bragg conditions with the YBCO (005) reflection.

The data was recorded as 2D scans in 2θ-χ for each temperature/time value (Fig. 2.11a), which was then integrated to obtain the relative intensity-2θ scans for each acquisition point (Fig. 2.11b, reporting an example of the oxidation of metallic copper to $BaCu_2O_2$ and Cu_2O followed by YBCO(005) growth upon a pressure increase at a fixed temperature). The treatment of the raw data was elaborated by PhD student J. Banchewski, in our group.

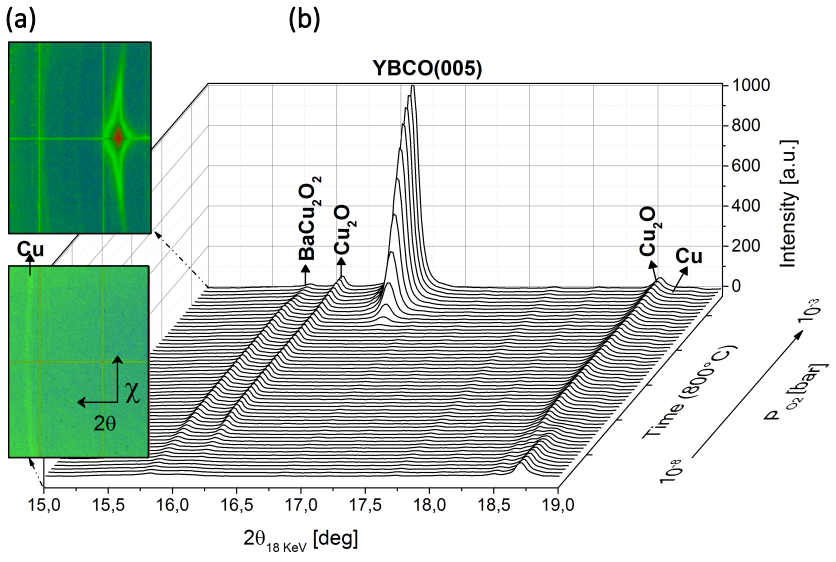

***Fig. 2.11**:* Representation of the data from in-situ experiments at SOLEIL. ***(a)** 2θ- χ images and **(b)** their integration in χ for each acquisition time delivers 2θ- intensity scans that can be plotted versus time/temperature.*

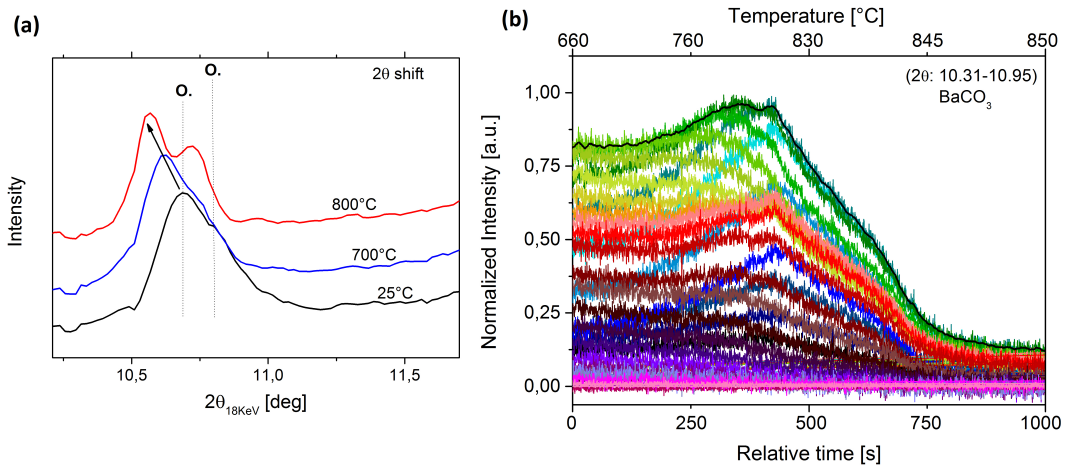

***Fig. 2.12**: Data analysis procedure from in-situ experiments. **(a)** XRD scans at different temperatures from in-situ experiments, showing the 2th shift due to the temperature increase. **(b)** Evolution of the 2θ range relative to the peak shown in (a).*

Note that a significant 2θ shift occurs due to the temperature variation during the experiment (Fig. 2.12a, example for the peak relative to the orthorhombic *O.* $BaCO_3$ phase). To take into account this aspect, once the raw data was treated, in-situ analysis proceeded in the following way: the evolution of a specific phase over time was obtained plotting a selected 2θ range (different for each phase) versus time (or temperature); then, the sum of all the 2θ contribution was then chosen as the final phase evolution, as shown in Fig. 2.12b (thin black line).

2.4.3 Elemental Analysis

CHNS elemental analysis (EA) was performed with a Perkin Elmer 2400 series elemental analyzer. Standard deviations range from +/- 0.03 to 0.4 for the reported % values relative to C, and from +/- 0.04 to 0.1 for the % values relative to H. On the other hand, the detection limits are 0,20% for H and 0,72% for C.

2.5 Physical characterization techniques

2.5.1 Superconducting quantum interference device (SQUID) measurements

A commercial superconducting quantum interference device (SQUID) magnetometer from Quantum Design equipped with a superconducting magnet of 7 T was used to record the magnetic properties of the films at ICMAB. SQUID measurements were run on both YBCO films and YBCO precursor samples.

For YBCO films, this technique was used to evaluate the critical current density, J_c.

J_c(T) measurements are performed in Zero Field Cooled conditions (ZFC) by cooling down the films to 5K in self-field; then the magnetic moment is saturated with a 5T magnetic field which is suddenly removed: J_c(T) is then measured during the temperature increase and no external field.

Conversely, $J_c(H)$ is measured at constant temperature upon an increase of the magnetic field up to 7 T in the hysteretic magnetization curves.
Inductive critical current densities were derived from the following equation:

$$J_c = \frac{3m}{\pi R^3 t} \quad (2.11)$$

Where m is the magnetization value, R is the radius (approximated to 2.57 mm for 5x5 mm^2 samples) and t is the sample thickness.

For YBCO precursor samples in the form of powder: magnetic measurements were performed on Cu-containing species (Chapter 3.2) to obtain the magnetic susceptibility (χ). All measurements were carried out in a magnetic field of 1000 Oe and corrected for the blank of the sample holder (diamagnetic gel capsule). χ was then obtained in c.g.s. units with the following formula:

$$\chi = \text{Magnetic moment (emu)} / \text{Field (Oe)} / \text{Cu moles} \quad (2.12)$$

2.5.2 Electrical transport measurements

Electrical transport measurements were carried out at ICMAB by a member of our group, J. Banchewski, using a PPMS Quantum Design system with the Van der Pauw method. The method relies on the use of 4 electrodes, or ohmic contacts, placed along the sample perimeter, to directly measure the voltage drop caused by an applied electrical current. Measurements can be performed while increasing the temperature or changing the magnetic field, B. From the voltage and knowing the film thickness, the resistivity as a function of the temperature and the Hall carrier density as a function of B can be determined. Critical temperature values were determined with the derivative criterion from the resistivity plot as a function of the temperature.

2.5.3 Optical microscopy

Film samples were observed with an optical microscope from Zeiss Jenavert, in order to evaluate the quality of the sample, such as the presence of cracks and buckling after pyrolysis. Samples showing any of these features were discarded before growth.

2.5.4 Scanning electron microscopy (SEM)

Surface morphology characterization was carried out with a FEI QUANTA 200 FEG SEM of FEI CompanyTM at ICMAB. No specimen preparation is required since the final YBCO films, after oxygenation, is electrically conductive.

The samples are placed in a high-vacuum chamber and bombarded with a focused beam of high-energy electrons. From the interactions of this beam with the atoms of the sample, several signals are generated containing information about topography and composition of the sample. In particular, secondary electrons are produced which are transformed into an image containing topographic information. Conversely, the X-rays emitted from the expulsion of electrons in excited atoms bombarded by the incident beam permit to identify the chemical composition of specific areas of the sample, i.e. single grains. This last technique is called Energy Dispersive X-ray Spectroscopy (EDX).

Surface characterization can deliver important information regarding the texture (for example, a/b grains can be clearly identified from their needle-like structure) and the homogeneity of the film (i.e. presence of holes or large grains).

2.5.5 Transmission electron microscopy (TEM)

The microstructure of the films was studied with a scanning transmission electron microscopy (STEM) using two different instruments: a FEI Titan 60-300 microscope equipped with an X-FEG gun, a CETCOR probe corrector and a Gatan TRIDIEM 866 ERS energy filter operated in STEM mode at 300 kV. This equipment was used at the Advanced Microscopy Laboratory in Zaragoza, Spain, and images were collected by members of our group, Dr. Roger Guzman and Dr. Bernat Mundet. On the other hand, a FEI Titan 80-200 CREWLEY, equipped with a Cs probe-corrector, a Super-X EDX system and operated at 200kV, was used at the Ernst-Ruska Center in Jülich. Images were collected by Dr. Max Sieger and Dr. Alexander Meledin.

Samples for STEM were prepared with conventional methods, such as FIB (Focus Ion Beam) and Ar ion milling.

Complementary techniques for chemical composition studies were coupled to TEM analysis: in particular, EELS (Electron Energy Loss Spectrometry) identifies the quantity and type of atoms present in a specific sample area by measuring the change in kinetic energy of the electron beam after they interact with the sample. Complementary to EELS, EDX analysis can also be coupled to TEM and it was specifically used at the Ernst-Ruska Center in Jülich for most of the chemical characterization.

TEM images are crucial to characterize the YBCO matrix, identify crystalline phases and lattice defects.

PYROLYSIS STUDIES OF THE METALORGANIC PRECURSORS

Chapter 3

3.1 Thermal decomposition of Yttrium propionate

This first section will analyze the thermal behavior of the yttrium precursor solution prepared as described in Chapter 2 from the acetate salt in propionic acid. Its thermal behavior will be studied with the aid of thermal analysis techniques and chemical characterization methods to understand the pyrolysis in different atmospheres and sample geometries. In particular, the difference between film and powder decomposition will be highlighted and clearly demonstrated in terms of decomposition temperatures and volatiles. Three main reaction routes take place: hydrolysis, oxidation and the radical path. Once the general decomposition mechanism is understood, it will be put into context of the pyrolysis of the CSD-YBCO solution.

3.1.1 Characterization of the initial product

The FTIR and XRD pattern of as-deposited YProp3 are shown in Fig. 3.1a and b, respectively. Since the FTIR spectra of both the film and powder samples are nearly identical, their chemical structures are expected to be the same; both show the appearance of the propionate stretching bands (absent in the acetate). Also the results from elemental analysis (Table 3.1) of the dry YProp3, obtained from the corresponding YAc3 solution, agree with the expected composition of YProp3, providing further support for the replacement of acetate groups by propionates. Conversely, although the XRD pattern of the present work is similar to [32], there are significant differences between our FTIR and XRD pattern and those reported in the literature [32,35–37], also there are significant differences among the different structures reported in the literature. Indeed, in carboxylates, the carboxylate bond and the crystalline structure depend strongly on the presence of crystallization water [99–102], so that the distance between the asymmetric and symmetric carboxylic bands [$\Delta\nu = \nu_{as}(COO^-) - \nu_s(COO^-)$] can be used to determine the type of carboxylate-to-metal complexation structure [36,100,103–105]. Thus, for propionates, by comparison between $\Delta\nu$ and that of sodium propionate ($\Delta\nu_{Na\text{-}prop}$=134.6 cm^{-1}) [106] it has been proposed that [100,103] a chelating coordination exists when $\Delta\nu << \Delta\nu_{Na}$-prop, bridging coordination occurs when $\Delta\nu \leq \Delta\nu_{Na\text{-}prop}$, while monodentate coordination appears when $\Delta\nu >> \Delta\nu_{Na\text{-}prop}$.

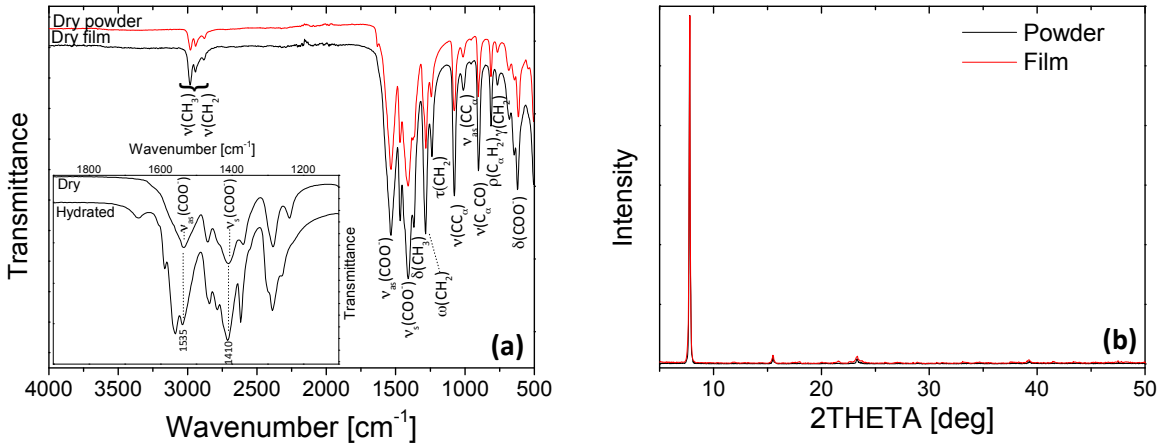

Fig. 3.1: Chemical characterization of the Y metalorganic precursor. ***(a)*** *Infrared spectra and* ***(b)*** *XRD of the* $YProp_3$ *film and powder initial product.*

Compound	Found (Expected)	
	wt%C	wt%H
YAc_3 (anhydrous)	(27.09)	(3.41)
$YProp_3$ (anhydrous)	34.36 (35.08)	4.59 (4.91)
B (O_2, 600°C)	0.98	-
D' (N_2, 600°C)	-	-
F (vacuum, 500°C)	9.69	-

Table 3.1: Elemental analysis of the Y precursors. *Initial compounds and decomposition products of* $YProp_3$ *are reported. (-) values inferior to detection limits.*

Nasui et al [36] obtained $\Delta\nu$=135 cm^{-1}, which was assigned to a mixed structure of chelating and bridging. From XRD, Martynova et al [105] found three different coordination modes for the carboxylate ligands in $YProp_3$ monohydrate: tridentate chelating-bridging, bidentate chelating and bidentate bridging, reporting a splitting of ν_{as}(COO-) and ν_s(COO-) in three bands that can be assigned to these different structural functions of the ligand. In this work, the shape of ν_{as}(COO-) and ν_s(COO-) of the dry salt does not show a clear splitting, but different coordination modes that are compatible with the results of Nasui and Martynova are nevertheless present. In fact, from the FTIR spectra of our dry $YProp_3$ films (Fig. 3.1a), $\Delta\nu$=125 cm^{-1}, suggesting the presence of a bidentate chelating coordination mixed with some bridging coordination.

It is important to note that the modes of the carboxylate binding depend on the presence of crystallization water (see inset in Fig. 3.1a) but, since decomposition is not coupled to dehydration, once dehydration is completed, the evolution of the decomposition of the propionate should be independent of the initial structure and water amount.

3.1.2 Dehydration and solvent evaporation

The decomposition as a function of temperature, for films deposited on LAO substrates, was monitored by TG (Fig. 3.2) coupled to EGA-FTIR and EGA-MS.

For films, the first mass loss starts during the drying stage at 80°C and corresponds to water and propionic acid evaporation; it is also observed by TG for thick films until 150°C. This is expected since solvent removal depends on time and film thickness; in fact, the boiling point for the acid is relatively high (140°C) and the remaining powder is very hygroscopic. Thus, between drying stage and TG experiment, atmospheric water may be absorbed.

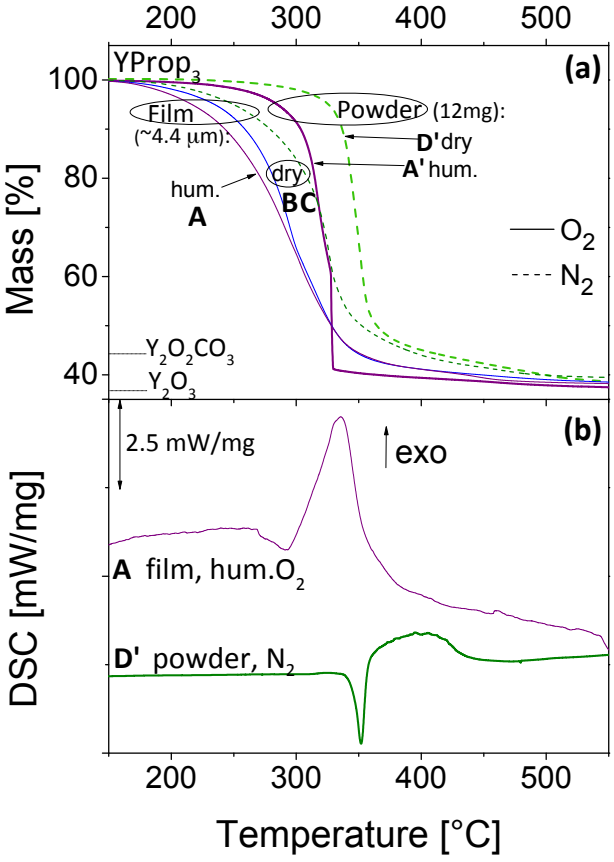

Fig. 3.2: TG-DSC analysis relative to $YProp_3$ decomposition. *Effect of atmosphere and sample layout on* ***(a)*** *TG curves and* ***(b)*** *DSC signal at 5K/min.*

3.1.3 Thermal decomposition at atmospheric pressure: organic ligand

It has long been established that in inert atmosphere salts of carboxylic acids thermally decompose to yield CO_2 and symmetrical ketones as major products [33,34], following a free-radical reaction [107–109]. The same volatiles where observed by Grivel [32] for the thermal decomposition of $YProp_3$ in Ar, proposing the reaction scheme **α** (radical) shown in Fig. 3.3: the mechanism results in a single dTG peak and an oxycarbonate intermediate that then yields yttria.

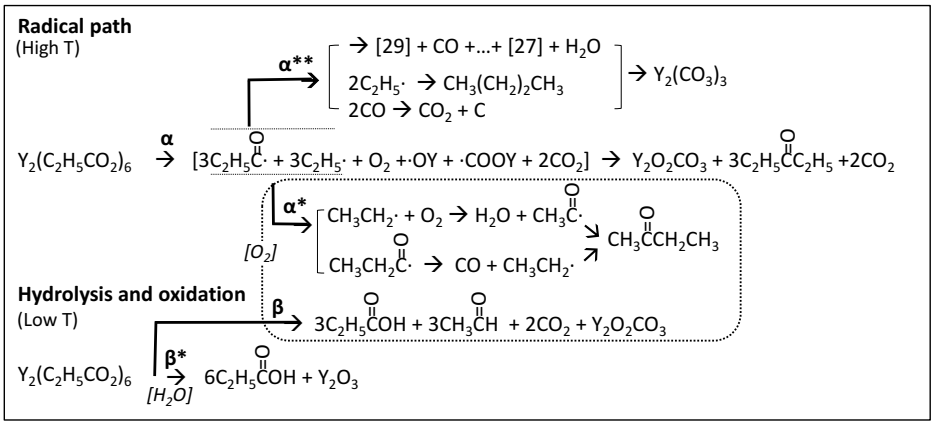

Fig. 3.3: Proposed reaction scheme for $YProp_3$ decomposition.

In agreement with this scenario, for $YProp_3$ powder in inert atmosphere (both N_2 and Ar, Fig. 3.4**D'**) we observe a single-step reaction around 355°C where the main volatiles are 3-pentanone and CO_2 (by EGA-FTIR and EGA-MS), and it is in agreement with the presence of an endothermic peak in the DSC signal (Fig. 3.2) at 355°C that is consistent with the formation of radicals. Thus, in inert conditions, the homolytic cleavage of the molecule and the recombination of the acyl and alkyl radicals would result in the formation of the symmetrical ketone 3-pentanone.

However, when the same compound was studied in inert conditions but after deposition on a substrate, the volatiles identified by IR are mainly propionic acid, along with the symmetrical ketone (Fig. 3.4**C**). Since both powder and film are obtained from the same solution, this difference can be attributed to the fact that films are much more sensitive to residual atmospheres than powders [23,110]. The effect of the residual oxygen was confirmed by increasing the flow of nitrogen in the TG; the higher the nitrogen flow, the higher the amount of 3-pentanone and the smaller the formation of propionic acid. Conversely, in a humid oxygen atmosphere, Fig. 3.4**A**, we observe that 1) the peak related to propionic acid is more prominent while 3-pentanone is no longer observed; 2) the evolution of propionic acid is shifted to lower temperatures and 3) the single step process in inert atmosphere becomes a two-step decomposition with splitting of the DTG signal into two peaks. IR analysis of volatiles shows that the first step is related mainly to the formation of propionic acid while the second step to CO_2 and acetaldehyde. The same behavior is observed with a flow of dry oxygen, although in this case the relative prominence of the first step is less significant than in the case of a humid atmosphere (Fig. 3.4**B**, 2-µm film), and, for thicker films (~4µm, Fig. 3.4**B**), the splitting is only evident in humid O_2, suggesting that water vapor favors the removal of the propionate groups as acid.

Since in the presence of oxygen degradative oxidation is likely to take place, for films in a dry O_2 atmosphere decomposition can be triggered by the oxidation of the propionate groups to acetaldehyde, CO_2 and propionic acid to produce the reaction scheme shown in **β** (Hydrolysis + oxidation) of Fig. 3.3. This is in agreement with the volatiles observed and the DSC signal in Fig. 3.2 which is no longer endothermic. Clearly, in humid O_2 and humid N_2 (not shown), the formation of propionic acid independent from acetaldehyde and CO_2 is due to the occurrence of mechanism **β*** in water vapor and low temperatures. However, **β*** does not reach completion in humid O_2 or in humid N_2 because, at higher temperatures, it is interrupted by the occurrence of **β** and **α**, respectively.

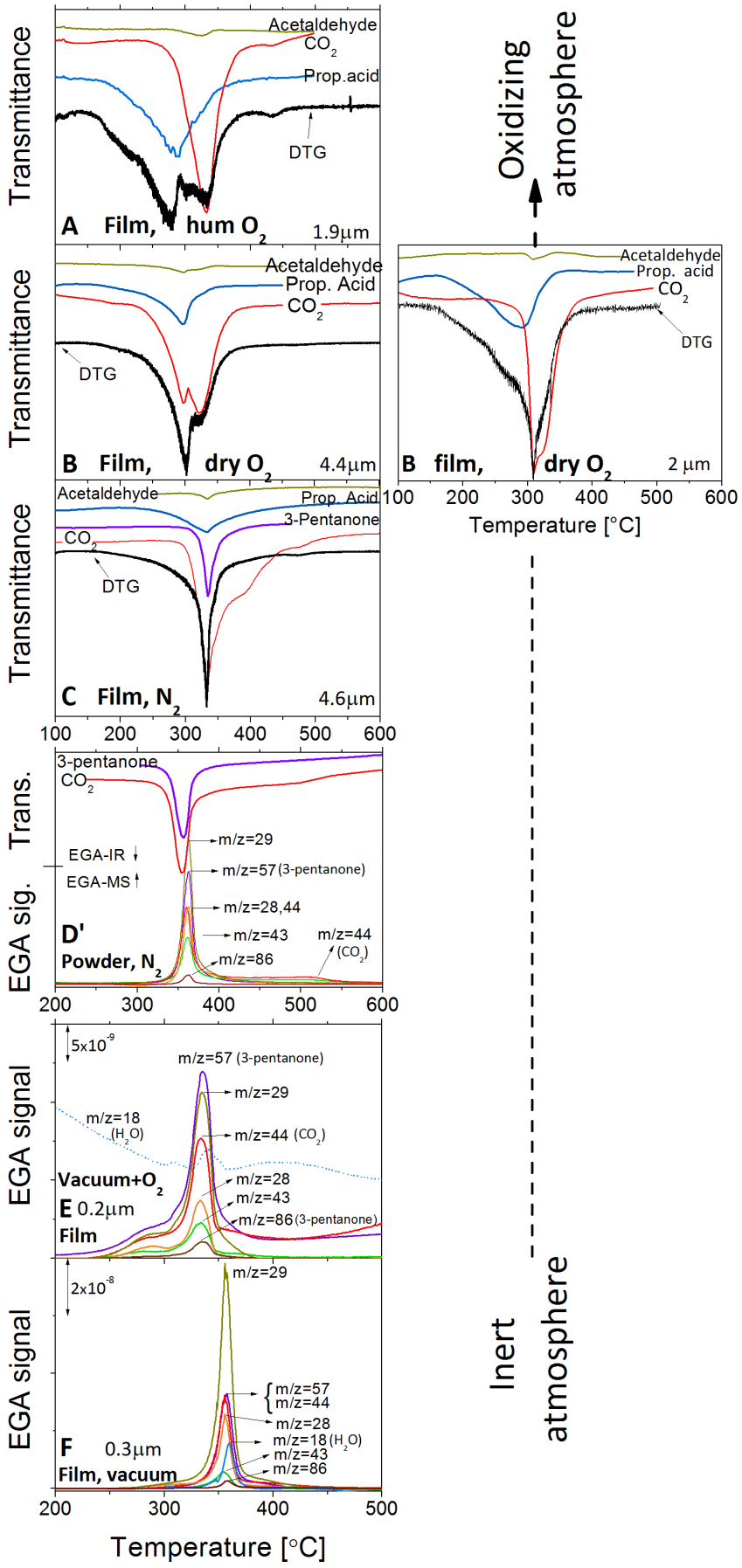

Fig. 3.4: EGA analysis of $YProp_3$ at 5K/min. *Films and powders are shown in different atmospheres.*

Finally, in dry N_2 (**C**) and relatively thick films, 3-pentanone formation was observed with propionic acid and thus **β** and **α** (favored by the presence of residual O_2 and water vapor in the TG furnace) are competing, given the impossibility of creating a fully inert atmosphere in thin films [26,110].

3.1.4 Thermal decomposition at atmospheric pressure: oxycarbonate

Both paths, **α** and **β**, lead to the formation of an oxycarbonate (expected relative final mass ~ 44%): quenches of the solid residue in Fig. 3.5 at around 52% in relative mass show the disappearance of CH_x groups with the increase of the COO^- stretching bands. From literature, yttrium carbonate decomposes to form yttrium oxycarbonates between 350 and 470°C [111,112]. $Y_2O_2CO_3$ is stable up to 470°C and decomposes in a single step to form yttrium oxide between 500 and 600°C [113,114]. From Fig. 3.4**A** we observe a peak in the evolution of CO_2 around 440°C for films in humid oxygen that can be attributed to the decomposition of $Y_2O_2CO_3$. Indeed, the observed mass loss and the FTIR spectra in Fig 3.5 confirm this conclusion. Conversely, for films in nitrogen (Fig. 3.4**C**), we observe that the decomposition is completed at a higher temperature (470°C) and two peaks related to the evolution of CO_2 are observed. This stage is much slower and gradual compared to experiments performed on films in O_2. The formation of CO_2 at higher temperatures is the result of the removal of carbon rich residues, which occurs through reaction with oxygen. Therefore, the more inert the atmosphere (and the longer CO_2 out-diffusion path going from films to powder), the higher the final decomposition temperature. In fact, for the powder sample in nitrogen, the decomposition of the oxycarbonate is shifted to even higher temperatures (540°C, Fig. 3.4**D'**), and the sample quenched at a relative mass of 50% (380°C), is greyish, in agreement with the presence of some elemental carbon. On the other hand, quenches of the corresponding film in oxygen were white at both 50% and 41% in relative mass.

These facts account for the different final decomposition temperatures reported in the literature. For instance, despite the fact that the XRD pattern shows the formation of Y_2O_3 at 600°C (Fig. 3.5), the FTIR of the solid residue shows that decomposition is not fully completed at 600°C for both powder and film; complete removal of COO- bands in the range 1400-1500 cm^{-1} is only observed after heating up to 1200°C. Additionally, given the fact that, for films, more than one CO_2 peak is detected by EGA-FTIR, it is possible that, prior to the oxycarbonate, the decomposition passes through $Y_2(CO_3)_3$ and $Y_2O(CO_3)_2$.

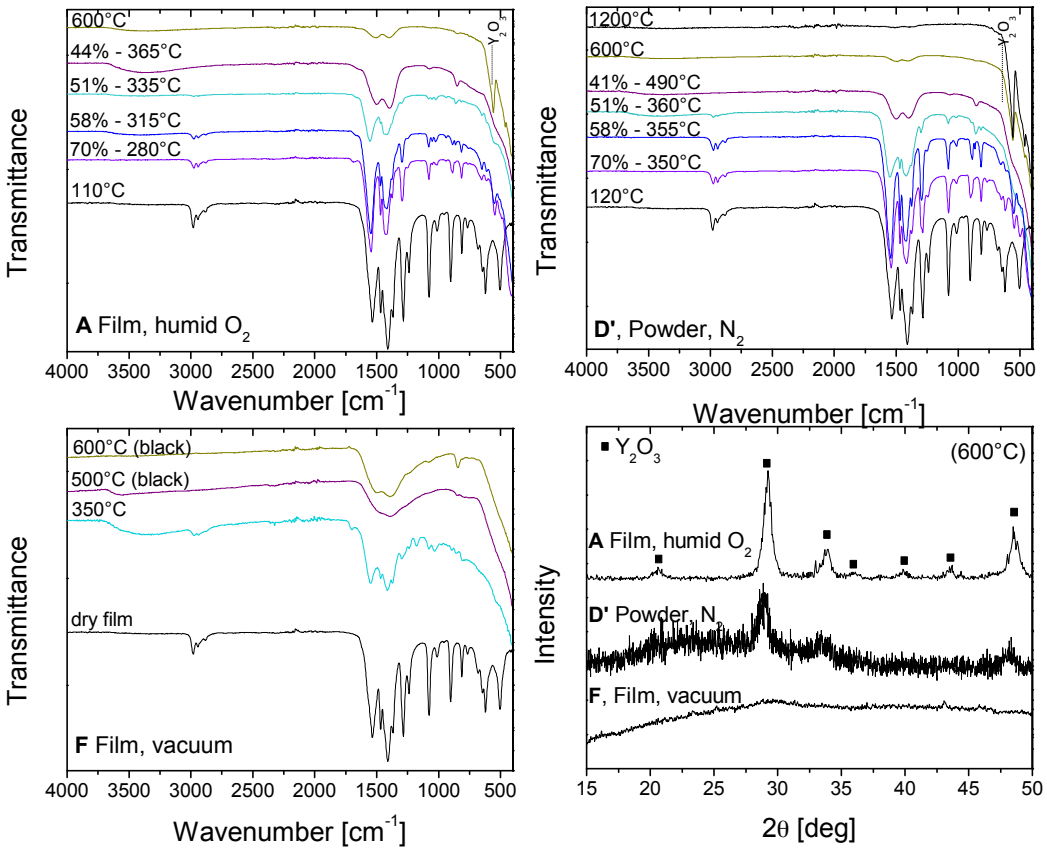

Fig. 3.5: Chemical characterization of the solid residue during $YProp_3$ decomposition. *FTIR and XRD analysis from decomposition at 5K/min in different atmospheres. Percentages are expressed as (m_f/m_i)%.*

3.1.5 Vacuum and inert decomposition

Unlike the TG results previously discussed, when the decomposition is carried out in vacuum (Fig. 3.4**E**,**F**), the final product is no longer white but black. Although a black Y_2O_3 has been reported to form at low PO_2 due to oxygen substoichiometry [115], we can notice that elemental analysis (Table 3.1) shows that a significant amount of carbon is still present at 500°C. This carbon could be attributed to elemental carbon (from disproportionation of CO) or a carbonate (expected ~10%C). Additionally, Fig. 3.5**F** shows that at 600°C the Y-O FTIR band at 560 cm^{-1} is missing, while the contribution of broad bands in the conjugated carbonyl region is much more significant for experiments performed in vacuum (Fig. 3.5**F**) than in experiments performed at atmospheric pressure in oxidative, Fig. 3.5**A**, or inert atmosphere, Fig. 3.5**D'**.

The decomposition of the propionate in vacuum (Fig. 3.4**E**,**F**) produces also 3-pentanone (m/z= 57, 29, 86) and CO_2 (m/z= 44), along with C_2H_x fragments of m/z=29 [C_2H_5], 28 (CO or [C_2H_4]), 27 [C_2H_3], 26 [C_2H_2] (not shown). Compared with **E**, in the highest vacuum (**F**) we notice a higher abundance of m/z= 29,28,27 with respect to 3-pentanone. Formation of CO instead of CO_2 would account for the greater COO- content in the product, while C_2H_5 formation in turn would explain the excess of m/z=29 and the presence of m/z=43, upon recombination to give butane (m/z= 43,29,28,27). Finally, in vacuum, radicals tend to survive longer due to a larger free path between collisions, and they may undergo further fragmentation (instead of recombining to form

3-pentanone or butane), explaining the excess of fragments m/z=29 to 26, and water. All these competing reactions are displayed in **α**** (Fig. 3.3).

In fact, when some oxygen is introduced (Fig. 3.4**E**), the amount of fragments m/z=26 to 29 decreases along with water. Reaction scheme **α** is favored with respect to carbonization, although not enough to remove all carbon and the final compound is still black, but its FTIR shows a small contribution from the characteristic Y_2O_3 band at 560 cm^{-1} (not shown).

Finally, at atmospheric pressure of argon (Fig. 3.4**D'**) we observe some carbonization. In fact, although the final product is Y_2O_3 (white), the quench at 52% (Fig. 3.5**D'**) is slightly grey and EGA-MS shows unexpected amounts of fragments of m/z=27, 28, 29. Thus, in **D'**, **α**** competes with **α**, but the residual carbon is oxidized to CO (also detected by EGA-FTIR) and CO_2, in correspondence of a gradual decrease of the TG curve between 400-500°C (Fig. 3.2**D'**) and, in agreement with literature, only 3-pentanone and CO_2 are detected by EGA-FTIR, thus α dominates over **α****.

3.1.6 Films versus powders

It is important to stress that, due to gas diffusion, films decompose differently than powders, in a given atmosphere. In fact, the decomposition process of $Y(CH_3CH_2CO_2)_3$ for films starts earlier (150°C versus 250°C for powders, Fig. 3.2) but stretches over a wider range of temperatures. As illustrated in Fig. 3.6, decomposition shifts to higher temperature as the film thickness increases. The effect seems to be bigger for the step at low temperature, indicating that the thinner the film, the earlier the evolution of propionic acid (shifted by 20°C to lower temperatures when nominal thickness is reduced from 4.8 µm to 0.5 µm). Similarly, for powders deposited on LAO, the decomposition temperature decreases when the particles size is reduced from ≈500 µm to a few µm (by grounding).

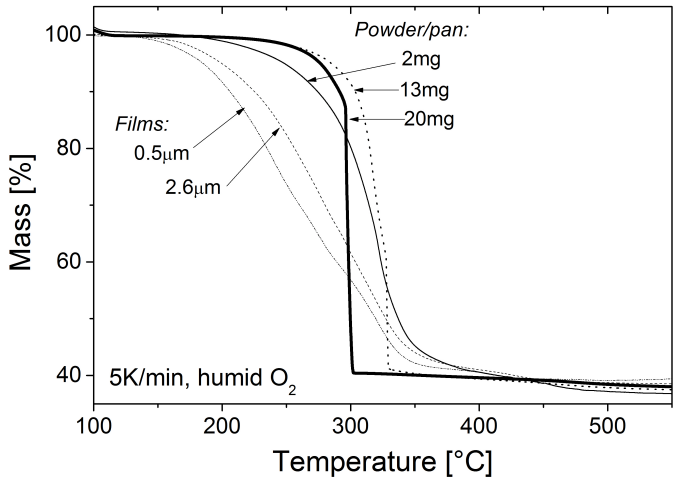

***Fig. 3.6**:* TG analysis of $YProp_3$ as a function of sample geometry. *Films and powders with different thickness and mass, respectively, are compared.*

Since the kinetics of the **β** reaction scheme is limited by oxygen and water diffusion, the large surface to volume ratio of films makes gas renewal next to the surface much more efficient, favoring this mechanism. For this reason, in films with humid or oxidative atmosphere, only propionic acid is detected, but no 3-pentanone. Route **α** is not seen until the thickness approaches a few microns (≈5 μm) for experiments at atmospheric pressure in N_2, and for very thin films only in experiments performed in vacuum. On the other hand, keeping the mass constant (nominal thickness ≈4.4 μm), the decomposition seems to be accelerated in this order: humid O_2 > dry O_2 > nitrogen/vacuum (Fig. 3.2a). This is in agreement with the fact that the formation of the radicals, path **α**, requires higher temperatures as compared with hydrolysis and oxidation of the molecule.

In powders, due to the slow intra-particle oxygen transport [23], the local atmosphere near particles is almost inert and process **β** shifts to higher temperatures. This shift of process **β** favors the occurrence of **α**, to the point that in N_2 **β** is almost suppressed; we observe a long plateau before decomposition starts and the volatiles observed correspond to route **α** (Fig. 3.7**D'**). As a confirmation, we enhance the inter-particle oxygen transport by spreading particles on a substrate instead of placing them inside a crucible, and we observe in oxygen the same behavior as in films: formation of propionic acid instead of 3-pentanone (Fig. 3.7**B'**).

The formation of a local inert atmosphere would explain why Nasui et al. [36] reported the presence of ketones by MS instead of propionic acid when the powder sample was decomposed in air. In fact, for powders inside a crucible we observe slight differences between the volatiles formed in oxidizing or inert atmosphere but in all cases ketones and CO_2 are the main volatiles (Fig. 3.7**C'**, **D'**). However, while in inert conditions most radicals rearrange as 3-pentanone, the presence of oxygen (**C'**, and **C** in smaller amount due to the sensitivity of the film to residual O_2) may oxidize some, resulting in the formation of 2-butanone (reaction scheme **α***) along with the symmetric ketone. In fact, 1) EGA-MS shows the presence of the characteristic fragments of 2-butanone (m/z=43, 72) well separated from those of 3-pentanone (m/z=57, 86); 2) additionally the ratio of fragments 43/57 increases by one order of magnitude going from inert to oxidizing atmosphere (from **F**,**E**,**D'** to **C'**), while the 57/86 ratio remains constant; 3) lastly, EGA-FTIR, besides being in agreement with the presence of 2-butanone (Fig. 3.7**C'**), shows formation of CO and H_2O in **C'** (as expected in **α***), and their contribution decreases with decreasing O_2 content in the atmosphere (going from **C'** to **D'** in Fig. 3.7). Finally, small amounts of propionic acid and acetaldehyde are also detected by MS and IR at the beginning of decomposition in oxygen, as a consequence of the occurrence of reaction scheme **β** at the particles' surface.

Therefore, the significant increase of fragment m/z=43 in the presence of an oxygen atmosphere can be attributed to the oxidation of the C_2H_5 fragment of the ligand to produce acetaldehyde (**A** and **B**), and to yield 2-butanone upon recombination of $CH_3C{=}O\cdot$ and $C_2H_5\cdot$ according to **α*** (in **C'** where radicals are formed). On the other hand, in the absence of oxygen, upon simple recombination without oxidation of the radicals, butane could be formed (in **E**, **F**).

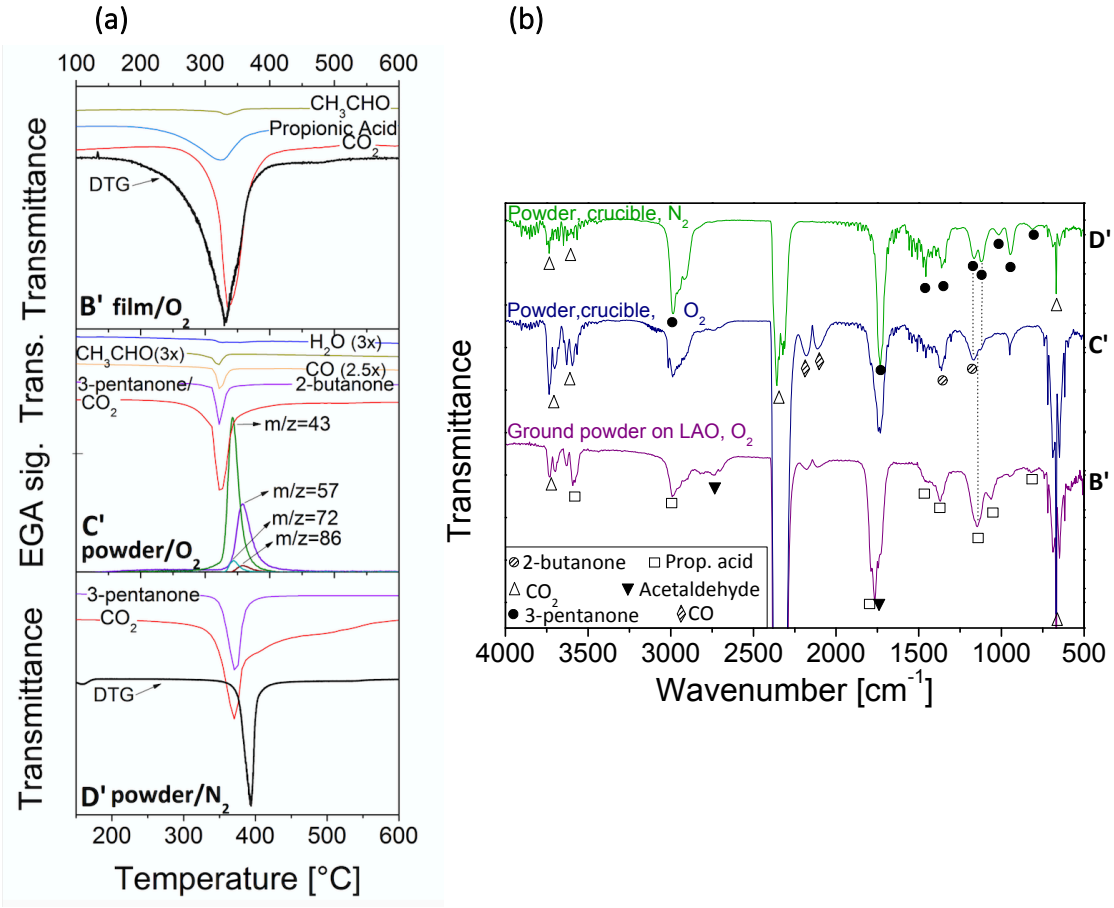

Fig. 3.7: EGA analysis of $YProp_3$ at 10K/min. ***(a)*** *Evolution of the volatiles varying atmosphere and sample geometry and* ***(b)*** *Infrared spectra at the decomposition peak of the corresponding EGA experiment in (a).*

3.1.7 Thermal explosion

From Fig. 3.6, it is apparent that when the powder mass in a humid oxygen atmosphere reaches a critical value, the TG curve no longer exhibits a smooth evolution but shows a discontinuity in its derivative followed by a very abrupt mass loss and the differential thermal analysis curve exhibits a very sharp exothermic peak; these two features (not observed in N_2) are characteristic of a thermal runaway [23,116–118]. When a thermal runaway occurs, the reaction becomes locally unstable; it reaches a high temperature state and accelerates enormously so that it is virtually adiabatic (all the heat released by the reaction contributes to the sample temperature increase) [119–123].

From the physical parameters of $Y(C_2H_5CO_2)_3$ (Table 3.2) we calculated the critical film thickness (H_{cr}) at which a thermal runaway would happen for the sample in the form of film in humid O_2, and the critical mass (m_{cr}) for which thermal explosion would occur in the case of powders in humid O_2 inside a 70-µl alumina pan (finite cylinder geometry, diameter of 4.95 mm) according to the equations laid out in Materials and Methods [90].

Knowing the aforementioned parameters, from equation 2.5, the critical thickness above which combustion would occur for a $YProp_3$ thin film is 937 μm at a heating rate of 5K/min, which means that for films a thermal explosion is impossible to reach [90,124]. This can be explained thanks to the greater surface of the substrate, which helps dissipating the heat, preventing combustion from occurring. On the other hand, from equation 2.9 and 2.10, the sample critical mass for Y-$Prop_3$ was found to be around 13 mg for a heating rate of 5K/min. This is in agreement with the evolution of the TG curve with the sample mass shown in Fig. 3.6, where, for a 13-mg sample, we observe the characteristic sharp mass loss related to a thermal runaway.

Physical parameter	unit	value
Specific heat capacity, c	[J/(kg·K]	1247 (180°C)
Activation Energy, E_A	[kJ/mol]	83.46
Pre-exponential Constant, A	[s^{-1}]	4.6×10^5
Enthalpy of Reaction, q	[J/kg]	4.26×10^6
Apparent Density, ρ	[kg/m^3l]	630
Thermal Conductivity, λ	[W/(m·K)]	0.06

***Table 3.2**:* Physical parameters of $Y(C_2H_5CO_2)_3$. *The values are calculated as described in Chap. 2.*

3.1.8 Discussion

The thermal decomposition of yttrium propionate was shown to be sensitive to both the nominal furnace atmosphere and the sample geometry.

Overall, based on the furnace atmosphere, several reaction paths can be identified which, after an intermediate oxycarbonate, lead to the same decomposition product (Y_2O_3) but different volatiles. At low temperatures, humid atmospheres induce hydrolysis of the propionate ligand to generate the corresponding acid (propionic acid). In a dry O_2 atmosphere, a slightly higher temperature is required for the oxidative degradation of the organic ligand to take place, producing smaller molecules (CO_2, acetaldehyde, propionic acid). Finally, in inert atmospheres, the salt is stable until higher temperatures, which eventually promote decomposition through the radical reaction path.

The fact that a humid atmosphere promotes $YProp_3$ thermal decomposition at low temperatures is very significative for CSD methods. Decomposition of the organic material needs to be carried out at low temperatures to avoid excess phase coarsening which can be detrimental for the YBCO growth. In fact, it justifies the use of humid O_2 during the pyrolysis of the metalorganic solution studied in this thesis.

The presence of an intermediate oxycarbonate ($Y_2O_2CO_3$) before formation of the oxide can explain why the hydrolysis-based reaction path cannot consume all propionate units in Y_2Prop_6 to produce the Y_2O_3 oxide. As we will see in the following sub-chapters (3.2 and 3.3), the extent of the hydrolysis path depends on the metalorganic salt and its ability to form directly the

corresponding oxide without intermediate carbonate/oxycarbonates/oxalates or other M-CO_x containing phases.

Finally, the thermal decomposition of $YProp_3$ is significantly affected by the sample geometry: films and powders exhibit different kinetics and decomposition routes. Due to the local gas (O_2) depletion in the inter-particles voids of powders, the local atmosphere in the bulk is almost inert; thus, powders are considerably more stable than the corresponding films in the same atmospheres, and tend to decompose following the high-temperature radical path. In fact, this path is observed even in a nominal O_2 atmosphere, next to the oxidative one.

Conversely films decompose earlier than powders in the same atmosphere, due to the fast gas renewal at their surface, which makes H_2O vapor/O_2 locally available to promote the low-temperature decomposition paths (hydrolysis and oxidation). In fact, hydrolysis and oxidation take place even in inert atmosphere in films, next to the radical paths, due to the high sensitivity to the local atmosphere which contains residual air (H_2O vapor/O_2).

For the same geometrical reasons, the high surface/volume ratio induces a fast heat dissipation, and thus combustion is never observed in $YProp_3$ films, while it occurs in powders.

These results support the idea that it is of the utmost importance to analyze films in order to disclose the actual phenomena occurring during the pyrolysis of YBCO precursor films.

3.2 Thermal decomposition of copper propionate

This section will continue with the study of the single-component solution based on the copper precursor; the same analytical techniques as the previous section will be applied to identify the reaction volatiles and solid products in order to understand the thermal behavior of the copper propionate salt in the same general conditions of atmospheres and sample geometry. It will be shown that similar reaction routes as for the decomposition of $YProp_3$, namely hydrolysis and oxidation, are at play but with different relative importance. Additionally, a third reaction route, copper reduction, takes place. This difference between those two classes of metal propionates will be discussed in terms of the role of the metal ion in the decomposition mechanism. As a further proof, the possible decomposition routes will be supported by computational calculations.

3.2.1 Characterization of the initial product

In excess propionic acid, acetate groups are replaced by propionates. In fact, the elemental analysis results of the dry salt are in good agreement with the expected values for $CuProp_2$ (Table 3.3), and with the EA results of $CuProp_2$ obtained from an acetate-free solution (by reacting $CuCO_3$ in excess propionic acid). Additionally, the FTIR spectrum of the film displayed in Fig. 3.8 coincides with the reported assignments in [125]. The single-crystal analysis (not shown) performed on our single-crystal corresponds to the anhydrous $CuProp_2$ database structure (CCDC 1133510) [126], which consists of Cu dimers connected by bridging carboxylate ligands. Since the XRD powder-diffraction curve of the ground crystal coincides with that of our films (Fig. 3.8, inset), this structure (CCDC 1133510) was used later on for ab-initio calculations. In fact, our films' magnetic behavior (Fig. 3.9) is as expected for binuclear copper complexes where an antiferromagnetic super-exchange interaction exists between the Cu(II) atoms [49,127,128] due to bridging ligands, and which is responsible for the lower magnetic moment, μ_{eff}, in $CuProp_2$

crystalline powders with respect to Cu(II) compounds in aqueous solutions (exp. range of 1.9-2.2 μ_B) [129,130]. In fact, by comparing the distance between the asymmetric and symmetric stretching band of the carboxylate bond [35,106] [$\Delta\nu = \nu_{as}(COO^-) - \nu_s(COO^-)$] of our $CuProp_2$ with those of other carboxylates from literature, our $\Delta\nu$=165 cm^{-1} value suggests a bridging ligand coordination [131,132].

Coordination water is expected to change the structure, but the OH stretching band of water does not increase significantly over time, indicating that $CuProp_2$ is not very hygroscopic.

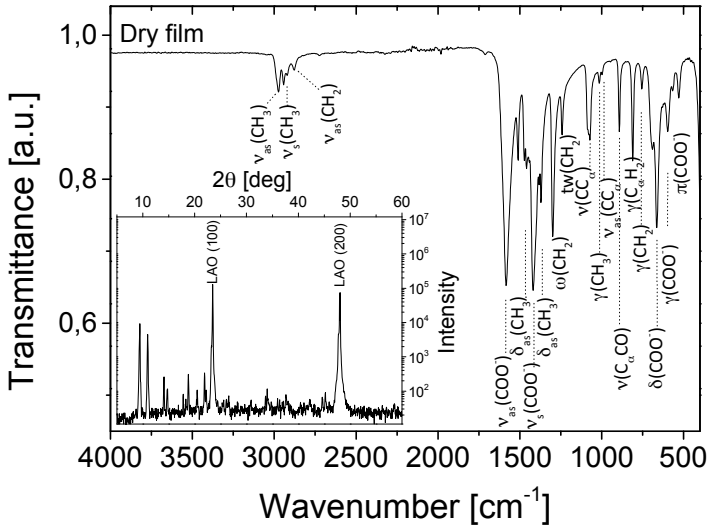

Fig. 3.8: Chemical characterization of the Cu metalorganic precursor. *IR (assignments according to* [125]*) and (inset) XRD pattern of $CuProp_2$ as film after drying.*

Compound	Found (Expected), mass %	
	wt%C	wt%H
$CuProp_2$ from $CuAc_2$	33.71 (34.37)	4.29 (4.81)
$CuProp_2$ from $CuCO_3$	33.86 (34.37)	4.38 (4.81)
A (Film, hum O_2, 210°C)	4.70	0.38
A (Film, hum O_2, 500°C)	-	-
D (Film, dry N_2, 230°C)	4.85	1.32
D (Film, dry N_2, 500°C)	-	-
D' (Powder, dry N_2, 500°C)	3.56	-

Table 3.3: Elemental Analysis of the Cu precursors. *Initial compounds and decomposition products are shown. (-) values inferior to detection limits.*

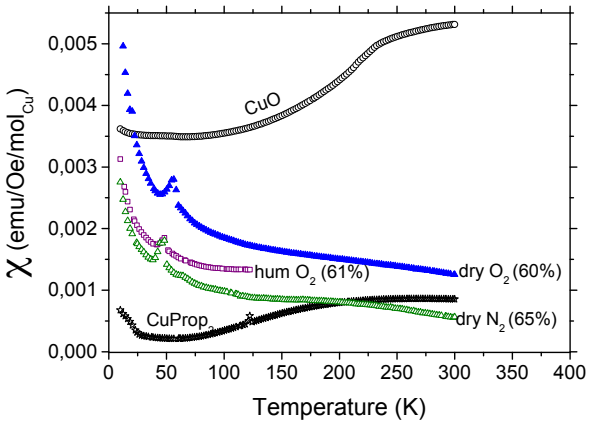

Fig. 3.9: Magnetic characterization from decomposition of $CuProp_2$. *Molar susceptibility (χ) as a function of temperature for initial ($CuProp_2$) and final product (CuO) and for films quenched at a given m_f/m_i %. The small peak between 50-55K can be attributed to O_2 traces on the sample surface during measurements, and it is independent of the sample properties.*

3.2.2 Thermal decomposition of $CuProp_2$ at atmospheric pressure in films

During sample preparation, no water uptake is observed after drying the film at 95°C Therefore, no dehydration is observed in the thermogravimetric analysis and DSC (Fig. 3.10a and b, respectively); the first mass loss step corresponds to the ligand decomposition. The main volatiles evolved during this step are identified in the TG-FTIR spectra in Fig. 3.11 and their detailed evolution as a function of atmosphere and temperature is shown in Fig. 3.12.

The general decomposition mechanism for films involves two stages (labeled as I and II in Fig. 3.10a) to yield CuO at 500°C (Fig. 3.13a exp. **A**,**C**,**D**). Most of the mass loss (≈92%) takes place during the first stage and involves formation of propionic acid (Fig. 3.11). From Fig. 3.10a, the first stage is not influenced by the presence of O_2 but it is accelerated by the presence of a humid atmosphere, and in fact step I in **A** (humid O_2) and **B** (humid N_2) ends at 190°C, whereas it ends 10°C above in **C** (dry O_2) and **D** (dry N_2). Therefore, H_2O vapor shifts the TG curve to low temperatures because it favors the hydrolysis of the salt through reaction scheme **α** (Table 3.4); this shift is enhanced for thinner films, indicating water vapor diffusion to be the reaction-rate limiting mechanism. So, for instance, in humid O_2, $CuProp_2$ XRD reflections disappear and CuO crystalizes between 185 and 210°C (Fig. 3.13b, **A**). Conversely, in dry N_2, CuO crystallization is delayed to 195°C-215°C (Fig. 3.13b, **D**). For any atmosphere, a change in the $CuProp_2$ structure is observed during its decomposition as $\Delta\nu_{COO^-}$ decreases from 165 to 125 cm^{-1} (Fig. 3.14). Similarly, the molar magnetic susceptibility at different decomposition stages (Fig. 3.9) shows that the antiferromagnetic interactions decrease with increasing paramagnetic Cu(II) contribution, probably due to the breaking of the copper(II) carboxylate dimers [133].

After the first stage, a plateau in the TG curve is observed at m_f/m_i≈42% (200-230°C), corresponding to an intermediate product with a change of decomposition mechanism. The films quenched at ~200-230°C are dark, and in all atmospheres, their FTIR absorptions (Fig. 3.14**A** and 3.14**D**) show the presence of residual carboxylate and copper oxide (bands below 500 cm^{-1}), with a high Cu/propionate ratio (combining EA and TG results: $Cu_{12}O_{14}C_3H_4$), and a lower carbon content (Table 3.3) than the theoretical value for copper carbonates (6-10%)[134]. This harder-

to-decompose intermediate may suggest the formation of CuO clusters stabilized by the remaining propionates, similarly to the way nanoparticles have been reported to form from solvent-less routes [135], although usually synthesized through wet chemistry [136,137]. This intermediate later decomposes producing mostly acetaldehyde (from oxidation of C_2H_5 fragments of the ligand) and CO_2.

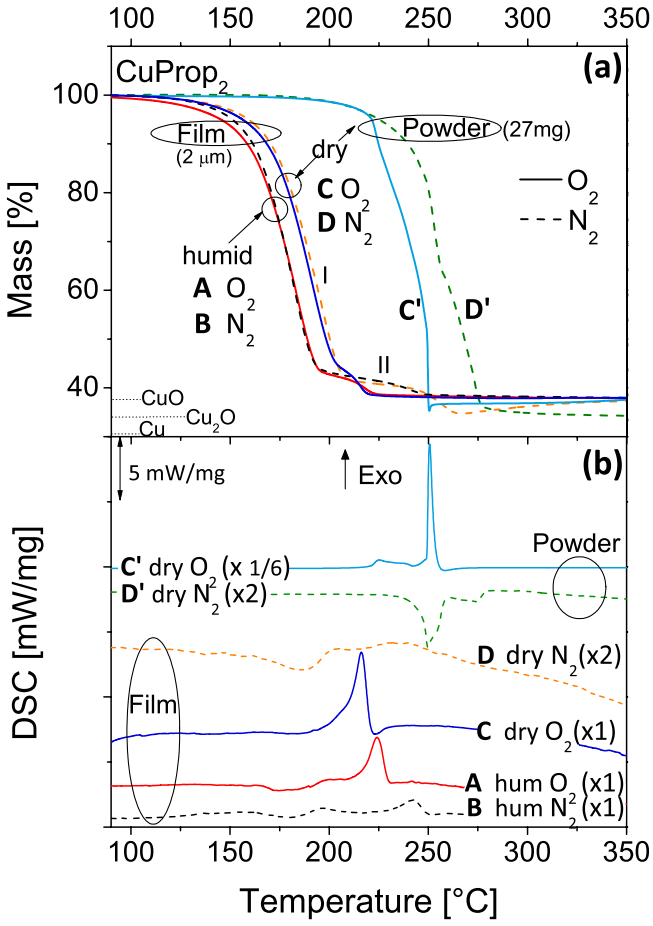

Fig. 3.10: TG-DSC analysis from decomposition of $CuProp_2$. ***(a)*** *TG curves at 5K/min and* ***(b)*** *corresponding DSC signal normalized by the initial sample mass. For a quantitative DSC analysis, see Table 2.*

This second decomposition stage is accelerated by oxygen and it is not affected by humidity (see Fig. 3.10): in oxygen, decomposition occurs at 220°C (solid lines in Fig. 3.10, **A** and **C**), whereas without oxygen, **B** and **D**, it is delayed to 240 and 260°C, respectively (dashed lines in Fig. 3.10; this stage occurs at even higher temperatures in more inert atmosphere). Apparently, stage II involves oxidation because the mass-loss step is accompanied by an exothermic DSC peak (Fig. 3.10b). This is in agreement with reaction scheme **β** (Table 3.4). Except for the experiment in dry N_2 (**D**), the sample mass is quite stable beyond 260°C. Furthermore, in all films at 500°C, XRD analysis reveals only the presence of CuO (Fig. 3.13a, **A**), and EA (Table 3.3) confirms that neither carbon nor hydrogen is left.

Only in the case of dry N_2, this second step coincides with Cu(II)O reduction to $Cu(I)_2O$ (Fig. 3.13b, **D**) upon CO_2 evolution (Fig. 3.12**D**) at 260°C. The fact that Cu(I) is obtained out of the Cu(II)-Cu(I) thermodynamic equilibrium conditions suggests a redox reaction between the remaining carbon (4 wt% in Table 3.3) and CuO. In fact, a sample heated in humid O_2 and quenched before the II stage begins, experiences CuO reduction (like in **D**) when heated in vacuum, releasing CO_2 and CO (not shown). However, by 350°C, given the high sensibility of films to residual oxygen, the Cu_2O film is oxidized again to CuO (Fig. 3.13a, **D**), and at 500°C no carbon and hydrogen are left (Table 3.3). Finally, note that the presence of water vapor (**B**, humid N_2) is enough to prevent this reduction.

To further confirm these decomposition reactions and exclude any possible influence of remaining acetate ligands, the decomposition of a powder obtained from an acetate-free precursor solution ($CuCO_3$ in excess propionic acid) was studied as a comparison, spread on a LAO substrate to approach the conditions of experiment **A**. The decomposition temperatures were very similar and the volatiles were the same as in exp. **A**, confirming that the reaction schemes proposed are the expected ones for the decomposition of $CuProp_2$.

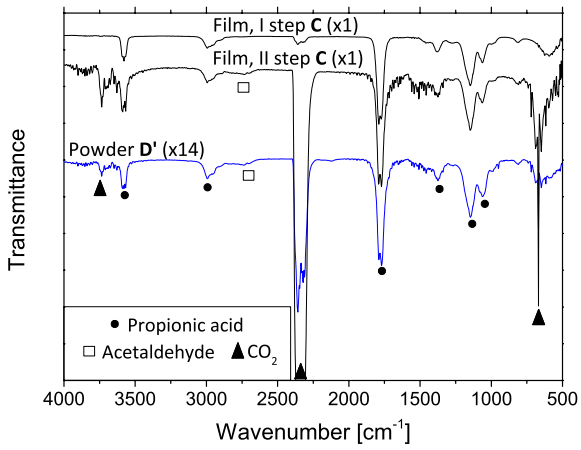

Fig. 3.11: Gas infrared spectra from decomposition of $CuProp_2$. *The gases evolved are relative to the decomposition peak temperatures shown in Fig. 3.12. The spectra are normalized by the $CuProp_2$ moles involved in the mass-loss step (n_I, n_{II} for films, n_i for powders).*

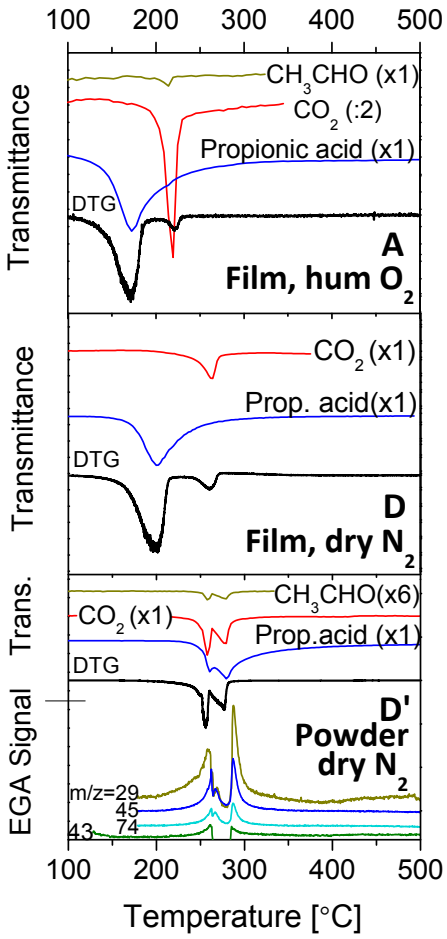

Fig. 3.12: TG-EGA analysis of $CuProp_2$ decomposition at 5K/min. *As in Fig. 3.11, the transmittance is normalized by the Cu moles responsible for the IR signal at each step, to emphasize the relative importance of a volatile. m/z=44 was also detected in **D'** but is not shown for clarity.*

3.2.3 Thermal decomposition of $CuProp_2$ at atmospheric pressure in powders

For "bulk" $CuProp_2$ powder (m_i of tens of mg), the residual water vapor in nominally dry O_2 (**C'**) and N_2 (**D'**) atmospheres has no effect on decomposition and, consequently, powders decompose at much higher temperatures (≈ 250°C, Fig. 3.10a) than films.

In dry N_2 (**D'**), decomposition is endothermic (Fig. 3.10b), which is consistent with the reduction of copper (like in process **γ** of Table 3.4). XRD and FTIR measurements (see Fig. 3.13b and Fig. 3.14**D'**, respectively) on samples quenched at ~250-265°C, around the mass derivative discontinuity, indeed reveal the formation of Cu_2O; just after quenching from 265°C, a fraction of the sample is liquid, and green portions emerge as it quickly solidifies, resulting in an XRD peak at 2θ=6.5 (△ in Fig. 3.13b, **D'**, 260°C) and new C=O FTIR bands (△ in Fig. 3.14**D'**) at 1740 cm^{-1}. In fact, the sample mass loss at this temperature (65% m_f/m_i) is in agreement with Cu(I)Prop formation, but the XRD peak at low angles might suggest its oxidation to a basic copper propionate [138] during cooling, after coming into contact with atmospheric air. The volatiles consist of CO_2, acetaldehyde and propionic acid. Finally, the product at 500°C consists of Cu and Cu_2O (Fig. 3.13a), and a significant 3 wt% of carbon residues (Table 3.3, **D'**). This is probably due to the very inert local atmosphere when compared to the film (experiment **D**). This was also observed for other copper compounds (with long alkyl chains) in N_2 at 500°C [139].

In dry O_2 (**C'**), the reactive atmosphere displaces decomposition to lower temperature (Fig. 3.10a) but it does not impede Cu reduction. In fact, the final abrupt mass-loss step observed at 250°C in the TG curve (and sharp exothermic peak in the DSC curve) is a clear signature of combustion, and in such a fast reaction mode complete oxidation is usually not possible [90]. After combustion, the sample mass reaches a minimum below the expected mass for the formation of CuO, but the subsequent mass increase (and the final black color) shows that it is then oxidized again to the expected CuO final product. The very fast transformation rates reached under the combustion result in a decomposition in inert conditions, oxygen has no time to diffuse, so eventually copper is reduced.

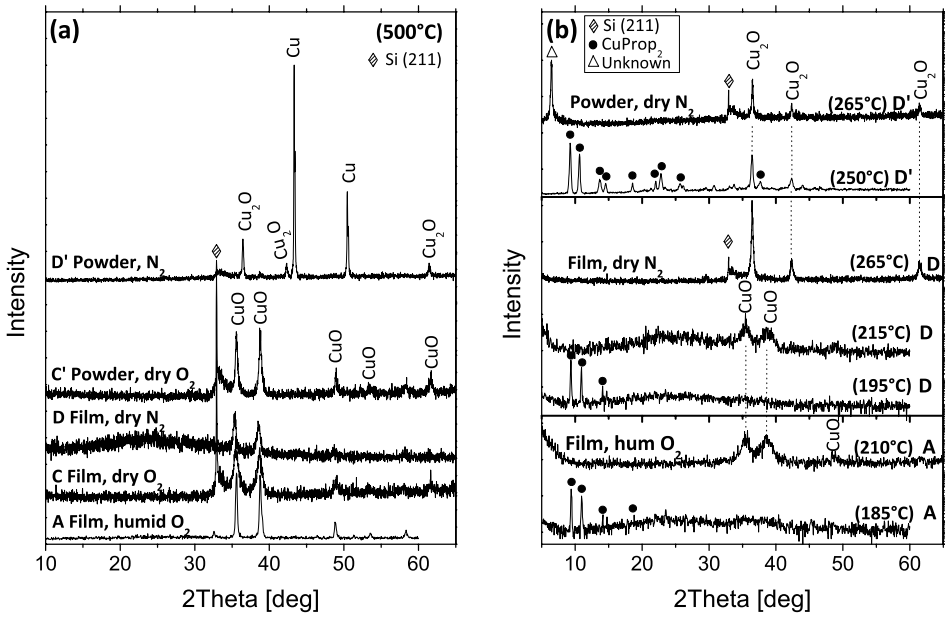

Fig. 3.13: XRD analysis of the solid residue during $CuProp_2$ decomposition. *The silicon peak corresponds to the sample holder.*

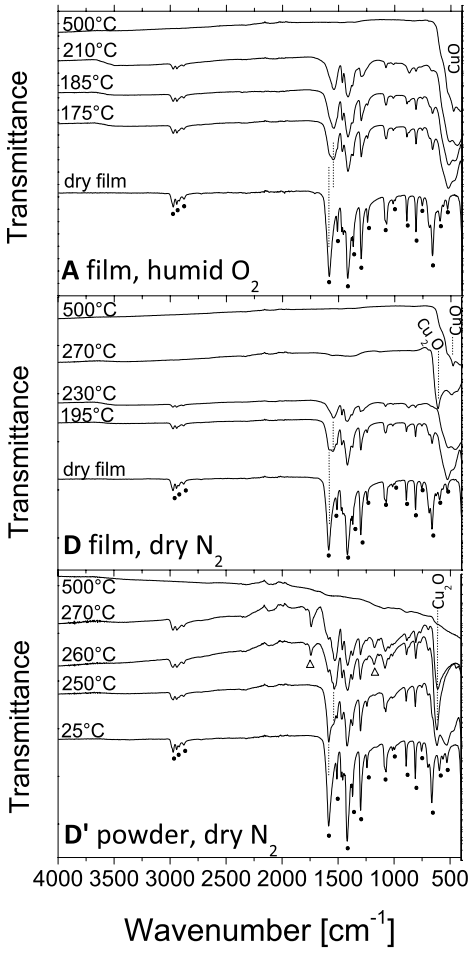

***Fig. 3.14**:* Infrared evolution of the solid residue during decomposition of $CuProp_2$. *Symbols: (•) $CuProp_2$; (Δ) unknown phase. The analysis corresponds to decomposition at 5K/min of Fig. 3.10.*

3.2.4 Thermal decomposition of $CuProp_2$ in film and powder at low pressure

At low pressure (experiment **E**), volatilization of the film occurs: the substrate is left with a blackish color, consistent with both copper oxide residues and elemental carbon, but the mass loss is close to 99%, and XRD analysis could not detect anything. A blue compound is found on the cold parts of the quartz tube which by FTIR and XRD analysis is revealed to be similar to Cu(II)$Prop_2$. Volatilization of Cu(II)$Prop_2$ occurs simultaneously with decomposition, since EGA-MS (Fig. 3.15**E**) detects a small amount of volatiles, mainly related to propionic acid (m/z=74, 45, 29, 28, 27). Volatilization of copper propanoate was already observed by [125] above 167°C in vacuum, and it is consistent with a series of findings, for example that volatile binuclear Copper(I) carboxylates are among the decomposition products of Cu(II) carboxylates [140], and with the general strong tendency of copper complexes of even longer chains to sublimate at low pressure [141,142].

On the other hand, when the powder is heated in vacuum to 500°C (**E'**, **E''**), at 10-25°C/min instead of 5°C/min, the sample decomposes between 150 and 300°C, yielding Cu(0). However, the crucible is almost empty, while the sample chamber has turned pink. Unlike E, where no m/z=44 is detected, the main fragments coming from the gas species are m/z=29,28,27 (C_2H_x), 44 (CO_2)

and 45 (COOH), which could be in agreement with propionic acid (m/z=29,28,27,45), acetaldehyde (m/z=29,44) and CO_2 found by TG-MS-FTIR experiments (Fig. 3.12**D'**). In **E'**, the first peak at 240°C follows scheme **α** and is due to residual water, as the water signal points inward (m/z=18). The CO_2 peak at 260°C is due to copper oxide's reduction to Cu(0) by elemental carbon, just like in **D**. Increasing mass and heating rate in **E''**, decomposition proceeds according to **γ** as in **D'**. Thus, **E'-E''** can be the consequence of pushing experiment **D-D'** to very low O_2 partial pressures, where only metallic copper is formed.

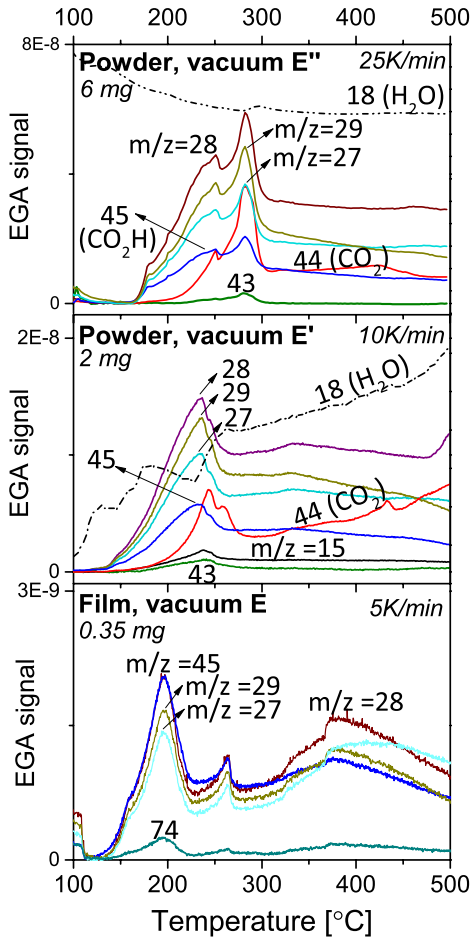

Fig. 3.15: EGA-MS of $CuProp_2$ decomposition in vacuum. *Different conditions of sample mass and heating rate are shown.*

3.2.5 Thermochemistry calculations

As a further confirmation of the reactions proposed in Table 3.4, the experimental enthalpies of reaction for film and powder decomposition obtained from DSC (Fig. 3.10b) were compared with the theoretical values of electronic energy for the same reactions.

Hydrolysis (**α**) is predicted to be slightly endothermic, as observed for stage I in all experiments in film (**A**, **B**, **C**, **D**). This assignation is especially significant for the experiments in nominally dry atmosphere (**C** - O_2 and **D** - N_2), because it leads to the conclusion that residual humidity is enough to sustain this reaction.

Oxidation of the organic ligand (**β**) is exothermic and can occur at different degrees: thus, stage II in films in O_2 (**A** -humid, **C** -dry) is attributed to oxidation to acetaldehyde (entry iii and *iv*, in agreement with the detected volatiles) and its exothermicity decreases from **C** to **A** to **B** (humid N_2) as the degree of oxidation goes from *iv*, to *iii* to *ii*. **D** (dry N_2) represents an intermediate situation between films in O_2 and powders in N_2, since only partial reduction to Cu_2O occurs as the residual propionate decomposes in Stage II (**γ**). The latter (slightly endothermic) triggers the reduction of the CuO formed from stage I at the expenses of a stronger oxidation of the remaining organic ligand (probably to CO_2 and H_2O) according to *viii-x* (slightly exothermic), and combined they could explain why stage II is not accompanied by a relevant DSC peak (Fig. 3.10b).

Concerning powder in N_2 (**D'**), the predicted slight endothermic character of the reduction reaction (*vi* of **γ**) is confirmed by experiment. In dry O_2 (**C'**), the heat evolved is lower than in films (**A**, **C**) indicating a lower degree of ligand oxidation (**β**) due to local O_2 depletion as reaction gases evolve [90], and as **γ** compete with **β**. This fact does not impede combustion occurring at the end of decomposition because, in contrast with the good thermal contact with the substrate for films, heat dissipation is much less efficient for powder [90].

Reaction scheme	Reaction	Δ_r**E (VASP/PBE)** *[Kcal/mol)*	Δ_r**H exp.** *[Kcal/mol)*
i $CuProp_2 + H_2O \rightarrow CuO + 2C_2H_5CO_2H$	Hydrolysis (**α**)	22.1	19 (**A**, film, stage I) 12 (**B**, film stage I) 17 (**C**, film, stage I) 18 (**D**, stage I)
ii $CuProp_2 + O_2 \rightarrow CH_3CHO + C_2H_5CO_2H + CO_2 + CuO$	Oxidation (**β**)	-49.5	-80 (**B**, film, stage II)
iii $CuProp_2 + 2O_2 \rightarrow 2CH_3CHO + H_2O + 2CO_2 + CuO$		-121.1	-240 (**A**, film, stage II)
iv $CuProp_2 + 9/2O_2 \rightarrow CH_3CHO + 3H_2O + 4CO_2 + CuO$		-364.5	
v $CuProp_2 + 7O_2 \rightarrow 6CO_2 + 5H_2O + CuO$	Full oxidation	-607.9	-380 (**C**, film, stage II) -170 (**C'**, powder, O_2)
vi $CuProp_2 \rightarrow CO + CH_3CHO + C_2H_5CO_2H + Cu$	Reduction (**γ**)	48.6	19 (**D'**, powder, N_2)
vii $CO + ½O_2 \rightarrow CO_2$		(-67.6*)	33 (powder, Ar)
viii $2CO \rightarrow C + CO_2$		(-41.2*)	
ix $C + O_2 \rightarrow CO_2$		(-94.0*)	
x $CuO + ¼\ C \rightarrow ½\ Cu_2O + ¼CO_2$		(-6.1*)	<0 (**D**, film stage II)

Table 3.4: Decomposition enthalpies of $CuProp_2$. *Experimental enthalpy of decomposition ($\Delta_r H$ exp) and calculated electronic energy of reaction ($\Delta_r E$) for possible decomposition paths of $CuProp_2$. (+) for endothermic and (-) for exothermic reactions. *literature values of $\Delta_r H$. experimental values are normalized by the $CuProp_2$ mass that decomposes at the DSC step, which is calculated from TG curves. Thus, for all films except the case of dry N_2 (**D**), stage II is normalized by the amount of remaining $CuProp_2$, undecomposed from stage I. In the specific case of **D**, Stage II is normalized by the amount of CuO formed after stage I and that undergoes reduction to Cu_2O. Comparison with the theoretical values is meant to show which reaction scheme contributes the most to decomposition.*

3.2.6 Discussion

$CuProp_2$ decomposition kinetics depends on the geometry (film or powder) and the furnace atmosphere. A humid atmosphere triggers decomposition at lower temperature (Fig. 3.9) in films, promoting the hydrolysis (**α**) of the salt, and this shift is helped by reduced thickness. Films are so sensitive to humidity that the residual water vapor in nominally dry conditions (**C** and **D**) has a similar effect. Conversely, sensitivity to residual humidity or O_2 is lost for powders, which decompose at a much higher temperature. In fact, in bulk form, attention has to be paid to the local atmosphere created at the interparticle voids during decomposition [23,26]. This phenomenon results in inert or even reducing local conditions leading to similar behavior for powders in N_2 and in O_2: Cu(II) reduction (path **γ**) even in nominally pure O_2 (**C'**), and to a higher difficulty for carbon removal. Anyway, the nominal atmosphere has an effect on the decomposition process: combustion occurs in pure O_2. The difference in behavior between films and powders found for the particular case of $CuProp_2$, agrees with that of other metal organic salts [23].

Changing atmosphere affects the final product (Cu versus CuO) rather than the nature of the volatiles coming from decomposition (which is the case of $YProp_3$), which in both inert and oxidizing atmosphere consist of oxidized forms of the ligand. While in O_2 this is clearly understood from the high availability of oxygen, in inert atmosphere it can be explained by the oxidation of gaseous products contributing to the metal center reduction from Cu(II) to Cu(I) and Cu(0) according to reaction scheme **γ**. In fact, step II in **D** is more delayed than **B** due to decreasing oxygen availability (as H_2O vapor), but oxidation of residual ligand to CO_2 can still be pushed by the CuO/Cu_2O reduction.

This is in agreement with the hypothesis that [43], in inert conditions, metal ions that easily undergo redox reactions, like Cu, Ag and Hg, promote the formation of the corresponding carboxylate acid, while the evolution of ketones is favored by the opposite class of metals (i.e. Y, Ca..), emphasizing the role of the metal ion in affecting the salt decomposition. This would explain why metal carboxylates that would normally release ketones, yield an acid in the presence of iron or copper salts [107,143].

No alkene was found, unlike for the decomposition of even chain Cu/Hg carboxylate [40,41], suggesting that the chain length may also play a role in the decomposition pathway or that the decomposition mechanism is a result of the general catalytic activity of copper, resulting in the oxidation of ethylene to acetaldehyde [144].

Lastly, reducing the pressure from atmospheric to 10^{-6} bar causes volatilization of the salt to occur, but at different stages of decomposition, according to the geometry of the sample and heating rate: the higher the surface to volume ratio (films, **E**), the faster the volatilization with respect to decomposition; conversely, at higher heating rates and thicker samples (**E''**), decomposition is more significant than volatilization. On the other hand, at atmospheric pressure, as the mass loss is never below than that of the expected compounds, any significant volatilization of copper species can be ruled out, until tested thicknesses of 300 nm. Additionally, the presence of water vapor is expected to prevent volatilization by shifting decomposition to low temperatures thanks to scheme **α**. Indeed, the hydrolysis-driven decomposition of the carboxylate salts, already also found for the $YProp_3$ case, can explain the advantage of using humid atmospheres in the framework of CSD-YBCO film pyrolysis; in fact, humidity is critical to reduce the decomposition temperatures of the thermal treatment.

3.3 Thermal decomposition of a Barium propionate-acetate salt

This section will conclude the understanding developed on the single-salt YBCO precursor solutions by analyzing the thermal decomposition of the barium precursor salt. Thermal analysis and chemical characterization techniques will be applied in the same general framework developed in the previous two sections, as a function of different sample geometry and furnace atmospheres. It will be shown that barium acetate and barium propionate follow a similar thermal behavior as the $YProp_3$ salt, but that they also constitute a third example of metal propionate decomposition where only two main reaction paths can be identified: the radical mechanism and the oxidative degradation. No hydrolysis takes place as a consequence of the fact that the carbonate and not the oxide is the stable phase after pyrolysis to 600°C.

3.3.1 Characterization of the initial product

The elemental analysis results of the powder obtained from the $BaAc_2$ precursor solution and from an acetate-free ($BaCO_3$) precursor solution are shown in Table 3.5. For the latter, the values are in agreement with $BaProp_2$ formation. Conversely, the product obtained from the $BaAc_2$ solution shows a C and H% inferior to the theoretical value for the full replacement of acetates by propionates, indicating that some acetate ligands remain in the structure. In fact, the FTIR spectrum of the dry film in Fig. 3.16 shows the appearance of the $-CH_2$ propionate bands, but the small contribution at 930 and 648 cm^{-1} (C–C stretching and COO deformation [145]) indicates the presence of acetate groups; the XRD on a single crystal (shown in Fig. 3.16b) confirms the specie to be a mixed carboxylate with structure $Ba_7Prop_8Ac_6{\cdot}4H_2O$, similar to what proposed by [29]. The carboxylate ligands are bound in bridging fashion to the Ba ions, in agreement with the small distance between the asymmetric and symmetric stretching of the COO^- bond [100,103,104,131,132]: $\Delta\nu = \nu_{as}(COO^-) - \nu_s(COO^-) = 120.7\ cm^{-1}$. In particular, three Ba atoms have coordination number 9 and one Ba 8; the unit cell reported in Fig. 3.16b, shows that Ba(1) is surrounded by two H_2O molecules, and the majority of the ligands are bidentate bridging, with a tridentate chelating bridging between Ba(3) and Ba(4).

Compound	Found (Expected) wt%C	wt%H
$BaProp_2$ (from $BaCO_3$)	25.3 (25.42)	3.5 (3.56)
Ba-Prop-Ac (from $BaAc_2$)	23.1	3.4
A film in hum. O_2 (600°C)	6.3 (6.09)	-
A' powder in hum. O_2 (600°C)	6.4 (6.09)	-

Table 3.5. Elemental analysis of the Ba precursors. *Initial compounds and some decomposition products are shown; (-) values inferior to detection limits.*

One might expect the ratio propionates/acetates to vary as a function of concentration and solvents ratio. In fact, decreasing $[Ba^{2+}]$, the acetate contribution is no longer distinguishable by FTIR; similarly, $BaProp_2$ is favored in a solution of only propionic acid. Additionally, the powder-

diffraction obtained from the single-crystal differs slightly from the powder diffraction pattern of the dry film (both in Fig.1, inset), indicating different water amount or even different propionate/acetate ratio between the two, due to the fact that they were generated by different processes, crystallization versus precipitation (solution deposition), respectively. However, the FTIR spectrum of the crystal shown in Fig. 3.17 (together with other TA analysis run on single-crystal which will be discussed later) is very similar to that of the powder sample of Fig. 3.16.

The mixed carboxylate specie (labelled as "Ba-Prop-Ac") will be the focus of the present section, and its decomposition will be understood in comparison with "$BaProp_2$" (from now on indicating the precursor obtained from the $BaCO_3$ solution) and "$BaAc_2$" (referring to the commercial sample).

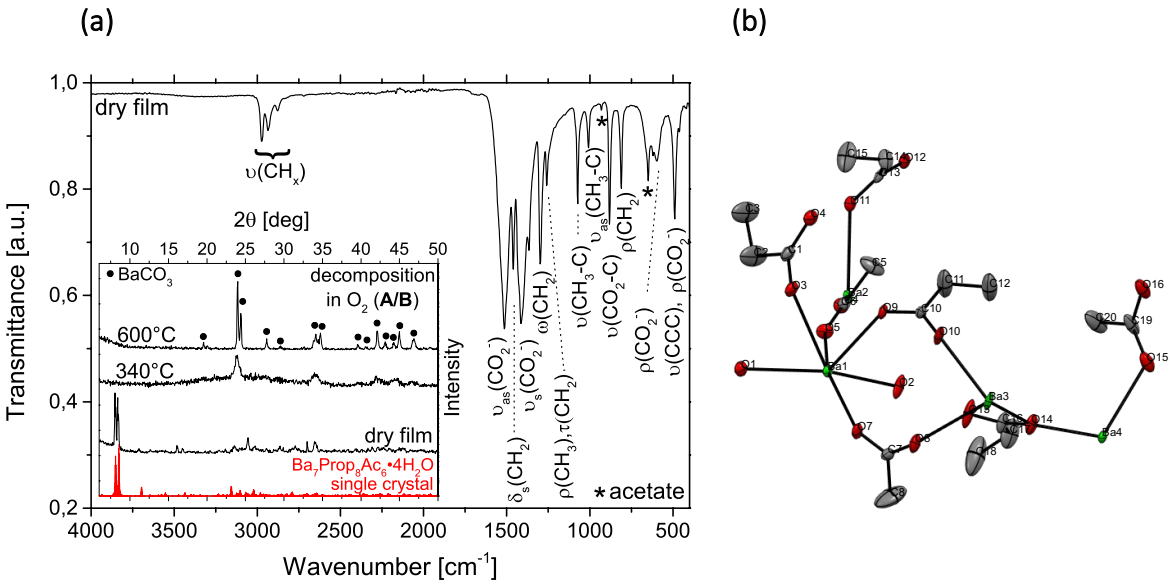

Fig. 3.16: Chemical characterization of the Ba metalorganic precursor. ***(a)*** *Infrared and (inset) XRD analysis of the phase evolution from decomposition.* ***(b)*** *Unit cell of $Ba_7Prop_8Ac_6{\cdot}4H_2O$ from single-crystal XRD analysis, belonging to the space group P $2_1/c$, monoclinic system with a=13.993 Å, b=15.388 Å and c= 15.417 Å. Hydrogen atoms are not shown for clarity.*

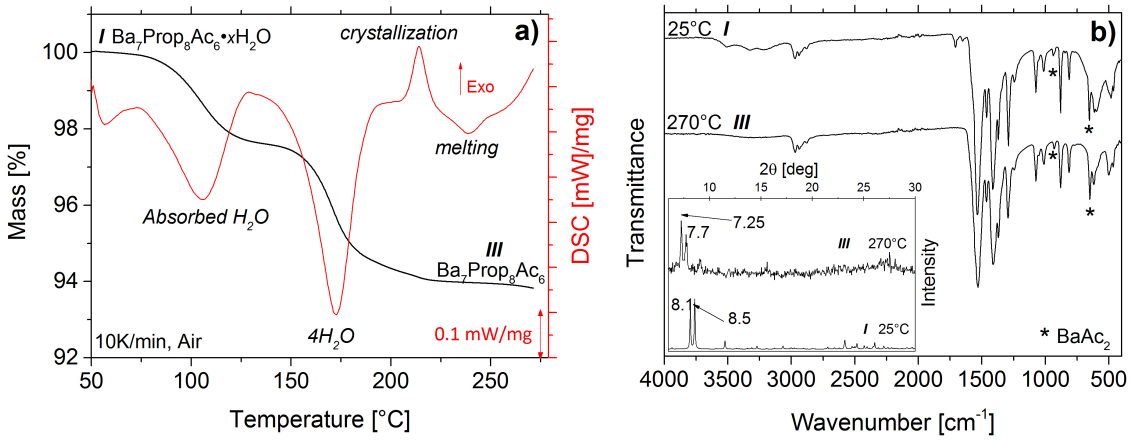

Fig. 3.17**:* Thermal analyses of a $Ba_7Prop_8Ac_6 \cdot 4H_2O$ crystal. ***(a) *thermogravimetric curve of the crystal showing dehydration (endothermic peaks) followed by recrystallization (exothermic) and melting (endothermic). Since films are dried before a TG experiment, it is not possible to appreciate dehydration.* ***(b)*** *corresponding FTIR and XRD analysis (inset), showing that after melting, crystallization occurs.*

3.3.2 Powder decomposition

The mass evolution and the DSC curves for the thermal decomposition of Ba-Prop-Ac as a function of the atmosphere are reported in Fig. 3.18a and b, respectively. For comparison, the evolution of $BaProp_2$ and $BaAc_2$ in humid O_2 as film is reported in the same graph.

The dehydration process is briefly illustrated in Fig. 3.17, where water removal can be fully appreciated from the TA experiment run on a single-crystal, rather than on the film and powder sample, due to the preparation process of the latter which involves a drying stage. Interestingly, Fig. 3.17 shows that crystallization water is retained until roughly 200°C. Similarly, during the drying stage, films and powders are a colorless gel up to 120-190°C (depending on thickness) due to the fact that propionic acid as well as water are hard to remove.

In inert atmosphere (**B'**, N_2), Ba-Prop-Ac as powder is stable up to 400°C. Before 400°C, only two small endothermic peaks are observed (Fig. 3.18) at 230°C and 380°C, which indicate that melting occurred (additionally confirmed by repeating the experiment under visual observation for the low peak temperature). Although normally two melting peaks are interpreted as arising from two different phases in the sample, the same two peaks are also observed for the pure $BaProp_2$ (although shifted in temperature, see Fig. 3.18). For a pure substance, this feature has been explained in terms of recrystallization effects [146], where the first peak is representative of continuous melting and recrystallization into a different solid phase with higher melting temperature, and has also been observed for other barium carboxylates [147]. When performing two consecutive heating ramps up to 280°C, at the second ramp the low-temperature melting disappears while the one at 380°C remains (see Fig. 3.19). A general shift of the XRD peaks to lower 2θ is observed after heating to 280°C, after dehydration and the first endothermic peak have taken place. Decomposition starts above 400°C: Ba-Prop-Ac decomposes following the radical decomposition path that is common in carboxylates [33,34,36,148], releasing symmetrical ketones to form $BaCO_3$ (inset in Fig. 3.16) between 450 and 500°C. Among these ketones, the main volatile is 3-pentanone ($C_2H_5COC_2H_5$, Fig. 3.20) coming from the propionate ligands and, in less extent, acetone (CH_3COCH_3), coming from the acetate part.

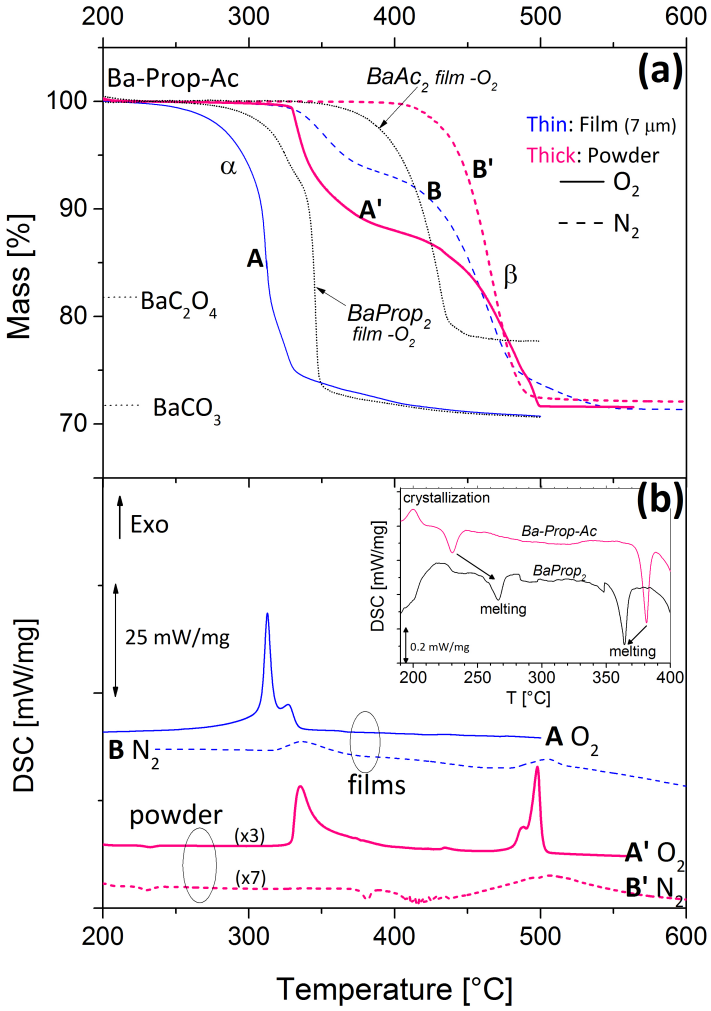

***Fig. 3.18**: TG-DSC analysis for the decomposition of Ba-Prop-Ac. **(a)** TG curves and **(b)** corresponding DSC signal during decomposition at 5K/min in different atmospheres.*

Since there is an excess of propionate groups with respect to the acetate ones, the main contribution comes from the 3-pentanone. In fact, $BaProp_2$ follows a similar decomposition path with similar resulting volatiles in N_2 (Fig. 3.21), which is represented by reaction scheme **β** in Fig. 3.22. No CO_2 is detected, as expected from the stoichiometry of reaction, indicating that no other reaction paths are competing with **β**. Below 1000°C, neither BaO nor BaO_2 are expected to form. In addition to the XRD results, the thermogravimetric analysis in Fig. 3.18 shows the corresponding TG final mass (72.0%) to be in agreement with $BaCO_3$ formation (expected: 69.6-72.7% for $BaProp_2$ and $Ba_7Prop_8Ac_6$, respectively) and the elemental analysis results (EA in Table 3.5) confirm the presence of C in the sample, with complete removal of all hydrogen atoms. However, the final product is not white (as expected for $BaCO_3$), but gray, suggesting that some carbon residue may be left in the sample up to 600°C. If the dark color were due to sub-stoichiometry of oxygen, we would expect the mass to increase upon further heating of the sample in oxygen. However, when the latter is re-heated in O_2 up to 700°C, the mass slightly decreases and the final color is white (and the FTIR spectrum still confirms the presence of $BaCO_3$). Therefore, the black color could be assigned to carbon residue left in the sample upon decomposition in inert atmosphere.

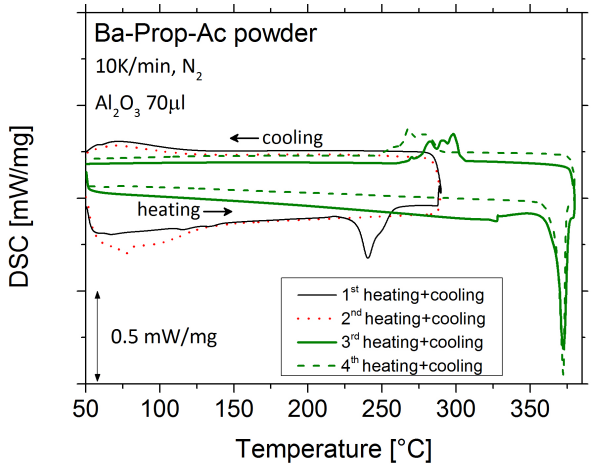

Fig. 3.19: DSC signal of the Ba precursor in dry N_2. *The DSC analysis is relative to the powder obtained drying the solution, and it shows that only the high-temperature endothermic peak is reversible.*

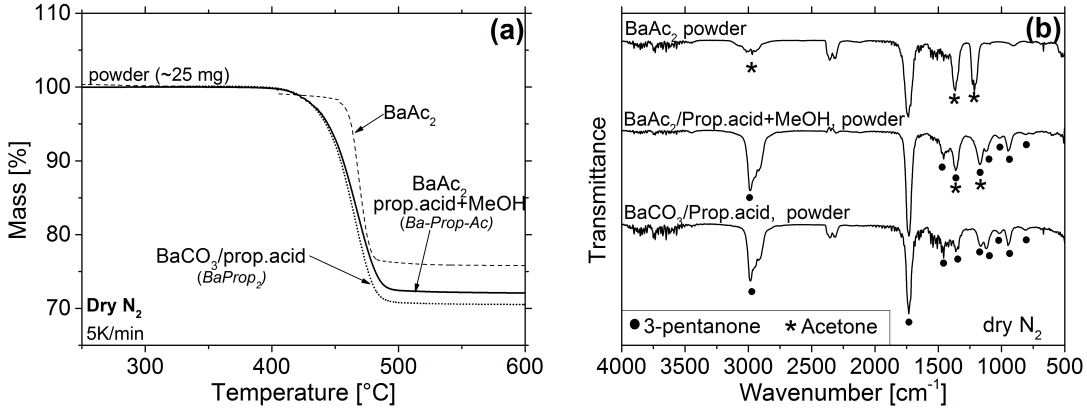

Fig. 3.20: Comparison of the thermal behavior of different Ba precursors in dry N_2. ***(a)*** *TG curves and* ***(b)*** *Infrared of the gas species at the decomposition peak temperature of the TG curves shown in a). Since the center and bottom IR spectra are very similar, the contribution to Ba-Prop-Ac decomposition coming from the acetate part is relatively small.*

In oxygen (both humid and dry, **A'**), decomposition of powders starts earlier (around 310°C) and involves two steps. The first step consists of oxidative exothermic reactions (denoted as reaction scheme **α** in Fig. 3.18 and Fig. 3.22) and will be described in the following section. The second step takes place in the same temperature range as the radical mechanism previously described. Thus, two mechanisms compete: when the oxidative decomposition is slowed down by the slow gas diffusion in the powder, oxidation of the ligand is not complete so that the remaining salt continues decomposing following the radical path as the temperature increases. But 3-pentanone is not observed in a nominal atmosphere of O_2 (or humid O_2) suggesting that the radicals $C_2H_5CO\cdot/C_2H_5\cdot$ do not recombine. In fact, the O_2 can drive oxidation of $C_2H_5CO\cdot$ to CO_2 while the alkyl groups are converted to ethane (C_2H_4) and ethylene (C_2H_6) (Fig. 3.21**A'** and reaction scheme **γ** in Fig. 3.22). In O_2 (**A'** in Fig. 3.18b) the DSC signal is, in fact, more exothermic than in N_2 (**B'** in Fig. 3.18b). $BaProp_2$ decomposes following the same path (Fig. 3.23), and for this reason the contribution of the acetate part is not considered in Fig. 3.22.

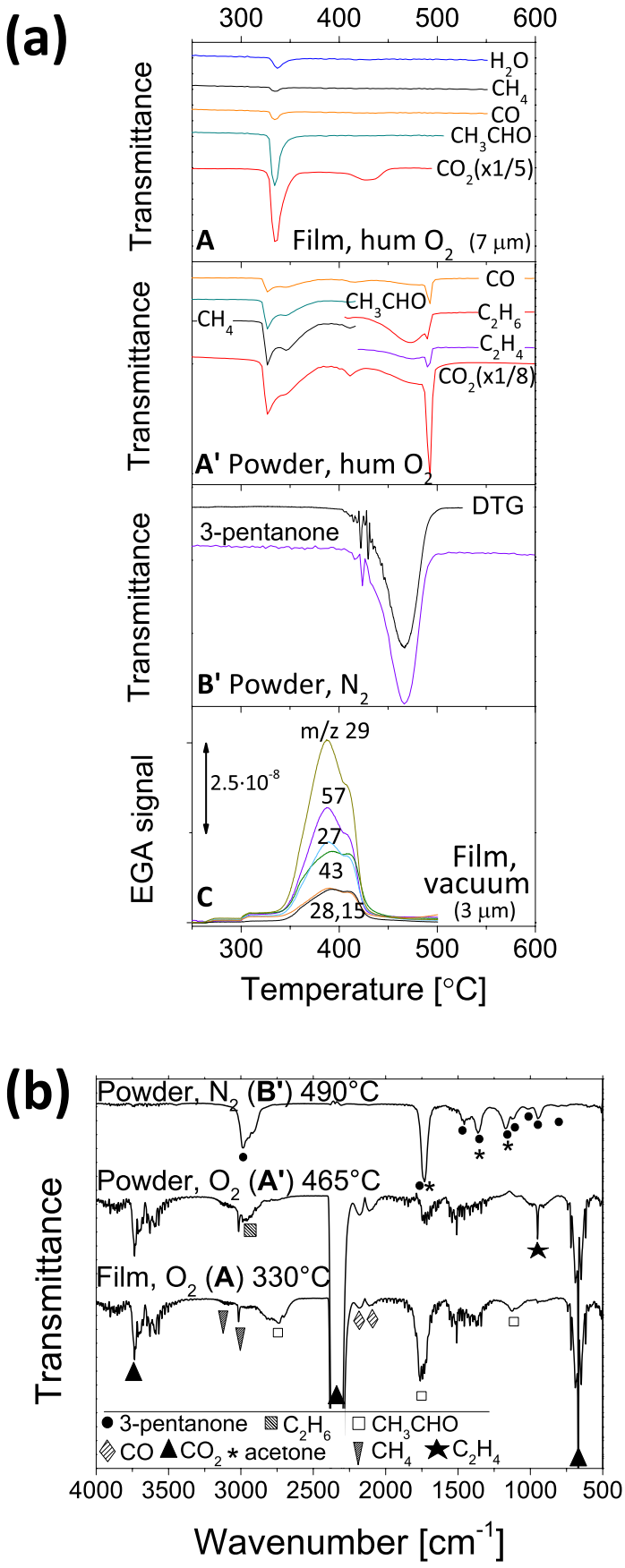

***Fig. 3.21**: TG-FTIR and EGA-MS analysis for Ba-Prop-Ac decomposition. **(a)** Evolution of the volatiles at 5K/min and **(b)** corresponding FTIR spectra of the volatiles*

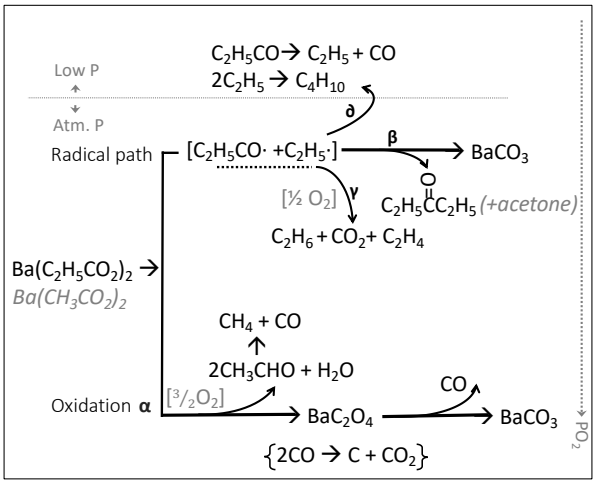

Fig. 3.22: Proposed decomposition reactions for $BaProp_2$.

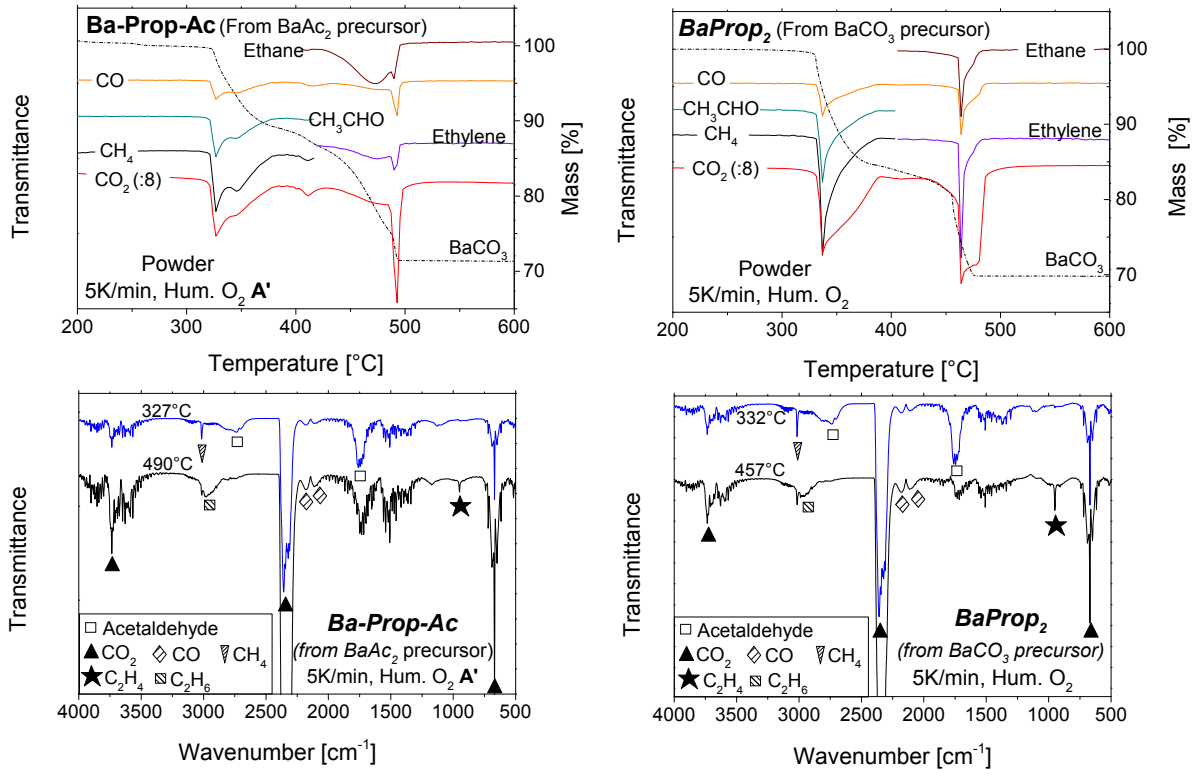

Fig. 3.23: Comparison of the thermal behavior of different Ba carboxylate precursors in O_2. *The TG curves of ~40-mg powders obtained from two different Ba precursors show similar behavior. (Bottom) Corresponding Gas-Infrared spectra of the TG curves shown above.*

3.3.3 Film decomposition

Decomposition in oxidative atmosphere

The mixed Ba carboxylate films are stable until 200-230°C (Fig. 3.18a), the exact temperature depending on film thickness (Fig. 3.24). Then, in both humid and dry O_2 (**A**), decomposition starts roughly in correspondence of the first melting peak. Independently of the fact that several sudden changes in the TG curve appear as the thickness increases (Fig. 3.24) which will be discussed later on, decomposition in oxygen is mainly driven by oxidation, as suggested by the DSC exothermic peak (Fig. 3.18). As shown in Fig. 3.21a and b, several reactions overlap as the C-C chain is oxidized first to acetaldehyde (CH_3CHO) and CO_2, and then further decomposed to methane (CH_4) and CO. In dry and humid O_2, the decomposition shows similar behavior: water does not seem to accelerate decomposition, contrarily to other propionates such as $YProp_3$ and $CuProp_2$, and the volatiles do not differ from the dry O_2 case, as no propionic acid can be detected. Even for thin films (see Fig. 3.24), the final product consists of $BaCO_3$, even in the presence of water vapor.

The infrared spectra of the solid residues (Fig. 3.25) show that before yielding the final product $BaCO_3$, formation of an oxalate occurs, as the COO^- stretching band shifts above 1580 cm^{-1} [149]. The oxalate is not a stable intermediate and, as soon as it is formed, it decomposes to $BaCO_3$ already around 330-350°C (Fig. 3.25). To confirm the presence of the oxalate, a sample quenched in humid O_2 at 340°C (Fig. 3.26) was decomposed in vacuum, yielding CO_2 as main volatile. Although CO is expected for BaC_2O_4 decomposition to yield $BaCO_3$, the dark color of the final product indicates the presence of carbon that can be attributed to disproportion of CO to $C+CO_2$ [150,151]. In fact, the final product is grayish/black already for 6-7 µm where the slow local out-diffusion of the CO enhances CO disproportion; only thinner films (~2 µm) are white due to the faster CO out-diffusion with respect to its production. After 350°C, as the $BaCO_3$ is formed, decomposition slows down and it is not complete until 450°C, when the mass is stable at ~71% (Fig. 3.24). Fig. 3.21**A** shows that CO_2 alone is detected by gas-IR above 400°C.

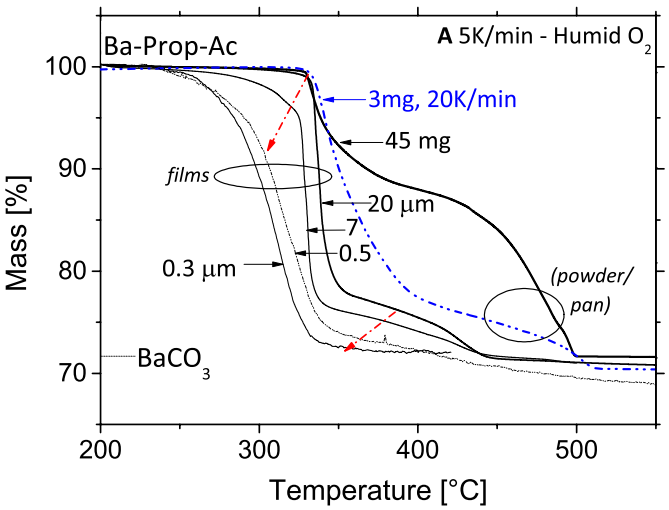

Fig. 3.24: Effect of thickness on the TG curves of Ba-Prop-Ac*: the thicker the film, the slower the O_2 diffusion. The discontinuity of the TG curve at ~340°C is characteristic of both films and powders, showing no thermal activation changing the heating rate.*

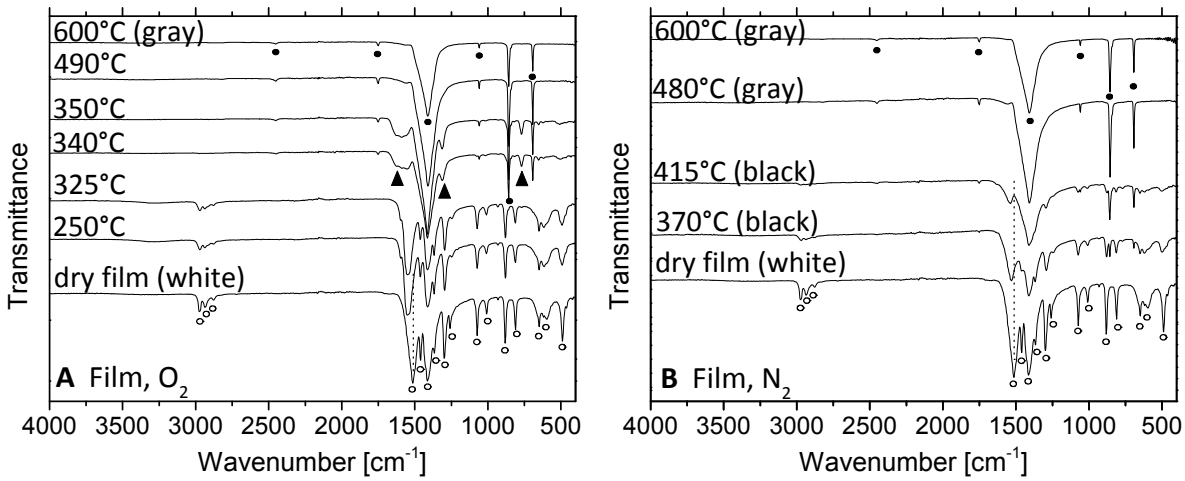

***Fig. 3.25**:* Infrared evolution of the solid residue from Ba-Prop-Ac decomposition. *Symbols: (°) Ba-Prop-Ac, (●) $BaCO_3$, (▲) Barium Oxalate (BaC_2O_4).*

To clarify if the mass loss at this stage is due to the oxalate decomposition (expected final mass for BaC_2O_4 formation starting from $BaProp_2$ and $Ba_7Prop_8Ac_6$: 79.5%-83.0%, respectively) or to the acetate part (expected final mass for the removal of all propionates in $Ba_7Prop_8Ac_6$: 81.9%), Ba-Prop-Ac TG curves can be compared with those of $BaProp_2$ and $BaAc_2$ (Fig. 3.18). The Ba-Prop-Ac salt curve measured in O_2 is closer to that of $BaProp_2$ than to that of $BaAc_2$, which decomposes ~100°C above (dotted lines in Fig. 3.18). The $BaProp_2$ salt exhibits the same volatiles as $Ba_7Prop_8Ac_6$ in oxygen, the only difference being that it decomposes to $BaCO_3$ in a single mass-loss step at ~350°C during which the oxalate (BaC_2O_4) is still formed (detected by FTIR while it converts to $BaCO_3$). This suggests that the mass loss step above 350°C in the mixed carboxylate salt is not due to the oxalate decomposition but to the decomposition of the acetate part of the salt, in agreement with the higher decomposition temperature of $BaAc_2$. This effect is shown in Fig. 3.24 where, as the Ba-Prop-Ac film thickness increases, decomposition slows down after 350°C. The effect seems to be more important in humid than in dry O_2, probably because O_2 concentration and thus its diffusion rate through the film is lower in the presence of water vapor, hence oxidation is slowed down. As a further proof, Fig. 3.26 shows that the same quenched sample at 340°C yields mainly m/z=43 (acetone) upon further decomposition, due to the remaining barium acetate, while the contribution of propionate groups is residual. The XRD results in Fig. 3.16 (inset) show that the final product is the orthorhombic phase of $BaCO_3$ at 500°C, as expected [152,153].

As introduced above, decomposition in O_2 shows the presence of several sudden changes in the slope of the TG curve (Fig. 3.24) with increasing film thickness. The abrupt mass loss at 330-340°C is probably caused by the fast O_2 diffusion through the liquid as soon as Ba-Prop-Ac melts. Afterwards, above 350°C, formation of $BaCO_3$ slows down gas diffusion again. Although the second melting event is expected to occur at a higher temperature than those of the fast mass loss, it can shift due to the presence of decomposition products generated by the early reaction of O_2 with the sample surface. In fact, this discontinuity of the TG curve at ~340°C is characteristic of both films and powders, showing no thermal activation changing the heating rates (Fig. 3.24, curve at 20°C/min).

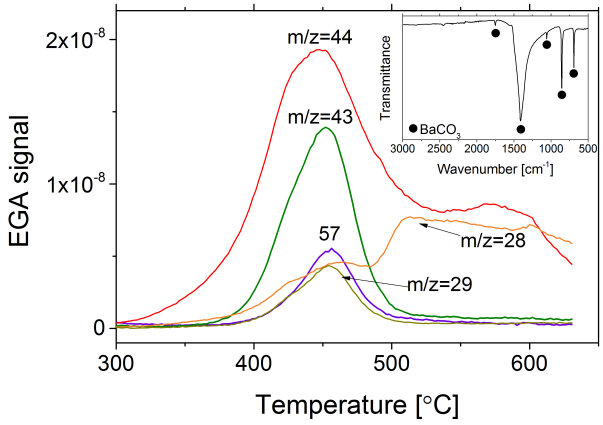

***Fig. 3.26**:* EGA-MS analysis from decomposition of barium species. *The EGA-MS results are relative to the decomposition in vacuum of a quenched film obtained from decomposition of Ba-Prop-Ac in humid O_2 at 340°C; inset: FTIR of the final product at 600°C. The volatiles detected help identify what remains after decomposition to 340°C in an O_2 atmosphere: BaC_2O_4 (m/z=44) and the acetate part (m/z=43, acetone), while remaining propionate groups are only residual (m/z=57,29 from 3-pentanone).*

Decomposition in N_2 atmosphere

When the film is decomposed in nominally humid and dry N_2 (**C**), the behavior differs from the powder sample in N_2 (**B'**) and resembles that of powders in O_2 (**A'**): reaction **α** and reactions **β** and **γ** take place at low and high temperature, respectively. In fact, decomposition is triggered at the discontinuity in the TG curve at ~330°C generated by the melting event; this first step between 320 and 380 °C becomes more important with decreasing film thickness (not shown) and, therefore, it can be ascribed to residual oxygen content in the nominally oxygen-free atmosphere; in fact it has already been shown that the thinner the film, the more prone to oxidize [26]. During this stage, CO_2 is detected by TG-FTIR, along with acetaldehyde and propionic acid. In fact, since O_2 is residual, it is not enough to get full oxidation (reaction **α**) and partial oxidation takes place according to:

$$Ba(C_2H_5CO_2)_2 + O_2 \rightarrow CH_3CHO + C_2H_5CO_2H + BaCO_3.$$

As the $BaCO_3$ is formed (see Fig. 3.25**B)**, it acts as a diffusion barrier to O_2, and oxidation cannot reach completion. Thus, a second step at a higher temperature (between 400-470°C) occurs. Reaction schemes **β** (favored in N_2) and **γ** (triggered by O_2) compete. Given the fact that the volatiles evolve during a longer period of time than in O_2 atmosphere, they become more diluted and, consequently, their TG-IR signal is smaller; nevertheless CO_2 (related to **γ**) could be clearly detected. The last mass loss between 470-530°C, which corresponds again to CO_2 release, is due to decomposition of the acetate part since it is not observed for the $BaProp_2$ salt decomposed in the same conditions. For this reason, Fig. 3.21**A'** reports the TG-FTIR analysis of powders in O_2, since they follow a similar trend. The overall decomposition behavior of films in nominally inert atmosphere can be interpreted as a mix of decomposition in an oxidizing atmosphere and in inert atmosphere (reaction **β**). Note that the DSC signal in Fig. 3.18b is always exothermic.

Decomposition in vacuum

Since residual oxygen is extremely low in vacuum, only in these conditions CO_2 is not detected for films (Fig. 3.21**C**). The main fragments are m/z= 57, 29 (coming from 3-pentanone) along with C_2H_x fractions of the ligand (m/z=29,28,27). A very similar behavior is observed in vacuum for $BaProp_2$ (see Fig. 3.27), for which the same volatiles are detected, including m/z=43. This last fragment could be CH_3CO or C_3H_7, coming from acetone or from butane, respectively. However, since in this particular case no acetate groups are present, m/z=43 can be ascribed to butane formation, according to reaction scheme ***∂*** of Fig. 3.22. This interpretation can also explain part of the m/z=43 coming from the Ba-Prop-Ac decomposition in vacuum (**E**), indicating that the main component in the mixed carboxylate salt is still made up of propionates, thus justifying again the reaction schemes of Fig. 3.22. Interestingly, in vacuum decomposition is shifted down by almost 100°C with respect to the case of inert atmosphere at atmospheric pressure (dry N_2, **B'**), although they both proceed through the radical path. This early decomposition is probably triggered by the barium carboxylate (second peak) melting, which is shifted to lower temperatures as the pressure decreases.

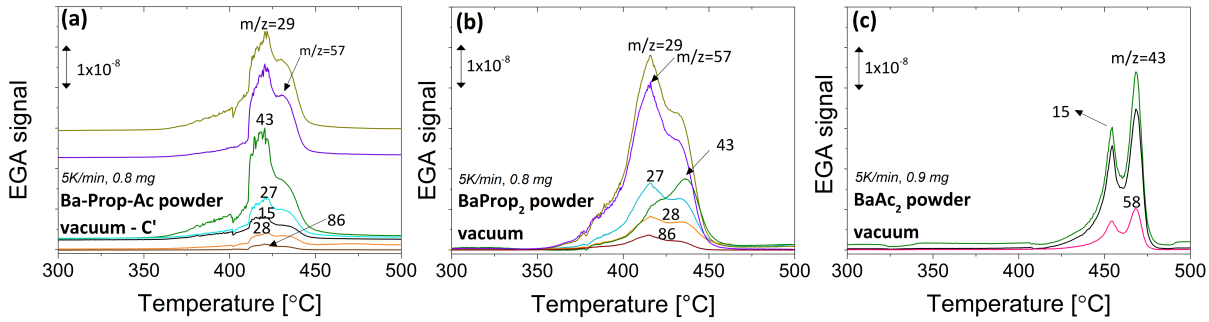

Fig. 3.27: Comparison of EGA-MS experiments relative to different barium precursors. *The results on the powders decomposed at 5K/min, show that the thermal behavior of* ***(a)*** *Ba-Prop-Ac is similar to that of* ***(b)*** *$BaProp_2$ but very different from that of* ***(c)*** *$BaAc_2$. In* ***(c)*** *the double peak is ascribed to the melting event of $BaAc_2$ (T_{onset} ~455°C from on-going TG-DSC studies, see also Chap. 4.2), which triggers its decomposition in inert atmosphere; in fact, it has been seen that in N_2 the decomposition temperature for powders of $BaAc_2$ is not thermally activated, which is a signature of melting.*

3.3.4 Discussion

$BaProp_2$ and Ba-Prop-Ac decomposition is diffusion-controlled: in an oxidizing atmosphere, films decompose at a temperature lower than powders due to the faster gas exchange [23,27], which helps the low-temperature decomposition mechanism triggered by oxygen. Unlike the $CuProp_2$ and $YProp_3$ cases, a humid atmosphere does not clearly accelerate decomposition through the hydrolysis of the salt (and propionic acid release), since this reaction path would require formation of the oxide and not the oxalate-carbonate sequence of products. Besides that, $BaProp_2$ thermal decomposition seems to follows the expected radical mechanism at high temperatures and inert atmospheres already found for $YProp_3$ and for those carboxylate salts where the metal center does not easily undergo reduction [43]. In fact, local residual oxygen depletion around the sample in the form of powder suppresses the oxidative reaction in a

nominally inert N_2 atmosphere. In contrast, films in this atmosphere are affected by the residual oxygen content and, as it occurs in O_2, they decompose at a temperature lower than powders.

The Ba-Prop-Ac thermogravimetric behavior in films is less smooth with respect to that of other metalorganic precursors as films (see the case of $CuProp_2$ and $YProp_3$) because it is disrupted by the melting events. O_2 diffusion is accelerated in the melt, while any solid decomposition product (oxalate and carbonate) slows down gas diffusion. Only a study as a function of thickness has revealed this dependence, which could be otherwise mistaken for intermediates.

The presence of acetaldehyde among the volatiles of this work cannot necessarily be related to the presence of acetate ligands in the salt [29], since acetaldehyde was also detected among the gaseous products of the $BaProp_2$ salt [44]. In fact, although the crystal consists of a mixed propionate-acetate complex, the thermal behavior of the solution and the powder in all atmospheres tends to that of $BaProp_2$, in terms of kinetics and volatiles, and the presence of acetate ligands is hard to detect from EGA alone. It is thus possible that the Prop/Ac ratio of the crystal (obtained from a long aging of the solution) differs slightly from that of the dry solution (used for film and powder decomposition). In fact, the final mass is always inferior to the expected 72.7% for the $Ba_7Prop_8Ac_6$-$BaCO_3$ conversion which, counting the presence of residual carbon and the instrumental error (especially in films due to the small amount of material), points towards a slightly higher Prop/Ac ratio.

Our results are significant for understanding FF-YBCO film pyrolysis. In particular, the propionate/acetate ratio in the ternary solution is also expected to depend on concentration and solvents ratio. The presence of other acetate salts (i.e. those of Cu and Y) in solution can further alter this equilibrium and, eventually, it may favor formation of the mixed carboxylate complex. If this complex is formed instead of $BaProp_2$, decomposition of thick films in O_2 would end at higher temperatures. Although $BaCO_3$ constitutes a challenge for the epitaxial growth of FF-YBCO, in the conditions of this work and for the isolated barium precursor, no specific case was found were a carbonated product can be avoided in favor of a hydroxide or an oxide, not even in humid atmospheres.

3.4 Partial conclusions

The thermal decomposition of the isolated FF-precursor components showed that films behave differently than the corresponding powders due to the higher surface/volume ratio that enhances the local atmosphere gas renewal and heat dissipation. Conversely, in the bulk form, gas diffusion is slowed down and so is also heat transport and dissipation due to the gas-depletion inter-particle. This leads to the fact that powders experience a more inert local atmosphere in the bulk; since inert atmospheres induce decomposition at higher temperatures with respect to O_2 atmospheres, powders are more thermally stable than films, which decompose earlier in the same furnace atmosphere.

The decomposition of the three metalorganic powders follows the same order also when in the form of films, where the barium precursor shows the highest thermal stability, followed by the yttrium propionate and the copper propionate.

In inert furnace atmospheres, the three metalorganic species are more stable than in oxidative or humid atmospheres. In N_2, $BaProp_2$ and $YProp_3$ decompose following a radical mechanism, with generation of 3-pentanone and formation of a carbonate, $BaCO_3$, and an oxide, Y_2O_3, respectively. Conversely, $CuProp_2$ decomposition is driven by the nature of the metallic cation which is more prone to undergo reduction: thus, formation of metallic Cu is accompanied by oxidation of the propionate units to propionic acid, acetaldehyde and CO_2.

In an O_2 atmosphere and for the three metalorganic salts, oxidative degradation of the propionate unit takes place at lower temperatures than the radical mechanism. Since the Ba-Prop-Ac decomposition product cannot be an oxide at such low temperatures due to the difficulty to break the BaO—C(=O)R bond, the oxidation path generates first an oxalate and then a carbonate, which are both an indication of the retainment of two and one carbonyl groups (C=O), respectively. Thus, the oxidative degradation of Ba-Prop-Ac generates mostly acetaldehyde and CO_2 from the cleavage of the BaOC(=O)—R bond. Conversely, for $YProp_3$ and $CuProp_2$ oxidation is smoother, releasing acetaldehyde, propionic acid and CO_2 to form the corresponding oxide.

Humid atmospheres are efficient in decreasing the amount of residual carbon and the decomposition temperature especially for the $CuProp_2$ as its decomposition proceeds almost entirely through the hydrolysis of the salt. They are less efficient for $YProp_3$ (and $BaProp_2$) where formation of an intermediate oxycarbonate (and oxalate) does not permit a full hydrolysis of the propionate units. Thus, for the Y and Ba precursors the oxidation path is preferred to the hydrolysis, only in part for the Y and fully for the Ba salt.

In the context of YBCO this study explains why humid atmospheres are beneficial for the pyrolysis step, and why $BaCO_3$ cannot be avoided as decomposition product in the conditions under study.

PYROLYSIS STUDIES OF THE TERNARY SOLUTION AND ADDITIVE EFFECT

Chapter 4

4.1 TEA effect on single-component precursor solutions

This section will make use of the knowledge developed in Chapter 3 from the decomposition of single-component solution to understand the effect of common additives, in particular triethanolamine, on the thermal behavior of those same solutions. Specifically, solutions of YAc_3, $BaAc_2$ and $CuAc_2$ in a 1/1 mixture of propionic acid and non-anhydrous MeOH with a 5% v/v of TEA, labelled as sol. **TY**, **TB** and **TC**, respectively. For comparison purposes, also solutions without propionic acid were prepared from the corresponding $MProp_x$ salts dissolved in MeOH with 5% TEA, labelled as sol. **TY'**, and **TC'** (more details in section 2.2.1).

Thermal analysis techniques and chemical characterization methods will be applied to identify the thermal decomposition mechanism and chemical species that develop during pyrolysis of films and powders in different atmospheres. The aim will be to understand the effect of TEA during and after pyrolysis of the ternary solution in films in humid O_2, that is known to result in more stress-free films.

4.1.1 Thermal decomposition of Ba-Prop-Ac/TEA (sol. TB)

Ba-Prop-Ac/TEA solution (solution **TB**) exhibits the simplest behavior of the three under study, and for this reason is discussed first. The FTIR spectra in Fig. 4.1a of the dry films show characteristic TEA vibration bands, and the partial replacement of acetate groups by propionates [102] with formation of a mixed Ba-Prop-Ac complex [29]. The XRD of the dry film (Fig. 4.1b) is in agreement with that of the mixed carboxylate salt Ba-Prop-Ac described in Chapter 3, suggesting that no new TEA-Ba complex is formed.

The thermogravimetric curve shown in Fig. 4.2 exhibits three main mass loss steps: a first one between 50 and 150°C, which corresponds to water and propionic acid evaporation. A second TG step with 27.7% mass loss (theoretical for TEA removal: 28.4 and 29.28% starting from $BaProp_2$ and $BaProp_8Ac_6$, respectively) takes place between 150-300°C. In the low-temperature region of this range (150-210) a gradual mass loss occurs while the FTIR of the solid residue

shown in Fig. 4.1 (210°C) reveals that while TEA is evolving, an IR band at 1735 cm^{-1} emerges. This band can be assigned to an esteric bond between propionate groups and TEA's OH groups. Indeed, this band also appears in a solution of only TEA and propionic acid, as shown in Fig. 4.3.

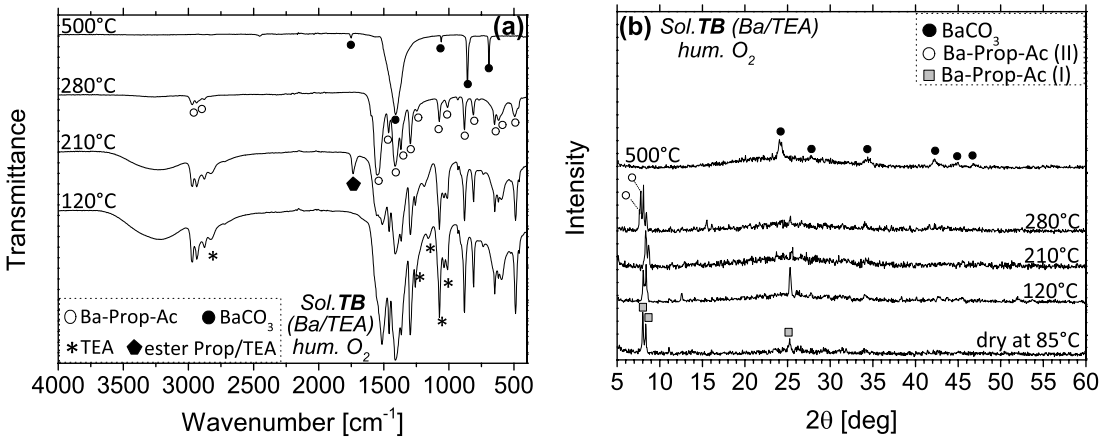

***Fig. 4.1**:* Chemical characterization of the solid residue from decomposition of Ba/TEA solutions. ***(a)** FTIR analysis and **(b)** XRD pattern of the quenched films during decomposition of solution **TB** (Ba/TEA) in humid O_2 at 5°C/min.*

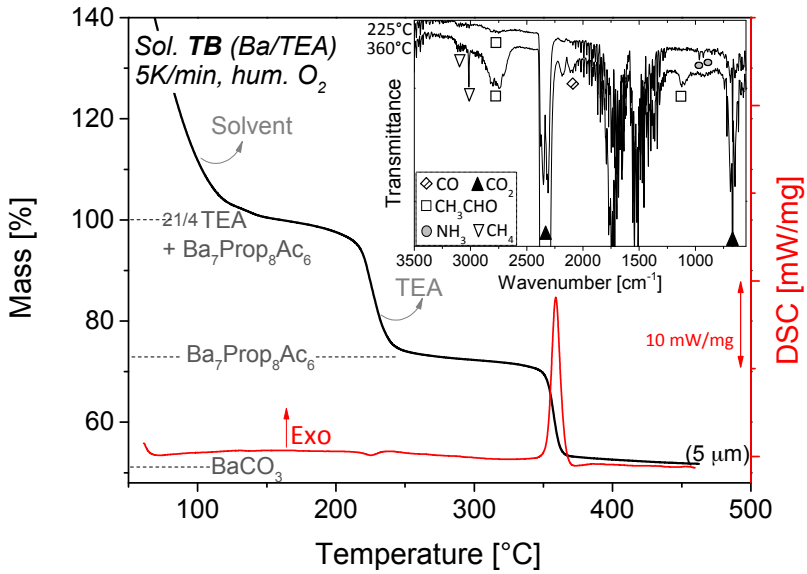

Fig. 4.2: TG-DSC-FTIR analysis of Ba/TEA film in humid O_2. *Inset: Infrared spectra of gas species detected from the corresponding TG-FTIR analysis at 5°C/min.*

Since it is known from the previous chapter that during the barium carboxylate salt decomposition, propionic acid evolves up to 150-200°C, it is reasonable to believe that the propionate units involved in the esterification come from the solvent. In fact, if they came from the salt, the last mass loss in Fig. 4.2 relative to Ba-Prop-Ac decomposition should be smaller. An endothermic DSC signal at 220°C is also consistent with some TEA evaporation, although it was not possible to identify it by infrared in the gas phase due to the little amount evaporating which is further reduced by its condensation along the path, a phenomenon already noted by [55].

Additionally, between 210 and 300°C, the high temperatures promote TEA decomposition and in fact the infrared of the gaseous products shows TEA's decomposition products: ammonia and acetaldehyde (TG-FTIR in inset of Fig. 4.2).

Simultaneously, the XRD curves in Fig. 4.1b above 200°C show new peaks shifting toward lower angles, indicating a change in the barium carboxylate structure after solvent and water elimination which take place during TEA removal. As expected, also its carboxylic stretching bands have shifted from 1512 cm^{-1} to 1549 cm^{-1} during the 200°C-interval before oxidative degradation begins. Both effects observed by XRD and FTIR were also noticed for the barium salt alone (Chap. 3.3) and attributed to dehydration, recrystallization and melting. The main TEA absorptions and the ester peak disappear after this stage, leaving a FTIR spectrum at the beginning of the third stage (280°C) that is identical to that of Ba-Prop-Ac shown in Fig. 3.15.

The third TG step occurs between 300-500°C and corresponds to the decomposition of Ba-Prop-Ac to $BaCO_3$, with a characteristic exothermic peak and with a ratio $m_{500°C}/m_{300°C}$ for this step of 71.2% (theoretical: 69.9 and 72.7% starting from $BaProp_2$ and $Ba_7Prop_8Ac_6$, respectively). Acetaldehyde, CO_2, methane and CO are detected in humid O_2, in agreement with what previously shown in Chapter 3.3.

The expected final mass with respect to the initial dry film considering a simple addition of all components in solution ($BaProp_2$/Ba-Prop-Ac + TEA) is between 49.85 and 51.41%, in agreement with the thermogravimetric curve that lies at 51%. EA results in Table 4.1 at 500°C shows a C% value slightly above the expected one for $BaCO_3$, which might be in agreement with the gray color of the final product (expected to be white) due to residual carbon remaining, just as in the case of Ba-Prop-Ac alone. With respect to Ba-Prop-Ac alone (see Chapter 3), the thermogravimetric behavior is very similar as well as the final decomposition temperature. Also, the EGA-MS analysis of a film of solution **TB** decomposed in vacuum yields identical results to the EGA-MS of Ba-Prop-Ac without TEA, confirming that TEA evaporation in vacuum takes place before the salt decomposition.

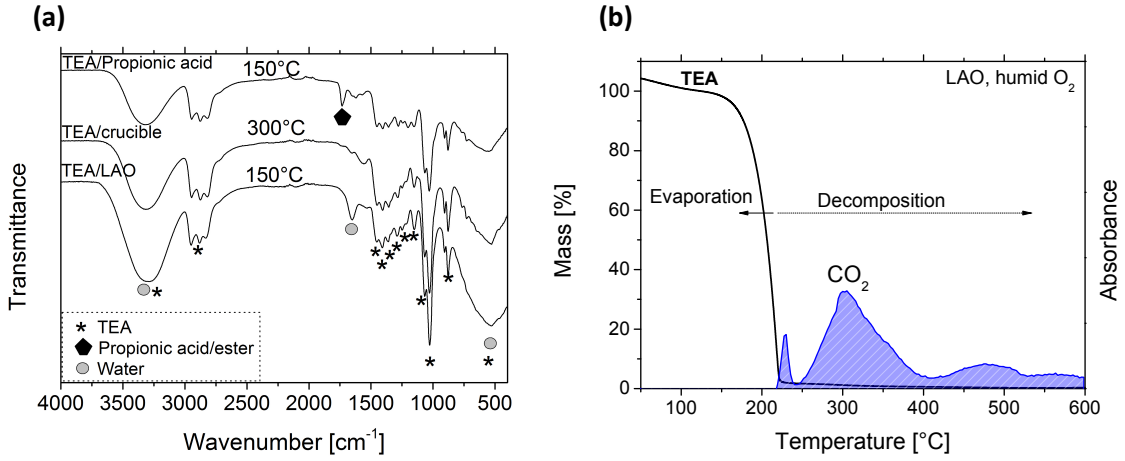

***Fig. 4.3**:* Thermal analysis of TEA and TEA/propionic acid solutions. ***(a)** FTIR of solid residue after TEA is decomposed to a given temperature and FTIR of a solution of TEA in propionic acid at 150°C. The probable esterification reaction between the -OH terminal groups of TEA and the carboxylic group of the propionic acid may result in the peak at 1736 cm^{-1}. **(b)** TG-IR analysis of TEA in humid O_2 at 5°C/min.*

Compound	Found (expected), mass wt %	
	wt %C	wt %H
TY (Y/TEA, 600°C)	1.3 (0)	- (0)
TY (Y/TEA, 500°C)	2.6	0.4
TC (Cu/TEA, 500°C)	- (0)	- (0)
TB (Ba/TEA, 500°C)	6.7 (6.09)	- (0)

Table 4.1: Elemental analysis of the metal carboxylate/TEA solutions. *The results are relative to the decomposition products of metal carboxylate/TEA solutions in humid O_2 at 5°C/min. (-) values inferior to detection limits. Expected values correspond to yttria, copper oxide and barium carbonate.*

4.1.2 Thermal decomposition of $CuProp_2$/TEA (sol. TC)

Decomposition in oxidative atmosphere

The FTIR analysis of the dry film from $CuProp_2$/TEA (solution **TC**) in Fig. 4.4a shows the appearance of the TEA IR bands and of $CuProp_2$ vibrations [31,123], in agreement with the expected replacement of acetate groups by propionates of the solvent when this is in excess [102]. But the XRD pattern, Fig. 4.4b, is significantly different from that of $CuProp_2$ shown in Chapter 3, suggesting a possible coordination between TEA and $CuProp_2$.

The TG analysis in humid O_2 reported in Fig. 4.5 shows that after solvent removal and dehydration below 150°C, four overlapping steps centered at 155, 210, 245 and 328°C take place: they correspond to exothermic peaks (DSC signal in Fig. 4.5, top). The gas species evolved during decomposition in humid O_2 consist of propionic acid, acetaldehyde, CO_2 and NH_3 (Fig. 4.5). Since only NH_3 can be easily assigned to TEA decomposition, while all other gas species are the expected volatiles for both TEA and for $CuProp_2$ decomposition, interpretation of TG-FTIR results is not straightforward.

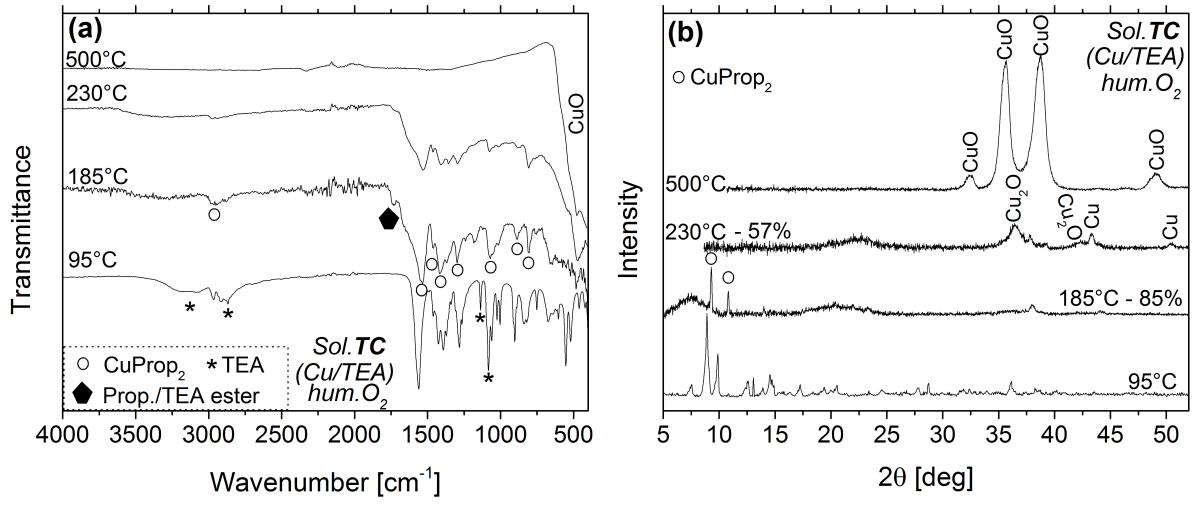

Fig. 4.4: Chemical characterization of the solid residue from decomposition of $CuProp_2$/TEA solutions. ***(a)*** *FTIR analysis and* ***(b)*** *XRD patterns.*

The four mass steps can be grouped into two main stages which correspond to $CuProp_2$ accompanied by some TEA release, and TEA decomposition, respectively.

In particular, the first stage, between 100-230°C, matches with $CuProp_2$ decomposition and TEA removal: the FTIR (Fig. 4.4a) of the solid residues quenched at 185°C shows that the main TEA vibrational band at 1082 cm^{-1} is decreasing; simultaneously, the $CuProp_2$ reflections are detected by XRD (Fig. 4.4b) [124] while it decomposes to propionic acid and CO_2 (TG-FTIR analysis in Fig. 4.5) according to the expected hydrolysis and degradative oxidation path. Between 95 and 185°C, an IR band at 1735 cm^{-1} appears in the solid residue, Fig. 4.4a, which may be assigned to some TEA/propionate esteric bond, although a similar absorption band was observed for the $CuProp_2$ decomposition in correspondence of its reduction to Cu(I).

The second stage, between 230-500°C, is affected by the fact that decomposition of TEA takes place at these temperatures in oxygen: between 230°C-270°C, CO_2, acetaldehyde and NH_3 from oxidative degradation are detected while Cu(II) is reduced to Cu_2O and Cu (XRD in Fig. 4.4). The presence of CO_2 between 210-250°C (Fig. 4.4) could be an indication of this redox reaction due to carbon left by TEA. The last mass loss, releasing CO_2 at 328°C, is again indirectly attributable to the presence of TEA, since the end of decomposition is shifted to almost 100°C higher with respect to the case of $CuProp_2$ film alone, for which it is over by 250°C (see Chapter 3). In fact, at higher temperatures in O_2, a TG-IR experiment run on TEA alone and reported in Fig. 4.3b shows that TEA is oxidized to CO_2. The final product consists of CuO, as shown by XRD and FTIR in Fig. 4.4, and no carbon or hydrogen is detected by EA (Table 4.1). The experimental final mass lies at 32%, slightly above the expected value of 28.9 %. A solution of $CuProp_2$ with 5% TEA in only MeOH (sol. **TC'**) yields the same TG-IR behavior and for comparison it is shown in Fig. 4.5.

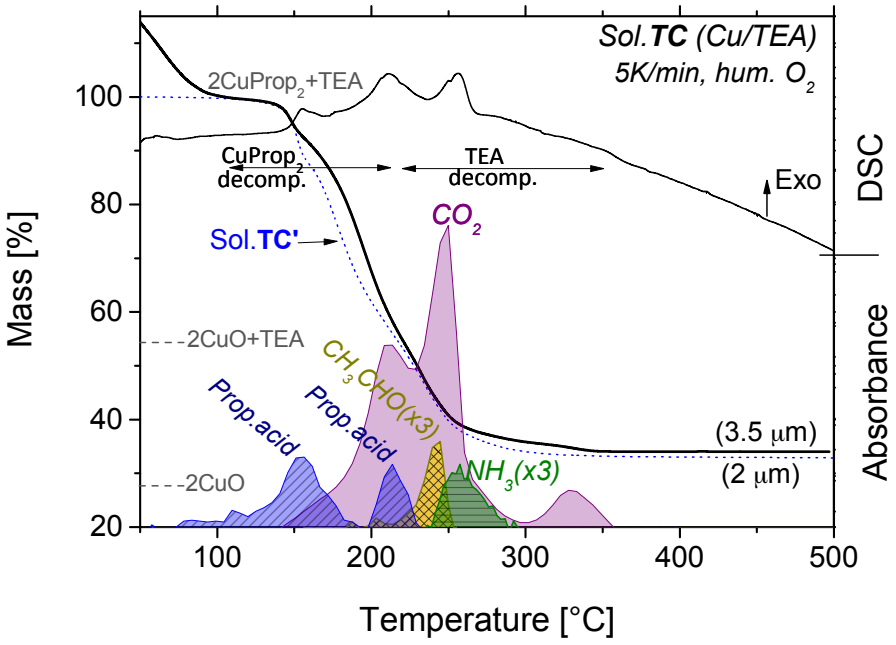

Fig. 4.5: TG-DSC-FTIR analysis of $CuProp_2$/TEA in humid O_2. *Films from sol.* ***TC*** *are shown, decomposed at 5°C/min.*

Decomposition in inert atmosphere

It is known that both $CuProp_2$ and TEA, independently, exhibit a strong tendency to evaporate at low total pressure. But when decomposition of solution **TC** is carried out in vacuum (Fig. 4.6, bottom, EGA-MS experiment), $CuProp_2$ evaporation is considerably reduced. In fact, unlike the case of $CuProp_2$ alone in the form of film, with the addition of TEA, no $CuProp_2$ is recovered from condensation along the quartz tube, and the mass loss is not significantly higher than the expected value; the final product at 500°C consists of a shiny metallic copper film, indicating that $CuProp_2$ evaporation is definitely reduced in vacuum when TEA is added.

However, from the EGA-MS analysis in Fig. 4.6, only a low-temperature stage is observed: the most intense peak, at 200°C, still shows evolution of propionic acid (m/z=45, 29, 28, 27) corresponding to $CuProp_2$ decomposition, but an excess of m/z=28 (CO, N_2 or C_2H_4) with respect to the case without TEA (Chapter 3) is detected. This might be an indication that a TEA effect is present up to 200°C, and thus that also its evaporation is reduced when $CuProp_2$ is added, due to the coordination between TEA and Cu^{2+} of the carboxylic salt. To better understand the thermal decomposition of sol. **TC** in inert atmosphere, the effect of evaporation should be avoided by *i)* studying decomposition in powders instead of films and *ii)* under an atmospheric pressure of an inert gas, such as N_2, instead of at low total pressures.

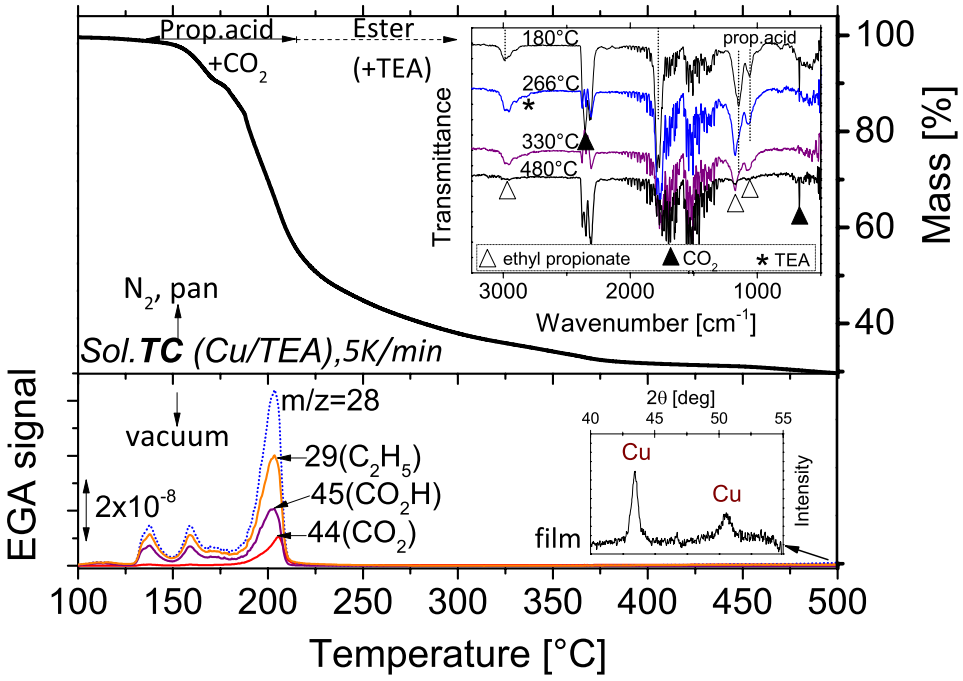

Fig. 4.6: TG-FTIR and EGA-MS analysis of $CuProp_2$/TEA in inert atmosphere. *Top graph: TG-FTIR analysis of solution **TC** in atmospheric pressure of N_2. Inset: FTIR spectra of the volatile at selected temperatures. Bottom graph: EGA-MS analysis from decomposition in vacuum of $CuProp_2$/TEA at 5°C/min.*

The TG behavior during decomposition in N_2 of the corresponding powder obtained from solution **TC** is reported in Fig. 4.6 (top graph). Exothermic events still take place in the first stage, before 230°C, in correspondence of propionic acid and CO_2 release, coming from the beginning of $CuProp_2$ decomposition in N_2. The main difference from the humid-O_2 case lies in the formation of a TEA-propionate ester evolving at 260°C, in the second stage; this ester is ethyl propionate,

detected among the volatiles by TG-FTIR (inset in Fig. 4.6) along with some TEA, while CH_3CHO and NH_3 that would come from TEA decomposition alone are no longer noticeable.

This ester (ethyl propionate) comes from a decomposition process; thus, it is different from the ester observed by FTIR (band at 1735 cm^{-1}) in the solid residue at low temperatures in sol. **TB**, Fig. 4.1a (but also later on in sol. **TY**) which instead comes from esterification between TEA and propionic acid (see also Fig. 4.3a). This difference will be further commented in section 4.1.3, in the case of sol. **TY**. Indeed, ethyl propionate can be ascribed to the decomposition path described by the following reaction scheme:

$$^{x}/_{3}N(C_2H_4OH)_3 + M(C_2H_5CO_2)_x \rightarrow xC_2H_5C(=O)-OC_2H_5 + MO_x + {}^{x}/_{6}N_2 \qquad (4.1)$$

Where M is the metal cation (Cu or Y).

Note that, in vacuum, formation of ethyl propionate is probably disfavored by the low decomposition temperature (200°C) and the tendency for both TEA and $CuProp_2$ to evaporate at low total pressures. Note also that in N_2, $CuProp_2$ in powder form and without TEA, decomposes with a sharp mass loss followed by copper reduction to Cu(0); conversely in sol. **TC** the presence of overlapped decomposition between TEA and the carboxylic salt makes decomposition smoother.

Finally, note that according to reaction scheme 4.1, generation of ethyl propionate as volatile corresponds to the formation of the oxide CuO instead of the metallic Cu. Indeed, in the same decomposition conditions (powders in N_2) only Cu and Cu_2O are observed during decomposition of $CuProp_2$ without TEA (Chapter 3) at 360°C; conversely, during decomposition of $CuProp_2$ with TEA, also CuO is detected at 360°C (sol. T**C**, see Fig. 4.7), which indicates that less reduction is occurring at intermediate temperatures. But the quenched $CuProp_2$/TEA powder at 360°C is black even though the main XRD reflections belong to Cu(0), maybe due to residual carbon. It is reasonable to believe that when TEA decomposes simultaneously to $CuProp_2$ forming the ester (stage II of Fig. 4.6) instead of propionic acid, it prevents Cu(II) reduction in N_2 through reaction scheme *4.1.*

Once formed, this copper oxide is eventually reduced to Cu(0) in inert atmosphere, further helped by the residual carbon, which evolves as CO_2. CO_2 is indeed detected between 480-500°C (see inset in Fig. 4.6). The final mass lies at 29.6%, higher than the expected value for Cu, indicating presence of residual carbon, just as found for the case of the thermal decomposition of powders of $CuProp_2$ in N_2.

Thus, formation of the ethyl propionate ester requires higher temperatures than the low-temperature range (100-200°C) where $CuProp_2$ is expected to decompose in O_2 (see Fig. 4.8), and for this reason, its contribution to decomposition in humid O_2 is minor (and propionic acid remains the main volatile). Due to the fact that, as demonstrated in Chapter 3, an increase in $CuProp_2$ film thickness causes a shift of decomposition to higher temperatures, some ethyl propionate is also detected even in humid O_2 above 200°C for CuO films thicker than 3 μm.

Finally, even increasing the TEA/Cu ratio in solution to 1/1 in order to push the equilibrium towards the ester instead of towards propionic acid is unsuccessful: the main volatile in humid O_2 is still propionic acid (not shown).

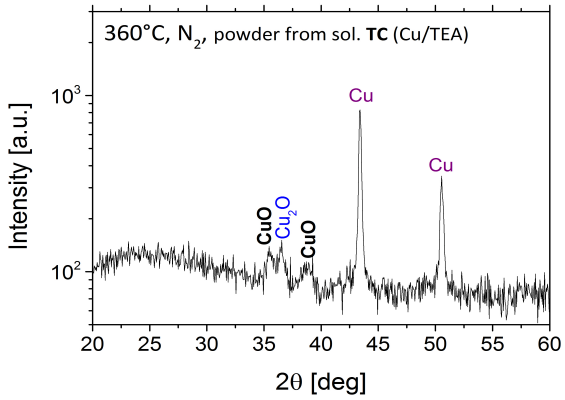

Fig. 4.7: XRD analysis of a quenched Cu/TEA sample during decomposition. *The powder sample was quenched at 360°C during decomposition in N_2.*

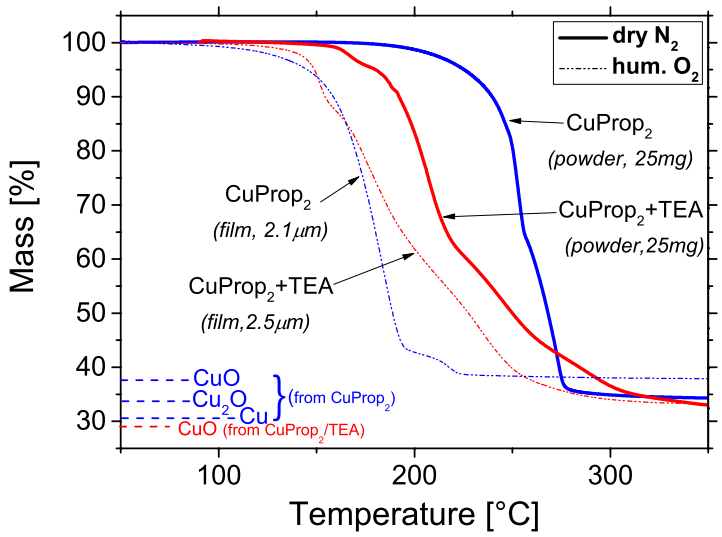

Fig. 4.8: Comparison of TG curves for $CuProp_2$ with and without TEA. *The comparisons are relative to the pyrolysis in dry N_2 and humid O_2 at 5°C/min. Dashed horizontal lines: theoretical final mass to yield copper oxides and Cu from $CuProp_2$ (in blue) and $CuProp_2$/TEA (sol **TC**, in red).*

4.1.3 Thermal decomposition of $YProp_3$/TEA (sol. TY)

Decomposition in oxidative atmosphere

As shown from the TG curve of Fig. 4.9, the solution of $YProp_3$/TEA (solution **TY**) is hard to dry at low temperature, since evaporation and decomposition overlap: after drying at 80°C, the film is still a colorless viscous liquid and the FTIR spectrum of Fig. 4.10a shows the TEA IR bands and those of $YProp_3$ (Chapter 3). To remove the contribution of propionic acid as solvent and for the sake of clarity, the time-resolved evolution of the volatiles reported in the TG-FTIR analysis of Fig. 4.9 is relative to solution **TY'** (dotted lines). In fact, **TY'** is prepared by dissolving $YProp_3$ in MeOH, instead **TY** by dissolving YAc_3 in a mixture of propionic acid and MeOH (see Chap. 2). For both **TY** and **TY'**, the expected total mass loss of 21.2%, calculated considering the sum of $YProp_3$ and TEA in solution, is in agreement with the experimental value of 24.5% of Fig. 4.9, taking into account that the FTIR analysis (Fig. 4.10a) of the solid residue at 600°C reveals the presence of residual $Y_2O_2CO_3$.

Three main stages can be identified when decomposition is carried out in humid O_2.

The first one, between 50 and 150°C (Fig. 4.9), involves dehydration and evaporation of the solvent (propionic acid). In fact, in the solid residue, Fig. 4.10a, the main propionic acid and H_2O IR absorptions decrease going from 90°C to 150°C. In particular, the disappearance of the broad band between 2500-400 cm^{-1} is a sign of solvent removal, but also the general intensity decrease in the 1300-1700 cm^{-1} region (where the $YProp_3$ bands are) is due to the solvent. This step also corresponds to the appearance of an esteric band at 1736 cm^{-1} in the FTIR of the solid residue, as noticed also for sol. **TB**. This band probably arises because the temperature increase promotes esterification between TEA and propionic acid. In **TB** this was explained by the fact that no coordination took place between TEA and Ba ions, thus all TEA (Ba/TEA=2/1.5, see Chap.2) is free to react with the solvent (prop. acid). In sol. **TY**, there is always some free TEA since TEA is in excess with respect to Y^{3+} (Y/TEA=1/1.5). Conversely, esterification of the solvent in **TC** is minor, due to the fact that Cu is in excess with respect to TEA, and TEA is coordinated to $CuProp_2$.

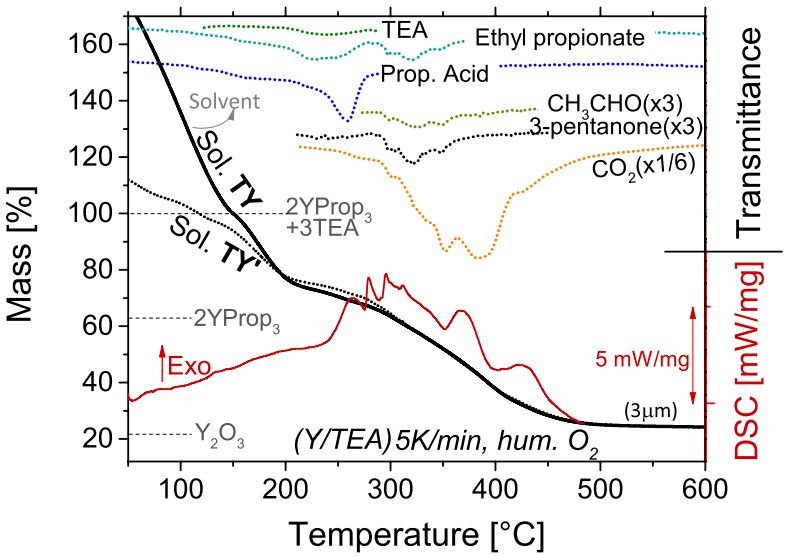

Fig. 4.9: TG-DSC-FTIR analysis of $YProp_3$/TEA in humid O_2. *The relative time-evolution of the main volatiles detected by TG-FTIR analysis from sol. **TY'** (dotted lines) is reported in the top.*

The second stage, between 150-300°C, corresponds to 37% mass loss. The main volatiles detected are propionic acid and ethyl propionate, but also TEA's vibrational bands [55] are observed. The propionic acid comes from $YProp_3$ decomposition in humid O_2; ethyl propionate, already observed also for solution **TC**, originates from the simultaneous decomposition of both TEA and $YProp_3$ according to reaction scheme 4.1: in fact, the yttrium propionate IR bands of the solid residue, Fig. 4.10a, start to decrease already at 150°C and by 240°C their intensity has significantly decreased. In addition, the FTIR of the solid residue, Fig. 4.10a, reveals that TEA contribution disappears somewhere between 240 and 340°C. Lastly, the fact that TEA's vibrational bands are also observed among the volatiles is in agreement with the fact that evaporation takes place in films before 200°C and that there is an excess of TEA with respect to Y (1.5/1, respectively).

The last stage of Fig. 4.9, between 300-500°C, mostly includes $YProp_3$ decomposing to Y_2O_3, since most TEA has been previously consumed.

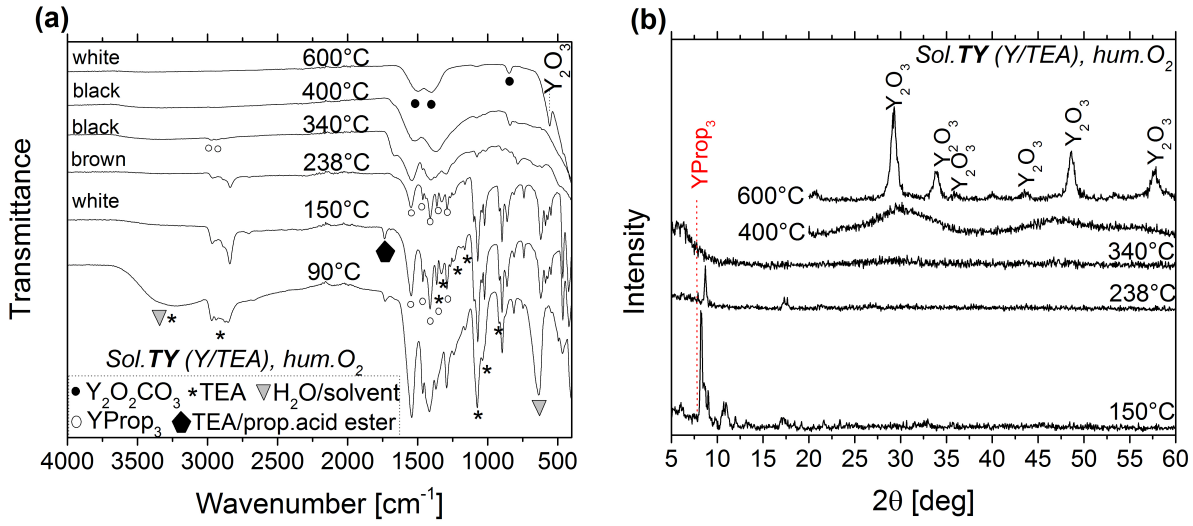

Fig. 4.10: Chemical characterization of the solid residue from decomposition of $YProp_3$/TEA. ***(a)*** *FTIR analysis and* ***(b)*** *XRD patterns of quenched samples during the thermal decomposition relative to Fig.4.8.*

In fact, first, between 300 and 400°C, the remaining $YProp_3$ decomposes to Y-oxycarbonate, $Y_2O_2CO_3$, observed by FTIR in Fig. 4.10a and in agreement with [36,37,147]. This occurs upon release of CO_2, acetaldehyde and 3-pentanone (TG-FTIR in Fig. 4.9, top). Note that the CO_2 peaks between 300-330°C could also be ascribed to the end of TEA decomposition, since at higher temperature its oxidative degradation takes place [55] releasing CO_2 (Fig. 4.3b). However, the XRD analysis of Fig. 4.10b shows the presence of amorphous species in this last stage (300-600°C), between $YProp_3$ decomposition and Y_2O_3 crystallization. Finally, between 400-500°C, $Y_2O_2CO_3$ decomposes to Y_2O_3 (identified by XRD, Fig. 4.10b) with CO_2 release. The EA results in Table 4.1 confirm the presence of carbon in the final product, due to the small remaining amount of $Y_2O_2CO_3$ with respect to Y_2O_3, similarly to the case of $YProp_3$ without TEA.

Note that, the ester band in the solid residue (~1736 cm^{-1}, Fig. 4.10a) disappears before 230°C, while ethyl propionate is detected among the volatiles between 200-350°C. As previously mentioned, these two esters are attributed to different processes. Ethyl propionate is ascribed to reaction scheme 4.1. In fact, the boiling point of ethyl propionate is just below 100°C, thus as soon as it is formed it is expected to evaporate; therefore, ethyl propionate cannot correspond to the ester IR band of the solid residue at 1736 cm^{-1}. This band might arise majorly from esterification of propionic acid (solvent) in the low-temperature region before its evaporation is completed.

Decomposition in inert atmosphere

In inert atmosphere of N_2 (Fig. 4.11), decomposition of the powder sample from sol. **TY** follows the same general behavior: TEA still evolves in the low-temperature stage at 250°C while CO_2 is detected at higher temperatures, namely 310, 340, 430°C, along with ethyl propionate.

But the EGA-IR analysis of Fig. 4.11 (top, inset) shows that the ethyl propionate contribution increases in N_2: in fact, this ester becomes the main volatile, while the contribution of TEA and 3-pentanone decreases with respect to the film decomposition in humid O_2 (the only propionic acid detected seems to come from solvent evaporation below 200°C) and no ammonia is detected.

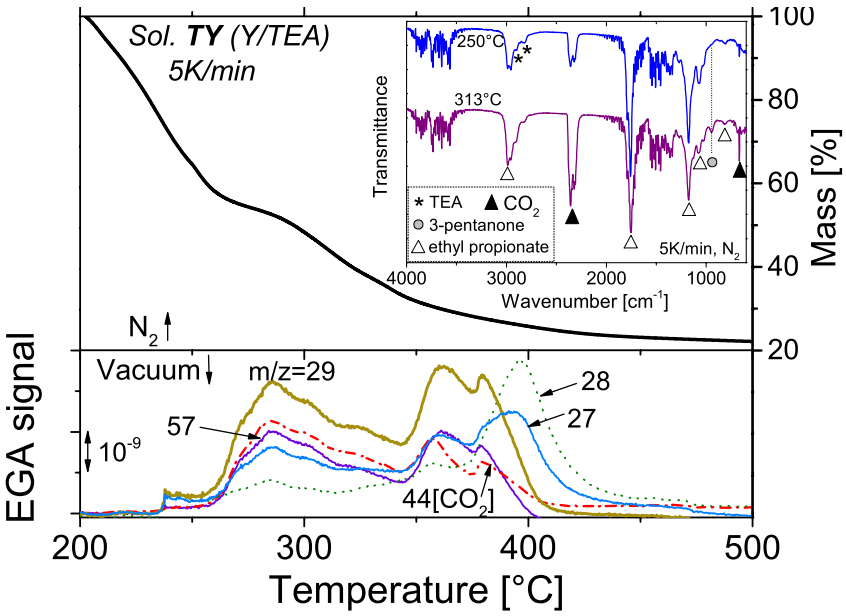

Fig. 4.11: TG-FTIR and EGA-MS analysis of $YProp_3$/TEA in inert atmosphere. *TG-FTIR (IR spectra in inset) and EGA-MS results (bottom) at 5°C/min in N_2 and vacuum, respectively.*

This is probably related to several facts, such as that:

- the lack of oxygen delays the precursor decomposition, resulting in a major overlap of TEA and $YProp_3$ decomposition, which in turns favors esterification;
- that the bulk form prevents TEA volatilization, which results again in a major overlap of TEA and $YProp_3$ decomposition. In fact, the behavior of the two TG curves of sol. **TY** (hum. O_2 and N_2) compared in Fig. 4.12, is quite similar, but the first mass loss (TEA) is shifted to lower temperatures in films in humid O_2 since in films volatilization in enhanced with respect to decomposition.
- reaction scheme 4.1 occurs through a radical reaction, which is favored by inert furnace atmospheres.

Therefore, reaction 4.1 summarizes the dominant driving reaction for decomposition of TEA/$MProp_x$ species in N_2.

The EGA-MS analysis in Fig. 4.11, bottom, performed on a film of sol. **TY** decomposed in vacuum supports the TG-IR results, showing the presence of at least 2 stages of decomposition between 250-400°C, while for the $YProp_3$ alone only one (at 360°C) is present (Chapter 3.1). The two peaks, centered at 280 and 360°C, include fragments that can be related to both ethyl propionate (m/z=29, 57) and 3-pentanone (m/z=57,29); but they both show the evolution of CO_2 (m/z=44), a signature of the occurrence of the 3-pentanone decomposition path (see Chapter 3.1). The prevalence of this path in vacuum with respect to the esterification may be a consequence of some TEA evaporation at low pressure. Then, at 400°C, m/z=28 is detected, which could be assigned to C_2H_4, N_2 or CO. This excess of m/z=28 is not detected during the decomposition of $YProp_3$ without TEA, in vacuum; thus, it is an indication that less TEA evaporation occurs at these low total pressures as a consequence of its coordination with the metal carboxylate salt. The FTIR of the final product from decomposition of sol. **TY** in vacuum shows residual -C=O bands (supposedly from $Y_2O_2CO_3$), and it is very similar to that of the isolated $YProp_3$ decomposed in vacuum.

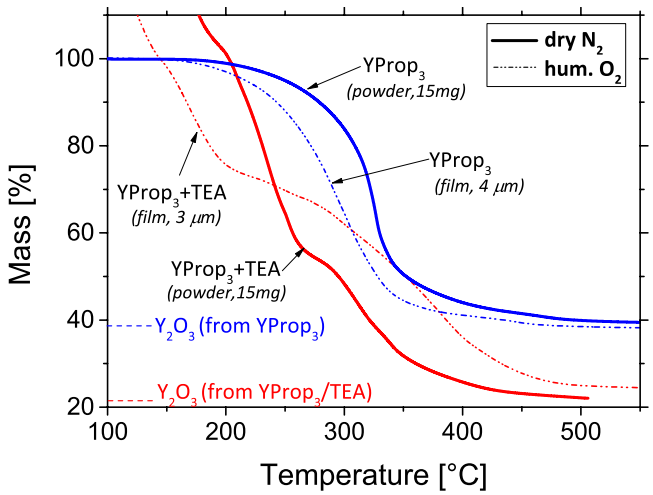

Fig. 4.12: Comparison of TG curves for $YProp_3$ with and without TEA, *during pyrolysis in dry N_2 and humid O_2 at 5°C/min. The esterification path for sol.* ***TY*** *requires lower temperatures than the 3-pentanone path, thus it occurs in both humid O_2 and dry N_2. Dashed horizontal lines: expected final mass to form Y_2O_3 for $YProp_3$ (in blue) and $YProp_3$/TEA (in red).*

4.1.4 Discussion

Thermal analyses are a useful tool to study the effect of adding TEA to the three different metalorganic solutions: i) the well-defined TG mass losses, ii) the fact that the mass loss is the sum of all TEA and the metal salt in solution, iii) detection of TEA or its decomposition products among the volatiles, iv) the endothermic signal of the TEA evaporation step and v) the same TG, EGA-MS behavior and final decomposition temperature with respect to the $MProp_x$ without TEA, suggest that in the case of $BaProp_2$ there is no coordination with TEA, as predicted by [51].

Conversely, TEA changes Cu and Y decomposition pathways, partly because of TEA coordination with Y and Cu, but not with Ba; and partly because of the overlap of the two processes, namely the decomposition of the metalorganic salt and that of TEA (Ba salt decomposes at higher temperatures) which results in less separable mass losses.

But the decomposition mechanism follows from the tendency to either break the Cu—OC=O bond to form the corresponding acid, or the YO—C=O bond for carbon esterification. In fact, for the copper case, the low-temperature mechanism with propionic acid formation is still faster and preferred in humid O_2, thus $CuProp_2$ decomposition is almost over when TEA's start. But in N_2, $CuProp_2$ can survive to higher temperatures (260°C) for the ester to be produced. For the $YProp_3$ case, since its decomposition temperature is higher than that of $CuProp_2$ in humid O_2, esterification is more significant. This ester is not observed in TEA decomposition alone [55], nor it is formed in the TEA-free solutions of the three metalorganic salts shown in Chapter 3. Conversely, the barium salt oxidative degradation is based on the preferred cleavage of the MOC(=O)—C bond, as it tends to form BaC_2O_4 and $BaCO_3$ which only later on (T>>600°C) decompose to BaO [29,147]: that and the fact that its decomposition temperature and TEA's are so far apart, results in very little ester being formed.

It follows that the atmosphere has a different effect on decomposition when TEA is added to the carboxylate salt, since it changes the decomposition temperature range of the carboxylate salt, while it has no effect on the evaporation of TEA; i.e., it controls the overlap of the two processes (decomposition of TEA and of the salt) which eventually affects the degree of

esterification and decomposition pathway. Similarly, the sample geometry, film versus powder, can promote or impede, respectively, TEA evaporation, and thus control the overlap of the two processes.

However, the change in decomposition temperature due to a change of atmosphere is more significant for the pyrolysis of the single-salt solutions without TEA than in the case of single-salt solutions with TEA; this is probably a consequence of the fact that the esterification path can partly take place also in humid O_2, although in dry N_2 it is the predominant decomposition path.

In the framework of CSD methods, some effects need to be acknowledged when TEA is added: a shift in the final decomposition temperature with respect to the metalorganic salt without TEA, of 100°C and 50°C for the Cu and Y case, respectively; a slightly higher amount of residual carbon might remain at 600°C for the Y case, in humid O_2. Similarly, the presence of TEA causes an unexpected redox-reaction pattern not observed for the $CuProp_2$ alone. In fact, reduction of Cu(II) occurs during decomposition in humid O_2 for sol. **TC** ($CuProp_2$/TEA), due to the residual carbon from TEA; but this copper is eventually oxidized to CuO, which is the final product at 500°C. Conversely, in N_2, more Cu(II) reduction is expected during decomposition, but instead reaction scheme 4.1 generates CuO during pyrolysis; eventually this CuO undergoes reduction to Cu, which is the final product at 500°C. This result could be interesting for CSD methods if the barium carboxylate thermal decomposition could be driven by a similar reaction path, to form directly the oxide (BaO) instead of the carbonate at low temperatures.

Although only a fixed TEA amount was studied in this work, the M/TEA molar ratio can also play a role, influencing the amount of overlapped decomposition. In a combined solution of all the three analyzed, we would expect the TEA to mostly influence the copper and yttrium carboxylate decomposition. Perhaps the key aspect emerging from the thermogravimetric analysis is that, when TEA and the metal carboxylate display similar decomposition temperatures, the additive can provide smoother mass losses which translate into a gradual gas release. That is also reflected in the smaller effect of a change of atmosphere on the TG curves, unlike the case of the isolated salts. Similarly, the effect of switching from films to powders is less pronounced than for the isolated salts (especially for the Y case), although it is still evident in the fact that films in O_2 decompose earlier than powders because in the latter there is gas (i.e. O_2) depletion in the inter-particles voids of the bulk [23]. This more robust behavior justifies TEA application as a solution stabilizer in thin film fabrication, upon the need to contrast the abrupt film shrinkage due to rapid decomposition.

Despite that, in the context of chemical solution deposition methods, where long-chain additives are used as stabilizers, the final decomposition temperatures and intermediate phases can play an important role in the final properties of the film, even when the final phases might not differ from the additive-free case.

4.2 Pyrolysis of the ternary propionate-based YBCO solution

The following section will be focused on the study of the thermal decomposition of binary solutions of YBCO precursors, prepared based on the single-component solutions studied in Chapter 3. The final aim will be that of understanding the pyrolysis of a complex, multi-component ternary YBCO precursor solution (sol. **T** in Chapter 2). The building blocks of these solutions will

be metal acetates dissolved in the 1/1 mixture of propionic acid and MeOH. For this reason, first, in section 4.2.1, the thermal decomposition of the **Cu**-**Ba**, **Cu**-**Y** and **Y**-**Ba** binary solutions will be analyzed; second, section 4.2.2 will discuss the ternary solution pyrolysis. As already mentioned in Chapter 2, depending on the initial Ba-Cu ratio, ternary solutions will be labelled as 2-3 (Y/Ba/Cu=1/2/3) and 3-7 (Y/Ba/Cu=1/2/4.66).

Thanks to the knowledge previously developed in Chapter 3, the study will be specifically aimed at the in-situ analysis of film samples during their pyrolysis in humid O_2. The study will be carried out with TA techniques and chemical characterization methods.

Finally, the objective throughout this section will be to understand the effect of the water content in the ternary solution; water, in high content (> 2%, see Chapter 2.1) is linked to $BaCO_3$ crystallization into a non-thermodynamically stable phase after pyrolysis. For reasons that will be explained in Chapter 5, this phase needs to be avoided to guarantee optimal YBCO growth conditions. Thus, all solutions under TA study are analyzed in non-anhydrous conditions. Given the importance of this phase, its possible origins and potential ways to avoid it will be discussed across this section.

4.2.1 Thermal decomposition of binary solutions

A comparative thermogravimetric study of single-salt and binary precursor solutions is reported in Fig. 4.13. The aim is to help visualize the main differences in the thermal decomposition arising from binary interaction effects, which will be analyzed in detail in the following section.

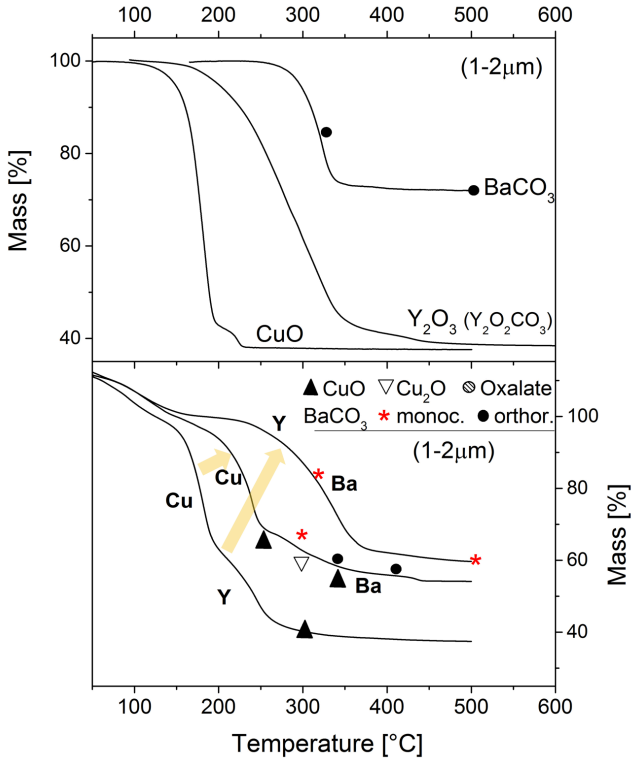

Fig. 4.13: TG analysis of single and binary precursor solutions. *(top)* ***Cu***, ***Y*** *and* ***Ba*** *solutions and (middle)* ***Cu-Ba***, ***Cu-Y*** *and* ***Y-Ba*** *solutions in humid O_2 at 5°C/min. The symbols on the TG curves indicate roughly when the corresponding phases appear; reduction of copper to Cu(I) and the appearance of the monoclinic $BaCO_3$ phase only occurs in binary mixtures, but not in the single-salt solutions.*

Cu-Ba binary solution

A binary solution of the Cu and Ba precursors (see Materials and Methods, Chapter 2) is analyzed by TG and FTIR/XRD, and the results are reported in Figs. 4.13 and 4.14, respectively.

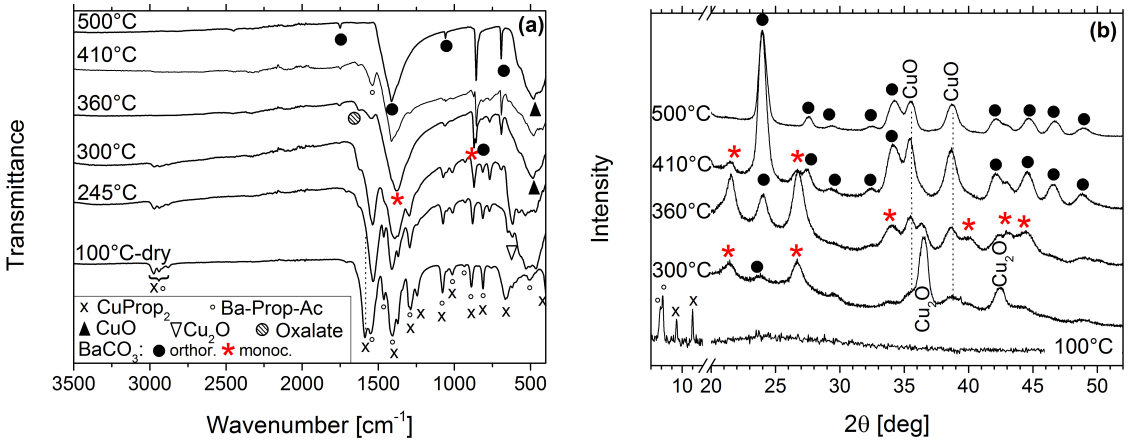

Fig. 4.14: Chemical characterization of the solid residue from decomposition of **Cu-Ba** solutions. ***(a)*** *Infrared evolution and* ***(b)*** *corresponding XRD analysis of the solid residue for ~1-µm films during decomposition in humid O_2 at 5°C/min. The unexpected monoclinic phase of $BaCO_3$ appears in correspondence of the copper(II) reduction to $Cu(I)_2O$, but eventually it is converted to the stable orthorhombic phase.*

From the IR analysis of the solid residue, we can notice the presence of the intense $CuProp_2$ band at 1585 cm^{-1}, corresponding to the C=O stretching, next to the equivalent band for the Ba-Prop-Ac salt which has shifted from 1513 to 1546 cm^{-1}. As expected, the acetate groups have been fully replaced by propionates in the case of the Cu salt, since the FTIR of the dry film is very similar to that of $CuProp_2$; for the barium case, we expect the formation of a mixed Ba-Prop-Ac complex [29]. In our multi component solution it is not possible to affirm weather this is fully true by FTIR since $BaAc_2$ most intense bands are covered by those of $CuProp_2$, in higher stoichiometric amount. However, the IR bands at 933 cm^{-1} in Fig. 4.14a could be an indication of the presence of acetate groups. In support of this statement, the XRD analysis reported in Fig. 4.14b from the powder recovered from the solution, shows two reflections at 2θ=8.1° and 7.9°, which are in agreement with the presence of such mixed carboxylate complex.

The TG curve of Fig. 4.13 shows that decomposition starts after solvent evaporation, with two main steps between 150 and 450°C. By comparison with the isolated precursors (reported in Fig. 4.13, top), it is reasonable to think that the first mass loss between 150-250°C corresponds to $CuProp_2$ degradation to CuO. In fact, the FTIR of the solid residue (Fig. 4.14a) shows the CuO IR bands appearing at 245°C. The second mass loss corresponds to the Ba-carboxylate salt decomposition: between 300-360°C, an oxalate FTIR band appears at 1630 cm^{-1}, assigned to BaC_2O_4, showing that the Ba-Prop-Ac salt decomposition is taking place. Although the behavior of the single component may drive to the conclusion that only BaC_2O_4 is expected to form, we cannot exclude the possible formation of a mixed Ba-Cu oxalate, while the stoichiometric excess of copper is in the form of the oxide. Formation of the oxalate is followed by copper reduction to Cu_2O, with a maximum intensity at 300°C, as shown by XRD in Fig. 4.14b. Simultaneously, as soon as some

BaC_2O_4 is formed, it is converted to $BaCO_3$. Surprisingly, unlike the single-salt solution of Ba-Prop-Ac, the $BaCO_3$ does not crystallize into its thermodynamically stable phase (orthorhombic, ***O***) but into the monoclinic phase (***M***), Fig. 4.14b (300°C). As Cu_2O is re-oxidized to CuO after 360°C (see XRD in Fig. 4.14b), also the monoclinic phase is reconverted to the stable orthorhombic structure. At 500°C, $BaCO_3$ ***O*** and CuO are the final products observed by XRD.

Finally, note how in Fig. 4.13, the copper precursor decomposition is shifted by roughly 50°C higher with respect to binary solutions of Cu-Y precursors. It is indeed harder to dry, most probably due to the fact that the Ba-Prop-Ac salt carries crystallization water/propionic acid until roughly 200°C in the form of a colorless compact film, acting as a protective layer that slows down gas diffusion. This behavior can be observed by naked eye for the Ba precursor alone, where this colorless protective layer disappears after 190-200°C, leaving a white powder.

Cu-Y binary solution

For binary solutions of the Cu and Y precursors, the FTIR of the dry film shown in Fig. 4.15a indicates the replacement of acetate groups by propionates, as expected from the behavior of the separate components. Additionally, the presence of $YProp_3$ and $CuProp_2$ is confirmed by XRD in Fig. 4.15b.

In the TG curve of Fig. 4.13, two stages can be clearly identified: one between 100-200°C, and a second one between 200 and 400°C, after which the mass is stable. In the first stage decomposition of $CuProp_2$ takes place. No copper(II) reduction is observed at 300°C, neither by FTIR nor XRD. This is in agreement with the fact that all organic material has already decomposed before that temperature, leaving only the stable oxidized phase expected in humid O_2. The final products consist of Y_2O_3 and CuO, both clearly identified by XRD.

From Fig. 4.15b it is evident that CuO crystallizes in the stable thermodynamic phase. Conversely, given the width of the diffraction peaks and the separation between the base-centered (bc) Y_2O_3 and face-centered (fc) Y_2O_3 peaks, it is very difficult to determine the crystalline phase of yttria; nevertheless, yttria seems to have grown in the face-centered (fc) cubic phase rather than the base-centered (bc) phase.

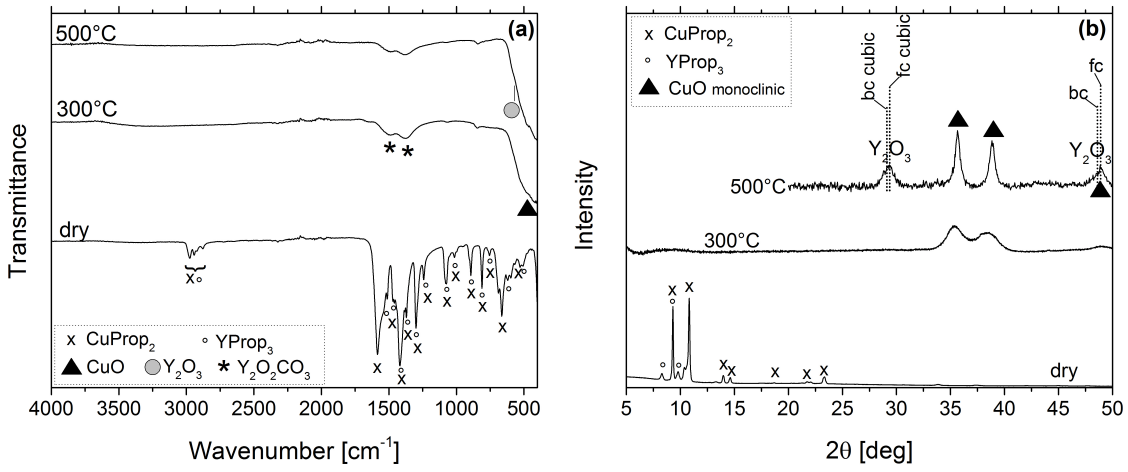

Fig. 4.15*:* Chemical characterization of the solid residue from decomposition of the Cu-Y solution. ***(a)*** *Infrared and* ***(b)*** *XRD evolution of the solid residue in humid O_2 at 5°C/min.*

Y-Ba binary solution

In binary solutions of the yttrium and barium carboxylate salts, the dry film consists of $YProp_3$ (FTIR bands labelled with a "+" sign in Fig. 4.16) and Ba-Prop-Ac (bands labelled with empty circles). From the XRD analysis, the crystalline phases cannot be distinguished, probably because the film was not enough dry, and propionic acid was still retained. The TG curve of Fig. 4.13 displays one main mass loss step, and again, due to the presence of the Ba precursor, the $YProp_3$ decomposition has slightly shifted to relatively higher temperatures.

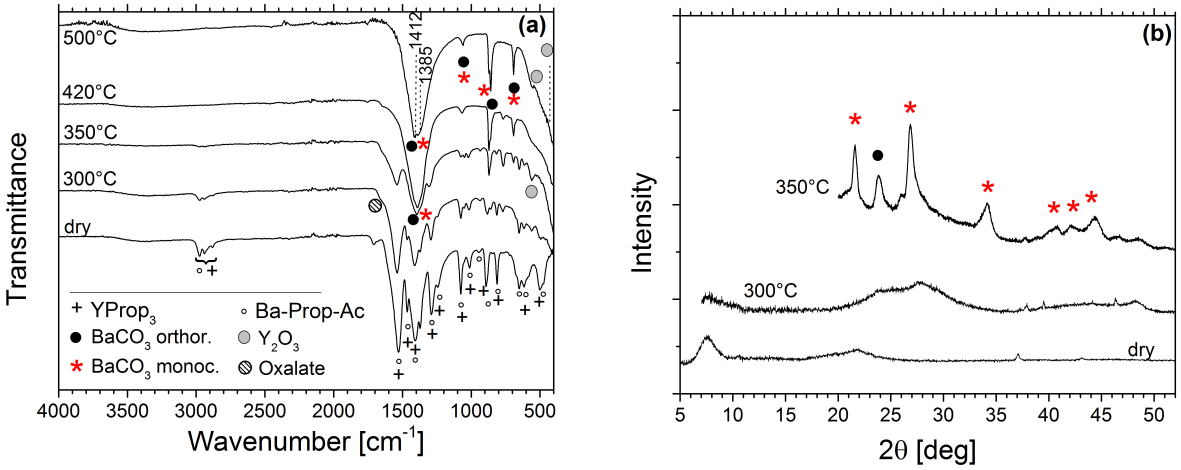

Fig. 4.16: Chemical characterization of the solid residue from decomposition of **Y-Ba** solutions. ***(a)*** *Infrared and* ***(b)*** *XRD evolution of the solid residue for thick films (>1μm) in humid O_2 and 5°C/min, showing the $BaCO_3$ crystallization into both the orthorhombic and monoclinic phase.*

Film samples quenched at different temperatures and analyzed by FTIR and XRD (Fig. 4.16), indicate that at 300°C the $BaCO_3$ phase begins to crystallize (Fig. 4.16b). Both infrared and X-ray evolution of the solid residue shows that at 350C° the monoclinic $BaCO_3$ phase (labelled as *) is again found next to the stable orthorhombic phase (distinguished from the two peaks above and below 1400 cm^{-1}, as marked in Fig. 4.16a). Unlike the case of Cu-Ba binary solutions, at 500°C the ***O*** phase is not recovered.

Some FTIR spectra of the solid residue at 500°C for films and powder samples are reported in Fig. 4.17a, while the inset shows the corresponding TG curves from which they were obtained. Given the small amount of material for the 0.1μm film, the XRD analysis (instead of IR) was carried out for this film at 500°C, and it is reported in Fig. 4.17b. From the infrared and XRD analysis in Fig. 4.17, it is clear that the amount of monoclinic phase with respect to the orthorhombic phase at 500°C increases with increasing film thickness; additionally, ***M*** is never again converted to the orthorhombic structure before 500°C. Thus, at 500°C, the final product consists of Y_2O_3 and a mixture of monoclinic and orthorhombic $BaCO_3$.

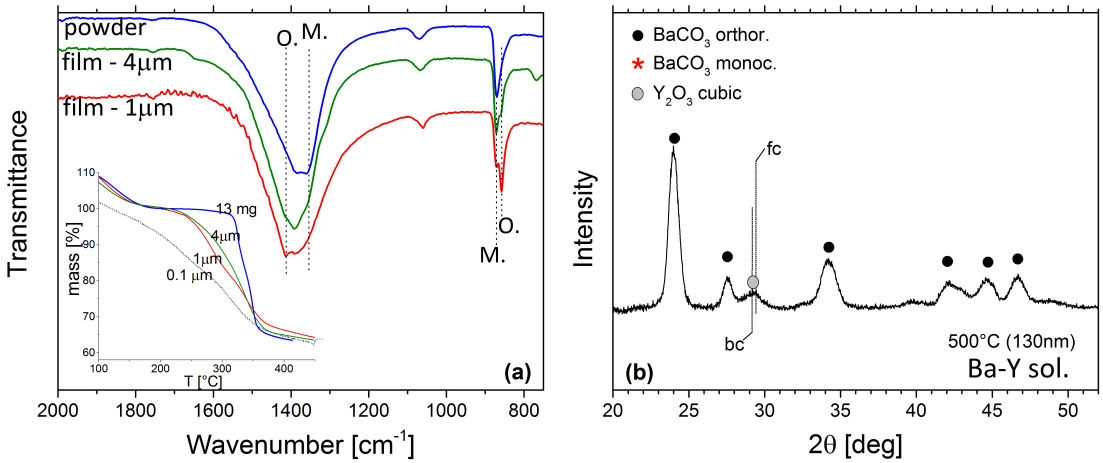

Fig. 4.17: Effect of the sample geometry on the decomposition of the **Y-Ba** precursor. ***(a)*** *FTIR spectra of the solid residue at 500°C of several films of a* ***Y-Ba*** *precursor solution from decomposition at 5°C/min in humid O_2, showing the relative amount of monoclinic to orthorhombic phase. Inset: corresponding TG curves. The TG curve relative to 0.1 µm film, could not be seen by FTIR; however, the XRD analysis in* ***(b)*** *shows the presence of only orthorhombic $BaCO_3$.*

$BaCO_3$ crystallization: Ba precursor melting

As mentioned at the beginning of section 4.2, the presence of a non-thermodynamically stable phase of $BaCO_3$ (***M***), is detrimental for the YBCO growth stage. Understanding and controlling the formation of different crystalline phases is of special interest in the context of the optimization of each CSD step. Therefore, the present section will deal with the analysis of the origin of ***M*** during pyrolysis, in order to find suitable conditions where this phase can be avoided; further details about its effects during the growth of YBCO will be postponed to the next chapter (Chap. 5).

One of the evidences related to the presence of ***M*** is the fact that its formation only occurs during pyrolysis in the presence of the copper or the yttrium precursors; conversely only the thermodynamic stable phase, orthorhombic (***O***) $BaCO_3$, crystallizes during the pyrolysis of the Ba precursor single-component solution.

A possible explanation is the idea that other crystalline phases can act as crystallization seeds due to comparable lattice parameters. If this seed crystallization is occurring, it should be more favorable when the Ba precursor is in liquid form prior to decomposition.

Indeed, it was previously shown in Chapter 3 that between 200-260 and 330- 350°C, two melting events of the Ba-Prop-Ac (and $BaProp_2$ as well) precursor take place, and that the last one strongly affects the thermal behavior of the salt. The melting temperature in O_2 was observed to be lower than the endothermic melting peaks detected in N_2, and it was explained as due to the presence of decomposition products mixed with the barium salt. We might expect a similar effect when other species (such as the Cu or Y precursors) are mixed with the Ba-Prop-Ac salt.

Some lattice parameters for possible candidates are reported in Table 4.2. As it can be seen, small lattice parameters could be expected to promote formation of the ***M*** phase: for example, fcc (face-centered cubic) Y_2O_3 or metallic Cu.

	Lattice parameters	***Reference***	***Entry***
$BaCO_3$ Orthor. (**O**)*	6.4, 5.3, **8.9**	PDF 45-1471. Amcsd 0000235	1
*$BaCO_3$ Monoc.(**M**)*	6.9, 5.3, **4.5**	PDF 78-2057	2
*Y_2O_3 bc cubic**	10.6, 10.6, 10.6	Amcsd 0017468	3
Y_2O_3 fc cubic	5.3, 5.3, 5.3	PDF 43-0661	4
$Y_2O_2CO_3$ hex	3.8, 3.8, 15	[113]	5
$YAc_3{\cdot}4H_2O$ triclinic	8.9, 9.4, 10.6	[154]	6
$Y_2Prop_6{\cdot}2H_2O$ triclinic	9.6, 12.1, 13.2	[105]	7
$Y_2Prop_6{\cdot}H_2O$ monoclinic	15.9, 16.5, 8.4	-	8
*CuO monoclinic**	4.68, 3.48, 5.12	PDF 48-1548. Amcsd 0018817	9
CuO cubic fcc	4.2	PDF 78-0428	10
Cu_2O cubic	4.27	PDF 65-3288. Amcsd 0009326	11
Cu cubic	3.6	Amcsd 0011145	12

***Table 4.2**:* Cell parameters of some Y, Ba and Cu species. *Metal carboxylate precursors, intermediates and products that might influence crystallization of $BaCO_3$ into the monoclinic phase are shown. Entry 8 was derived from the single-crystal structure from the powder diffraction analysis performed on a film of the Y precursor solution (YAc_3 in prop. acid/MeOH). The * symbol refers to the thermodynamic stable phase or most common phase of a specific specie that can crystallize in more than one phase.*

In the case of the **Y-Ba** solution, in Fig. 4.17a, the sample with the most significant ***M*** contribution corresponds to the TG curve were the mass loss takes place at the highest temperatures; this might suggest that as the thickness increases, a bigger portion of the Ba-Prop-Ac salt survives to higher temperatures (superior to 330°C) so that more precursor can decompose in the melted state. Here, the presence of $YProp_3$ or its decomposition products could act as crystallization seeds promoting the ***M*** $BaCO_3$ phase.

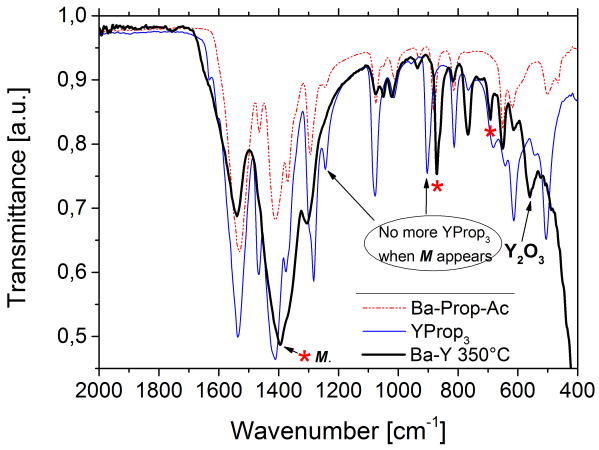

***Fig. 4.18**:* Detailed FTIR analysis of the **Y-Ba** solution during decomposition. *Comparison of the IR spectra of the Y and Ba precursor salt and the **Y-Ba** solution decomposed to 350°C, when the $BaCO_3$ is crystallizing majorly into the monoclinic phase.*

To understand if the Y-carboxylate salt has any influence, we can first look at the crystal structure. From table 4.2, the lattice mismatch of the ***M*** phase with some Y carboxylate precursors (entry 6-8) seems to be too large to promote such seed-induced crystallization. Additionally, the FTIR of the solid residue of a quenched decomposition product of the **Y-Ba** solution is reported in Fig. 4.18, compared with the FTIR spectra of $YProp_3$: no Y carboxylate precursor ($YProp_3$) seems to be present at 350°C while the ***M*** phase is appearing. This leaves the Y_2O_3 phase as a more probable candidate.

For the case of the **Cu-Ba** solution, the ***M*** phase appears in correspondence of copper(II) reduction to Cu(I), thus after all $CuProp_2$ has been consumed, ruling out any possible influence of the Cu precursor salt. Indeed, Cu_2O crystal structure (Table 4.2) has small lattice parameters that may promote ***M*** instead of ***O*** crystallization. As Cu_2O is reconverted to the stable monoclinic CuO by oxidation, also the monoclinic $BaCO_3$ is reconverted to the orthorhombic phase.

$BaCO_3$ crystallization: water content

As introduced in Chap.2 and at the beginning of this chapter, high water content in solution corresponds to the presence of ***M*** $BaCO_3$ in the pyrolyzed films. Regarding the effect of the water content in solution, we might expect water to either affect the Ba species, or the Y/Cu species.

For example, as shown in Table 4.2, in the case of $YProp_3$, increasing the amount of crystallization H_2O leads to smaller lattice parameters accompanied by a change from monoclinic to triclinic structure (entry 7,8).

Conversely, for the Ba case, both $BaProp_2$ and the mixed Ba-Prop-Ac exhibit two melting temperatures: one between 200-260°C, and one between 350-400°C owing to two different crystalline phases. Since the low-temperature melting occurs after dehydration, the presence of the first melting might be influenced by the crystallization process in the barium precursor solution, and thus, for example, by the water amount in solution. Thus, an anhydrous solution might induce crystallization in a phase between the first and second melting event.

To test the influence of the first melting peak, a Ba-Y solution was also prepared dissolving an annealed (at 280°C for 25 minutes in N_2, see Fig. 3.19) $BaProp_2$ precursor as the barium source, which before dissolution only shows the high temperature melting. After pyrolysis of this solution to 500°C, $BaCO_3$ crystallization only occurs in the ***O*** phase. However, the solution is not stable; additionally, the ***M*** phase reappears within a second pyrolysis in the same day, probably as a consequence of a change in the crystalline structure as water is absorbed.

4.2.2 Thermal decomposition of ternary solutions

Thermal analysis of the ternary solution

The thermogravimetric analysis of non-anhydrous ternary solutions of 2-3 and 3-7 composition is reported in fig. 4.19, along with single-component and binary solutions, for comparison.

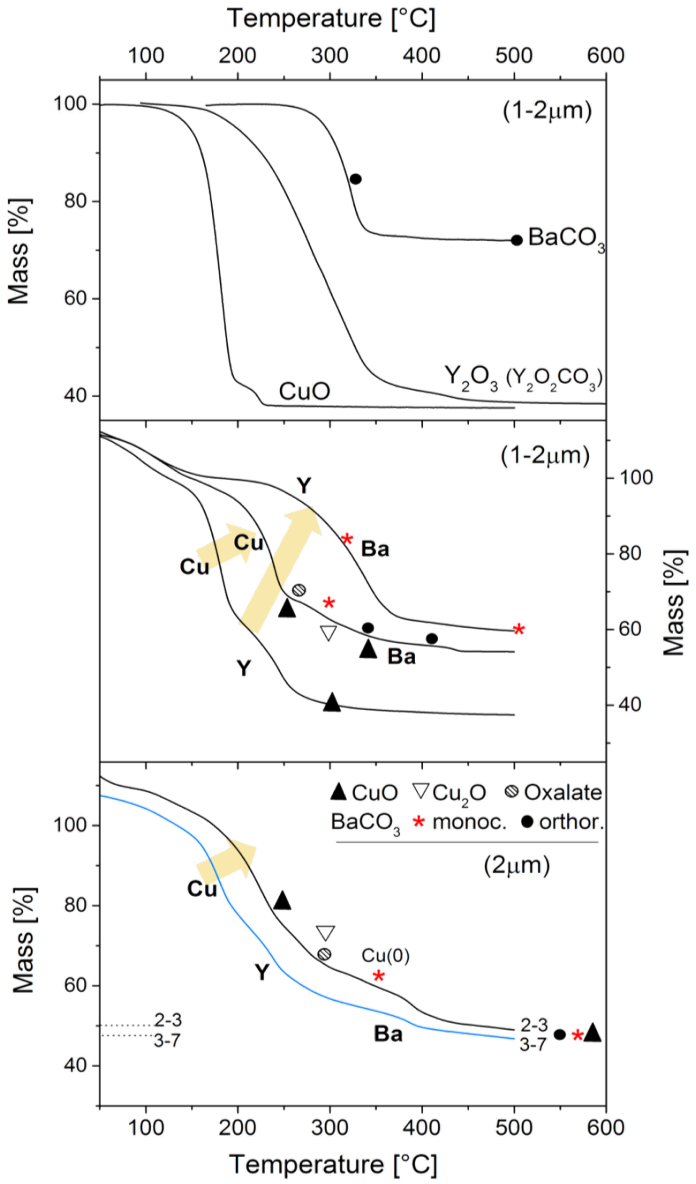

Fig. 4.19: TG analysis of single-component, binary and ternary solutions. *(top) single-component, (middle) binary and (bottom) ternary solutions (sol.* ***T****, Chapter 2) of FF-YBCO in humid O_2 at 5°C/min. The symbols on the curves indicate roughly when the corresponding phases appear; reduction of copper only occurs in binary and ternary solutions, to Cu(I) and to Cu(0), respectively. Conversely, in single-component solution no reduction is observed. Crystallization of the* ***M*** *$BaCO_3$ phase takes place in both binary and ternary solutions, but not in single-salt solutions.*

The 3-7 solution seems to start to decompose at a lower temperature, with $CuProp_2$ mostly decomposed before 200°C (see Fig. 4.19). Conversely, in the 2-3 composition, the beginning of decomposition hardly takes place before 200°C comparing similar thicknesses. This could be again explained by the fact the Ba salt forms a protective layer that slows down gas diffusion and thus $CuProp_2$ decomposition; since in a 3-7 solution the Ba/Cu ratio is lower than in the 2-3 composition, this effect is less important, hence decomposition starts earlier.

From the chemical characterization (infrared and X-ray diffraction analysis) of quenched film samples of a 2-3 solution, reported in Fig. 4.20, it is evident that $CuProp_2$ decomposition is the first to take place, between 150 and 250°C. In fact, by 250°C, the CuO X-ray reflections have appeared (Fig. 4.20b). While decomposition of the other salts takes place, at ~300°C CuO is first reduced to Cu_2O and then to metallic copper, Cu, at 350°C. This suggests the fact that the residual carbon (or CO produced from decomposition) of the other two salts pushes towards the reduction of CuO, upon CO_2 release.

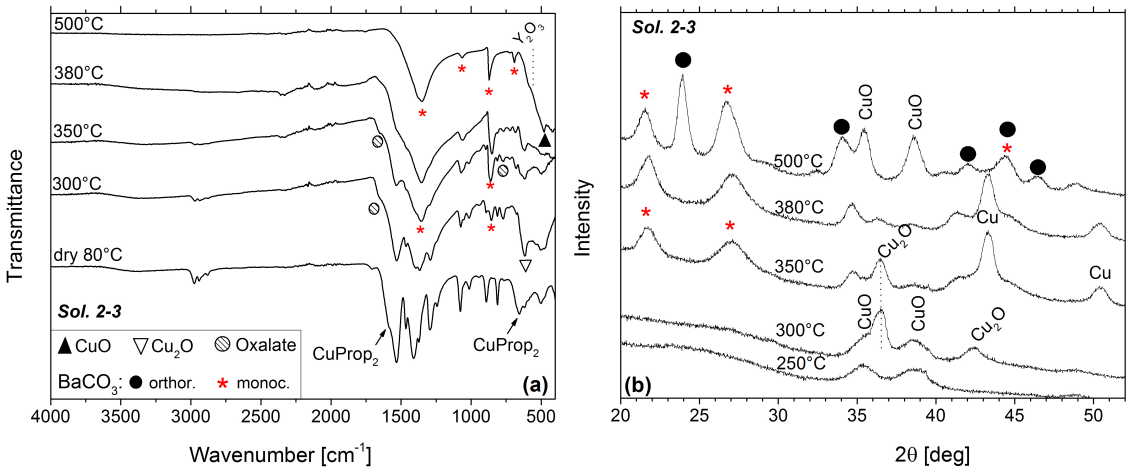

Fig. 4.20: Chemical characterization of the solid residue from decomposition of non-anhydrous ternary films. ***(a)*** *FTIR and* ***(b)*** *XRD evolution of the solid residue in humid O_2 at 5°/min, for 1-μm film of 2-3 solution. Note that reduction of Cu(II) takes place during decomposition, due to the carbon carried by the other salts: in fact, while in binary solutions it reaches oxidation state +1, in ternary solutions it is pushed to Cu(0), since more metal propionates are present. Also note the formation of $BaCO_3$ monoclinic (**M**) in the presence of Cu(0)/Cu_2O. Once crystallized,* ***M*** *does not fully convert to the orthorhombic phase, unlike the case of a binary Ba-Y solution.*

In fact, the TG-IR analysis of a 2-3 film shown in Fig. 4.21 confirms that propionic acid and CO_2 are detected at the low temperature decomposition stage, between 150 and 250°C, which corresponds to $CuProp_2$ degradation. This is followed by a series of CO_2 peaks; since not just one, but two carboxylate salts are added with respect to a Cu-Ba binary solution, reduction is pushed all the way to Cu due to the higher availability of carbon to produce CO_2. Simultaneously to copper reduction to Cu_2O and Cu, $BaCO_3$ starts to crystallize between 300-350°C in the monoclinic phase (Fig 4.20). In the last stage, between 350-450°C, copper is re-oxidized to Cu(II) and some orthorhombic $BaCO_3$ phase appears.

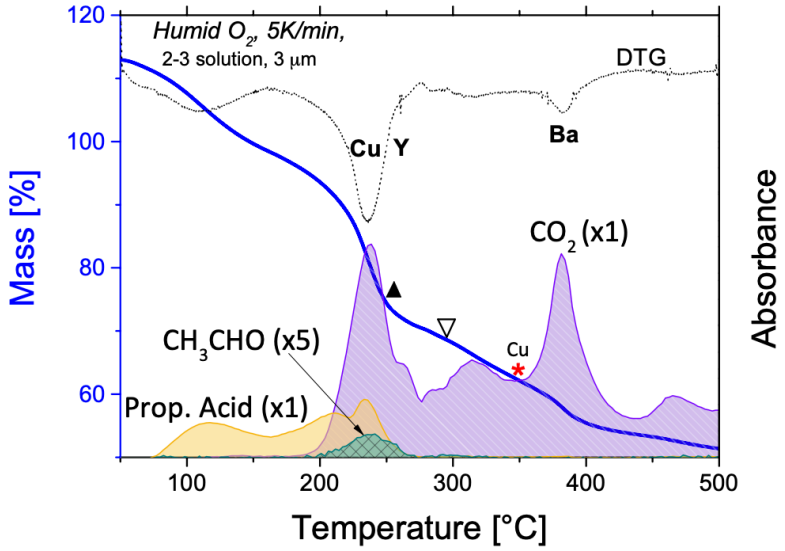

Fig. 4.21: TG-FTIR analysis of a 2-3 solution of YBCO during pyrolysis. *Decomposition is performed in humid O_2 at 5°C/min. Compared to films of the single-salt solutions, the main decomposition volatile is CO_2 and the decomposition process is shifted to higher temperatures.*

The final product consists of a mixture of orthorhombic and monoclinic $BaCO_3$, along with CuO (XRD in Fig. 4.20b). Y_2O_3 is hardly observed in films by XRD due to the small particle size. Overall, the ternary solution seems to follow the behavior of a Ba-Y binary solution, where the ***O*** $BaCO_3$ phase is not fully recovered at 500°C.

As expected, film thickness and sample geometry affect the decomposition temperature: very thin films start to decompose at lower temperatures than powders in a crucible, as depicted in Fig. 4.22 for a 3-7 ternary solution. Additionally, the higher the amount of precursor decomposed at high temperature, the bigger the amount of monoclinic $BaCO_3$ with respect to the orthorhombic phase, as already found for binary solutions of Y and Ba precursors.

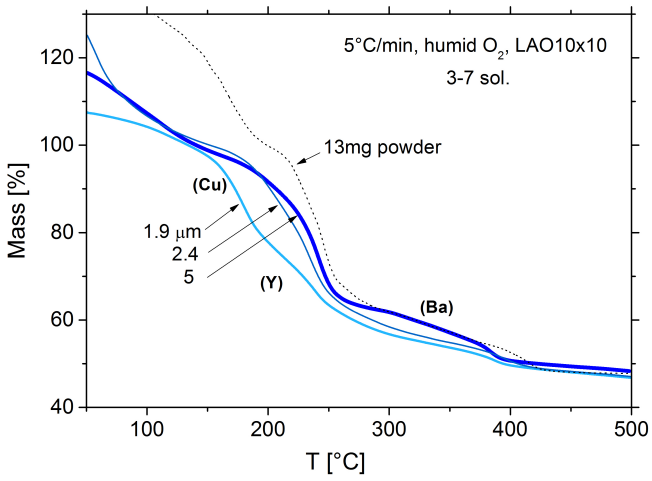

Fig.4.22*:* Thermal behavior of a 3-7 solution as a function of sample geometry. *The TG curves shift to high temperature as the film thickness increases.*

The M $BaCO_3$ phase: Ba precursor melting

Several strategies can be adopted in order to have reproducible initial conditions after pyrolysis, necessary to optimize the growth stage. In particular, as mentioned before, the presence of the ***M*** $BaCO_3$ is detrimental for the YBCO growth stage, and thus it is important to discuss the conditions in which this phase can be avoided in favor of the thermodynamically stable one, also in the context of the ternary solution.

The quest for better cost-effective CSD methodologies urges to look for alternative conditions in which the ***M*** phase can be avoided. A second type of ternary solution (sol. **t'**, in acetic acid and H_2O), where the dry film is made up of only metal acetates instead of majorly (due to the Ba-Prop-Ac salt) propionates, was pyrolyzed. Its thermal behavior is reported in Fig. 4.23a. Independently of the water content and time, mostly only the ***O*** phase is observed at 500°C (Fig. 4.23b). It seems that both H_2O amount and propionate/acetate ratio in solution play an independent role in the $BaCO_3$ crystallization.

Therefore, several other solutions were compared where the ratio of $MProp_x/MAc_x$ in the dry film is reduced; this was achieved by replacing some propionate metalorganic precursors with acetates in a H_2O-based solution. Note that, although the initial type of salt in these mixtures is known, ligand exchange can still take place after dissolution of the salts, changing the chemical nature of the metalorganic species in equilibrium. After pyrolysis of these solutions to 500°C, the amount of **M/O** detected by FTIR in Fig. 4.23b decreases with decreasing amount of $MProp_x$ with respect to MAc_x (sol. **t'**, **t''**, **t'''**).

Unfortunately, the acetate-based solutions required a very low concentration of salts to enhance solubility. In this scenario, the new precursor solutions should be designed considering the need of a higher molarity for thick film deposition. In particular, Fig. 4.23 also reports a new solution currently under study in our group where the precursors are metal acrylates: the FTIR in Fig. 4.23b after pyrolysis to 500°C anticipates the presence of majorly orthorhombic $BaCO_3$, even in non-anhydrous conditions of pyrolysis.

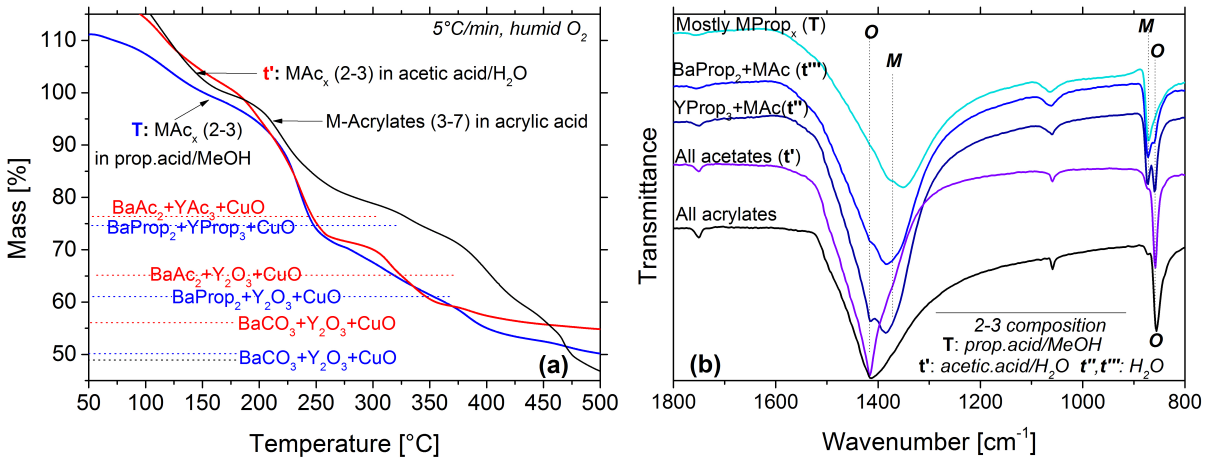

Fig. 4.23: Thermal analysis of solutions with different M-Prop/M-Ac ratios. ***(a)*** *TG analysis at 5°C/min in humid O_2 of solution* ***T*** *(100% refers to the dry $MProp_x$/BaProp-Ac film after solvent evaporation),* ***t'*** *(100% refers to the dry film composed of metal acetates after solvent evaporation) and a metal-acrylate-based solution. Colored dotted lines refer to the expected final mass for (red lines) solution* ***t'*** *and (blue lines) solution* ***T****.* ***(b)*** *corresponding FTIR analysis at 500°C after pyrolysis.*

Based on the analysis of the binary solutions (in particular, sol. **Y-Ba**), the fact that in solution **t'** only ***O*** $BaCO_3$ is formed could be related to the absence of melting events of the barium precursor during decomposition. In fact, unlike $BaProp_2$ and other barium carboxylates with longer carbon chains [147], $BaAc_2$ does not show a low-temperature melting, while the high-temperature one is observed to occur at T_{onset}~455°C from TG-DSC analysis (see next section). Since films of solution **t'** decompose much before this temperature (~100°C earlier, Fig. 4.23a), decomposition in **t'** is expected to take place with the barium precursor in its solid state. In fact, in this solution, the main mass losses seem to have already taken place by 300°C, relatively earlier when compared to solution **T**.

The M $BaCO_3$ phase: water content

On the other hand, as already mentioned, for films pyrolyzed working in anhydrous conditions (see Chap. 2), the ***O*** $BaCO_3$ phase is the only phase recovered at 500°C. The need to work in anhydrous conditions to optimize the YBCO growth stage is indeed first reported in the thesis of Dr. L. Soler [155]. However, the reason why H_2O is linked to the presence of $BaCO_3$ ***M*** has never been disclosed yet.

Indeed, the influence of residual water in a solution containing metal propionates is trickier to understand. The presence of water in solution is expected to change the crystalline structure of the salts; for example, it induces the formation of an unstable phase of the barium precursor, with two melting events; the melting temperatures may therefore depend on the salt crystallization and solution history. Water may even be expected to influence the equilibrium that results in the replacements of acetate groups by propionates: for example, of the three metal acetate precursors, only $BaAc_2$ does not exhibit a strong tendency to hydrate, while $CuAc_2$ and YAc_3 are stable with crystallization water (see Fig. 4.24). Similarly, both $BaProp_2$ and Ba-Prop-Ac show crystallization water, which is retained up to relatively high temperatures (190-200°C, Chapter 3). Also, $YProp_3$ tends to hydrate while $CuProp_2$ is stable in anhydrous form.

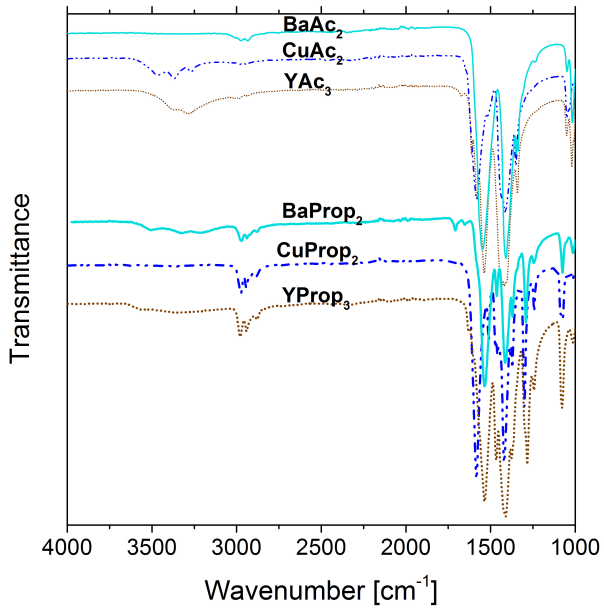

***Fig. 4.24**:* FTIR analysis of some YBCO metalorganic precursors (acetates and propionates). *Some spectra show the presence of crystallization water (broad band between 3000-4000 cm^{-1}, and peak at 1660-1700 cm^{-1}). The salts with an anhydrous FTIR spectrum are stable over time.*

Therefore, anhydrous solutions could be expected to promote the presence of $BaAc_2$ or acetate-rich Ba-Prop-Ac carboxylates rather than propionate-based barium salts. This affects the presence of the first melting peak in the low-temperature region where decomposition of the Y precursor takes place (200-300°C), which was not detected for the $BaAc_2$ species. It also affects the temperature at which the (second) melting event occurs, which follows the order: $BaProp_2$ < Ba-Prop-Ac < $BaAc_2$ (see Fig. 4.25 for the DSC endothermic peaks). In turn, the high-temperature melting of the acetate-based Ba precursor reduces the effects of the Cu and Y phases on the $BaCO_3$ crystallization.

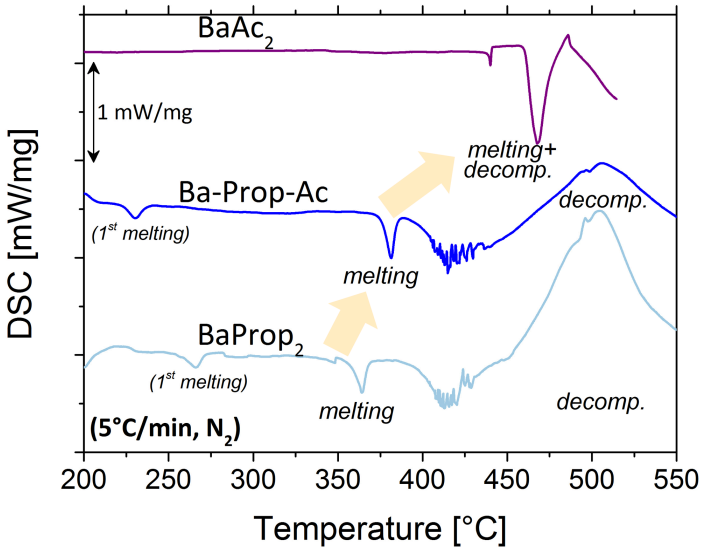

***Fig. 4.25**: DSC signal during decomposition of Ba species as a function of their prop/ac ratio. Specifically, $BaAc_2$, Ba-Prop-Ac and $BaProp_2$ in powders (25-35 mg) are shown. The endothermic DSC peak relative to their melting is indicated with an arrow as it shifts to high temperatures. In the case of $BaAc_2$, films decompose at lower temperatures (see Chap. 3.3), while melting and decomposition overlap only in powders. In fact, on-going studies revealed that in N_2 the decomposition temperature of $BaAc_2$ as powder is not thermally activated, which is a signature of the occurrence of melting prior to decomposition.*

Lastly, although the presence of the ***O*** phase seems to depend on the specific barium precursor used, we cannot exclude the influence of other parameters, such as the molar concentration of the salts, or the degree of their intermixing after dissolution. For example, a strong homogenous intermixing of precursors in solution could induce the formation of a more amorphous film after deposition, where the crystal structure of the salts can be expected to play a less significant part.

In conclusions, this reflects the importance of the chemical solution design step in CSD methods; when new features arise in complex solutions, thermal analysis techniques and chemical charaterization methods are crucial to underpin the best conditions to attain control in order to ensure optimal YBCO growth conditions.

4.3 Partial conclusions

This chapter showed that the study of complex solutions (single component with TEA, binary and ternary solutions) can still be undertaken with the aid of thermal analysis techniques. Even though the knowledge developed from the single-salt solution studies is crucial to understand and confirm the interpretation of binary and ternary mixtures, the thermal behavior of such complex solutions cannot be expected to be the simple sum of the behavior of its components.

Regarding the use of additives, in this chapter it was proven that the presence of TEA is responsible for a smoother decomposition process, justifying its use during CSD pyrolysis to favor stress-free films. The esterification reaction path that occurs between TEA and propionate units is responsible for this effect. This path can only take place if TEA's decomposition temperature and that of the metalorganic salts overlap; otherwise, this path competes with the thermal behavior characteristic of the isolated metalorganic salt.

As a consequence, the esterification path takes place in both humid O_2 and N_2 for the Y precursor, and mostly only in N_2 for the Cu precursor. Conversely, the barium precursor is not affected much by the presence of additives, due to the absence of TEA-Ba coordination, its high decomposition temperature and its intrinsic decomposition path.

The thermal behavior of the ternary metalorganic solution is very sensitive to the experimental conditions and the solution history, more than expected from the study of the single-component solutions. Unexpected interactions lead to copper reduction even when decomposition takes place in humid O_2, and to the $BaCO_3$ crystallization into the monoclinic (**M**) phase instead of the thermodynamically expected orthorhombic phase.

These results are not observed in the single-component solutions, but they were however shown to originate already at the level of the binary solutions.

The interest in understanding the origins of the **M** $BaCO_3$ phase lies in the fact that its presence has been observed to be detrimental for the YBCO growth step, in most growth conditions. Therefore, avoiding the formation of this specie is essential to optimize the growth step. One of the hypotheses for the presence of the monoclinic phase is that the melting of the barium precursor during pyrolysis results in the **M** phase only when crystal seeds of other metal species are present in the melt, although those species are yet to be clearly identified.

Conversely, copper reduction is caused by carbon residues from decomposition of the other metalorganic salts.

So far, only two situations have been found where the monoclinic $BaCO_3$ phase is avoided in favor of the thermodynamically stable orthorhombic phase:

- when rigorously anhydrous conditions are adopted in the presence of metal propionates, probably due to the fact that water can change the crystalline structure of the $BaProp_2$ and Ba-Prop-Ac precursors, or the Ba acetate-propionate equilibrium in solution, thus changing the melting temperature;

- when metal acetates or acrylates are used instead of propionates, probably as a consequence of the fact that the Ba precursor decomposes before its melting can take place.

Although the absence of melting events in the Ba precursor seems to promote the presence of the ***O*** $BaCO_3$ phase, this issue will require further investigation to be confirmed.

TRANSIENT LIQUID ASSISTED GROWTH (TLAG) OF YBCO

Chapter 5

5.1 Fundamental principles of TLAG

This Chapter will introduce the basis of the YBCO growth approach from fluorine-free precursors as analyzed and developed in our group; the general theory behind this growth route will be explained and visualized with the aid of crystalline phase time evolution derived from the in-situ X-ray diffraction performed at SOLEIL Synchrotron (as previously described in the Materials and Method section). Secondly, this chapter will focus on a particular route within this growth approach with the aim of tuning the growth conditions in order to identify the region of the phase diagram where epitaxial growth is possible and high performances are promising. Finally, in this chapter, it will be demonstrated the robustness of the method by extending it to thick films and tape.

5.1.1 Basic characteristics of TLAG

TLAG (Transient Liquid Assisted Growth) is a novel approach to YBCO crystallization based on the presence of a transient liquid in the ternary BaO-CuO-Y_2O_3 system, (Fig. 5.1a) originating from the CuO-BaO eutectic reaction [156]. In fact, upon heating the CuO-BaO system, a $BaCuO_2$ mixed oxide is formed which exhibits an eutectic melting, in agreement with the binary phase diagram of Fig. 5.1. Upon the Y_2O_3 nanoparticles dissolution in the Ba-Cu-O liquid and the Y diffusion to the substrate interphase, heterogenous YBCO nucleation can occur from Y reaction with the melt. Thus, YBCO crystallizes heterogeneously forming epitaxial nuclei with respect to the substrate, pushing the liquid and unreacted phases to the surface.

The remarkable novelty of this approach is that the liquid can be generated in a region of the phase diagram where the solid YBCO would be the stable phase (from which the name "transient liquid"); hence, as soon as it is formed, it reacts with Y_2O_3 to form YBCO, and growth rates can be of the order of hundreds of nm/s. This hinges upon the principle that there is no nucleation barrier to form a liquid, unlike for a crystalline phase, and the fact that Y dissolution in the Ba-Cu-O eutectic melt is several orders of magnitude faster than in the solid BaO-CuO matrix. Therefore, crystallization of the thermodynamic equilibrium phases is delayed by the kinetic hindrances that generate the transient liquid, which thus becomes kinetically preferred over the solid product.

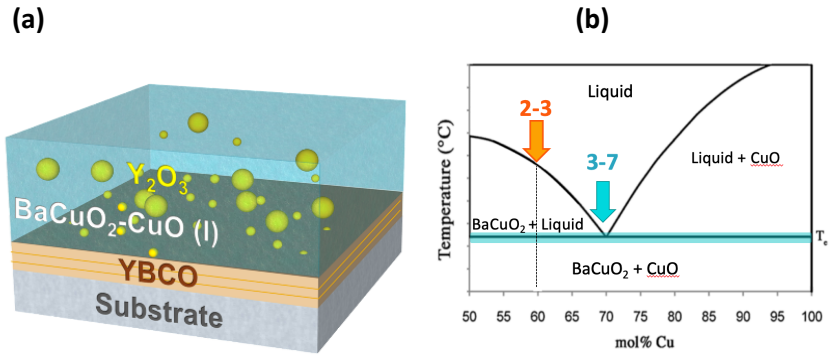

Fig. 5.1: Schematics of TLAG. ***(a)*** *Diagram showing the principles of TLAG: the Y_2O_3 particles dissolving in the BaO-CuO eutectic liquid;* ***(b)*** *Ba-Cu phase diagram as a function of Cu% with the two liquid compositions discussed in this dissertation: 2BaO-3CuO (2-3) and 3BaO-7CuO (3-7).*

Fig. 5.2 reports the phase diagram of YBCO, with the BaO-CuO melting line plotted as a function of temperature and composition, and temperature and pressure [157,158]. While thermodynamics is useful to describe the relative degree of stability of different phases, for a system there also exist metastable conditions which are selected by kinetics, depending on their relative rates of transformation. In fact, our results show that a metastable liquid phase can also be achieved before the eutectic line, originating from the same kinetic factors as TLAG. The concept can be understood in the context of metastable phases, as represented in Fig. 5.2a.

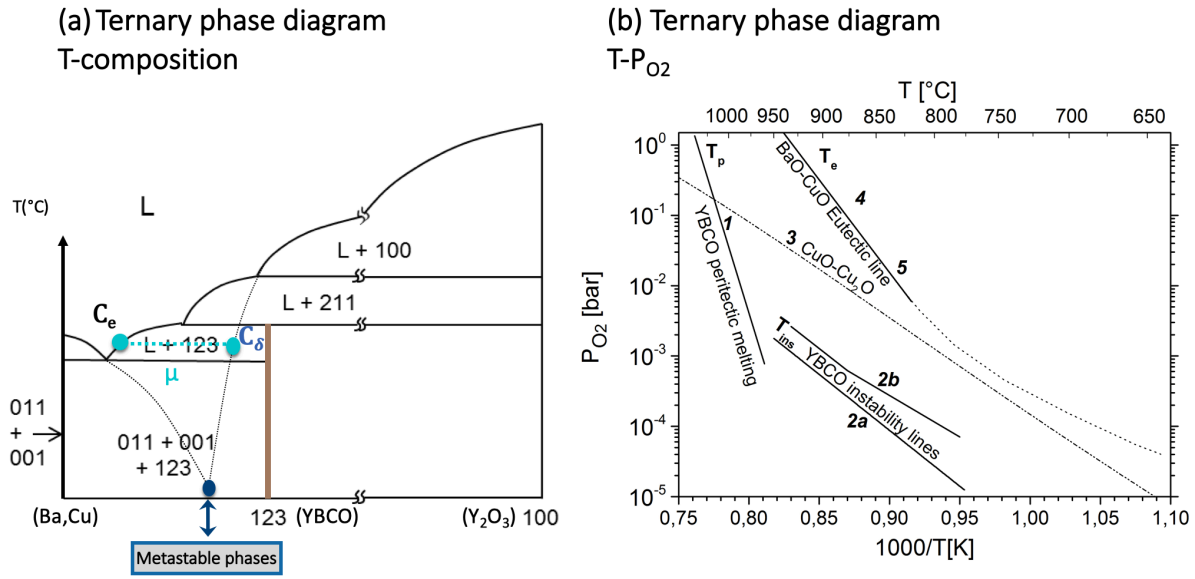

Fig. 5.2: Ternary phase diagrams in the TLAG approach. ***(a)*** *the Ba-Cu-Y ternary phase diagram as a function of Y% indicating the possible formation of metastable phases that make TLAG a kinetically driven process;* ***(b)*** *ternary YBCO phase diagram as a function of oxygen pressure and temperature, indicating the YBCO peritectic melting line (T_p,* [159] *) and instability line (T_{ins}, 2a* [158]*and 2b* [71]*), together with the BaO-CuO eutectic line (T_e) derived from studies on powder oxides (lines 4* [158] *and 5* [157]*).*

5.1.2 Fundamental aspects of crystallization in TLAG

Crystallization is defined as a first-order phase transformation upon which, in TLAG, a solid crystalline product is obtained from a liquid. All in all, crystallization takes place in two distinct steps: nucleation and growth. Nucleation involves the formation of the first stable nuclei, which will be generally favored by a low surface energy of the new phase; the stable nuclei will then reach a macroscopic size during the growth stage. Finally, the coalescence of the grown nuclei will form a film. Overall, growth occurs through two main physical processes:

- Diffusion of the solute to the growth interphase
- Surface kinetic processes, such as surface diffusion of the molecules once they have been absorbed on the substrate terraces.

Even though a theoretical analysis of all these models can be found elsewhere [18,160], in general the main driving force of these phenomena leading to crystallization from a solution is referred to as supersaturation. Supersaturation represents the relative chemical potential of the new phase ($\Delta\mu_c$) with respect to the mother phase ($\Delta\mu_s$), as below:

$$\Delta\mu = \Delta\mu_s - \Delta\mu_c \tag{5.1}$$

Where the chemical potential is mathematically defined as follows:

$$\Delta\mu = kT\cdot\ln(C_\delta^L / C_e^L) = kT\cdot\ln(\sigma+1) \quad > 0 \tag{5.2}$$

With:
$$\sigma = (C_\delta^L / C_e^L) - 1 \tag{5.3}$$

Hence, on a system where the Y coming from the yttria nanoparticles represents the solute dissolved into the eutectic liquid, $\Delta\mu$ depends on the difference between the Y equilibrium concentration C_e^L, and the real Y concentration C_δ^L in the liquid. In other words, from Fig. 5.2a, this difference becomes the driving force for the Y-123 (YBCO) phase crystallization from the liquid (L): thus, for nucleation to begin, so for the precipitation of a solid (YBCO) from a liquid (Ba-Cu-O), $\Delta\mu$ needs to be bigger than 0. The following diagram (Fig. 5.3) sums up the main steps of TLAG.

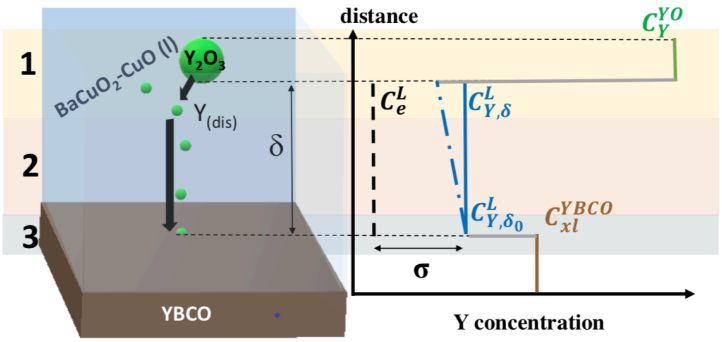

Fig. 5.3: The main steps of the TLAG process. *Diagram showing that above the Ba-Cu-O eutectic line the Y_2O_3 particles dissolve and diffuse to the substrate interphase where YBCO nucleation takes place. Reproduced from L. Soler's thesis* [155].

Initially, Fig. 5.3 step 1, the Y concentration is represented by the Y_2O_3 particles; the dissolution (Fig. 5.3, step 2) of the Y_2O_3 particles in the Ba-Cu-O melt originates the concentration of Y in the liquid, $C^L_{Y,\delta}$ (1), which depends on the initial Y_2O_3 amount; upon Y diffusion through a certain distance δ to the interphase (2) where YBCO can nucleate and grow, the real Y concentration becomes $C^L_{Y,\delta 0}$. Finally, (step 3), the Y concentration in the growing YBCO is represented by C^{YBCO}_{xl}. Note that an increase of the initial Y concentration corresponds to an increase of supersaturation.

Epitaxial nucleation of YBCO can be achieved tuning the supersaturation conditions. Higher supersaturation means higher driving force towards nucleation, but also less control in the c-axis orientation, in favor of random and a/b nucleation. To obtain c-axis nucleation, it is thus fundamental to be in the right supersaturation conditions. Although the experimental parameters that can be tuned are limited, supersaturation can be controlled by playing with the following parameters, namely: the initial Y concentration in solution, which is known (however the real concentration in the melt, $C^L_{Y,\delta}$, is actually unknown), temperature, oxygen partial pressure and heating rates. The Y equilibrium concentration, C^L_e, can be varied by changing the Ba/Cu molar ratio, as shown in Fig. 5.1b; for example, the eutectic composition is characterized by the transition from a solid to a full liquid, while for other compositions a liquid phase is in equilibrium with a solid (CuO or $BaCuO_2$) as not all Ba and Cu are converted into the melt. In particular, an increase of the copper molar amount, Cu% in the diagram of Fig. 5.1b, causes C^L_e to decrease; under the same $C^L_{Y,\delta}$ conditions, a decrease of C^L_e in turn causes the difference between C^L_e and $C^L_{Y,\delta}$, which is the supersaturation in Fig. 5.3, to decrease. Therefore, the eutectic composition (3-7) is characterized by a smaller C^L_e compared to the stoichiometric melt (2-3), thus supersaturation is lower in the 3-7 melt. Two solution compositions will be studied, the stoichiometric 2BaO-3CuO (2-3) and the eutectic 3BaO-7CuO (3-7). The effect of these parameters will be analyzed in the following sub-chapters.

Once $BaCuO_2$ crystallizes, the system needs to form the $BaCuO_2$+CuO (liq). One of the points to take into account for this process is that the liquid formation does not only occur from oxides (CuO, Y_2O_3) but also carbonates ($BaCO_3$) that are produced from the pyrolysis of the metalorganic precursors, as shown in Chapter 3 and 4. In these conditions, $BaCuO_2$ crystallization relies upon an extra step: the decomposition of $BaCO_3$. Based on this requirement, several other PhD students have been jointly working on the TLAG approach, which led to the development of the two main growth routes that are depicted in Fig. 5.4, with the relative working window for the TLAG process:

- The *temperature route* (T-route), which consists in heating up the sample at constant pressure in a region where YBCO is stable (10^{-2} bar ≤ P_{O2} ≤ 10^{-4} bar). Here, the decomposition kinetics of $BaCO_3$ overlap with YBCO formation: YBCO is formed while $BaCO_3$ decomposes. Slow heating rates thus result in random YBCO formation, since YBCO grows before the right nucleation conditions can be met. The key parameter is the heating rate: very fast ramps (> 1200°C/min) enable to reach the c-axis growth window for YBCO nucleation. However, some of the problems yet to be solved include substrate reactivity with the highly corrosive melt and poor wettability, especially for low-supersaturation solutions. This route can be represented with the following (not balanced) reaction:

$$BaCO_{3(s)}+CuO_{(s)}+Y_2O_{3(s)} \rightarrow [Ba\text{-}Cu\text{-}O]_{(l)}+Y_2O_{3(s)} \rightarrow YBa_2Cu_3O_{6.5(s)}+xCuO_{(s)} \quad (5.4)$$

Where x varies as a function of the initial Ba/Cu ratio in solution, going from x=0 in the 2-3 melt to x≠0 in the 3-7 melt.

- The *pressure route* (P-route), where, conversely, the strength is the capability to decouple $BaCO_3$ decomposition from YBCO growth. This can be achieved by heating up the sample at constant pressure ($P_{O2} \leq 10^{-5}$ bar) in a region of the phase diagram where YBCO is thermodynamically unstable, thus below its instability line (T_{ins}). YBCO crystallizes in a second step, when the pressure is rapidly raised at a constant temperature to enter the region of YBCO stability. That offers the possibility to optimize two separate steps, which in turn will show beneficial to widen the epitaxial window and decrease substrate reactivity, since the time the substrate is in contact with liquid is very much reduced.

Given the potentialities of the pressure route, the next sub-chapters will be focused on this approach and the main reaction routes will be laid out. More details about T-route in TLAG can be found in L. Soler's thesis [155].

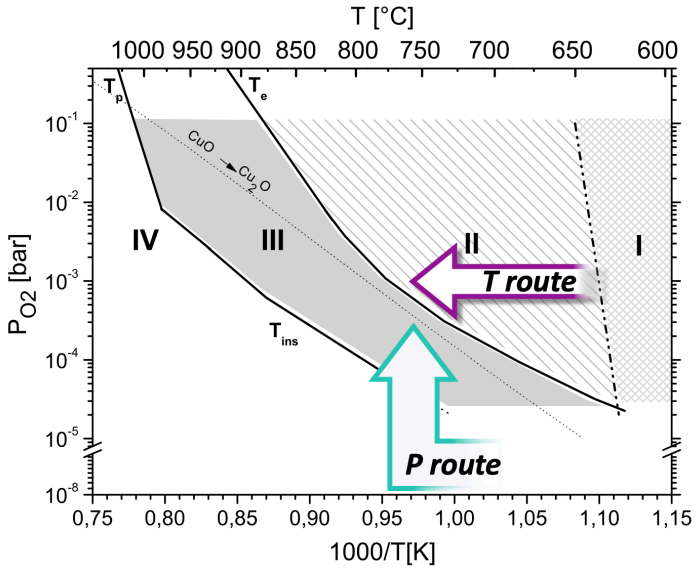

***Fig. 5.4**:* Main growth routes of TLAG. *The T-route consists in heating up the sample at constant PO_2 and ultrafast heating rates; the P-route is based on heating up the sample in the region of YBCO thermodynamic instability and then moving above the instability line through a fast pressure jump. Roman numbers indicate different regions: II is the region of the metastable liquid, III is the region of the eutectic liquid.*

5.1.3 Time-resolved phase evolution

Beginning from the pyrolyzed sample cointaining CuO, $BaCO_3$ and Y_2O_3, the following section will outline the phase evolution that governs the P-route in both steps, before and after YBCO growth, thus exploring the instability region and the YBCO phase diagram region, respectively.

The next two figures depict two different reaction paths that can occur during the first step of the pressure route, in the YBCO instability region; the two paths correspond to two different P routes: the Cu route and the $BaCu_2O_2$ routes. These two possible paths can be achieved playing with both oxygen partial (P_{O2}) pressure and total pressure (P_{TOT}). The difference is driven by the copper oxidation state, which can thermodinamically exist as Cu(I) and Cu(0) in the YBCO instability region:

- $CuO \rightarrow Cu_2O$ ($BaCu_2O_2$ route: 10^{-6} bar$\leq P_{O2} \leq 10^{-5}$ bar)
- $CuO \rightarrow Cu$ (Cu route: $P_{O2} < 10^{-7}$ bar)

The specific combination of P_{O2} and P_{TOT} can affect the final YBCO film properties even within the same route; independently of how these phases are generated, the advantage of having Cu(0) is that lower total pressures can be adopted with respect to the $BaCu_2O_2$ route; with that, the operational window is widened since the effect of residual local CO_2 is decreased (see next sub-chapter); higher temperatures can be reached (up to 870°C tested) without substrate reactivity or corrosive liquids. On the other hand, $BaCu_2O_2$ can generate a melt at $P_{O2} = 10^{-5}$ bar above 840°C, according to [71], although it was not observed in this work; this is in agreement with the strong interplay of kinetic and thermodinamic aspects in the TLAG approach.

$BaCu_2O_2$ route

Heating up at $P_{O2}=10^{-5}$ bar, CuO undergoes reduction to Cu_2O, and the specific temperature at which this is achieved increases with higher heating rates. For example, in Fig. 5.5 reduction takes place above 780°C, nearly 180°C higher than the equilibrium temperature. As soon as Cu_2O is formed, $BaCO_3$ decomposition is driven by the formation of $BaCu_2O_2$ and the characteristic reaction path for this route can be expressed as:

$$BaCO_{3(s)}+CuO_{(s)}+Y_2O_{3(s)} \rightarrow BaCO_{3(s)}+Cu_2O_{(s)}+Y_2O_{3(s)} \rightarrow BaCu_2O_{2(s)}+Y_2O_{3(s)} \quad (5.5a)$$

Where the equation is not balanced to generalize the path independently of the liquid composition employed.

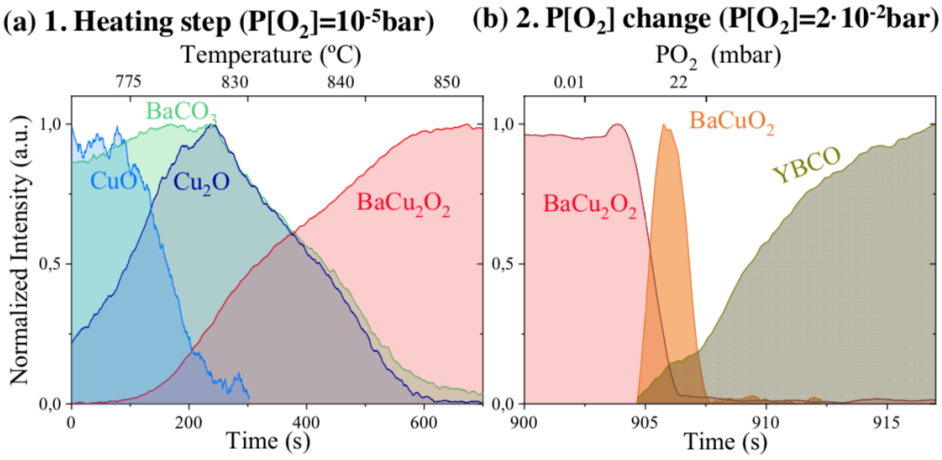

Fig. 5.5: Example of the phase evolution during the $BaCu_2O_2$ route. *The time-resolved phase evolution is relative to the case of the 2-3 melt at a heating rate of 300°C/min.*

In the second step of the pressure route, the P_{O2} is increased to cross the YBCO T_{ins} line. For YBCO to crystallize, Cu(I) needs to be oxidized to its final oxidation state, Cu (II), and in fact $BaCuO_2$ is formed from the $BaCu_2O_2$ oxidation (Fig. 5.5). Since the $BaCuO_2$ phase is not termodinamically stable in the ternary system where Y_2O_3 is present, as soon as it is formed it melts and YBCO grows according to equation 5.5b, just like in T-route. The specific time and temperature evolution of the time-resolved phase evolution shown in Fig. 5.5 depend on the particular growth parameters chosen.

$$BaCu_2O_{2(s)}+Y_2O_{3(s)} \rightarrow [Ba\text{-}Cu\text{-}O]_{(l)}+Y_2O_{3(s)} \rightarrow YBa_2Cu_3O_{6.5(s)}+xCuO_{(s)} \quad (5.5b)$$

Cu route

At $P_{O2}<10^{-7}$ bar, CuO reduction is pushed all the way to metallic copper, passing by Cu_2O (Fig. 5.6). Simultaneously, $BaCO_3$ is decomposed to BaO; from in-situ XRD this phase cannot be detected, probably because it is amorphous. No barium cuprate phases are formed in this route due to this severe copper reduction to its metallic state. The Cu route can be expressed by eq. 5.5c:

$$BaCO_{3(s)}+CuO_{(s)}+Y_2O_{3(s)} \rightarrow BaO_{(s)}+Cu_{(s)}+Y_2O_{3(s)} \quad (5.5c)$$

In the second stage, when the pressure is raised to 10^{-5} bar, Cu is re-oxidized to Cu(I) forming $BaCu_2O_2$, and then to Cu(II) from which YBCO can crystallize following eq. 5.5b. When the pressure jump is performed to reach the region just below the instability line (for example to $P_{O2}<10^{-5}$ bar) the approach constitues a mixed P-route. Conversely, when the pressure jump is aimed at reaching the region where YBCO is stable, $BaCu_2O_2$ cannot be detected, and eventually YBCO is seen growing directly from $BaCuO_2$ in the case of 2-3 composition (Fig. 5.7). The rate of these transformations will be discussed by tuned in-situ XRD experiments performed at the SOLEIL Synchrotron.

Based on the aforementioned premises, the next section will deal with the main aspects related to $BaCO_3$, analyzing the parameters that govern its decomposition.

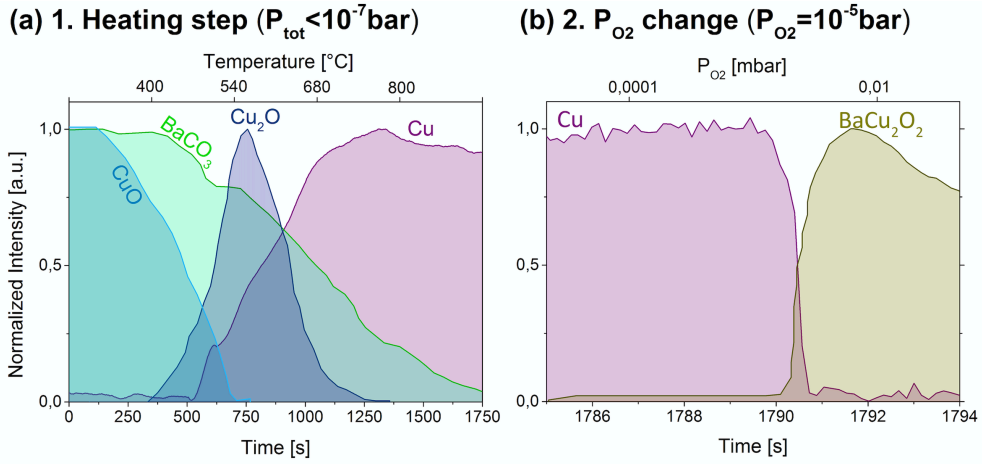

***Fig. 5.6**:* Example of the phase evolution during the Cu route before YBCO growth. *The case of 3-7 solution composition with heating rate of 25°C/min is shown. When the pressure is raised so to stop at the $BaCu_2O_2$ phase before reaching YBCO, the final properties of the film may vary so that this approach is called "Mixed P-route".*

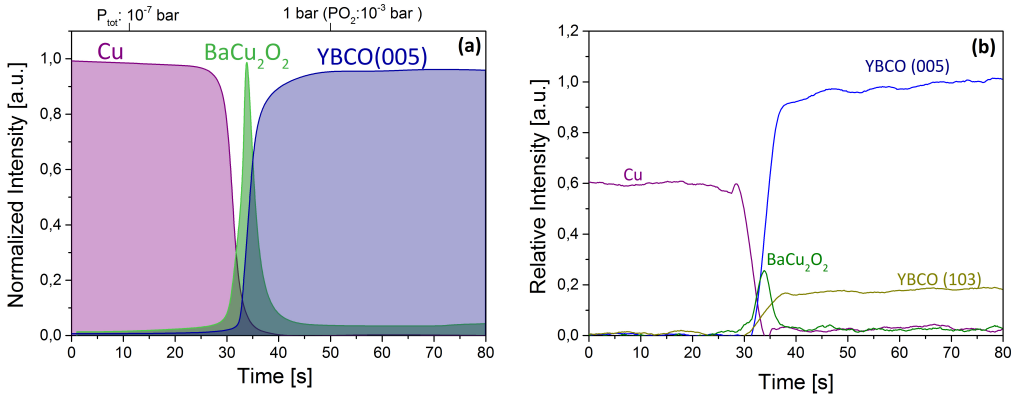

Fig. 5.7: Example of the phase evolution during the YBCO growth in Cu route *(upon a steep pressure increase at constant temperature) obtained from a heating rate of 25°C/min for 2-3 solution composition.* ***(a)*** *Normalized intensities and* ***(b)*** *relative intensities.*

5.2 $BaCO_3$ decomposition

One of the main criticisms for the use of FF-chemical methods with respect to the TFA-CSD route and the physical methods was for a long time thought to be the formation of $BaCO_3$ as solid intermediate after pyrolysis. Its decomposition in powder form occurs at very high temperatures, above 1000°C [79,80], higher than the processing YBCO temperature of interest. In a ternary system made up of the sintered oxide powders, $BaCO_3$ decomposition can be lowered by 100-200°C under the effect of very slow heating ramps (1°C/min) and thanks to the presence of CuO and Y_2O_3 [80] phases. Even though retained carboxylic groups were found in the YBCO powders obtained from the powder oxides decomposition [78], it has been already proven in Chapter 3 and 4 that films and powders behave differently. In this section we demonstrate in fact that $BaCO_3$ can be fully decomposed in FF-CSD-YBCO films at lower temperatures without carbon retain.

Since we already demonstrated that $BaCO_3$ formation cannot be avoided from FF-precursors after our pyrolysis conditions, it is crucial to underpin all the thermodynamic and kinetic parameters that will affect decomposition, namely temperature, pressure (both oxygen, P_{O2}, and CO_2 partial pressure, P_{CO2}), gas flow, heating ramps and film thickness. According to the base pressure and the general equations (eq. 5.4 and 5.5) and phase evolution graphs introduced in the previous section, during the heating ramp the following $BaCO_3$ decomposition reactions have been observed to occur:

- $BaCO_{3\,(s)} + CuO_{\,(s)} \rightarrow BaCuO_{2\,(s)} + CO_{2\,(g)}$ **(T route)** (*i.i*)
- $BaCO_{3\,(s)} + [Ba\text{-}Cu\text{-}O]_{\,(l)} \rightarrow [Ba\text{-}Cu\text{-}O]_{\,(l)} + CO_{2\,(g)}$ **(T route)** (*i.ii*)
- $BaCO_{3\,(s)} + Cu_2O_{\,(s)} \rightarrow BaCu_2O_{2\,(s)} + CO_{2\,(g)}$ **($BaCu_2O_2$ route)** (*ii*)
- $BaCO_{3\,(s)} \rightarrow BaO_{\,(s)} + CO_{2\,(g)}$ **(Cu route)** (*iii*)

Only reaction (*i*) leads directly to YBCO formation when the $BaCuO_2$ eutectic temperature is crossed, and it is at the basis of the T route. Equation (*i.ii*) follows from the overlap of two reaction paths: as $BaCO_3$ decomposes, $BaCuO_2$ crystallization takes place at the same time; when, upon the temperature increase, this process enters the region where $BaCuO_2$ melts, this liquid will be in the presence of undecomposed $BaCO_3$. Thus, in (*i.ii*) $BaCO_3$ decomposition is entwined with the liquid formation. Reaction path (*ii*) and (*iii*) constitute the main paths of the pressure routes and are characterized by the fact that $BaCO_3$ decomposition is not influenced by the eutectic melt, since no $BaCuO_2$ is formed at this stage.

In the previous equations, both P_{O2} and P_{CO2} play a major thermodynamic role: the O_2 partial pressure influences copper oxidation, thus regulating the presence of $Cu/Cu_2O/CuO$ and $BaCu_2O_2/BaCuO_2$ species, as shown in Fig. 5.8a; on the other hand, the CO_2 partial pressure directly affects the reaction rate and equilibrium of the $BaCO_3$ conversion into $BaO/BaCuO_2/BaCuO_2$ species (Fig, 5.8 b). While P_{O2} represents a tunable parameter that could be directly controlled, P_{CO2} is harder to estimate; in fact, values of total pressures do not really take into account local accumulations of carbon dioxide due to slow gas flow or static flux conditions that can depend on the furnace size and geometry. In the region where $BaCO_3$ decomposition occurs (700-850°C), the barium cuprate phases found are quite in agreement with the thermodynamic predictions shown in the graphs of Fig. 5.8, setting the P_{O2} limit between T route and P route at 10^{-5} bar. However, the presence of metallic copper (and thus of BaO instead of barium cuprate phases) is expected at lower P_{O2} (10^{-9}–10^{-13} bar) than the ones observed experimentally (P_{O2}~10^{-8}-10^{-9} bar, with P_{TOT}~10^{-7}-10^{-8} bar), indicating that other effects are playing a part, which will be discussed in the next subchapter (5.3).

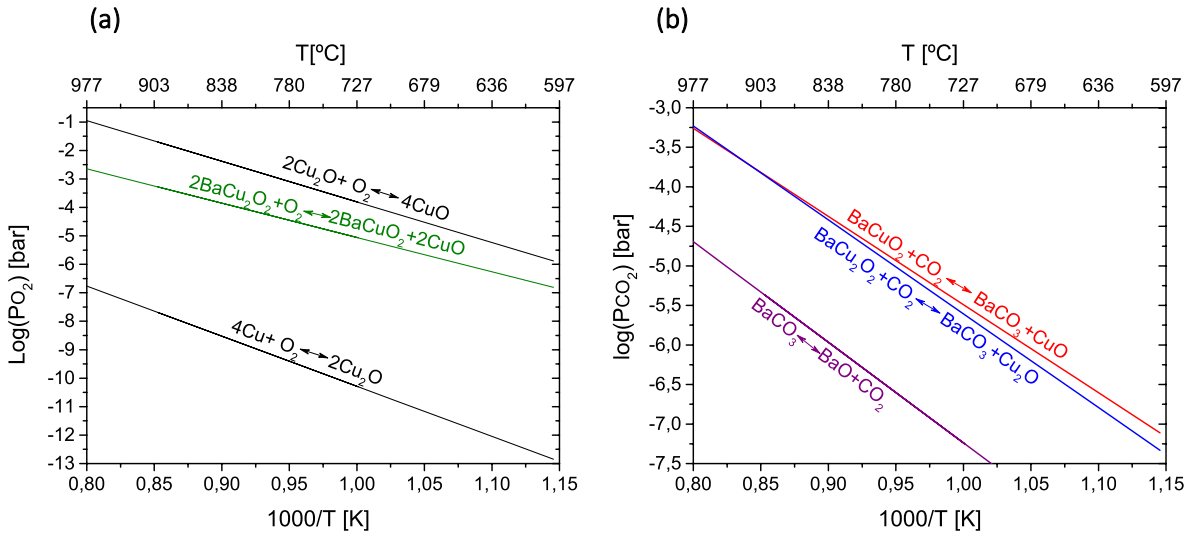

***Fig. 5.8**:* Thermodynamic equilibrium lines of O_2/CO_2 gas-solid reactions in TLAG. ***(a)** Oxidation reactions of copper* [161] *and of copper in barium cuprates* [157]*; the oxidation products are stable above the equilibrium lines depicted. Thermodynamics lines as a function of P_{CO2}* [157] *for **(b)** several $BaCO_3$ equilibrium reactions in the presence of copper (to $BaCuO_2$ and $BaCu_2O_2$) and without copper (to BaO). $BaCO_3$ is stable in the region above the equilibrium line.*

5.2.1 Decomposition in T-route ($P_{O2} \geq 10^{-4}$ bar)

Reaction (*i*) simplifies $BaCO_3$ decomposition path in T-route. Since, as soon as $BaCuO_2$ melts, YBCO grows, the complete reaction that takes into account $BaCO_3$ decomposition temperature shown in the following graphs involves formation of some YBCO. The rate at which reaction (i) occurs depends on the heating ramp (Fig. 5.9) and the P_{O2} (Fig.5.10).

At a fixed P_{O2} (Fig. 5.9), increasing the ramp by one order of magnitude, from 25 to 300°C/min, causes the decomposition time to decrease by approximately one order of magnitude and the temperature at which the transformation is at its maximum to shift by roughly 50°C higher (from 650-670, to ~700-720°C), as depicted in Fig. 5.9a. Normal working windows in T-route, in fact, involve ramps as high as 4800°C/min, where $BaCO_3$ decomposition can be as fast as 3s (see L. Soler's thesis [155]). This time enhancement is mainly a kinetic effect; $BaCO_3$ decomposition is a thermally activated process, thus fast heating ramps permit to achieve higher decomposition temperatures and given the exponential dependence of the reaction rate on temperature, the decomposition time is dramatically reduced. Although, as it will be shown in this section, fast decompositions are in agreement with kinetic theories, this behavior is further supported by the fact that $BaCO_3$ decomposition is driven by the presence of the eutectic melt. The liquid increases atomic diffusion and facilitates gas exchange between the film and the surface, speeding up CO_2 out diffusion. As a consequence, the 3-7 composition is slightly faster especially at low heating rates, thanks to the fact that full liquid can be achieved. Note from Fig. 5.11, however, that the points shown in Fig. 5.9 correspond to the region of the phase diagram below T_e, in the metastable liquid region.

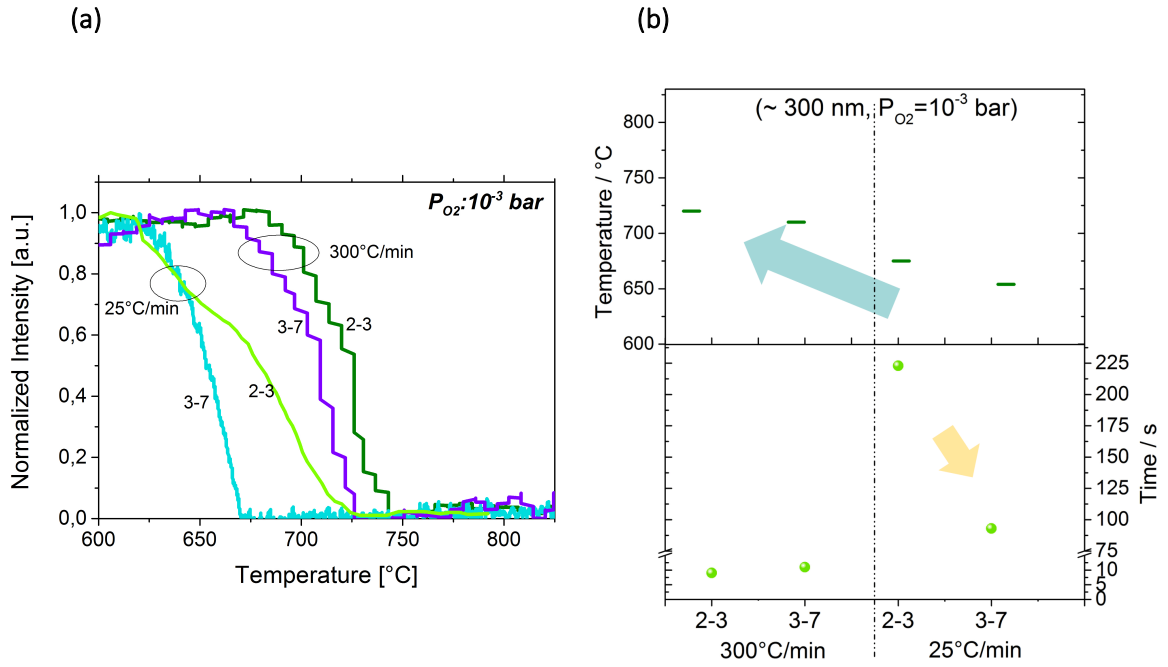

Fig. 5.9: $BaCO_3$ decomposition in T route: effect of heating rate. ***(a)*** *Raw data from in-situ XRD analysis of the $BaCO_3$ phase evolution with temperature at $P_{O2}=10^{-3}$ bar and* ***(b)*** *corresponding derivative points as a function of temperature.*

At a fixed heating rate, the effect of the oxygen partial pressure on $BaCO_3$ decomposition is shown in Fig. 5.10. The general trend involves a decrease of the decomposition temperature with decreasing P_{O2}, going from 10^{-2} to 10^{-4} bar of PO_2, for both 2-3 and 3-7 melt (for the latter going from 10^{-3} to 10^{-4} bar). Although decomposition times are in the order of a few minutes at this slow heating rate (25°C/min), decomposition becomes faster at lower PO_2, probably due to the vicinity of those points to the eutectic line (T_e) at low oxygen content, as shown in the phase diagram of Fig. 5.11.

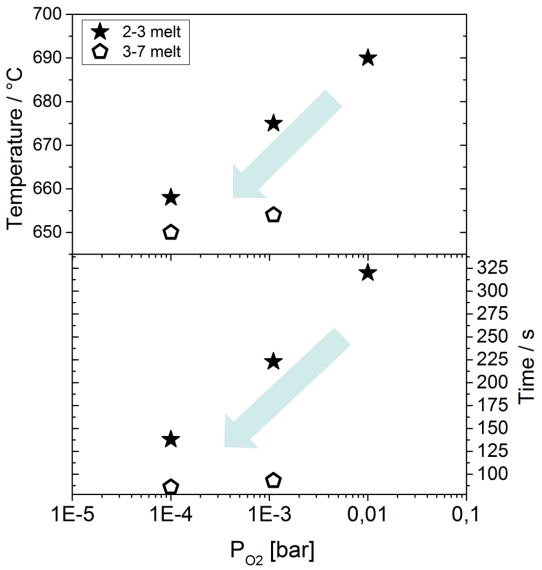

Fig. 5.10: $BaCO_3$ decomposition in T route: effect of P_{O2}. *Decomposition temperatures for $BaCO_3$ in T-route at 25°C/min obtained from in-situ XRD analysis.*

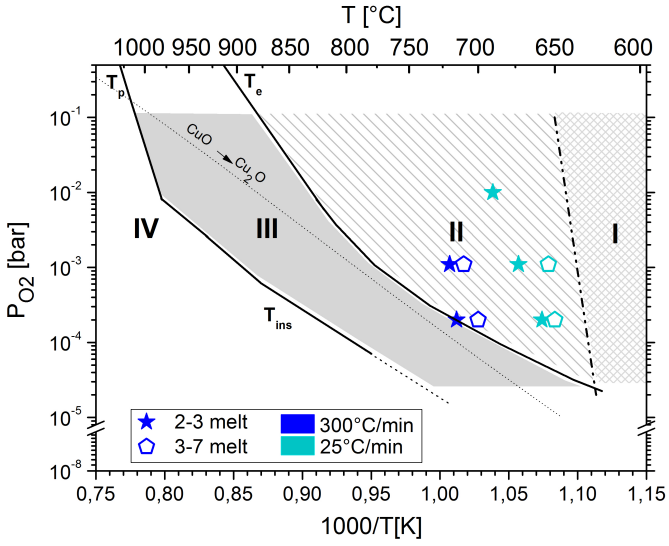

Fig. 5.11: Phase diagram of $BaCO_3$ decomposition in T route. *The T-P_{O2} region of $BaCO_3$ decomposition for reaction path (i) is shown as a function of heating rate and Ba/Cu ratio, for the data shown in Fig. 5.9 and 5.10. The points represent the temperature at which the reaction rate at constant P_{O2} is at its maximum.*

5.2.2 Decomposition in P-route

From the thermodynamic equilibrium values introduced in Fig. 5.8, one can suddenly see how, of the first two reactions with copper oxides, (*i*) is slightly less sensitive than (*ii*) to the residual CO_2 pressure due to the fact that the equilibrium P_{CO2} is higher in (*i*) than in *(ii)*. This means that local accumulation of CO_2 will push the equilibrium toward the reactants, slowing down $BaCO_3$ decomposition and this effect will be more important in (*ii*). This is especially significant when reactions (*i*) and (*ii*) are performed with similar total high pressures (but different P_{O2}), given the fact that residual CO_2 will be more affected by the total pressure and the gas flow. As we can see in fact from the in-situ XRD analysis reported in Fig. 5.12, decomposition in (*ii*), at $P_{O2}=10^{-5}$ bar and in the absence of flux takes about 17 minutes at 830°C with ramps of 300°C/min and for 350-nm films. This time can be detrimental for phase coarsening and thus final film performance. Reducing the total pressure or increasing the gas flow proved to be critical to reduce time and decomposition temperature: in fact, lower P_{TOT} corresponds to lower P_{CO2}, while bigger sample chambers help reduce local CO_2 accumulation. Thus, at $P_{TOT,Air}=10^{-7}$ bar or lower, and bigger sample chambers with horizontal flux of gas flow, $BaCO_3$ can be decomposed in half a minute at 300°C/min, about 40 times faster, with the main CO_2 peak revealed by EGA near 800°C. Note that reaction (iii) is the base reaction for the decomposition of $BaCO_3$ alone. This raises the flux and P_{TOT} as crucial factors in adjusting all the route parameters to YBCO growth.

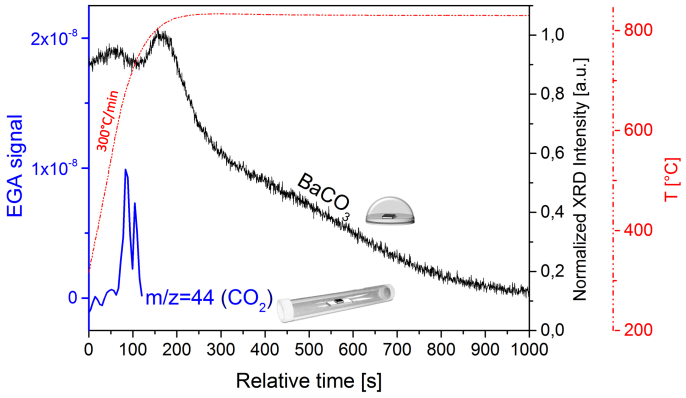

***Fig. 5.12**:* $BaCO_3$ decomposition in P route: effect of P_{TOT} and flux. *The analysis reported is relative to heating rates of 300°C/min in the step prior to the growth of YBCO, in two different furnaces and P_{TOT}.*

In order to finely tune growth conditions, the effect of other parameters on the $BaCO_3$ decomposition needs also to be taken into account. For this reason, a study for 2-3 and 3-7 solutions in reaction (*iii*) has been carried out as a function of film thickness and heating ramps. Fig. 5.13 summarizes the main results. No significant difference has been found changing solution composition for reaction (iii), while an important contribution is ascribed to the heating rate, which shifts the T_{dec} (the temperature at which the reaction rate is at its maximum) by nearly 100°C higher when the ramps are incresed by one order of magnitude. Nevertheless, the advantage of low pressures is that even 1-µm films can be easily decomposed way below the upper limit of the temperature range of interest, independently of the fact that an increase in film thickness slows down CO_2 out-diffusion, delaying the decomposition temperature.

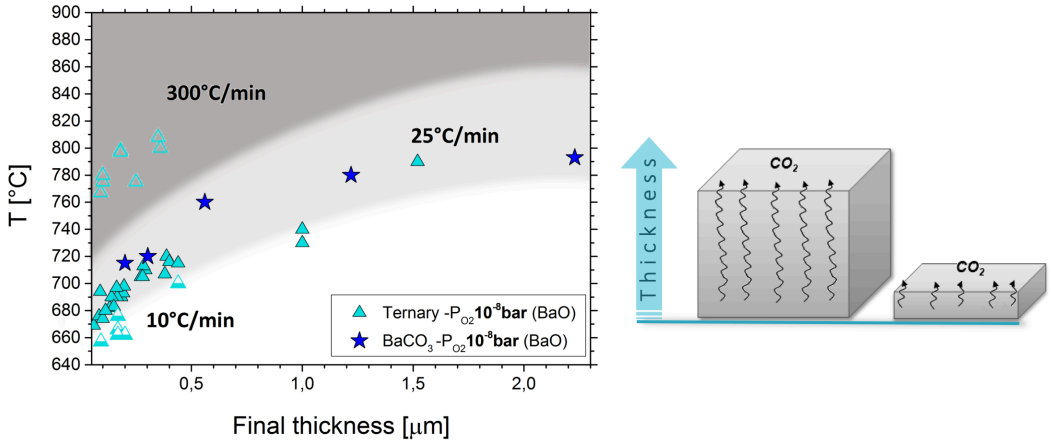

Fig. 5.13: $BaCO_3$ decomposition in Cu route. *Evolved Gas Analysis for $BaCO_3$ (star symbol) and ternary films (triangles) as a function of heating rate and film thickness, at $P_{TOT} < 10^{-7}$ bar ($P_{O2} \sim 10^{-8}$ bar). The symbols indicate the temperature at which the reaction rate is at its maximum. Right: schematic diagram of CO_2 out-diffusion as a function of thickness.*

All the above-mentioned factors represent a major difference that should be taken into account when tuning pyrolysis conditions on the desired $BaCO_3$ phase and particles size. In fact, we will show in this paragraph that the $BaCO_3$ decomposition depends on the $BaCO_3$ orthorhombic/monoclinic phase ratio (***O***/***M***), as also anticipated in Chap. 4. The XRD scans of three samples of 3-7 composition with different initial $BaCO_3$ phases after pyrolysis are shown in Fig. 5.14; they were decomposed in the $BaCu_2O_2$ route at 300°C/min and the $BaCO_3$ phase evolution plotted as a function of time and temperature in Fig. 5.15. Unlike the thermodynamically stable orthorhombic phase of Fig. 5.15 top, the monoclinic phase does not directly decompose, but it is first converted to the stable orthorhombic structure, which then decomposes (Fig. 5.15 center). As the initial ***M*** amount increases in the pyrolyzed sample, it is accompanied by a shift to higher temperatures for the ***M***→***O*** conversion, probably delayed by kinetic factors. The newly crystallized ***O*** phase has thus time to coarsen as it is formed, so that when decomposition of this phase starts the larger grain size slows down its decomposition. Sherrer grain size are about ~30nm or higher probably hindering decomposition, as depicted in Fig. 5.15. Conversely, when all initial $BaCO_3$ is ***O***, it can start decomposing at 22-nm grain size, in half the time. These results were collected for $P_{O2} \sim 10^{-5}$ bar ($P_{O2} \sim P_{TOT}$) and in conditions of nearly absent gas flow.

Reducing P_{O2} and the total pressure by almost one order of magnitude (from 10^{-5} to 10^{-6} bar) and decreasing the heating ramp (from 300°C/min to 25°C/min), conversion to the orthorhombic phase is faster (around 8 minutes, Fig. 5.16a), as the transformation is shifted to lower temperatures before particle coarsening can take place. Increasing the gas flow (using a quartz tube with horizontal linear flux) and sample chamber size, and further decreasing the total pressure to less than 10^{-7} bar ($P_{O2} \sim 10^{-8}$ bar), for the same thickness values and ramps (350 nm, 25°C/min), decomposition is complete within 5 minutes (as determined by the CO_2 evolution obtained from EGA analysis); the relative quenches are reported in Fig. 5.16b. This brings back the decomposition time to values similar to those of ***O*** pyrolyzed samples.

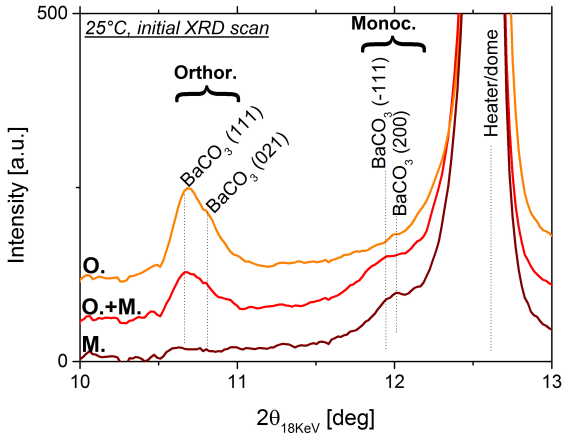

Fig. 5.14: XRD analysis of pyrolyzed samples with different $BaCO_3$ phases. *One sample is fully orthorhombic (**O**), one sample fully monclinic (**M**), and one sample is a mixture of both phases.*

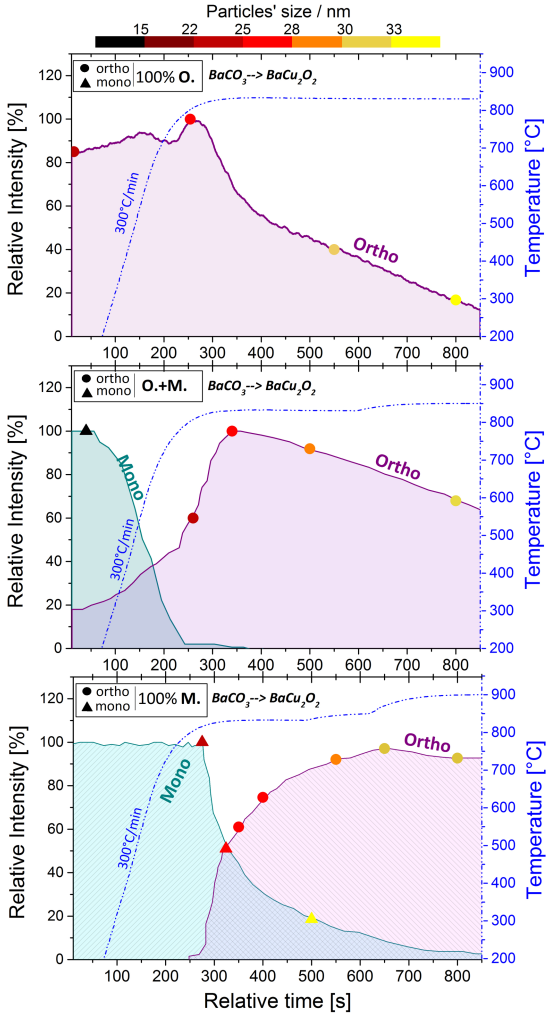

Fig. 5.15: Effect of the initial monoclinic (***M***) $BaCO_3$ amount. *In-situ XRD analysis for the decomposition of $BaCO_3$ to $BaCu_2O_2$; the **M** phase converts to the stable orthorhombic (**O**) $BaCO_3$ phase instead of decomposing, thus delaying the **O** decomposition.*

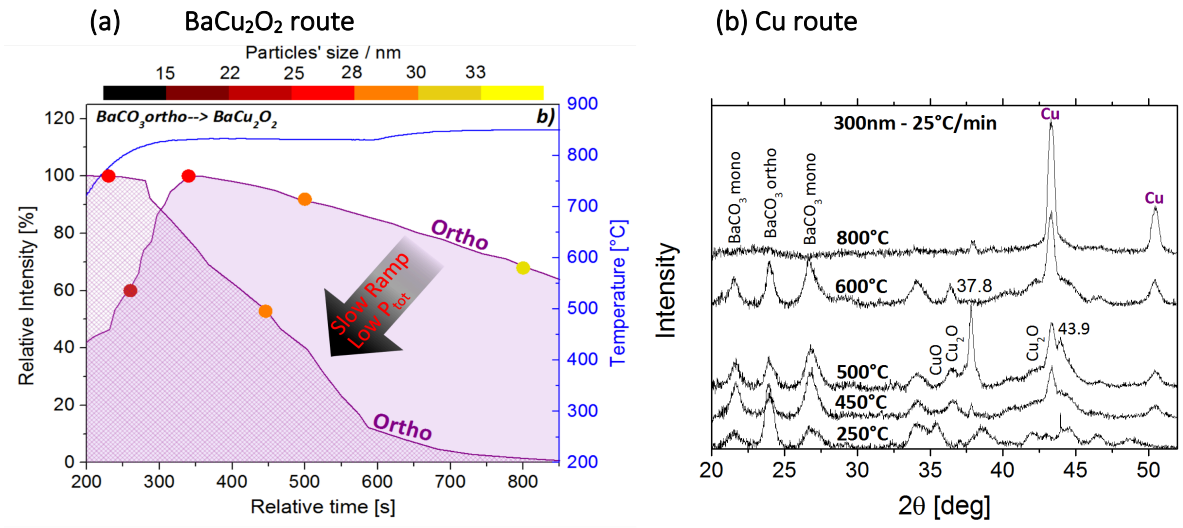

Fig. 5.16: Monoclinic $BaCO_3$ decomposition in $BaCu_2O_2$ and Cu route. ***(a)*** *In-situ XRD analysis of two samples with intial* ***M+O*** *$BaCO_3$ phase, decomposed in the $BaCu_2O_2$ route and* ***(b)*** *GI-XRD analysis of quenches of a sample with intial* ***M+O*** *$BaCO_3$ phase decomposed in Cu route (non-labelled peaks correspond to substrate peak tail). Both images show that slower heating rates and lower pressures facilitate the* ***O*** *phase decomposition even when coming from the* ***M*** *phase.*

5.2.3 Kinetic analysis

Formulation of the analysis

The experiments previously discussed (see, in particular, Fig. 5.13) indicated that the decomposition temperature increases with the film thickness. This suggests that $BaCO_3$ decomposition is a diffusion-controlled process, which means that CO_2 diffusion is significantly slower than the reaction rate for $BaCO_3$ decomposition. In turn, diffusion is a thermally activated process, which means that temperature plays a significant part in diffusion.

Therefore, to conclude the study of this section, a 2-step kinetic analysis has been carried out to obtain a temperature prediction for $BaCO_3$ decomposition as a function of the film thickness, as reported in Materials and Methods. The mathematical analysis was aimed at veryfing that CO_2 out-diffusion temperature increases with the thickness, independently of other parameters such as the specific decomposition reactions involved in each TLAG route.

The mathematical description of the diffusion process is based on the following assumptions and approximations:

- Diffusion theory: CO_2 flux through the layer of thickness d is taken into account with Ficks's law in the diffusion model introduced in [162], with the assumptions of steady state conditions ($\partial C/\partial t$ = constant, where C is the concentration); since the reaction under study involves a gas (CO_2 out-diffusion), the concentrations are replaced by the CO_2 partial pressures (∂P):

$$Flux = -D_{eff}\frac{\partial C}{\partial d} \quad \rightarrow \quad Flux = -D_{eff}\frac{\partial P}{\partial d} \tag{5.6}$$

- Diffusion is a thermally activated process: the diffusion coefficient D_{eff} follows an Arrhenius dependence (for thermally activated processes); thus the CO_2 flux becomes:

$$D_{eff} = D_0 \cdot e^{-E_a/RT} \quad \rightarrow \quad Flux = -D_0 \frac{\partial P}{\partial d} e^{-E_a/RT} \tag{5.7}$$

- $BaCO_3$ decomposition is diffusion controlled: the pre-exponential factor, A (with $A = -D_0 \frac{\partial P}{\partial d}$), of eq. 5.7, is integrated in ∂d considering D_0 and p independent of the thickness, d. The last assumption implies that the CO_2 partial pressure of equilibrium (p_{eq}) and that of the furnace atmosphere (p_0) do not depend on the thickness. In other words, the assumption is to be in the limit where CO_2 diffusion is significantly slower than the reaction rate for $BaCO_3$ decomposition (diffusion-controlled conditions, as opposed to reaction-controlled).

$$A = D_0 \frac{(p_{eq} - p_0)}{d^2} \quad \rightarrow \quad A \propto \frac{1}{d^2} \tag{5.8}$$

  We therefore defined the pre-exponential factor, A, as a function of thickness.

- Constant activation energy, E_a: in the first step of this methodology, E_a relative to $BaCO_3$ decomposition needs to be evaluated. If the process is diffusion-controlled, the activation energy is constant with varying thickness. Thus, we can use the isoconversional methods to calculate the activation energy in a specific condition, of constant pre-exponentioanl factor, A. To keep A constant, we compare the process in samples with similar thickness (d constant) and in the same experimental conditions (p_0 constant).

- I step - Friedman method: these conditions of constant A specifically corresponded to P_{tot}=1 bar and P_{O2}~10^{-2} bar (conditions of reaction (*i*)) with a thickness of ~0.5 µm. E_a for the $BaCO_3$ decomposition reaction was evaluated with the isoconversional Friedman method described in Chapter 2.2 (through a thermogravimetric analysis), at 3 different heating rates (5, 10, 25°C/min). The process was then repeated increasing the thickness, to ~1µm. In both conditions of thickness, an activation energy of roughly 360-380 kJ/mol was found, as depicted in Fig. 5.17a.

- II step - Kissinger method: Following this, the previous temperature-thickness data points obtained with thermogravimetric analysis were plotted in Fig. 5.17b along with other points derived from EGA analysis in the experimental conditions represented by eq (*iii*). Each temperature value represents the peak temperature T_M at which the decomposition reaction rate is at its maximum. In this second step, a modified isoconversional kinetic model was applied in order to fit the data in Fig. 5.17b. In particular, the Kissinger method, with starting point the Kissinger equation [91] as analitically solved in [92,93]:

$$x_M = x_0 + 2\frac{x_0}{2+x_0} \ln\left(\frac{\sqrt{-E_a \cdot A \cdot f(\alpha_M)/R\beta_M}}{\sqrt{-E_a \cdot A \cdot f(\alpha_0)/R\beta_0}}\right) \xrightarrow[Kissinger\ method]{} x_M = x_0 + \frac{x_0}{2+x_0} ln\left(\frac{\beta_0}{\beta_M}\right) \tag{5.9}$$

  With $x_M \equiv E_a/R\,T_M$, A is the pre-exponential constant of the Arrhenius equation, R the gas constant, β the heating rate, $f(\alpha_M)$ the function of the degree of transformation and x_0 is the value of x_M for a particular set of values of β_0 and A_0. When we compare the same

transformation (top and bottom of the logaritmic function) under the same experimental conditions (A_M= A_0) at different heating rates, β_M and β_0, all parameters but β are invariant and they cancel out, giving the right end part of eq. 5.9. In our case the aim is to compare different thicknesses at the same heating rate, so that in the logaritmic term, all parameters cancel out but A and the term becomes: $\ln\left(\frac{\sqrt{A_0}}{\sqrt{A_M}}\right)$.

$$x_M = x_0 + 2\frac{x_0}{2+x_0}\ln\left(\frac{\sqrt{-E_a\cdot A_M\cdot f(\alpha_M)/R\beta}}{\sqrt{-E_a\cdot A_0\cdot f(\alpha_0)/R\beta}}\right) \Longrightarrow x_M = x_0 + 2\frac{x_0}{2+x_0}\ln\left(\frac{\sqrt{A_0}}{\sqrt{A_M}}\right) \quad (5.10)$$

Replacing the expression (eq. 5.8) already found for A in eq. 5.10, and taking the square root out of the logaritm, we obtain:

$$x_M = x_0 + 2\frac{x_0}{2+x_0}\ln\left(\sqrt{\frac{A_0}{A_M}}\right) \Longrightarrow x_M = x_0 + \frac{x_0}{2+x_0}\,ln\,(\frac{d_0^2}{d_M^2}) \quad (5.11)$$

Which, from the definition of x_M and in the approximation that x_0>>2, can be rearranged as:

$$\frac{1}{T} = -2\frac{R}{E_a}\cdot\ln(d) \quad (5.12)$$

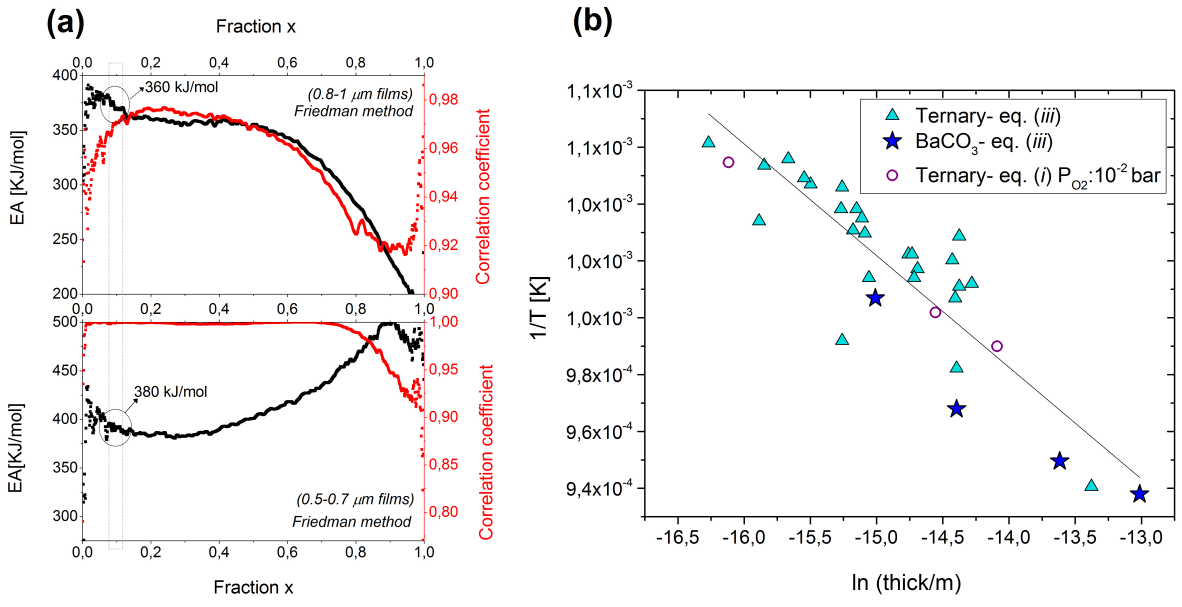

Fig. 5.17: Kinetic analysis of $BaCO_3$ decomposition in T and P routes. ***(a)*** *activation energy as a function of the degree of transformation x, obtained applying the Friedman method on the TG curves in reaction (i).* ***(b)*** *Fitting of the $BaCO_3$ $1/T_{dec}$ as a function of the ln(thickness) at slow heating rates (25°C/min) for two different reaction paths: ternary films decomposed according to reaction (i) with 2-3 melt and (iii) with both 2-3 and 3-7 melt (triangles) and single-component $BaCO_3$ films (stars). The points correspond to the temperature at which the decomposition reaction is at its maximum. For eq. iii they were derived from EGA experiments at $P_{tot(air)}<10^{-8}$ bar. For eq. i they were derived from TG experiments at $P_{O2}\sim10^{-2}$ bar.*

The data in Fig. 5.17b can be quite well fitted by the previous equation relating the temperature with the film thickness d through which the CO_2 diffusion occurs. From the slope ($2R/E_a$) of the fit, knowing the activation energy, a parameter of 1.5-1.9 was found, slightly inferior to the theoretical value of 2. The disagreement might be attributed to the fact that the theoretical assumptions take into account fully homogenous and porous-free films. However, the overall agreement of the experimental data with the CO_2 out-diffusion behavior shows that the activation energy is basically the same within these approximations, independently of the route, the solution composition, the **O**/**M** amount and the film inhomogeneities, meaning that CO_2 out-diffusion is a robust parameter governing $BaCO_3$ decomposition.

The main limitations of the method consist of:

- considering the transformation as diffusion-limited, which is an approximation that does not take into account different furnace geometries, gas flow conditions and total pressures that might also affect the $BaCO_3$ decomposition through the parameter p_0 (CO_2 partial pressure), which has been considered invariant in the analysis.
- taking as invariant also the diffusion coefficient D_0 and the activation energy E_a, which depend on the physical state of the system, and may differ considerably when considering solid state versus liquid state diffusion.

Results

The predictions of temperature and time delivered by the kinetic analysis are plotted in Fig. 5.18a, top and bottom, respectively, as straight lines. For comparison, the same graph includes the experimental points obtained from the different conditions shown before throughout section 5.2. To help the intepretation of the results, Fig. 5.18b places those experimental points in the YBCO phase diagram.

One of the main results is that very fast decomposition times (of the order of ~20-30 seconds) are predicted to occur at fast heating rates (300°C/min), just as found experimentally (~10 seconds). However, it can also be seen that some points deviate from the predictions in the case of the T-route (pink circles in Fig. 5.18a) performed at $P_{O2}<10^{-2}$ bar; in particular, these points correspond to experimental conditions of $P_{O2}=10^{-3}/10^{-4}$ bar (encircled with dotted lines in the phase diagram of Fig. 5.18b). Given the already commented complexity of the phase diagrams involved and the limitations of the kinetic analysis, other factors may be expected to affect the $BaCO_3$ decomposition; in particular these deviations in the metastable region of Fig. 5.18b could be ascribed to the presence of the metastable liquid and the vicinity to the eutectic line, which can enhance decomposition according to reaction *i.ii*. Finally, we also cannot discard that deviations are due to differences in the gas flow conditions and furnace geometry between the points recorded from in-situ XRD experiments and the laboratory conditions.

In conclusion, independently of the chosen values for all the parameters that govern $BaCO_3$ decomposition and that were previously introduced, in the window of interest that spans from ramps between 25 and 300°C/min, thickness up to 1 μm and to gas flows between 0.1 and 0.5L/min, it was shown in this section that $BaCO_3$ decomposition does not necessarily consitute a limiting factor in FF-YBCO CSD methodologies.

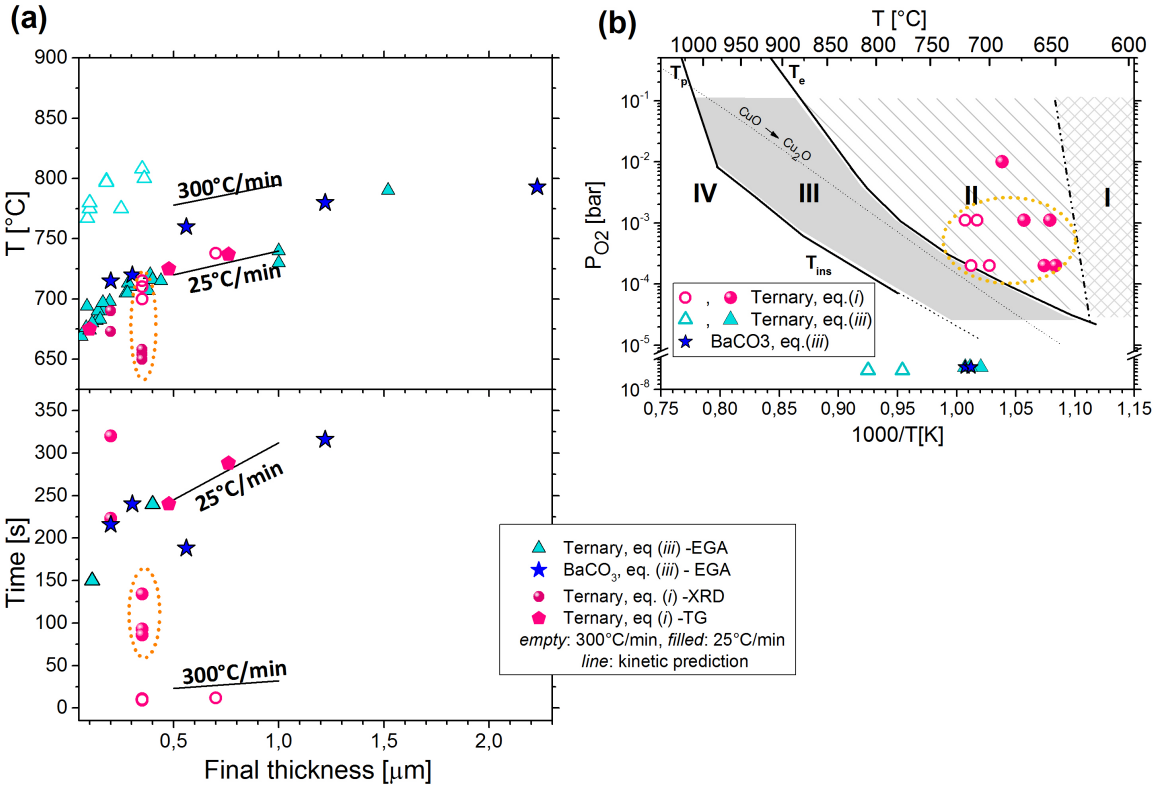

Fig. 5.18: Kinetic predictions for $BaCO_3$ decomposition in T and P routes. ***(a)*** *$BaCO_3$ decomposition temperatures (top graph) and time (bottom graph) in the conditions of reaction i and iii obtained from experimental EGA data (for P-route) and from TG and in-situ XRD experiments (for T-route); kinetic predictions are reported as straight lines.* ***(b)*** *the same points for 250-350 nm films are reported on the phase diagram as a function of temperature and P_{O2}. Heating rates: 300°C/min for empty symbols and 25°C/min for filled symbols. Only the heating rate is expected to influence decomposition temperatures and time in the context of the kinetic analysis. Deviations from kinetic predictions are encircled with dotted lines and they correspond to a region close to the eutectic line.*

5.3 The P-route

This section will first study the kinetics involved in TLAG, with special focus on the Cu route performed from P_{O2}~10^{-8} bar; we will demonstrate that Cu oxidation is not a limiting reaction to achieve ultrafast growth. In fact, in-situ XRD analysis performed at SOLEIL synchrotron will reveal that very high growth rates of YBCO are possible thanks to the fact that a liquid is involved. Secondly, the Cu route will be explored in terms of epitaxy and superconducting properties in relation to the YBCO phase diagram.

5.3.1 Copper redox kinetics

As previously mentioned, themodynamically, in the conditions of low total pressures of the furnace, Cu formation is not expected to take place below 700-800°C. However, at $P_{TOT} \leq 10^{-7}$ bar of air, metallic copper was observed to form starting at 300°C in laboratory conditions; depending on the experimental setup such as furnace geometry and size, this temperature was observed to shift to slightly higher values. This suggests that other factors other than thermodynamic equilibrium values have a role: for example, local accumulation of gas which can

lower the partial oxygen pressure, or strong furnace degassing. In the hypothesis that its presence in the low-temperature region is due to gas (i.e CO) relased by the furnace, the scenario may be the following:

$$CuO_{(s)} + CO_{(g)} \rightarrow Cu_{(s)} + CO_{2(g)} \quad (5.13)$$

Instead of the thermodynamic expected reaction:

$$2CuO_{(s)} \rightarrow Cu_2O_{(s)} + \tfrac{1}{2}\, O_{2(g)} \quad (5.14)$$

Independently of how it is obtained, as far as YBCO growth is concerned, it is clear from the XRD results that that Cu route exists, and, since the P_{TOT} conditions of the samples grown in this route do not vary throughout this thesis, it will be referred to as having base $P_{O2}\sim10^{-8}$ bar.

In this route, Cu oxidation can be very fast. The diagrams in Fig. 5.19 show some experimental values form in-situ XRD for Cu-O reduction at constant pressure (during the ramp up) and Cu oxidation at constant temperature (under a change of pressure) in the ternary system into account. In the first case of Fig. 5.19a, the reduction speed during the ramp up of the Cu route (at $P_{O2}\sim10^{-8}$ bar) depends on the heating rate: the faster the ramp, the quicker the Cu(I)-Cu(0) reduction, as the process shifts to higher temperatures with faster ramps. Also the inverse reaction, oxidation of metallic copper to copper oxide phases is fast, and it is shown by the filled symbol in Fig. 5.19a; this reaction was studied by heating up at $P_{O2}=10^{-3}$ bar a quenched sample containing Cu(0).

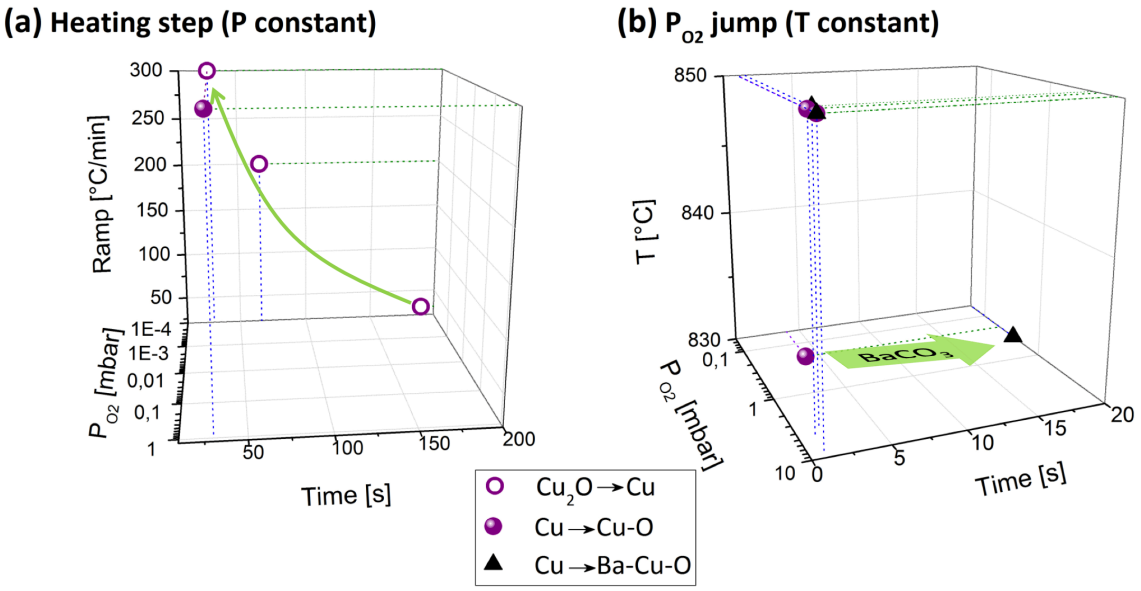

Fig. 5.19: Kinetics of copper phases redox reactions. *Values obtained from in-situ experiments at SOLEIL relative to 350-nm films (after YBCO growth).* ***(a)*** *reaction times at constant pressure during the heating ramp: the faster the ramp, the faster the $Cu_2O \rightarrow Cu$ reduction; the inverse reaction is shown at 1 mbar by heating up a previously quenched film in Cu route containing metallic copper.* ***(b)*** *Reaction times at constant given temperatures during the pressure jump to the indicated final P_{O2}: for all final pressures oxidation to Cu_2O/CuO and Cu-Barium cuprates is fast, unless $BaCO_3$ is not fully decomposed.*

Similarly, at constant temperature, Fig. 5.19b, in the same ternary system following $BaCO_3$ decomposition, Cu reoxidation only depends on the speed of the pressure jump. Thus, for jumps from P_{O2}~10^{-8} to P_{O2}>10^{-5} bar, Cu reoxidation to form barium cuprates (Ba-Cu-O) can be as fast as 2 s. However, if the sample still contains undecomposed $BaCO_3$ along with Cu, formation of $BaCu_2O_2$ is slower than the copper oxidation upon a pressure jump from P_{O2}~10^{-8} to 10^{-5} bar. We can conclude that Cu reoxidation is not a limiting reaction as much as $BaCO_3$ conversion to Barium cuprate phases.

5.3.2 YBCO growth rates

Based on the growth approaches introduced in the previous sections, in-situ XRD studies allowed to prove that ultra-fast YBCO growth can be achieved thanks to the Ba-Cu-O melt that speeds up Y diffusion. Fig. 5.20 shows the phase evolution of YBCO (005) reflection upon a fast ramp at constant pressure (T-route) and upon a pressure change at constant temperature (P-route).

The steep increase in intensity proves that growth rates of 100 nm/s can be achieved in both routes. This is an outstanding achievement of the liquid assisted growth approach, surpassing other known established growth techniques such as TFA-CSD route by 100 times. It reflects the exceptional potentiality of liquid assisted approaches when compared to the slower solid-solid and gas-solid reactions.

Additionally, the T-route reveals the presence of a metastable liquid slightly below the eutectic temperature of the BaO-CuO melt, which still allows for growth rates as high as 5 nm/s (see the first slope in Fig. 5.20 for the T route).

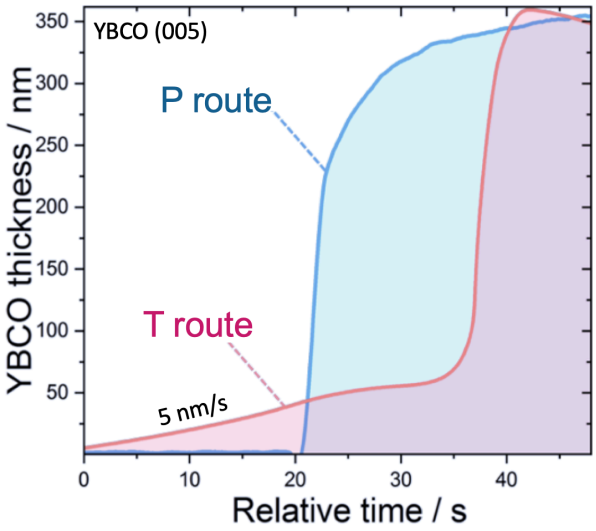

Fig. 5.20: YBCO growth rates in P and T routes. *The time-resolved phase evolution is relative to the YBCO (005) reflection obtained from in-situ XRD experiments at SOLEIL synchrotron.*

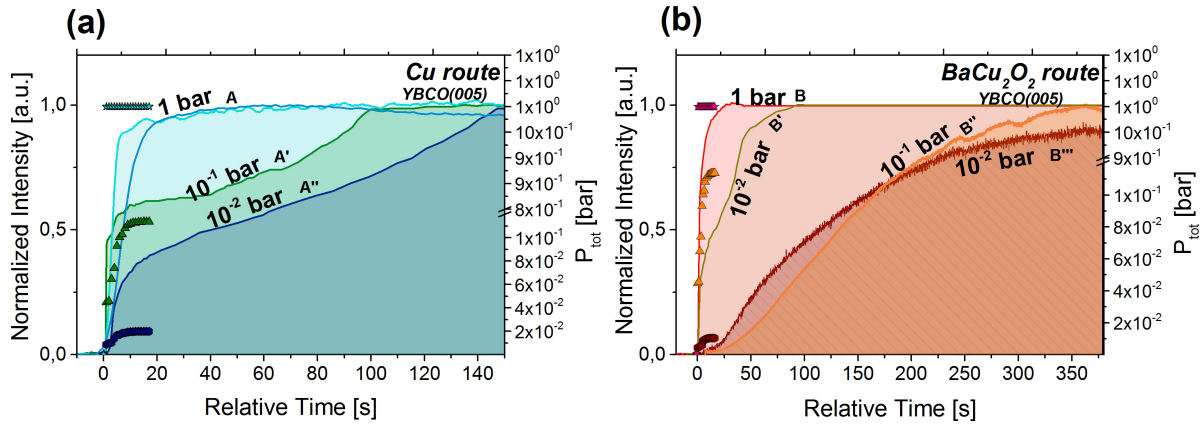

***Fig. 5.21**:* Time evolution of YBCO as a function of the final P in P route. *The in-situ analysis is relative to the 2nd step of the P-routes, during growth in the YBCO stability region. Filled lines: in-situ XRD phase evolution of the YBCO (005) reflection in **(a)** Cu route and **(b)** $BaCu_2O_2$ route as a function of the final P_{TOT}. P_{TOT} values reported: 10^{-1} and 10^{-2} bar of air and 1 bar of different gas mixtures corresponding to $P_{O2}=10^{-3}$ bar (for Cu route, exp. A) and $2.5 \cdot 10^{-4}$ bar for the $BaCu_2O_2$ route (exp. B). Scattered symbols: P_{TOT} evolution over time during YBCO growth. All experiments are relative to 3-7 composition samples except exp. A (2-3).*

In Fig. 5.21 it is reported the YBCO(005) evolution over time for different experiments during the pressure jump in the YBCO stability region, for both P-routes. The experiments of Fig. 5.21 were performed with pressure jumps in a wide range of P_{TOT} and P_{O2}, as well as temperature (shown later on, in Figs. 5.22 and 5.23). The YBCO growth slopes are quite different; three situations can be identified: experiments that show just one vertical slope (2 curves labelled as A in Fig. 5.21a, and exp. B in Fig. 5.21b), experiments with one slow slope (B'', B''', Fig. 5.21b) and experiments with mixed slopes (the first fast, the second one slow, exp A', A'', B', Fig. 5.21). This urges some considerations for the future exploration of the ultra-fast growth region, considering that the main parameters that can affect YBCO growth are P_{TOT}, P_{O2} and temperature:

- *Effect of total pressure*. The first thing of note from Fig. 5.21 is that only pressure jumps to P_{TOT}=1 bar (exp. A and B in Fig. 5.21, independenlty of the corresponding P_{O2} and temperature which are different) achieved one and very fast slope, suggesting the idea that there might be an effect of the total pressure. In fact, the scattered symbols referring to the P_{TOT} evolution in time show that the higher the final total pressure of the jump, the faster the pressure increase. Conversely, for final P_{TOT} smaller than 1 bar, there is a gradual pressure increase of roughly 10 s before reaching the final plateau value. However, when we look at the specific values, we see that for all experiments, within one second P_{TOT} already reaches a P_{O2} value within the YBCO stability region (Fig. 5.23), while the remaining time only corresponds to a minor P_{TOT} increase, of a factor 2. Therefore, P_{TOT} alone cannot be responsible for the differences in the YBCO growth slopes of Fig. 5.21.
- *Effect of O_2 partial pressure*. Next, we can compare the speed of the P jump in terms of P_{O2}. The speed of the pressure jump (defined as $\partial P/\partial t$, with $\partial P=P_f-P_i$) will always be bigger at constant ∂t for bigger pressure differences (∂P) performed from the same fixed base pressure. Thus, between exp. A' and A'' (both 3-7 composition with same thickness), ∂P_{O2} is larger for A' ($P_{f,O2}=10^{-2}$ bar) than for A'' ($P_{f,O2}=2 \cdot 10^{-3}$ bar) in ∂t=1 s; in fact, the first slope in A' is faster than in A''. However, this does not yet explain the presence of experiments

with two slopes of the YBCO growth rate, nor why jumps to the same final P_{TOT} and P_{O2} (such as exp. B' and B''') within the same route produce different growth slopes.

- *Effect of temperature.* Another YBCO growth parameter may be the temperature decrease during the pressure change, caused by the arrival of cold gas. Significant temperature drops as the one in Fig. 5.22 take place upon the pressure increase, which could not be avoided in the experimental conditions of the in-situ experiments. These drops are of the order of 20-50°C; they are bigger when the initial temperature before the jump is high (850°C); they also increase with increasing ∂P_{TOT}. Decreasing the temperature at a fixed pressure is expected to decrease the Y solubility in the liquid, and thus increase the supersaturation by shifting the process away from the YBCO T_{ins} line. High supersaturation in turn is expected to increase the YBCO growth rate. However, we observe the opposite: a drop in the YBCO growth slope. Therefore, the effect of higher supersaturation must be contrasted by the effect of crossing T_e: the temperature decrease must be responsible to slow down YBCO growth by shifing the growth away from the full liquid region to the region below T_e (metastable liquid region).

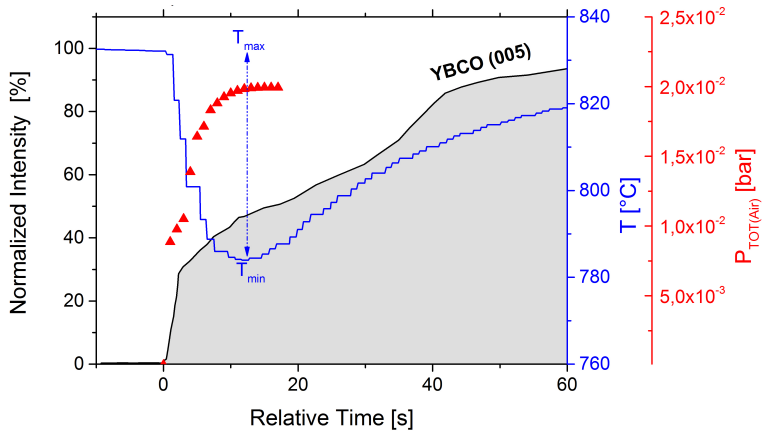

***Fig. 5.22**:* Effect of the pressure jump in P route. *Detailed evolution of: (line) temperature profile, (filled line) YBCO intensity and (scattered symbols) total pressure of air over time for one of the experiments shown in Fig. 5.21b (exp. B', $BaCu_2O_2$ route, $P_{TOT,Air}=2*10^{-2}$ bar).*

Indeed, the experiments shown in Fig. 5.21 correspond to different regions of the phase diagram, Fig. 5.23. Experiments with two growth slopes are represented in Fig. 5.23 by two bars of different colors, otherwise only one bar is used to represent the growth slope. Smaller growth rates (~3 nm/s, orange bars) correspond to YBCO growth taking place before T_e, while high growth rates (green bars) correspond to growth happening above the equilibrium eutectic line. This is in agreement with the results from the T route experiment shown in Fig. 5.20 which displays two slopes: a slow growth is achieved when crossing the metastable liquid region (below T_e) and a very fast one when the sample is above T_e. Similarly, in P route a very high growth rate is achieved above T_e, and then, upon the temperature drop, a slow growth continues below T_e.

Although T_e has a significant role in the YBCO growth rate, other parameters might also be affecting the growth rates, such as solution composition (2-3 versus 3-7), the presence of

coarsened phases, the heating rate of the ramp before growth (see next sections)... In fact, the experiments discussed in Fig. 5.21 were performed with heating rates between 25 (exp. A) and 300°C/min , in both 2-3 (exp. A) and 3-7 composition, with thickness between 100-200 (exp A) and 400 nm.

This requires to carry out a deeper analysis in the future in order to disentangle all the above-mentioned parameters.

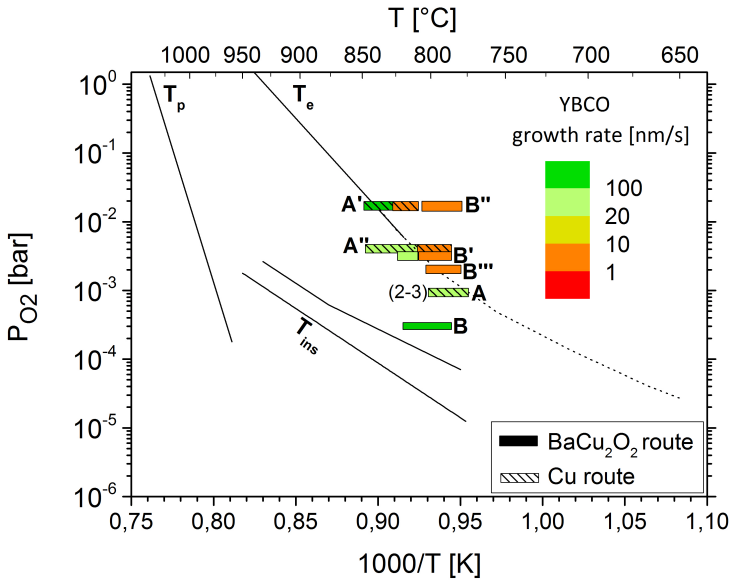

***Fig. 5.23**:* YBCO growth rates as s function of the phase diagram. *The final temperature and pressure of growth placed in the YBCO phase diagram and relative to the experiments shown in Fig. 5.21. The trend indicates that when growth is performed above T_e, growth rates are higher than in the metastable liquid region (below T_e). Samples represented by two bars with different colors stand for experiments displaying two slopes in the YBCO (005) intensity evolution of Fig. 5.21; the two slopes originate from the crossing of T_e during growth, due to the temperature drop upon the pressure jump.*

5.3.3 Cu-route: tuning growth parameters

Phase diagram exploration

Figs. 5.24 and 5.25 show the influence of the final temperature and oxygen partial pressure after growth from P-route for 2-3 and 3-7 solution composition, respectively. The X-ray diffraction analysis of the grown films shows that in both cases, final high P_{O2} (>10^{-3} bar) and low temperatures (700-800°C) support the nucleation of a/b grains. Conversely, the consequence of increasing P_{O2} and temperatures (840-850°C) is the nucleation of secondary phases, even epitaxial, such as the yttrium cuprate $Y_2Cu_2O_5$ and other mixed barium cuprates which were harder to identify and are labelled as *. Intermediate regions where these effects are reduced include P_{O2} of 10^{-4} to 10^{-3} bar at ~ 820-830°C. This corresponds to the nucleation of YBCO very close to the instability line (T_{ins}), where the driving force for nucleation is smaller (thus, the supersaturation is small), and a better nucleation control is achieved. Overall, the X-ray results show that epitaxial YBCO can be obtained in a relatively wide region, where the YBCO random nucleation is kept low and the main non-desired nucleation come from a/b grains. This region is depicted in Fig. 5.26.

Generally, secondary phases of unreacted barium cuprates, such as $BaCuO_{2+x}$ phases coming from the liquid, are more abundant in the 2-3 melt, Fig. 5.24, than the 3-7 melt; conversely, $Y_2Cu_2O_5$ is more significant in 3-7 composition (Fig. 5.25) due to the copper excess with respect to the 2-3 composition. Comparisons are made with respect to the YBCO(005) intensity.

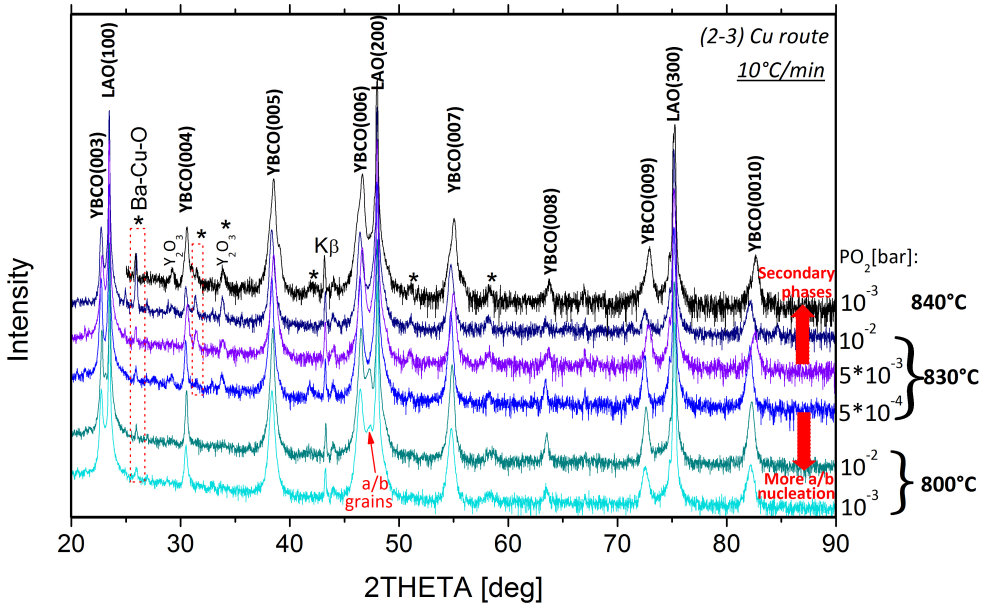

Fig. 5.24: XRD analysis of 2-3 YBCO films in Cu route. *Final growth temperatures and P_{O2} are indicated. At lower temperatures and higher P_{O2}, a/b nucleation is favored; conversely, at high temperatures and pressures, secondary phases appear, consisting of Y_2O_3 and Ba-Cu-O oxides not fully identified (thus labelled with *). High-resolution XRD analysis.*

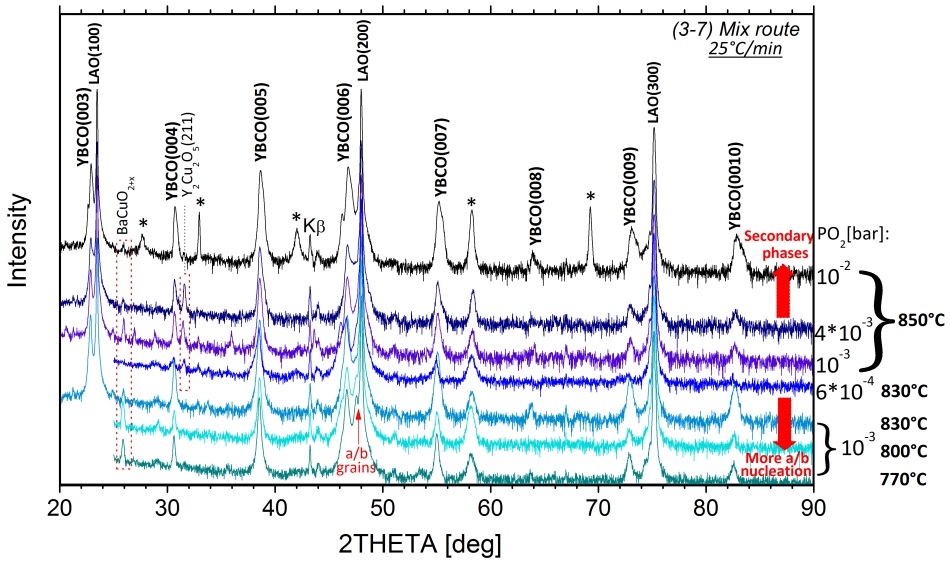

Fig. 5.25: XRD analysis of 2-3 YBCO films in Cu route. *Final growth temperatures and P_{O2} are indicated. At lower temperatures and higher P_{O2}, a/b nucleation is favored; conversely, at high temperatures and pressures, secondary phases appear; in particular the $Y_2Cu_2O_5$ phase and unknown * phase. High-resolution XRD analysis.*

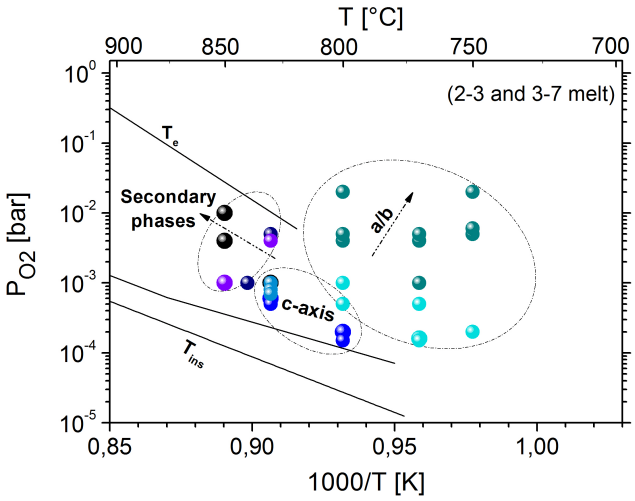

Fig. 5.26: Characteristics of the growth regions for YBCO films in the Cu route. *Samples are grown at slow heating rates (10-25°C/min) and they are relative to the XRD scans of Figs. 5.24 and 5.25. The regions of a/b nucleation, c-axis and secondary phase nucleation are shown. The different colors correspond to the XRD scans of Figs. 5.24 and 5.25.*

Plotting the critical current density, J_c, as a function of these parameters (P_{O2} and T, Fig. 5.27) reveals the best conditions for the superconducting properties to arise at 830°C and approximately $5 \cdot 10^{-4}$ - 10^{-3} bar in P_{O2}, in agreement with the XRD scan results. Overall, the highest J_c are achieved close to the YBCO instability line. The 3-7 melt deliver better critical current density values than the 2-3 melt, in agreement with the lower supersaturation conditions.

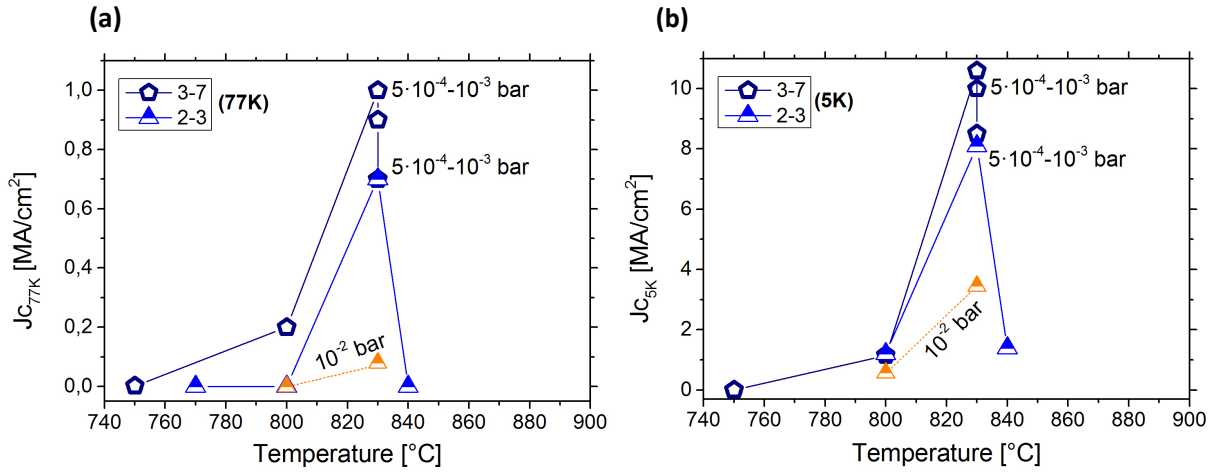

Fig. 5.27: Effect of the phase diagram region on the critical current density (J_c) values. *J_c values at **(a)** 77K and **(b)** 5K of 1-layer YBCO films as a function of final temperature and oxygen pressure of the growth heat treatment (at 1200°C/min to 600°C, then 25°C/min).*

Correlations between the rocking curves of the YBCO (005) reflection and the phase diagram region in terms of pressure and temperature (Fig. 5.28) are instead rather scattered.

Good texture, represented by low values of the FWHM of the rocking curves, is achieved throughout the region shown in Fig. 5.28, meaning that the J_c decrease has to be ascribed to other reasons.

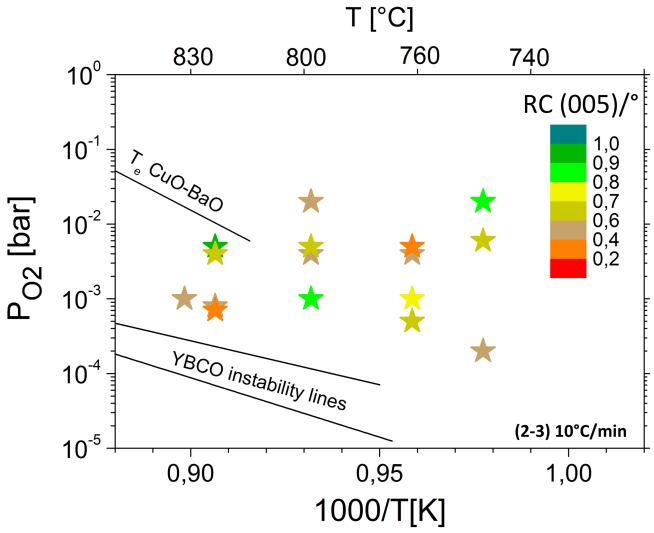

Fig. 5.28: Effect of the phase diagram region on YBCO rocking curves. *FWHM values from the XRD rocking curves relative to the YBCO (005) reflection are reported, for 2-3 composition samples grown in Cu route with slow heating rates.*

Solution composition: 2-3 versus 3-7 melt

Some conclusions will be now drawn from the comparison of samples grown from the 2-3 and the 3-7 melt.

In terms of morphology (see the SEM images in Fig. 5.29a,b), both 2-3 and 3-7 compositions show the presence of unreacted Ba-Cu-O phases in the grown film, next to CuO grains; in fact, the presence of CuO grains (shown by the grazing incidence scan in Fig. 5.29c) in the final YBCO film is expected for the 3BaO-7CuO composition since there is an initial excess of copper (Y/Ba/Cu=1/2/4.66) with respect to the YBCO stoichiometry.

Nevertheless, the 2-3 composition leads to more polycrystalline YBCO (Fig. 5.29a) and more unreacted barium cuprate phases than the 3-7 composition, as shown by the grazing incidence XRD scan in Fig. 5.29c. The reasons for the presence of unreacted phases will be discussed in the next section.

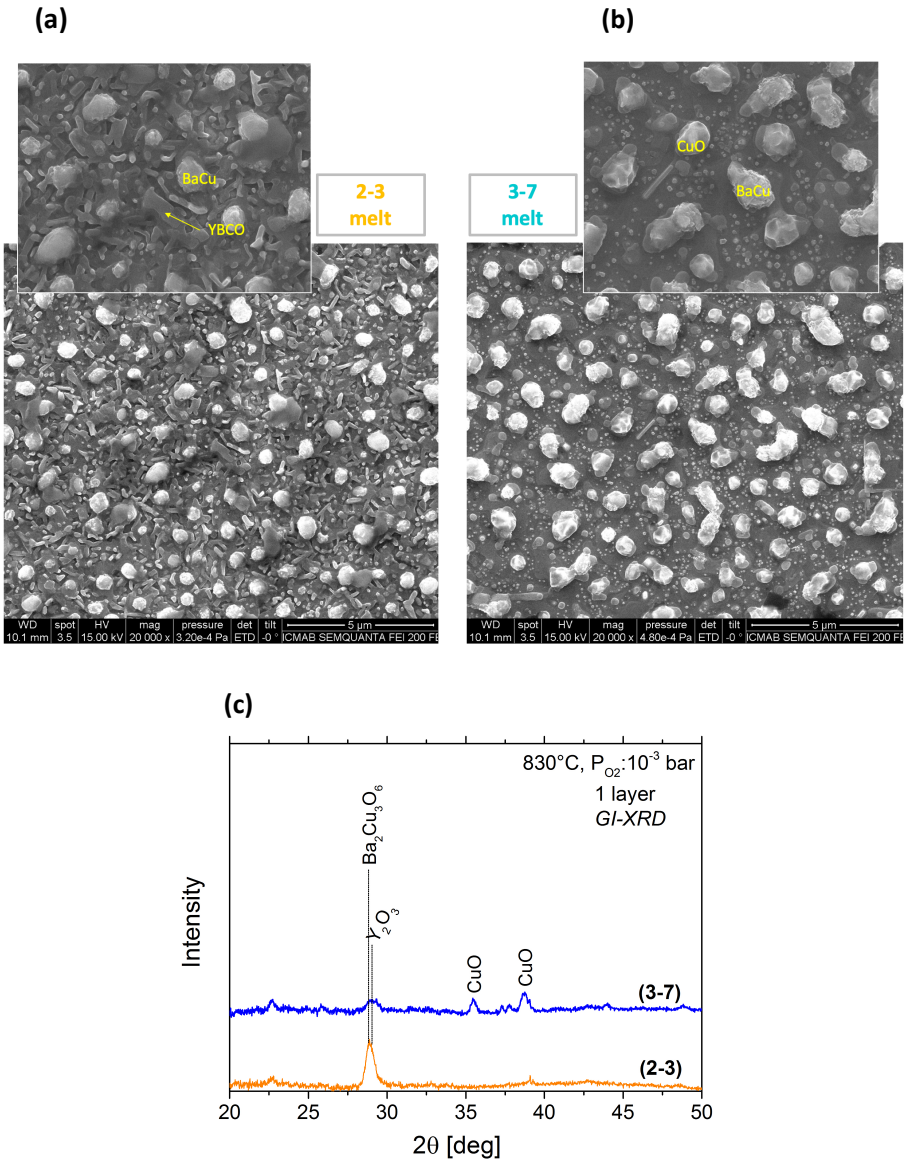

Fig. 5.29: Effect of supersaturation in films from the Cu route. *Comparison of the surface as shown by SEM measurements of two YBCO samples grown in the same conditions but with* ***(a)*** *2-3 melt and* ***(b)*** *3-7 melt. The 3-7 composition leads to less random nucleation.* ***(c)*** *corresponding grazing incidence (GI-XRD) scans, showing the presence of less unreacted precursors for 3-7 composition; note that the CuO reflections are expected in the grown samples with 3-7 composition due to the initial copper excess.*

Rocking curves of the YBCO (005) reflections in Cu route are generally significantly better for 2-3 composition than 3-7, as depicted in Fig. 5.30; despite that, the 3-7 melt delivered higher J_c, as shown previously in Fig. 5.27, for rocking values below 1°. However, a wide working window in terms of epitaxy can be achieved with both compositions, even for 2-3 composition (with J_c>0.1 at 77K) in the case of the Cu route, where the base pressure (both P_{TOT} and P_{O2}) is much lower than 10^{-5} bar. Conversely, from base pressure of $P_{O2}=10^{-5}$ bar, as the case of the $BaCu_2O_2$ route (analyzed in L. Soler's thesis, [155]) only 3-7 composition leads to epitaxial growth.

This last feature was explained by the fact that in the eutectic composition (3-7 melt) supersaturation is lower than in the stoichiometric (2-3) melt; in fact 3-7 compositions is tipically expected to lead to slighly less a/b grains and thus higher J_c than the 2-3 melt.

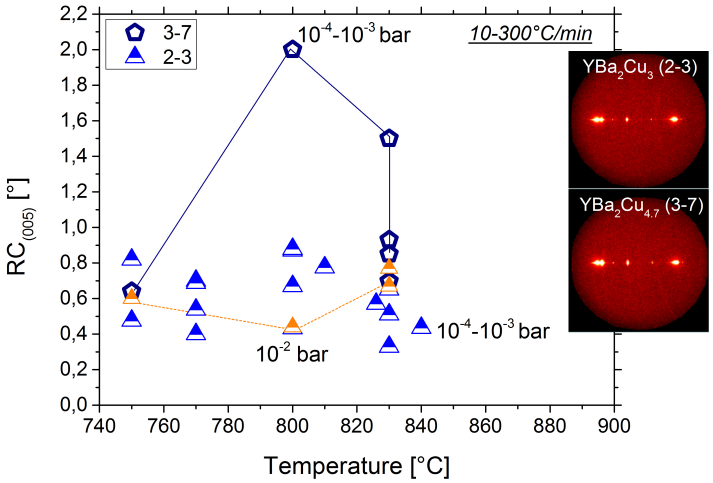

Fig. 5.30: Rocking curves analysis of YBCO films from 2-3 and 3-7 melts. *FWHM values from the rocking curves relative to the YBCO (005) reflection are shown as a function of the growth temperature, at different heating rates. All in all, 2-3 composition exhibits smaller RC values than 3-7. GADDS XRD images refer to samples at 830°C.*

Heating rate effect

One of the main challenges of the pressure routes is to avoid phase coarsening during the heating ramp at low pressure; in particular, in the presence of metallic copper, phase segregation is promoted by the fact that barium cuprate phases cannot be formed. As the CuO is reduced to first Cu_2O and then to metallic copper at relatively low temperatures, from ~ 400°C (see again Fig. 5.6), grain coarsening is favored. With the Debye-Sherrer formula (with upper sensitivity limit at ~150-200 nm) it has been possible to calculate typical grain sizes from in-situ XRD experiments, and the results are reported in Fig. 5.31: Cu_2O grain size increases from 15 to 50 nm before being completely converted to Cu, while Cu continues coarsening up to 80-100 nm.

If we compare the effect of the heating ramp at a fixed temperature (Fig. 5.31) in samples of 3-7 composition, for both Cu and Cu_2O, slower ramps correspond to more significant coarsening. In the case of metallic copper (bottom graph of Fig. 5.31), the 2-3 composition (filled circles) seems to induce less coarsening with respect to the 3-7 composition (filled star symbols), probably because of the less Cu amount.

However, independently of the ramp, the strong linear correlation between the temperature and the grain size is evident in Fig. 5.31, with the grain size increasing with increasing temperature. Thus, even fast ramps (>200°C/min) deliver huge metallic copper grains (superior to 60nm) at optimal growth temperatures. In conclusion, the Cu/Cu_2O grain size was found to depend on both the heating rate (decreasing with faster heating rates), and the temperature at which they are formed.

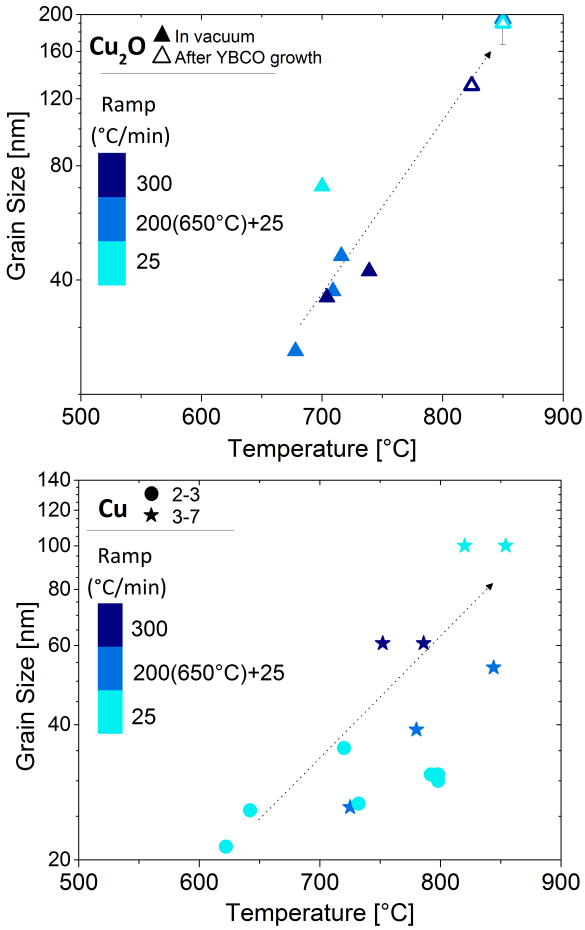

***Fig. 5.31**:* Effect of the heating rate on copper coarsening. *Cu_2O (top graph, from 3-7 composition) and Cu (bottom) particle size obtained applying the Debye-Sherrer formula to the in-situ XRD scans. Three different heating rates are shown: 25°C/min, 300°C/min and a mixed ramp where the film is heated up at 200°C/min before 650°C, and at 25°C/min after. Phase coarsening depends on both temperature and heating profile, and it is minor for 2-3 than 3-7 composition.*

The previous XRD analysis of the coarsening process from the in-situ experiments will now be complemented with the TEM analysis before the pressure jump (Fig. 5.32) and after growth (Fig.5.33) for samples grown in our laboratory conditions. Similar ramps are analyzed except for the case of the mixed ramp, which was slower in Fig. 5.31 due to the setup limitations of the in-situ experiments.

Specifically, Fig. 5.32 shows a cross section TEM image under the effect of a slow ramp, a mixed ramp and a fast ramp during the vacuum step (P_{O2}~10^{-8} bar), before the pressure jump. With slow ramps (25°C/min), big Cu blocks can be observed with size between 100-200 nm at 830°C, distributed throughout the film thickness. With faster ramps (300°C/min) slightly smaller (100-150 nm) metallic copper blocks appear, but still large, and they are mostly accumulated at the film surface. Sometimes also at the substrate interphase smaller grains are found. Much faster initial heating rates (1200°C/min) as in the case of the mixed ramp (Fig. 5.32, center image) reduce coarsening, keeping grain size below 80 nm, while the Cu grains remain more homogeneously distributed throughout the film thickness.

Although more detailed studies should be carried out at these fast heating ramps, since TEM images are representative of small areas of the sample, some conclusions can be derived from these first analyses.

As already shown in Fig. 5.31 from the XRD analysis, also the TEM images indicate that the heating ramp affects the grain size; very fast initial ramps before 600°C (1200°C/min) deliver the smallest Cu grain size, less than 100 nm (Fig. 5.32). Slow ramps, at 300°C/min, deliver ~100 nm grains, while even slower ramps, at 25°C/min, deliver the biggest grains, up to ~200 nm.

However, the TEM images may suggest the presence of another effect, where the heating ramp seems to have a significant influence on the grain distribution in the film and not only on their size. In fact, fast heating ramps after 600°C (300°C/min ramp, Fig. 5.32 left) seem to deliver important phase segregation (of Cu and BaO phases, see also Fig. 5.34a). Slower heating ramps after 600°C (Fig. 5.32 center and right image) deliver more homogenous phase distribution in the film. The importance of this effect requires however further confirmation.

In fact, to better understand the effect of the heating rate, SEM images of the grown samples after the pressure jump are also reported in Fig. 5.33 for comparison.

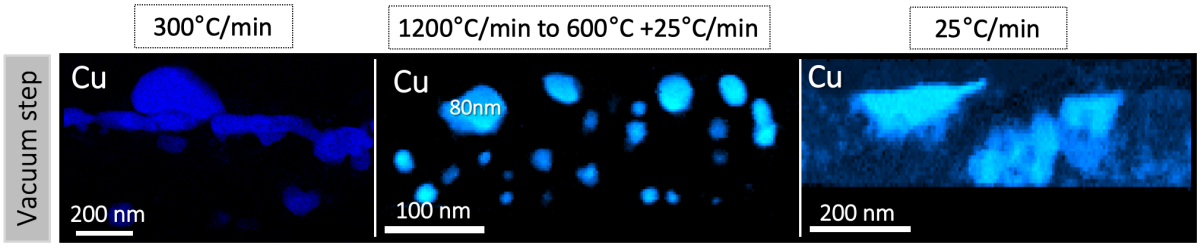

Fig. 5.32: Effect of the heating rate on the Cu route, vacuum step. *TEM with EELS maps for 2 layers with 3-7 composition quenched at P_{O2}~10^{-8} bar, 830°C . From left to right: slow ramps (25°C/min) cause phase coarsening of CuO/Cu grains. Fast ramps (300°C/min) cause the metallic copper grains to float to the film surface, accumulating mostly on the top with final grain size ~200 nm. Conversely, intermediate mixed ramps (center image) reduce coarsening while keeping the Cu grains more homogeneously distributed throughout the film thickness.*

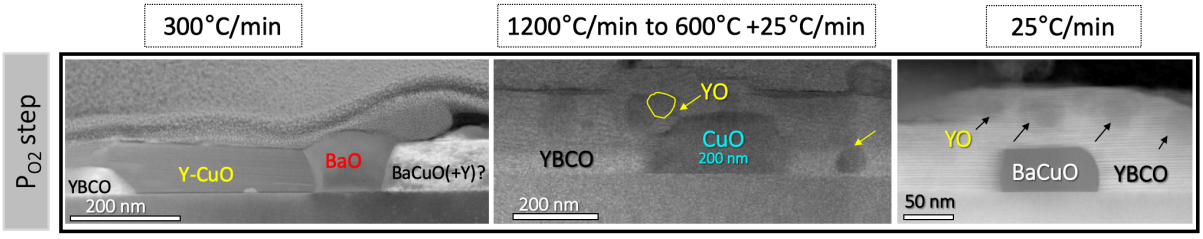

Fig. 5.33: Effect of the heating rate on the Cu route, YBCO growth step. *TEM of representative YBCO samples grown in Cu route in the same region of the phase diagram (830°C, P_{O2}~10^{-3} bar) as a function of the heating rate. Samples grown with slow ramps show some YO nanoparticles and Ba-CuO secondary phase grains; the Cu grain distribution generated at fast ramps in the vacuum step, cause more phase segregation in the growth step, generating large YBCO, BaO and Y-Cu-O blocks.*

The TEM images in Fig. 5.33 are relative to the final YBCO film grown with the previous ramps and the same final conditions (830°C, P_{O2}~10^{-3} bar). As it can be seen, the 300°C/min ramp induces huge percolation problems in the YBCO film in the form of large yttrium cuprate phases and BaO (more details in Fig. 5.34b), which becomes $BaCO_3$ when exposed to atmospheric air. These phases are most likely formed as a consequence of the fact that, as previously shown (Figs. 5.32 and 5.34a), before the pressure jump the precursor phases are strongly segregated, unavailable to homogeneously react to YBCO.

Although not clear yet, we may think that the presence of large BaO blocks is a sign that the effect of fast heating rates after 600°C (the region of $BaCO_3$ decomposition) is linked to $BaCO_3$. In fact, with 300°C/min-ramps, Cu coarsening decreases but $BaCO_3$ decomposition shifts to high temperature (~800°C, shown previously in Fig. 5.13) when compared to ramps of 25°C/min. The survival of $BaCO_3$ to higher temperatures (800°C versus 700°C) may cause it to coarsen due to the temperature activation, explaining the phase segregation of BaO and Cu grains. Conversely, if the heating ramp is 25°C/min, $BaCO_3$ disappears before reaching 800°C where it can coarsen, but then coarsening of metallic copper takes place .

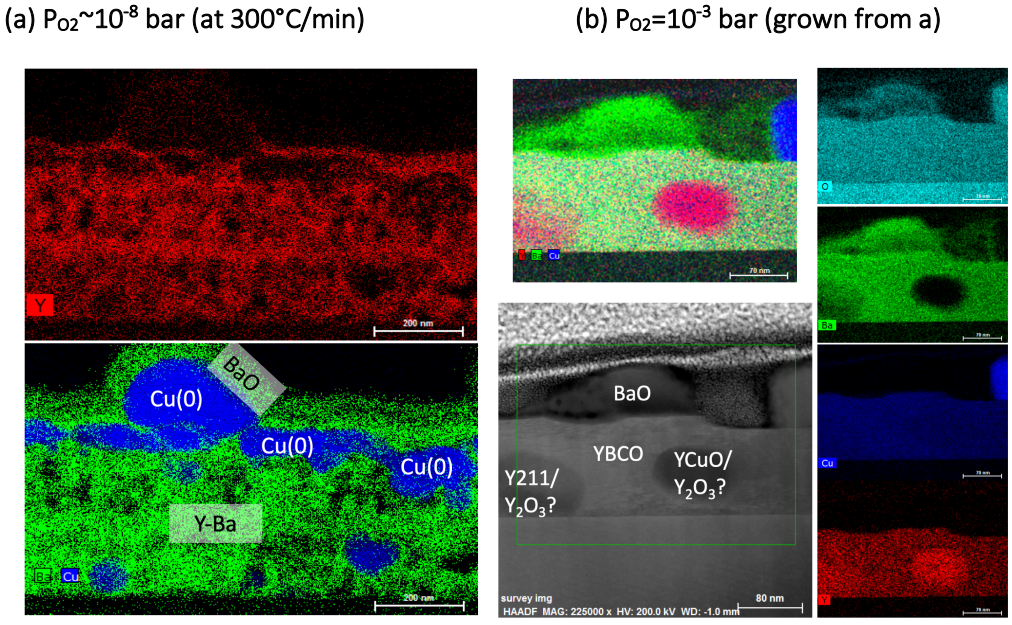

Fig. 5.34: Structure of YBCO films from the Cu route at fast ramps. *EELS maps from TEM measurements of films heated at 300°C/min with 3-7 composition:* ***(a)*** *the step at low* P_{O2} *before YBCO growth and* ***(b)*** *after the pressure jump indicated at the top.*

In fact, with slower ramps after 600°C, a more continuous YBCO film can be grown (Fig. 5.33, center and right); however, small (~30-50 nm) particles mostly made up of Y_2O_3 are always observed in the YBCO matrix, along with 100-nm barium cuprate phases and CuO blocks coming from the Cu coarsening in the vacuum step.

A TEM example of a sample grown with slow heating ramp is reported in Fig. 5.35, where the EELS maps clearly shows the presence of Y-rich regions corresponding majorly to Y_2O_3 particles. Finally, the GADDS-XRD scans show quite epitaxial samples for all heating ramps, Fig. 5.36, and even in 2-3 composition (not shown).

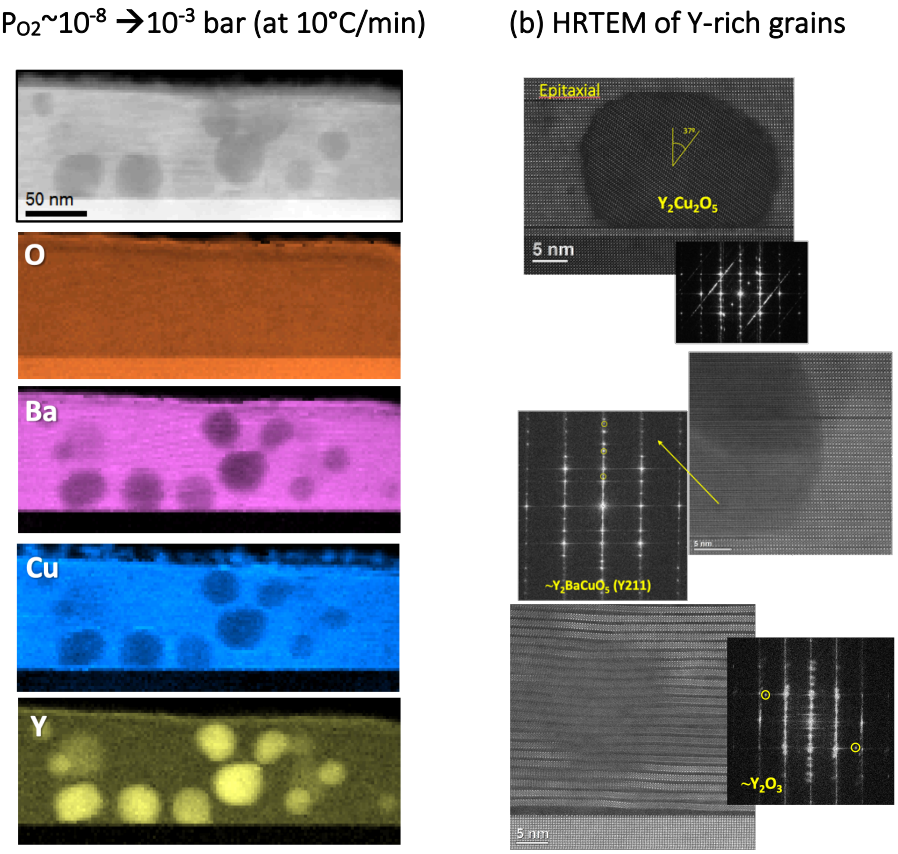

***Fig. 5.35**: Structure of YBCO films from the Cu route at slow heating rates. **(a)** TEM with EELS maps showing the presence of Y-rich regions in the YBCO matrix grown at 830°C at 10°C/min (2-3 composition); **(b)** High-resolution TEM of some Y-rich regions from different samples, with Y_2O_3 particles making up for the majority of these regions.*

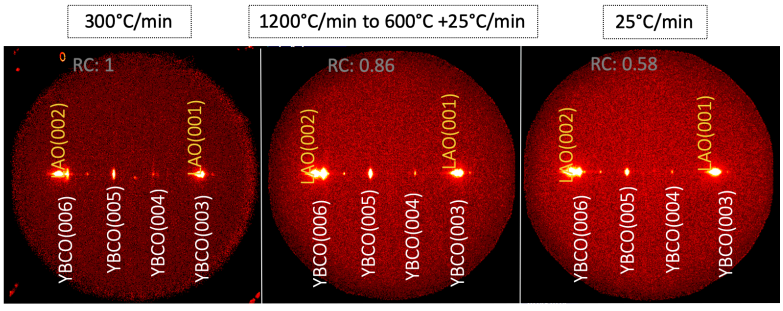

Fig. 5.36: Effect of heating rate on YBCO epitaxy. *The GADDS of 1-layer YBCO films shown in Fig. 5.31, grown from P_{O2}~10^{-8} bar in 3-7 composition, show that a good degree of epitaxy is maintained even changing heating rate. Although all samples are quite epitaxial in the same final conditions (830°C, P_{O2}~10^{-3} bar), their microstructure is quite different.*

The superconducting properties also follow a similar tendency under the effect of changing the heating rate; the trend can be easily visualized in Fig. 5.37, which compares samples grown in the same final conditions in the best region of the phase diagram previously discussed (830°C, P_{O2}: 10^{-4}-10^{-3} bar).

Intermediate ramps with a mixed heating profile (1200°C/min to 600°C and then 25°C/min to the final T) seem to yield the best results, with 1 M/cm² of J_c at 77K for ~200 nm film. In agreement with the TEM analysis, it may be ascribed to the fact that, ultra fast heating (1200°C/min) in the low-temperature region before $BaCO_3$ decomposition starts (600°C) prevent copper oxide phases from coarsening; as the ramp slows down to 25°C/min when $BaCO_3$ starts to decompose, the drastic segregation observed by TEM (at 300°C/min) is avoided. Heating ramps as fast as 300°C/min deliver very low J_c both at 5 and 77K, for 1 and 2 layers. Additionally, when fast ramps are adopted, the degree of epitaxy is compromised probably as a consequence of the strong phase segregation that can change the local liquid composition and thus the supersaturation: more a/b grains are observed (although harder to spot by XRD) by SEM (image in Fig. 5.38), along with Ba-Cu-O secondary phases.

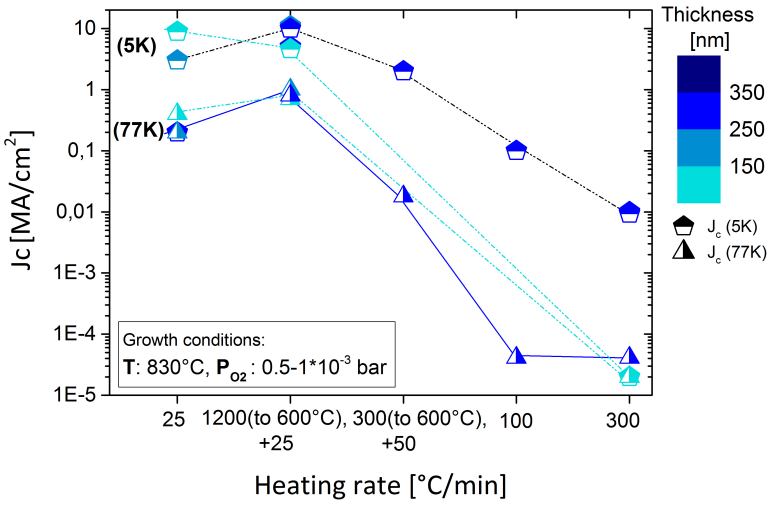

Fig. 5.37: Effect of the temperature profile on J_c. *YBCO films grown in Cu route at 830°C and final P_{O2} between 0.5-1 mbar. Films ≤150nm correspond to 1 layer in 2-3 composition, while films thicker than 150nm correspond to 1 and 2 layers of 3-7 composition.*

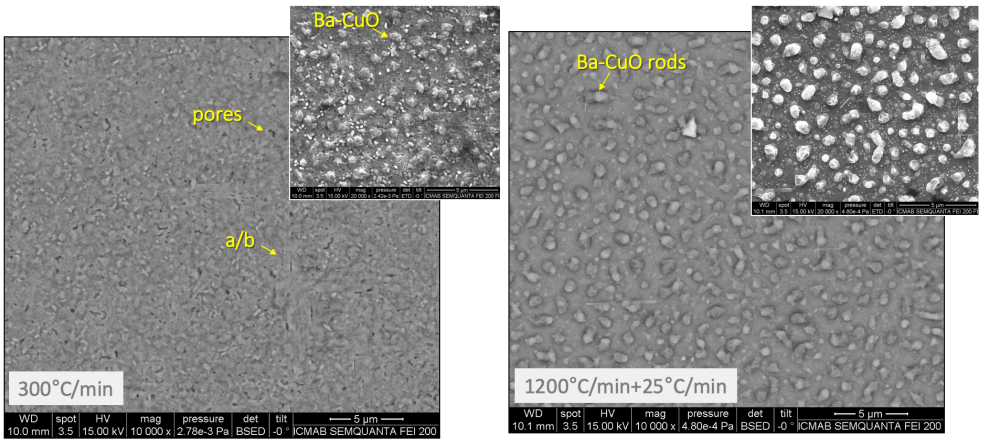

Fig. 5.38: Effect of the heating rate on the film morphology. The *SEM analysis of two YBCO samples (~200 nm) from 3-7 composition grown in Cu route shows that that fast ramps are responsible for more unreacted barium cuprate phases and a/b grains.*

5.3.4 Microstructure and properties

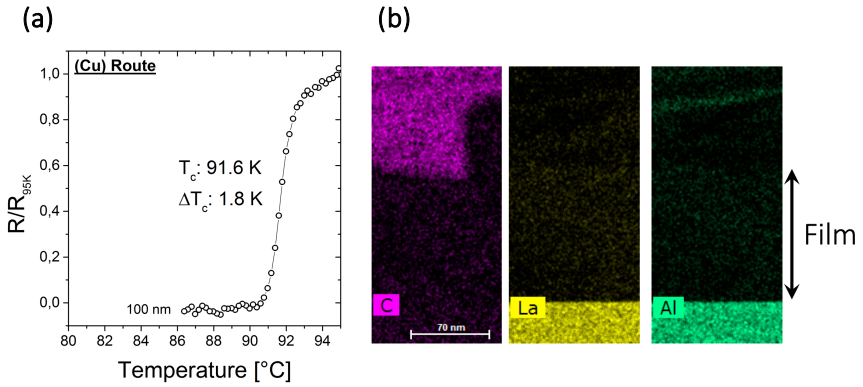

***Fig. 5.39**:* Properties of YBCO films from the Cu route. ***(a)** Resistivity evolution over temperature for a 2-3 composition YBCO film from transport measurements; **(b)** TEM EELS maps of a film grown on LAO, showing no contamination of the film upon substrate reaction with the eutectic melt; additionally, no carbon is detected after $BaCO_3$ decomposition.*

Overall, good critical temperatures (T_c) were obtained in Cu route with sharp resistivity drops, Fig. 5.39a, inferior to 2K (ΔT_c). This is in agreement with the TEM image of Fig. 5.39b, that shows that no carbon retained can be observed by TEM in the grown films, despite the initial presence of $BaCO_3$ due to the use of F-F precursors. In addition, even though the eutectic liquid is quite corrosive, no substrate reactivity was observed in this route, Fig. 5.39b. The values of Tc (>91K) were optimal for the samples anlyzed.

In terms of microstructural defects, intergrowths of the Y-248 phase ($Y_2Ba_4Cu_8O_x$) were observed in the Y-123 phase for both 2-3 and 3-7 melts, and they are shown in Fig. 5.40a: they consist of double CuO chains that appear as stacking faults. Films grown in Cu route with 2-3 composition, Fig. 5.40b, seem to have a better in-field behavior than the 3-7 composition.

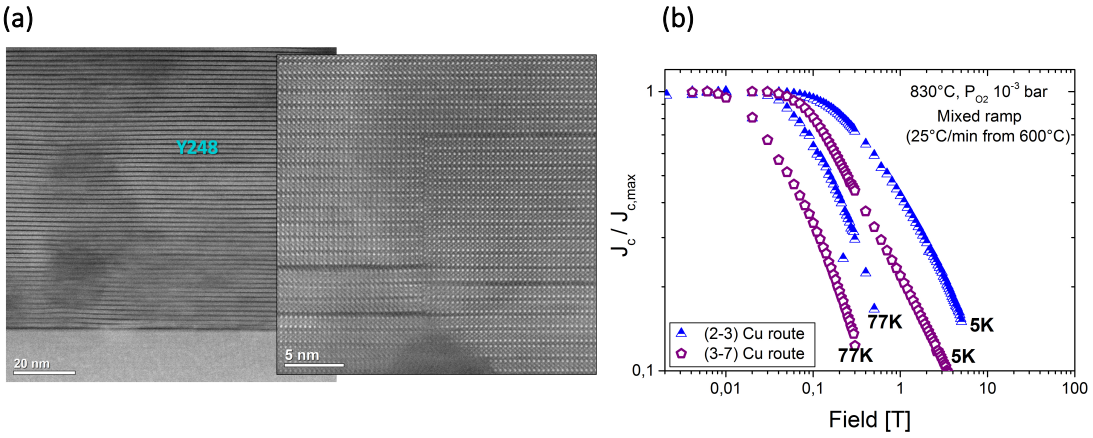

***Fig. 5.40**:* Microstructure and in-field properties of YBCO films from the Cu route. ***(a)** HRTEM characterization of the YBCO matrix showing the presence of Y-248 as stacking faults; **(b)** J_c decrease as a function of the magnetic field, for samples with J_c (at 77K) of 1 MA/cm^2 (3-7 composition) and 0.7 MA/cm^2 (2-3 composition).*

5.3.5 Alternative routes and outlooks

Overall, in terms of current percolation, large blocks of CuO, barium cuprates and yttria grains observed by TEM and GIXRD represent the main cause of the low current percolation. As alternative strategies, mixed routes were tested with the 3-7 melt to reduce the phase segregation problem present at slow heating rates in the form of large CuO grains which originate from the Cu(0) blocks.

In particular, one strategy was to increase the P_{O2} from 10^{-8} to 10^{-5} bar in order to convert Cu(0) to $BaCu_2O_2$, before letting YBCO grow, in order to force the dissolution of the large Cu grains. A quenched sample in the intermediate pressure region (10^{-5} bar) confirms that Cu conversion to $BaCu_2O_2$ took place (XRD scan in Fig. 5.41a), and that growth of YBCO from this phase still permits to reach epitaxial conditions (GADDS scans in Fig. 5.42). Therefore, the XRD analysis confirmed that a mixed route is viable, but further tuning of temperature, pressure and dwell times are necessary to find the optimal J_c conditions.

In fact, the first tests also reveal the presence of important phase segregation after conversion of Cu to $BaCu_2O_2$ (Fig. 5.41b), particularly in the form of large Y_2O_3 grains, up to 200 nm in a $BaCu_2O_2$ matrix. Since the dwell time of these first samples at $P_{O2}=10^{-5}$ bar ranged from 10 to 40 minutes, a strong phase coarsening is easy to occur. Although the YBCO growth from this sample by a further P_{O2} increase still permits to reach epitaxial nucleation, the superconducting properties are inferior in terms of J_c when compared to a sample grown in the same conditions but from the Cu route (SQUID in inset of Fig. 5.42). In fact, the X-ray analysis in grazing incidence, Fig 5.42, reveals the presence of unreacted yttria and barium cuprate phases. Since the previously shown in-situ experiments (Figs 5.6b and 5.19b) proved that only a few seconds are necessary to achieve full Cu oxidation to $BaCu_2O_2$, in the future the mixed route should be tested with shorter dwell times and in appropriate furnaces that permit multiple fast pressure changes.

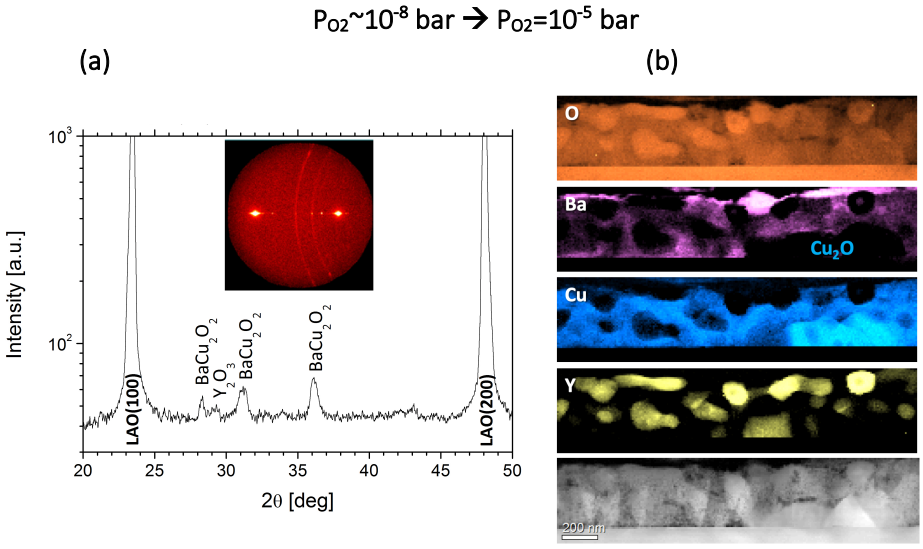

***Fig. 5.41**:* The Cu-$BaCu_2O_2$ mixed route. ***(a)** XRD analysis of a 3-7 composition quenched sample after 40-minute dwell at $P_{O2}=10^{-5}$ bar and 830°C from the Cu route at slow heating ramps (25°C/min). The XRD scan confirms the presence of the expected $BaCu_2O_2$ phase and Y_2O_3.* ***(b)** corresponding TEM with IEELS maps.*

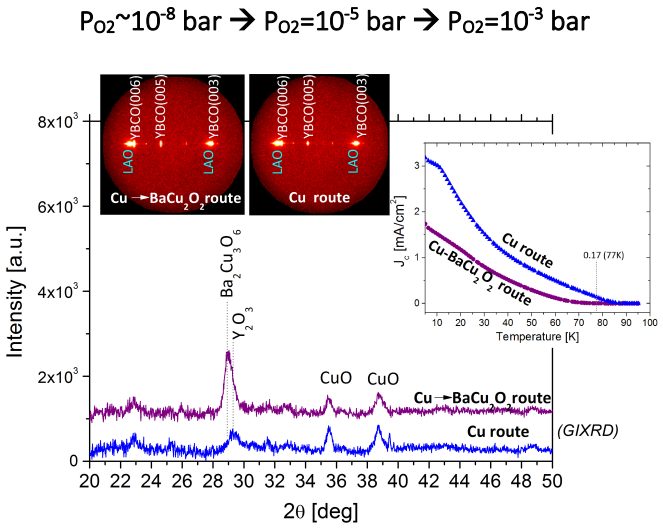

Fig. 5.42: The mixed route, YBCO growth step. *Comparison of 3-7 composition films grown with slow ramps (25°C/min) with the mixed approach shown in Fig. 5.41 and with the Cu route, analyzed by GIXRD and by (inset) SQUID. Growth conditions are 830°C and P_{O2}~10^{-3} bar. Although the samples are both epitaxial, percolation problems are still present.*

In the future, promising approaches might rely on mixed routes and on the $BaCu_2O_2$ route; in particular, in the latter, less phase segregation takes place since metallic copper is not formed, which is responsible for forcing Ba and Cu precursors to crystallize into separate phases. In fact, with the $BaCu_2O_2$ route, so far optimized for base pressures of P_{O2}=10^{-5} bar, J_c values superior to 1 MA/cm² (up to 5 MA/cm² for 90 nm films) have already been obtained with slow heating rates (see L. Soler's thesis, [155]). Conversely, one of the benefits in the use of low total pressures, such as those of the Cu route, is the easier $BaCO_3$ decomposition. Hence, as a possible solution to the segregation problem of the Cu route, the advantages of low P_{TOT} conditions should be combined with those of the $BaCu_2O_2$ route, by testing this route at lower total pressures (i.e. 10^{-6} bar) and under the effect of different temperature profiles.

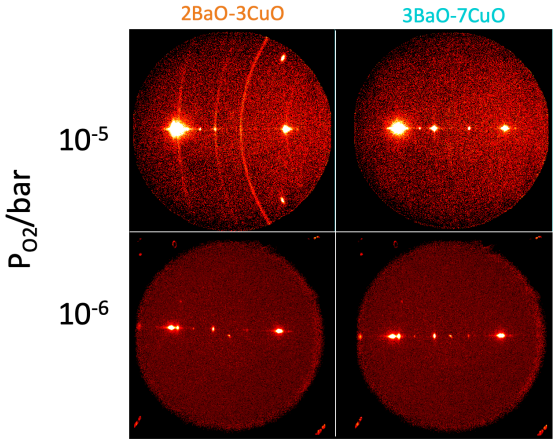

Fig. 5.43: Effect of the base P_{O2} in YBCO films from P route. The *GADDS analysis is relative to 100-200 nm YBCO grown from 2-3 and 3-7 melts at 830°C and P_{O2}=10^{-3}. Top samples are grown from $BaCu_2O_2$ route with base P_{O2}=10^{-5} bar (reproduced from L. Soler's thesis* [155]*) and bottom samples with base P_{O2}=10^{-6} bar (from the current thesis).*

In fact, the final film properties may depend not only on the route, but also on the specific route base pressure. For example, the GADDS images of Fig. 5.43 illustrate that, when the base pressure is as high as $P_{O2}=10^{-5}$ bar, solution stoichiometry has an important role in tuning supersaturation, which in turn controls the epitaxial growth; at this P_{O2}, optimum layers were obtained with the 3-7 composition, while the 2-3 melt had strong difficulties in reaching epitaxial conditions. However, recent samples grown from $P_{O2}=P_{TOT}=10^{-6}$ bar via the $BaCu_2O_2$ route deliver significantly good epitaxy even for the 2-3 melt. Therefore, also the effect of P_{O2} needs to be understood in the context of the different routes developed, and of future optimization strategies.

5.3.6 Towards thick films and tapes

Finally, the stability of the TLAG approach was also tested in the context of reaching thicker superconducting films and also of growth on metallic tapes. This would give us the full knowledge of the opportunities of this new approach for a practical technology.

Even though further work should be done in order to finely tune the growth conditions for thick films, early tests, reported in Fig. 5.44, already show that the Cu route is promising for achieving epitaxial YBCO in 1-µm layers (Fig. 5.44a). The resistivity measurements, Fig. 5.44b, show a high T_c and rather narrow transition widths for both 2-3 and 3-7 compositions, which suggests that no carbon retain occurs at the film grain boundaries, confirming that $BaCO_3$ can be easily decomposed even in these thick layers, as anticipated in section 5.2.

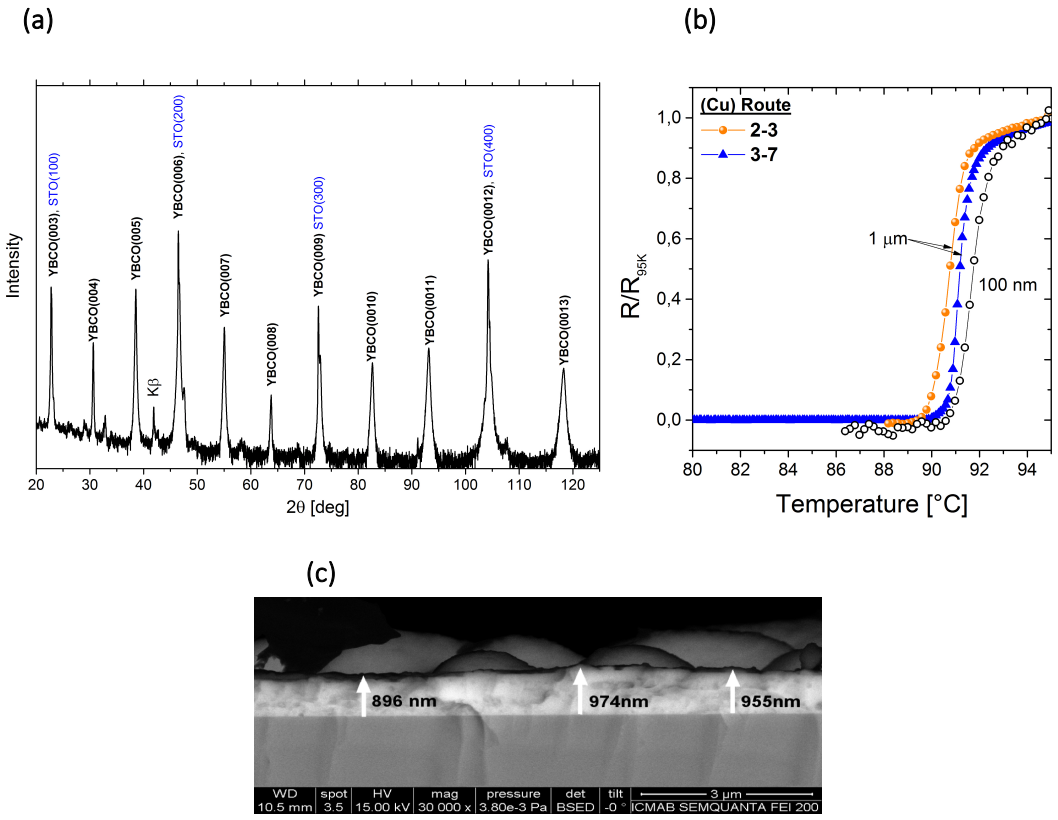

Fig. 5.44: Cu route-*TLAG in thick films: characterizations.* ***(a)*** *High-resolution XRD scan for 1µm YBCO films grown from the Cu route and* ***(b)*** *resistivity measurements for 2-3 and 3-7 compositions of 1 µm films grown in Cu route.* ***(c)*** *SEM cross-section of a thick film with J_c: 0.04 (77K) and 1.1 (5K) MA/cm^2.*

At 5K, J_c values for thick samples grown in Cu route at 830°C and $P_{O2}=10^{-3}$ bar, are just above 1 MA/cm², which means that there is room for improvement. The low superconducting properties are mainly ascribed to unreacted yttria and barium cuprates (such as $Ba_2Cu_3O_6$) generated by the trapped liquid, as shown by the grazing incidence XRD analysis of Fig. 5.45. Therefore, the main issue to face is still the significant need to reduce phase segregation of secondary phases.

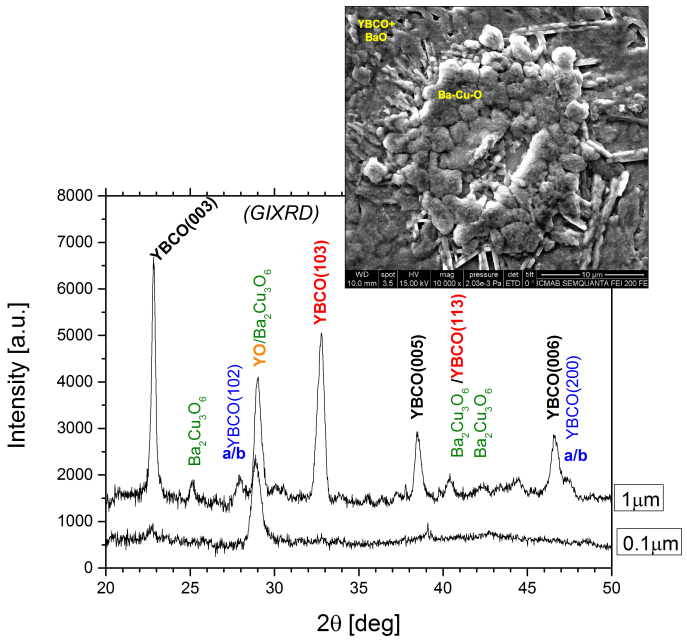

Fig. 5.45: Thin and thick YBCO films from Cu route. *Comparison of GIXRD scans of 100 nm and 1 μm 2-3 composition films grown in Cu route, showing the presence of secondary phases; top: SEM image showing the presence of Barium cuprate areas separated from YBCO regions.*

On the other hand, the Cu route showed also the ability to deliver good epitaxial YBCO samples even on metallic tapes, Fig. 5.46. Tapes from SuNAM Co. were employed, which had the following structure: Hastelloy C276 (100 μm)/Al_2O_3 (40nm)/Y_2O_3 (7nm)/MgO (10nm)/MgO (10nm)/$LaMnO_3$ (20nm), on top of which the superconducting layer is grown.

For samples grown on such tapes, the XRD analysis in Fig. 5.46a shows good c-axis nucleation with the presence of only the (00l) YBCO reflections; the rest of the peaks is ascribed to the tape, with the epitaxial $LaMnO_3$ (labelled LMO in the GADDS), the homo-epi MgO reflections, and the rings of the Hastelloy layer. Good T_c of 90K are also achieved on tape, Fig. 5.46b; the low J_c values, specifically J_c=0.1 MA/cm² (at 77K) and 1.9 MA/cm² (at 5K) confirm that optimization is still necessary on tape.

Given the promises of these first tests, the transfer of TLAG to thick films and tapes is being continued by several PhD candidates of the group.

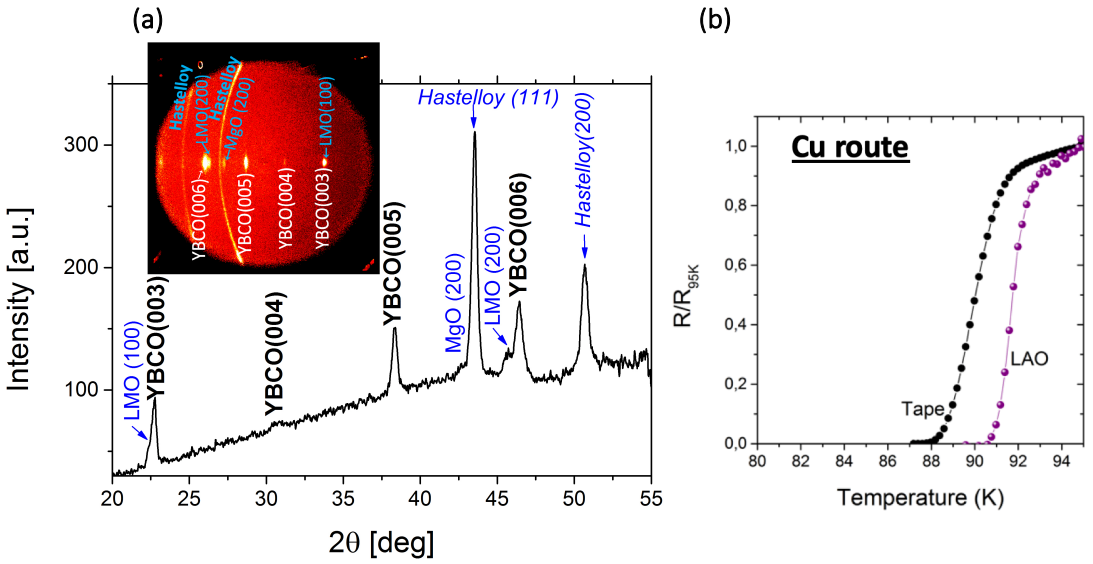

Fig. 5.46: Cu route-TLAG in metallic tapes: characterizations. ***(a)*** *GADDS scan of the 2-3 composition YBCO (100 nm) grown from the Cu route on SuNam tapes, showing the epitaxial $LaMnO_3$ (LMO) buffer layer, the epitaxial MgO layer and the rings assigned to the Hastelloy C276;* ***(b)*** *T_c from resistivity measurements of the sample shown in (a) compared to a sample grown on LAO in similar conditions. J_c : 0.1 (77K) and 1.9 (5K) MA/cm^2.*

5.4 Partial conclusions

In this chapter a new YBCO growth approach was introduced that combines the advantages of cost-effective chemical methods with those of liquid assisted growth. The TLAG novel approach is able to achieve growth rates of 100 nm/s thanks to the presence of a transient eutectic liquid of $BaCuO_2$-CuO composition, originating after the $BaCO_3$ intermediate is decomposed.

Based on weather $BaCO_3$ decomposition and YBCO growth are decoupled or not, two main YBCO growth routes were introduced within TLAG: the T route and the P route. We showed that the fast growth is intrinsic of the transient liquid since it can be obtained in both TLAG routes. However, the parameters influencing the fast growth are yet to be understood, especially in terms of phase diagram region and of the effect of the pressure jump during YBCO growth.

Unlike what previously thought, we demonstrated that $BaCO_3$ can be easily decomposed in this approach; although the main parameter governing its decomposition is the film thickness through which CO_2 out-diffusion occurs, its presence in FF-CSD methodologies does not constitute a limit even up to thick (1 μm) films, making this approach promising for the future optimization of FF-routes. The kinetic analysis confirmed the experimental data for $BaCO_3$ decomposition; in addition, since its theoretical formulation does take into account several parameters such as the presence of a liquid, the kinetic analysis may provide a further indirect proof of the presence of the transient liquid, due to the deviations observed close to the eutectic line.

The specific TLAG method studied in this chapter is based on the pressure route: once $BaCO_3$ decomposition has been achieved after heating up the sample at low oxygen pressure

where YBCO is not stable, a subsequent P_{O2} increase is responsible for the fast YBCO crystallization. Two pressure routes can be adopted which differ in the base P_{O2}. The $BaCu_2O_2$ route consists in heating up the mixture of oxides and carbonate from $P_{O2}=10^{-6}$-10^{-5} bar, while the Cu route from $P_{O2}\sim10^{-8}$ bar. While the 3-7 melt delivers the best results with both approaches thanks to the lower supersaturation, the 2-3 composition seems to be viable at $P_{O2}\leq10^{-6}$ bar.

One of the advantages of the Cu route is that low total pressures permit to overcome the problem of $BaCO_3$ decomposition; conversely, in the $BaCu_2O_2$ the minimum pressure is $P_{TOT}=P_{O2}=10^{-5}/10^{-6}$ bar; Therefore, $BaCO_3$ decomposition in this route is more affected by residual local CO_2, furnace geometry and gas flow.

With chemical methodologies, the final film properties depend strictly on the growth approach. In particular, they have been shown to depend on the temperature profile parameters in the Cu route: very fast ramps cause strong phase segregation along the film; fast ramps have to be adopted only in the low-temperature region before $BaCO_3$ decomposition starts, to reduce phase coarsening. In fact, the main severe drawback to be solved in the Cu route remains the strong phase segregation observed during the low-pressure step, which causes regions of trapped liquid that later on crystallizes into barium cuprate blocks. These large (~100nm) grains interrupt the YBCO matrix, setting the J_c upper limits at 1 MA/cm^2 at 77K.

Despite that, in the conditions of the Cu approach, the TLAG method is rather robust in achieving c-axis epitaxial YBCO in a wide region of the phase diagram and under different supersaturation conditions, film thicknesses and supports. In fact, rather good epitaxial samples could be obtained with both melts on tape and with 1 μm films on metallic substrates, even though the superconducting properties require further optimization in the future.

Future strategies to tackle the Cu route issues may include mixed growth approaches based on the P-routes, with the exploration of lower P_{TOT} ($<10^{-5}$ bar) in the $BaCu_2O_2$ route.

CONCLUSIONS AND PERSPECTIVES

Chapter 6

In conclusions, this thesis showed how advanced thermal analysis (TA) techniques permit to disclose the mechanism underlying film pyrolysis, and that TA are crucial for the development of the necessary knowledge to optimize the pyrolysis and growth steps of complex oxide films.

One of the key aspects is that in most solid-gas reactions, such as decomposition, gas and heat transport in films are different than in powders; in fact, films decompose differently than powders, due to the faster gas diffusion and heat dissipation as the surface to volume ratio increases. It follows that, if this is not acknowledged, many steps can be erroneously thought of as intermediate compounds. Therefore, the information derived from TA on powders is inaccurate and, more important, it can be misleading.

The intensive TA studies carried out on the single salt precursor solutions of FF-YBCO led to the understanding that thermal behavior depends on the nature of the metal cation:

- Those which easily undergo reduction (Cu) will tend to break on the M—OC=O site, while for the others (Ba, Y) the preferred cleavage site will be the MO—C(=O)—O bonds. Thus, in inert atmosphere the first group will release the corresponding acid (propionic acid) while the second class a symmetrical ketone (3-pentanone) through a radical mechanism.
- Humid oxidative atmospheres are better for pyrolysis as they reduce the amount of residual carbon and they shift decomposition to lower temperatures, since hydrolysis and oxidative degradation require lower temperatures to start than radical reactions.
- Humid-oxidative degradation of propionate ligands ranges from soft (with formation of propionic acid in humid O_2 and low temperatures, based on the preferred cleavage at the M—OC=O site) to hard (oxidation to acetaldehyde and CO_2 at higher temperatures, based on the cleavage of the MOC(=O)—C bond). Thus, the low-temperature oxidative degradation will be more effective for the $CuProp_2$-CuO conversion, while the high-temperature one will be preferable for the $YProp_3$-$Y_2O_2CO_3$ and $BaProp_2$-BaC_2O_4 conversion. Behind these intermediates the same general bond-cleavage rule can be applied. It follows that $BaCO_3$ cannot be avoided in favor of an oxide at low temperatures, even in humid atmosphere.
- With the additions of TEA, the decomposition process becomes more robust with respect to a change of atmosphere when the decomposition temperatures of the metal carboxylates are as

low as TEA's; this is a consequence of the fact that decomposition proceeds via an esterification reaction between TEA and the propionate units. Esterification is more important for the Y than the Cu salt, in agreement with their preferred cleavage bonds, while it is almost negligible for the Ba case. Although smoother mass losses are achieved adding TEA, its presence causes an increase (50 to 100°C) in the decomposition temperature range; it also affects the intermediate phases by acting on the copper redox behavior.

The knowledge developed from single-component solutions revealed to be essential to understand the thermal behavior of the ternary solution, although its behavior goes beyond the simple sum of its components. For instance, unexpected interactions were:

- CuO reduction, induced by the decomposition of the other salts;
- $BaCO_3$ crystallization into a non-thermodynamically stable phase (the monoclinic instead of the orthorhombic), which, although not fully understood yet, is probably due to seed-induced crystallization by the other metal species when melting of the barium precursor precedes its decomposition.

The monoclinic $BaCO_3$ phase, in fact, delays $BaCO_3$ decomposition, which in turn has a detrimental effect on the epitaxial conditions for YBCO growth. So far, two main strategies can be adopted to avoid the $BaCO_3$ monoclinic phase:

i) operating in rigorously anhydrous-working conditions, or

ii) using propionate-free precursors (such as acetates)

The first option requires the use of high purity solvents and atmosphere control environments that involve a significant complexity and cost. Conversely, the second strategy is straightforward and cost-competitive, but it requires a new solution design.

Having faced the main pyrolysis issues, the YBCO growth from the pyrolyzed oxides and carbonates was studied; a novel growth approach, TLAG, was introduced which is based on the growth of YBCO from a BaO-CuO transient liquid, generated after $BaCO_3$ decomposition.
The specific TLAG route analyzed in this thesis is the P route, characterized by decoupling $BaCO_3$ decomposition from YBCO growth; depending on the phases involved, two P routes were identified: the $BaCu_2O_2$ and the Cu route, which can be achieved by tuning the base pressure. In P route:

- $BaCO_3$ decomposition can be easily achieved at low total pressures ($<10^{-6}$ bar), where it can be decomposed even in up to 1-μm YBCO films.
- In terms of solution composition, lower supersaturation (i.e. eutectic composition) increases the epitaxy.
- The $BaCu_2O_2$ route (at $P_{O2}=10^{-5}$ bar) gave the best performances with thin films (5MA/cm for 90 nm) but it is more sensitive to residual local CO_2 (and thus flux and total pressure effects) in terms of $BaCO_3$ decomposition; as a consequence, it is more affected by non-anhydrous working conditions.
- Conversely, the Cu route has the disadvantage of a higher phase segregation due to Cu(0), which reduces film performances, but it is especially compatible for $BaCO_3$ decomposition in thick layers thanks to the low base pressure.
- The robustness of TLAG was proved by the fact that epitaxy could be achieved when the process was transferred to thick films (1 μm) and tapes.

Within CSD approaches, the TLAG method is the first reported route to achieve very high growth-rates, 100 times faster than other CSD routes, up to 100 nm/s, being competitive to recent liquid-growth processes by physical methods, while still reaching competitive J_c values with low cost chemical strategies. This puts HTS technology on the frontlines of addressing clean energy production and transportation.

However, the next breakthroughs in CSD methods would be to raise the thickness upper limit of competitive properties to 1-μm or thicker in a single deposition, and to transfer the approach to metallic tapes: one final challenge for CSD methods to lead the market as cost-effective routes for long-length HTS tapes manufacturing and perhaps address fast-increasing world energy demands thanks to the low-cost production.

BIBLIOGRAPHY

[1] R.J. Cava, B. Batlogg, R.B. Van Dover, D.W. Murphy, S. Sunshine, T. Siegrist, J.P. Remeika, E.A. Rietman, S. Zahurak, G.P. Espinosa, Bulk superconductivity at 91 K in single-phase oxygen-deficient perovskite Ba2YCu309-∂, Phys. Rev. Lett. 58 (1987) 1676–1679. doi:10.1103/physrevlett.58.1676.

[2] D.M. de Leeuw, C.A.H.A. Mutsaers, R.A. Steeman, E. Frikkee, H.W. Zandbergen, Crystal structure and electrical conductivity of YBa4Cu3O8.5+∂, Phys. C. 158 (1989) 391–396.

[3] H. Maeda, Y. Yanagisawa, Recent developments in high-temperature superconducting magnet technology (Review), IEEE Trans. Appl. Supercond. 24 (2014) 1–12. doi:10.1109/TASC.2013.2287707.

[4] B. Keimer, S.A. Kivelson, M.R. Norman, S. Uchida, J. Zaanen, From quantum matter to high-temperature superconductivity in copper oxides, Nature. 518 (2014) 179–186. doi:10.1038/nature14165.

[5] V.E. Sytnikov, V.S. Vysotsky, I.P. Radchenko, N. V. Polyakova, 1G versus 2G – comparison from the practical standpoint for HTS power cables use, J. Phys. Conf. Ser. 97 (2008) 012058. doi:10.1088/1742-6596/97/1/012058.

[6] A.P. Malozemoff, Second-generation superconductor wires for the electric power grid, (2012). doi:10.1146/annurev-matsci-100511-100240.

[7] Y. Shiohara, T. Taneda, M. Yoshizumi, Overview of materials and power applications of coated conductors project, Jpn. J. Appl. Phys. 51 (2012) 010007. doi:10.1143/JJAP.51.010007.

[8] X. Obradors, T. Puig, Coated conductors for power applications: materials challenges, Supercond. Sci. Technol. 27 (2014) 44003–44019. doi:10.1088/0953-2048/27/4/044003.

[9] V.L. Ginzburg, On the theory of superconductivity, Nuovo Cim. 2 (1955) 1234–1250. doi:10.1007/bf02731579.

[10] L.D. Landau, D. Ter Haar, Collected papers of L.D. Landau, Pergamon Press, Oxford, 1965.

[11] A.A. Abrikosov, On the magnetic properties of superconductors of the second group, Sov. Phys. JETP. 5 (1957) 1774.

[12] D. Larbalestier, A. Gurevich, D.M. Feldmann, A. Polyanskii, High-Tc superconducting

materials for electric power applications, Nature. 414 (2001) 368–377. doi:doi:10.1038/35104654.

[13] H. Search, C. Journals, A. Contact, M. Iopscience, I.P. Address, The critical current density of grain boundary channels in polycrystalline HTS and LTS superconductors in magnetic fields, 095006 (2013). doi:10.1088/0953-2048/26/9/095006.

[14] R. Feenstra, D.C. Larbalestier, A review of the influence of grain boundary geometry on the electromagnetic properties of polycrystalline YBa2Cu3O7-x films, J. Am. Chem. Soc. 91 (2008) 1869–1882. doi:10.1111/j.1551-2916.2008.02273.x.

[15] S. Graser, P.J. Hirschfeld, T. Kopp, R. Gutser, B.M. Andersen, J. Mannhart, How grain boundaries limit supercurrents in high-temperature superconductors, Nat. Phys. 6 (2010) 609–614. doi:10.1038/nphys1687.

[16] J. Bardeen, L.N. Cooper, J.R. Schrieffer, Theory of superconductivity, Phys. Rev. 108 (1957) 1175–1204. doi:10.1103/physrev.108.1175.

[17] S.S. Oh, H.S. Kim, H.S. Ha, R.K. Ko, D.W. Ha, H. Lee, S.H. Moon, S.I. Yoo, Progress in research and development for REBCO coated conductors by reactive co-evaporation, Prog. Supercond. Cryog. 15 (2013) 1–5. doi:10.9714/psac.2013.15.4.001.

[18] T. Schneller, R. Waser, M. Kosec, D. Payne, eds., Chemical solution deposition of functional oxide thin films, Springer, 2013. doi:10.1007/978-3-211-99311-8.

[19] T. Puig, J.C. Gonzáles, A. Pomar, N. Mestres, O. Castaño, M. Coll, J. Gásquez, F. Sandiumenge, S. Piñol, X. Obradors, The influence of growth conditions on the microstructure and critical currents of TFA-MOD YBa2Cu3O7 films, Supercond. Sci. Technol. 18 (2005) 1141–1150. doi:10.1088/0953-2048/18/8/020.

[20] A. Pomar, J. Gutiérrez, A. Palau, T. Puig, X. Obradors, Porosity induced magnetic granularity in epitaxial YBa2Cu3O7 thin films, Phys. Rev. B. 73 (2006). doi:10.1103/PhysRevB.73.214522.

[21] E. Bartolomé, F. Gömory, X. Granados, T. Puig, X. Obradors, Universal correlation between critical current density and normal-state resistivity in porous YBa2Cu3O7−x thin films, Supercond. Sci. Technol. 20 (2007) 895–899. doi:10.1088/0953-2048/20/10/001.

[22] W. Wu, F. Feng, K. Shi, W. Zhai, T. Qu, R. Huang, X. Tang, X. Wang, J.-C. Grivel, Z. Han, A rapid process of YBa2Cu3O7−δ thin film fabrication using trifluoroacetate metal organic deposition with polyethylene glycol additive, Supercond. Sci. Technol. 26 (2013) 055013. doi:10.1088/0953-2048/26/5/055013.

[23] P. Roura, J. Farjas, H. Eloussi, L. Carreras, S. Ricart, T. Puig, X. Obradors, Thermal analysis of metal organic precursors for functional oxide preparation: Thin films versus powders, Thermochim. Acta. 601 (2015) 1–8. doi:10.1016/j.tca.2014.12.016.

[24] H. Eloussifi, J. Farjas, P. Roura, S. Ricart, T. Puig, X. Obradors, M. Dammak, Thermal decomposition of barium trifluoroacetate thin films, Thermochim. Acta. 556 (2013) 58–62. doi:10.1016/j.tca.2013.01.022.

[25] H. Eloussi, J. Farjas, P. Roura, S. Ricart, T. Puig, X. Obradors, M. Dammak, Thermoanalytical study of the decomposition of yttrium trifluoroacetate thin films, Thin Solid Films. 545

(2013) 200–204. doi:10.1016/j.tsf.2013.07.082.

[26] P. Roura, J. Farjas, S. Ricart, M. Aklalouch, R. Guzman, J. Arbiol, T. Puig, A. Calleja, O. Peña-Rodríguez, M. Garriga, X. Obradors, Synthesis of nanocrystalline ceria thin films by low-temperature thermal decomposition of Ce-propionate, Thin Solid Films. 520 (2012) 1949–1953. doi:10.1016/j.tsf.2011.09.058.

[27] D. Sanchez-rodriguez, J. Farjas, P. Roura, S. Ricart, N. Mestres, X. Obradors, T. Puig, Thermal analysis for low temperature synthesis of oxide thin films from chemical solutions, J. Phys. Chem. C. 117 (2013) 20133–20138. doi:10.1021/jp4049742.

[28] J. Farjas, D. Sanchez-Rodriguez, H. Eloussifi, R.C. Hidalgo, P. Roura, S. Ricart, T. Puig, X. Obradors, Can We Trust on the Thermal Analysis of Metal Organic Powders for thin film preparation?, MRS Proc. 1449 (2012) 13–18. doi:10.1557/opl.2012.919.

[29] R.B. Mos, M. Nasui, T. Petrisor Jr, M.S. Gabor, R. Varga, L. Ciontea, T. Petrisor, Synthesis, crystal structure and thermal decomposition study of a new barium acetato-propionate complex, J. Anal. Appl. Pyrolysis. 92 (2011) 445–449. doi:10.1016/j.jaap.2011.08.007.

[30] Z. Lin, D. Han, S. Li, Study on thermal decomposition of copper(II) acetate monohydrate in air, J. Therm. Anal. Calorim. 107 (2012) 471–475. doi:10.1007/s10973-011-1454-4.

[31] M. Nasui, R.B. Mos, T. Petrisor Jr, M.S. Gabor, R.A. Varga, L. Ciontea, T. Petrisor, Synthesis, crystal structure and thermal decomposition of a new copper propionate [Cu(CH3CH2COO)2]·2H2O, J. Anal. Appl. Pyrolysis. 92 (2011) 439–444. doi:10.1016/j.jaap.2011.08.005.

[32] J. Grivel, Thermal decomposition of yttrium(III) propionate and butyrate, J. Anal. Appl. Pyrolysis. 101 (2013) 185–192. doi:10.1016/j.jaap.2013.01.011.

[33] J. Grivel, Thermal decomposition of lutetium propionate, J. Anal. Appl. Pyrolysis. 89 (2010) 250–254. doi:10.1016/j.jaap.2010.08.011.

[34] J. Grivel, Thermal decomposition of Ln(C2H5CO2)3•H2O (Ln=Ho,Er,Tm and Yb), J. Therm. Anal. Calorim. 109 (2012) 81–88. doi:10.1007/s10973-011-1745-9.

[35] I.A. Martynova, D.M. Tsymbarenko, N.P. Kuz'mina, Yttrium tris propionate monohydrate: synthesis, crystal structure, and thermal stability, Russ. J. Coord. Chem. 40 (2014) 565–570. doi:10.1134/S1070328414080077.

[36] M. Nasui, C. Bogatan (Pop), L. Ciontea, T. Petrisor, Synthesis, crystal structure modeling and thermal decomposition of yttrium propionate [Y2(CH3CH2COO)6·H2O]·3.5H2O, J. Anal. Appl. Pyrolysis. 97 (2012) 88–93. doi:10.1016/j.jaap.2012.05.003.

[37] M. Nasui, T. Petrisor Jr, R.B. Mos, A. Mesaros, R.A. Varga, B.S. Vasile, T. Ristoiu, L. Ciontea, T. Petrisor, Synthesis, crystal structure and thermal decomposition kinetics of yttrium propionate, J. Anal. Appl. Pyrolysis. 106 (2014) 92–98. doi:10.1016/j.jaap.2014.01.004.

[38] L. Ciontea, A. Angrisani, G. Celentano, T. Petrisor jr., A. Rufoloni, A. Vannozzi, A. Augieri, V. Galuzzi, A. Mancini, T. Petrisor, Metal propionate synthesis of epitaxial YBa2Cu3O7-x films, J. Phys. Conf. Ser. 97 (2008) 012302. doi:10.1088/1742-6596/97/1/012302.

[39] D.E. Wesolowski, Y.R. Patta, M.J. Cima, Conversion behavior comparison of TFA-MOD and

non-fluorine solution-deposited YBCO films, Phys. C Supercond. Its Appl. 469 (2009) 766–773. doi:10.1016/j.physc.2009.04.008.

[40] M.S. Akanni, O.B. Ajayi, J.N. Lambi, Pyrolytic decomposition of some even chain length copper(II) carboxylates, J. Therm. Anal. 31 (1986) 131–143. doi:10.1007/bf01913894.

[41] M.S. Akanni, H.D. Burrows, P.B. Begun, Product analysis, reaction mechanism and kinetics of the thermal decomposition of some even chain-length mercury(II) carboxylates, Termochimica Acta. 81 (1984) 45–58. doi:10.1016/0040-6031(84)85109-6.

[42] R. Szczęsny, E. Szlyk, Thermal decomposition of some silver (I) carboxylates under nitrogen atmosphere, J. Therm. Anal. Calorim. 111 (2013) 1325–1330. doi:10.1007/s10973-012-2485-1.

[43] M.S. Akanni, E.K. Okoh, H.D. Burrows, H.A. Ellis, The thermal behaviour of divalent and higher valent metal soaps : a review, Thermochim. Acta. 208 (1992) 1–41. doi:10.1016/0040-6031(92)80150-u.

[44] L.D.S. Mindrale, U.C. Bernard--, Comportement thermique des propionates hydrates de calcium, strontium et baryum, J. Therm. Anal. 12 (1977) 33–42. doi:10.1007/bf01909853.

[45] U. Hwang, H. Park, K. Koo, Behavior of barium acetate and titanium isopropoxide during the formation of crystalline barium titanate, Ind. Eng. Chem. Res. 43 (2004) 728–734. doi:10.1021/ie030276q.

[46] C. Ecjhao, K. Majid, R. Mushtaq, Synthesis, characterization and coordinating behaviour of aminoalcohol complexes with transition metals, E-Journal Chem. 5 (2008) S969–S979. doi:10.1155/2008/680324.

[47] A.A. Naiini, V. Young, J.G. Verkade, G. Hall, New complexes of triethanolamine (TEA): novel structural features of [Y(TEA)2](ClO4)3•3C5H5N and [Cd(TEA)2](NO3)2, Polyhedron. 14 (1995) 393–400. doi:10.1016/0277-5387(95)93020-2.

[48] K.H. Whitmire, J.C. Hutchison, A. Gardberg, C. Edwards, Triethanolamine complexes of copper, Inorganica Chim. Acta. 294 (1999) 153–162. doi:10.1016/s0020-1693(99)00274-1.

[49] B. Kozlevčar, P. Šegedin, Structural analysis of a series of copper(II) coordination compounds and correlation with their magnetic properties, in: Croat. Chem. Acta, 2008: pp. 369–379.

[50] R.M. Escovar, J.H. Thurston, T. Ould-ely, A. Kumar, K.H. Whitmire, Synthesis and characterization of new mono-, di-, and trinuclear copper(II) triethanolamine-carboxylate complexes, Z. Anorg. Allg. Chem. 631 (2005) 2867–2876. doi:10.1002/zaac.200500204.

[51] K.D.B.Æ.P. Lommens, Æ.J.F.Æ.D. Vandeput, I. Van Driessche, Sol-gel chemistry of an aqueous precursor solution for YBCO thin films, J. Sol-Gel Sci. Technol. 52 (2009) 124–133. doi:10.1007/s10971-009-1987-1.

[52] B. Schoofs, D. Van de Vyver, P. Vermeir, J. Schaubroeck, S. Hoste, G. Herman, I. Van Driessche, Characterisation of the sol-gel process in the superconducting NdBa2Cu3O7-y system, J. Mater. Chem. 17 (2007) 1714–1724. doi:10.1039/b614149h.

[53] S.G. De de Ávila, M.A. Logli, J.R. Matos, Kinetic study of the thermal decomposition of monoethanolamine (MEA), diethanolamine (DEA), triethanolamine (TEA) and methyldiethanolamine (MDEA), Int. J. Greenh. Gas Control. 42 (2015) 666–671. doi:10.1016/j.ijggc.2015.10.001.

[54] S.B. Fredriksen, K. Jens, Oxidative degradation of aqueous amine solutions of MEA, AMP, MDEA, Pz: a review, Energy Procedia. 37 (2013) 1770–1777. doi:10.1016/j.egypro.2013.06.053.

[55] I. Zghal, J. Farjas, J. Camps, M. Dammak, P. Roura, Thermogravimetric measurement of the equilibrium vapour pressure : Application to water and triethanolamine, Thermochim. Acta. 665 (2018) 92–101. doi:10.1016/j.tca.2018.05.007.

[56] V.T. Yilmaz, Y. Topcu, A. Karadag, Thermal decomposition of triethanolamine and monoethanolethylenediamine complexes of some transition metal saccharinates, Thermochim. Acta. 383 (2002) 129–135. doi:10.1016/s0040-6031(01)00685-2.

[57] A. Gupta, R. Jagannathan, E.I. Cooper, E.A. Giess, J.I. Landman, B.W. Hussey, Superconducting oxide films with high transition temperature prepared from metal trifluoroacetate precursors, Appl. Phys. Lett. 52 (1998) 2077–2079. doi:10.1063/1.99752.

[58] M. Yoshizumi, I. Seleznev, M.J. Cima, Reactions of oxyfluoride precursors for the preparation of barium yttrium cuprate films, Phys. C Supercond. 403 (2004) 191–199. doi:10.1016/j.physc.2003.12.004.

[59] X. Palmer, C. Pop, H. Eloussi, B. Villarejo, P. Roura, J. Farjas, A. Calleja, A. Palau, X. Obradors, T. Puig, S. Ricart, Solution design for low- fluorine trifluoroacetate route to YBa2Cu3O7 films, Supercond. Sci. Technol. 29 (2016) 024002. doi:10.1088/0953-2048/29/2/024002.

[60] Y. Chen, C. Wu, G. Zhao, C. You, An advanced low-fluorine solution route for fabrication of high-performance YBCO superconducting films, Supercond. Sci. Technol. 25 (2012) 069501. doi:10.1088/0953-2048/25/6/069501.

[61] X. Obradors, T. Puig, S. Ricart, M. Coll, J. Gazquez, A. Palau, X. Granados, Growth, nanostructure and vortex pinning in superconducting YBa2Cu3O7 thin films based on trifluoroacetate solutions, Supercond. Sci. Technol. 25 (2012) 123001. doi:10.1088/0953-2048/25/12/123001.

[62] T. Araki, I. Hirabayashi, Review of a chemical approach to YBa2Cu3O7−x coated superconductors — metalorganic deposition using trifluoroacetates, Supercond. Sci. Technol. 16 (2003) 71–94. doi:10.1088/0953-2048/16/11/r01.

[63] V. Solovyov, I.K. Dimitrov, Q. Li, Growth of thick YBa2Cu3O7 layers via a barium fluoride process, Supercond. Sci. Technol. 26 (2013) 13001–13020. doi:10.1088/0953-2048/26/1/013001.

[64] B.G. Marchionini, Y. Yamada, L. Martini, H. Ohsaki, High-temperature superconductivity: a roadmap for electric power sector applications, 2015–2030, IEEE Trans. Appl. Supercond. 27 (2017) 1–7. doi:10.1109/tasc.2017.2671680.

[65] V. Chepikov, N. Mineev, P. Degtyarenko, S. Lee, V. Petrykin, A. Ovcharov, A. Vasiliev, A. Kaul, V. Amelichev, A. Kamenev, A. Molodyk, S. Samoilenkov, Introduction of BaSnO3 and BaZrO3 artificial pinning centres into 2G HTS wires based on PLD-GdBCO films . Phase I of the

industrial R&D programme at SuperOx, Supercond. Sci. Technol. 30 (2017) 124001–124012. doi:10.1088/1361-6668/aa9412.

[66] O. Stadel, J. Schmidt, G. Wahl, F. Weiss, D. Selbmann, J. Eickemeyer, O.Y. Gorbenko, A.R. Kaul, C. Jimenez, Continuous YBCO deposition by MOCVD for coated conductors, Phys. C Supercond. 372–376 (2002) 751–754. doi:10.1016/s0921-4534(02)00898-5.

[67] N. Chen, S.J. Rothman, J.L. Routbort, K.C. Goretta, Tracer diffusion of Ba and Y in YBa2Cu3Ox, J. Mater. Res. 7 (1992) 2308–2316. doi:10.1557/jmr.1992.2308.

[68] A. Kuršumović, Y.S. Cheng, B.A. Glowacki, J. Madsen, J.E. Evetts, Study of the rate-limiting processes in liquid-phase epitaxy of thick YBaCuO fims, J. Cryst. Growth. 218 (2000) 45–56. doi:10.1016/s0022-0248(00)00519-4.

[69] W. Wong-Ng, L.P. Cook, Liquidus diagram of the Ba-Y-Cu-O system in the vicinity of the Ba2YCu3O6+x phase field, J. Res. Natl. Inst. Stand. Technol. 103 (1998) 379. doi:10.6028/jres.103.023.

[70] D.M. De Leeuw, C.A.H.A. Mutsaers, C. Langereis, H.C.A. Smoorenburg, P.J. Rommers, Compound and phase compatibilities in the system Y2O3-BaO-CuO at 950°C, Phys. C Supercond. 152 (1988) 39–49. doi:10.1016/0921-4534(88)90071-8.

[71] J.L. MacManus-Driscoll, J.C. Bravman, R.B. Beyers, Phase equilibria in the Y-Ba-Cu-O system and melt processing of Ag clad Y1Ba2Cu307-x tapes at reduced oxygen partial pressures, Phys. C Supercond. 241 (1995) 401–413. doi:10.1016/0921-4534(94)02369-7.

[72] X. Obradors, T. Puig, X. Granados, F. Sandiumenge, Melt textured YBa2Cu3O7: fundamental properties and current limitation applications, Phys. C Supercond. 378–381 (2002) 1–10. doi:10.1016/s0921-4534(02)01373-4.

[73] D.A. Cardwell, Processing and properties of large grain (RE)BCO, Mater. Sci. Eng. B. 53 (1998) 1–10. doi:10.1016/s0921-5107(97)00293-6.

[74] S. Jin, Progress in melt texturing of YBa2Cu3Ox superconductors, in: AIP, 1992. doi:10.1063/1.43602.

[75] T. Izumi, Y. Nakamura, Y. Shiohara, Crystal growth mechanism of YBa2Cu3Oy superconductors with peritectic reaction, J. Cryst. Growth. 128 (1993) 757–761. doi:10.1016/s0022-0248(07)80039-x.

[76] X. Qi, J.L. MacManus-Driscoll, Liquid phase epitaxy processing for high temperature superconductor tapes, Curr. Opin. Solid State Mater. Sci. 5 (2001) 291–300. doi:10.1016/s1359-0286(00)00040-1.

[77] Y. Yamada, Liquid-phase epitaxy processing of RBa2Cu3O7-*∂*, Supercond. Sci. Technol. 13 (2000) 82–87. doi:10.1088/0953-2048/13/1/311.

[78] F. Parmigiani, G. Chiarello, N. Ripamonti, Observation of carboxylic groups in the lattice of sintered Ba2YCu307-y high-Tc superconductors, Phys. Rev. B. 36 (1987) 7148–7150. doi:10.1103/physrevb.36.7148.

[79] I. Arvanitidis, D. Siche, S. Seetharaman, A Study of the thermal decomposition of BaCO3, Metall. Mater. Trans. B. 27 (1996) 409–416. doi:10.1007/BF02914905.

[80] P. Vermeir, I. Cardinael, J. Schaubroeck, K. Verbeken, B. Michael, P. Lommens, W. Knaepen, D. Jan, K. De Buysser, I. Van Driessche, Elucidation of the mechanism in fluorine-free prepared YBa2Cu3O7-δ coatings, Inorg. Chem. 49 (2010) 4471–4477. doi:10.1021/ic9021799.

[81] P. Vermeir, J. Feys, J. Schaubroeck, K. Verbeken, P. Lommens, I. Van Driessche, Influence of sintering conditions in the preparation of acetate-based fluorine-free CSD YBCO films using a direct sintering method, Mater. Res. Bull. 47 (2012) 4376–4382. doi:10.1016/j.materresbull.2012.09.033.

[82] J.L. MacManus-Driscoll, A. Kursumovic, B. Maiorov, L. Civale, Q.X. Jia, S.R. Foltyn, H.Wang, YBa2Cu3O7 coated conductor grown by Hybrid Liquid Phase Epitaxy, IEEE Trans. Appl. Supercond. 17 (2007) 2537–2541. doi:10.1109/tasc.2007.898171.

[83] A. Stangl, Oxygen kinetics and charge doping for high critical current YBCO films, Insitut de Ciència de Materials de Barcelona (ICMAB-CSIC), 2019.

[84] W.E. Wallace, Infrared Spectra, in: P.J. Linstrom, W.G. Mallard (Eds.), NIST Chem. WebBook, NIST Stand. Ref. Database Number 69, Institute of Standards and Technology, Gaithersburg MD, 20899, n.d. doi:https://doi.org/10.18434/T4D303.

[85] W.E. Wallace, Mass spectra, in: P.J. Linstrom, W.G. Mallard (Eds.), NIST Chem. WebBook, NIST Stand. Ref. Database Number 69, National Institute of Standards and Technology, Gaithersburg MD, 20899, n.d. doi:https://doi.org/10.18434/T4D303.

[86] D. Sánchez-Rodríguez, J.P. López-Olmedo, J. Farjas, P. Roura, Determination of thermal conductivity of powders in different atmospheres by differential scanning calorimetry, J. Therm. Anal. Calorim. 121 (2015) 469–473. doi:10.1007/s10973-015-4429-z.

[87] M. Pujula, D. Sánchez-Rodríguez, J.P. Lopez-Olmedo, J. Farjas, P. Roura, Measuring thermal conductivity of powders with differential scanning calorimetry, J. Therm. Anal. Calorim. 125 (2016) 571–577. doi:10.1007/s10973-016-5274-4.

[88] J. Farjas, P. Roura, Isoconversional analysis of solid state transformations. A critical review. Part I. Single step transformations with constant activation energy, J. Therm. Anal. Calorim. 105 (2011) 757–766. doi:10.1007/s10973-011-1446-4.

[89] J. Farjas, P. Roura, Isoconversional analysis of solid state transformations. A critical review. Part II. Complex transformations, J. Therm. Anal. Calorim. 105 (2011) 767–773. doi:10.1007/s10973-011-1447-3.

[90] D. Sánchez-Rodriguez, J. Farjas, P. Roura, The critical conditions for thermal explosion in a system heated at a constant rate, Combust. Flame. 18 (2017) 211–219. doi:10.1016/j.combustflame.2017.08.008.

[91] H.E. Kissinger, Reaction Kinetics in Differential Thermal Analysis, Anal. Chem. 29 (1957) 1702–1706. doi:10.1021/ac60131a045.

[92] P. Roura, J. Farjas, Analytical solution for the Kissinger equation, J. Mater. Res. 24 (2009) 3095–3098. doi:10.1557/JMR.2009.0366.

[93] J. Farjas, P. Roura, Exact analytical solution for the Kissinger equation : Determination of the peak temperature and general properties of thermally activated transformations,

Thermochim. Acta. 598 (2014) 51–58. doi:10.1016/j.tca.2014.10.024.

[94] G. Kresse, J. Hafner, Ab initiomolecular dynamics for liquid metals, Phys. Rev. B. 47 (1993) 558–561. doi:10.1103/physrevb.47.558.

[95] G. Kresse, J. Furthmüller, Efficiency of ab-initio total energy calculations for metals and semiconductors using a plane-wave basis set, Comput. Mater. Sci. 6 (1996) 15–50. doi:10.1016/0927-0256(96)00008-0.

[96] P.E. Blöchl, Projector augmented-wave method, Phys. Rev. B. 50 (1994) 17953–17979. doi:10.1103/physrevb.50.17953.

[97] J.P. Perdew, K. Burke, M. Ernzerhof, Generalized Gradient Approximation Made Simple, Phys. Rev. Lett. 77 (1996) 3865–3868. doi:10.1103/physrevlett.77.3865.

[98] S. Grimme, J. Antony, S. Ehrlich, H. Krieg, A consistent and accurate ab initio parametrization of density functional dispersion correction (DFT-D) for the 94 elements H-Pu., J. Chem. Phys. 132 (2010) 154104. doi:10.1063/1.3382344.

[99] H. Fric, M. Jupa, U. Schubert, The Solid-state Structures of a Non-hydrated Yttrium Carboxylate and a Yttrium Carboxylate Hemihydrate Obtained by Reaction of Yttrium Alkoxides with Carboxylic Acids, Monatshefte Für Chemie - Chem. Mon. 137 (2006) 1–6. doi:10.1007/s00706-005-0400-1.

[100] V. Zeleňák, Z. Vargová, K. Györyová, Correlation of infrared spectra of zinc(II) carboxylates with their structures, Spectrochim. Acta Part A Mol. Biomol. Spectrosc. 66 (2007) 262–272. doi:10.1016/j.saa.2006.02.050.

[101] E. Gobert-Ranchoux, F. Charbonnier, Comportement thermique des propionates hydrates de calcium, strontium et baryum, J. Therm. Anal. 12 (1977) 33–42. doi:10.1007/BF01909853.

[102] X. Palmer, C. Pop, H. Eloussi, B. Villarejo, P. Roura, J. Farjas, A. Calleja, A. Palau, T. Puig, S. Ricart, Solution design for low-fluorine trifluoroacetate route to YBa2Cu3O7 films, Supercond. Sci. Technol. 29 (2016) 24002. doi:10.1088/0953-2048/29/2/024002.

[103] G. Deacon, Relationships between the carbon-oxygen stretching frequencies of carboxylato complexes and the type of carboxylate coordination, Coord. Chem. Rev. 33 (1980) 227–250. doi:10.1016/S0010-8545(00)80455-5.

[104] K. Nakamoto, Y. Morimoto, A.E. Martell, Infrared Spectra of Metal Chelate Compounds. IV. Infrared Spectra of Addition Compounds of Metallic Acetylacetonates 1a, J. Am. Chem. Soc. 83 (1961) 4533–4536. doi:10.1021/ja01483a010.

[105] I.A. Martynova, D.M. Tsymbarenko, N.P. Kuz'mina, Yttrium tris-propionate monohydrate: Synthesis, crystal structure, and thermal stability, Russ. J. Coord. Chem. 40 (2014) 565–570. doi:10.1134/S1070328414080077.

[106] M. Kakihana, T. Nagumo, Assignment for the infrared spectrum of solid sodium propionate from low-temperature measurements in combination with 13C isotopic shifts, Zeitschrift Für Naturforsch. A. 42 (1987) 477–484. doi:10.1515/zna-1987-0509.

[107] R.A. Hites, K. Biemann, On the mechanism of ketonic decarboxylation. Pyrolysis of calcium

decanoate, J. Am. Chem. Soc. 94 (1972) 5772–5777. doi:10.1021/ja00771a039.

[108] M.S. Akanni, E.K. Okoh, H.D. Burrows, H.A. Ellis, The thermal behaviour of divalent and higher valent metal soaps: a review, Thermochim. Acta. 208 (1992) 1–41. doi:10.1016/0040-6031(92)80150-u.

[109] P.A. Barnes, G. Stephenson, S.B. Warrington, The use of TA-GLC-MS as a quantitative specific EGA technique for the investigation of complex thermal decomposition reactions : the thermal decomposition of Calcium propanoate, J. Therm. Anal. 25 (1982) 299–311. doi:10.1007/bf01912955.

[110] P. Roura, J. Farjas, J. Camps, S. Ricart, J. Arbiol, T. Puig, X. Obradors, Decomposition processes and structural transformations of cerium propionate into nanocrystalline ceria at different oxygen partial pressures, J. Nanopart. Res. 13 (2011) 4085–4096. doi:10.1007/s11051-011-0352-9.

[111] J.A. Goldsmith, S.D. Ross, Factors affecting the infra-red spectra of some planar anions with D3h symmetry-III . The spectra of rare-earth carbonates and their thermal decomposition products, Spectrochim. Acta Part A Mol. Spectrosc. 23 (1967) 1909–1915. doi:10.1016/0584-8539(67)80073-4.

[112] G.A.M. Hussein, Formation of high surface-area yttrium oxide by the thermal decomposition of different inorganic precursors, Thermochim. Acta. 244 (1994) 139–151. doi:10.1016/0040-6031(94)80214-9.

[113] N. Imanaka, M. Toshiyuki, Y. Mayama, K. Koyabu, Synthesis of crystalline yttrium oxycarbonate in a single phase, J. Solid State Chem. 178 (2005) 3601–3603. doi:10.1016/j.jssc.2005.09.024.

[114] S. Liu, R. Jiang, F. Luo, Synthesis and structure of hydrated yttrium carbonate, Y2(CO3)3·2.79H2O, Synth. React. Inorg. Met. Chem. 30 (2000) 271–279. doi:10.1080/00945710009351762.

[115] Y. Tsukuda, Properties of black Y2O3 sintered bodies, Mater. Res. Bull. 16 (1981) 453–459.

[116] J.P.A. Neeft, F. Hoornaert, M. Makkee, J.A. Moulijn, The effects of heat and mass transfer in thermogravimetrical analysis. A case study towards the catalytic oxidation of soot, Termochimica Acta. 287 (1996) 261–278. doi:10.1016/s0040-6031(96)03002-x.

[117] D. Sánchez-Rodríguez, H. Wada, S. Yamaguchi, J. Farjas, H. Yahiro, Self-propagating high-temperature synthesis of LaMO3 perovskite-type oxide using heteronuclearcyano metal complex precursors, J. Alloy. Compd. 649 (2015) 1291–1299. doi:10.1016/j.jallcom.2015.07.246.

[118] T. Boddington, F. Hongtu, P.G. Laye, M. Nawaz, D.C. Nelson, Thermal runaway by thermal analysis, Termochimica Acta. 170 (1990) 81–87. doi:10.1016/0040-6031(90)80526-5.

[119] K.C. Patil, S.T. Aruna, T. Mimani, Combustion synthesis: an update, Curr. Opin. Solid State Mater. Sci. 6 (2002) 507–512. doi:10.1016/S1359-0286(02)00123-7.

[120] O.S. Rabinovich, P.S. Grinchuk, M.A. Andreev, B.B. Khina, Conditions for combustion synthesis in nanosized Ni/Al films on a substrate, Phys. B. 392 (2007) 272–280. doi:10.1016/j.physb.2006.11.032.

[121] L. Thiers, A.S. Mukasyan, A. Varma, Thermal explosion in Ni-Al system: influence of reaction medium microstructure, Combust. Flame. 131 (2002) 198–209. doi:10.1016/s0010-2180(02)00402-9.

[122] N. Semenov, Thermal theory of combustion and explosion, Prog. Phys. Sci. 23 (1940).

[123] N. Semenov, Theories of combustion processes, Zeitschrift Für Phys. 48 (1928) 571–582.

[124] D. Sánchez-Rodriguez, J. Farjas, P. Roura, The Critical Condition for Thermal Explosion in an Isoperibolic System, AlChE J. 63 (2017) 3979–3993. doi:10.1002/aic.15727.

[125] J.A.R. Cheda, M. V García, M.I. Redondo, S. Gargani, P. Ferloni, Short chain copper(II) n-alkanoate liquid crystals, Liq. Cryst. 31 (2004) 1–14. doi:10.1080/02678290310001628500.

[126] Y.H. Chung, H.H. Wei, Y.H. Liu, G.H. Lee, Y. Wang, Reinvestigation of the crystal structure and cryomagnetic behaviour of copper(II) propionates, Polyhedron. 17 (1998) 449–455. doi:10.1016/s0277-5387(97)00367-7.

[127] A. Elmali, The magnetic super-exchange coupling in copper(II) acetate monohydrate and a redetermination of the crystal structure, Turk J Phy. 24 (2000) 667–672.

[128] X. Rocquefelte, K. Schwarz, P. Blaha, Theoretical investigation of the magnetic exchange interactions in copper (II) oxides under chemical and physical pressures, 2012. doi:10.1038/srep00759.

[129] R.L. Martin, H. Waterman, Magnetic studies with copper(II) salts. Part II. anomalous paramagnetism and *∂*-Bonding in anhydrous and hydrated copper(II) n-alkanoeates., J. Chem. Soc. (1957) 2545–2551. doi:10.1039/JR9570002545.

[130] V.V. Zelentsov, Magnetic susceptibility of some copper(II) carboxylates, J. Struct. Chem. 6 (1966) 819–823. doi:10.1007/bf00747102.

[131] R. Urlaub, U. Posset, R. Thull, FT-IR spectroscopic investigations on sol—gel-derived coatings from acid-modified titanium alkoxides, J. Non-Cyrstalline Solids. 265 (2000) 276–284. doi:10.1016/s0022-3093(00)00003-x.

[132] S. Doeuff, M. Henry, C. Sanchez, J. Livage, Hydrolysis of titanium alkoxides: modification of the molecular precursor by acetic acid, J. Non-Cyrstalline Solids. 9 (1987) 206–216. doi:10.1016/s0022-3093(87)80333-2.

[133] W.J. Newton, C. Oldham, B.J. Tabner, Magnetic susceptibility and electron spin resonance of some copper(II) unsaturated carboxylates, Chem. Informationsd. 11 (1980) 1379–1382. doi:10.1002/chin.198046063.

[134] H. Henmi, T. Hirayama, N. Mizutani, M. Kato, Thermal decomposition of basic copper carbonate, CuCO3•Cu(OH)2·H2O, in carbon dioxide atmosphere (0-50 atm), Thermochim. Acta. 96 (1985) 145–153. doi:10.1016/0040-6031(85)80017-4.

[135] M. Estruga, A. Roig, C. Domingo, J.A. Ayllón, Solution-processable carboxylate-capped CuO nanoparticles obtained by a simple solventless method, J. Nanopart. Res. 14 (2012) 1053–8. doi:10.1007/s11051-012-1053-8.

[136] D. Mott, J. Galkowski, L. Wang, J. Luo, C. Zhong, Synthesis of Size-Controlled and Shaped

Copper Nanoparticles, Langmuir. 23 (2007) 5740–5745. doi:10.1021/la0635092.

[137] M.A. Ben Aissa, B. Tremblay, A. Andrieux-Ledier, E. Maisonhaute, N. Raouafi, A. Courty, Copper nanoparticles of well-controlled size and shape: a new advance in synthesis and self-organization, Nanoscale. 7 (2015) 3189–3195. doi:10.1039/c4nr06893a.

[138] A. Echavarría, F. Echeverría, C. Arroyave, H. Gil, study of the copper corrosion mechanism in the presence of propionic acid vapors, J. Braz. Chem. Soc. 20 (2009) 1841–1848. doi:10.1590/s0103-50532009001000011.

[139] D. Deng, T. Qi, Y. Cheng, Y. Jin, F. Xiao, Copper carboxylate with different carbon chain lengths as metal–organic decomposition ink, J. Mater. Sci Mater Electron. 25 (2014) 390–397. doi:10.1007/s10854-013-1599-y.

[140] C. Reichert, D.K.C. Fung, D.C.K. Lin, J.B. Westmore, Thermal decomposition of copper (II) carboxylates: mass spectra of binuclear copper(I) carboxilates, Chem. Commun. (1968) 1094. doi:10.1039/c19680001094.

[141] Y. Pauleau, A.Y. Fasasi, Kinetics of sublimation of copper(II) acetylacetonate complex used for chemical vapor deposition of copper film, Chem. Mater. 3 (1991) 45–50. doi:10.1021/cm00013a015.

[142] F. KÖSY, A volatile compound of copper, Nature. 160 (1947) 21. doi:10.1038/160021a0.

[143] J.J. Duruz, H.J. Michels, A.R. Ubbelohde, Decomposition reactions of sodium propionate, J. Che. (1971) 1505–1509. doi:10.1039/j29710001505.

[144] D. Torres, N. Lopez, F. Illas, R.M. Lambert, Why Copper Is Intrinsically More Selective than Silver in Alkene Epoxidation : Ethylene Oxidation on Cu (111) versus Ag (111), J. Am. Chem. Soc. 127 (2005) 10774–10775. doi:10.1021/ja043227t.

[145] K. Ito, H.J. Bernstein, The vibrational spectra of the formate, acetate, and oxalate ions, Can. J. Chem. 34 (1956) 170–178. doi:10.1139/v56-021.

[146] D.J. Blundell, On the interpretation of multiple melting peaks in poly (ether ether ketone), Polymer (Guildf). 28 (1987) 2248–2251. doi:10.1016/0032-3861(87)90382-x.

[147] P. Torres, P. Norby, J. Grivel, Thermal decomposition of barium valerate in argon, J. Anal. Appl. Pyrolysis 116. 116 (2015) 120–128. doi:10.1016/j.jaap.2015.09.018.

[148] J.-C.C. Grivel, Thermal decomposition of yttrium(III) propionate and butyrate, J. Anal. Appl. Pyrolysis. 101 (2013) 185–192. doi:10.1016/j.jaap.2013.01.011.

[149] M.M. Torres, D. Palacios, C.D. María, A.C. González-baró, E.J. Baran, Vibrational spectra of barium oxalate hemihydrate, Spectrosc. Lett. 49 (2016) 238–240. doi:10.1080/00387010.2015.1133651.

[150] A.H. Verdonk, A. Broersma, Thermal decomposition of barium oxalate hemihydrate BaC2O4•0.5H2O, Thermochim. Acta. 6 (1973) 95–110. doi:10.1016/0040-6031(73)80009-7.

[151] D. Dollimore, The thermal decomposition of oxalates. A review, Thermochim. Acta. 117 (1987) 331–363. doi:10.1016/0040-6031(87)88127-3.

[152] J. Chaney, J.D. Santillán, E. Knittle, Q. Williams, A high-pressure infrared and Raman spectroscopic study of BaCO3: the aragonite, trigonal and Pmmn structures, Phys. Chem. Miner. 42 (2015) 83–93. doi:10.1007/s00269-014-0702-0.

[153] S.M. Antao, I. Hassan, BaCO3: high-temperature crystal structures and the Pmcn-->R3m phase transition at 811 ° C, Phys. Chem. Miner. 34 (2007) 573–580. doi:10.1007/s00269-007-0172-8.

[154] F. Ribot, P. Toledano, C. Sanchez, X-ray and spectroscopic investigations of the structure of yttrium acetate tetrahydrate, Inorganica Chim. Acta. 185 (1991) 239–245. doi:10.1016/S0020-1693(00)85449-3.

[155] L. Soler, Liquid-assisted ultrafast growth of superconductive films derived from chemical solution, Institut de Ciènces de Materials de Barcelona-CSIC, 2019.

[156] L. Soler, et al., Ultrafast transient liquid assisted growth of high current density superconducting films, (n.d.) submitted.

[157] T.B. Lindemer, E.D. Specht, The BaO-Cu-CuO system. Solid-liquid equilibria and thermodynamics of BaCuO2 and BaCu202, Phys. C Supercond. 255 (1995) 81–94. doi:10.1016/0921-4534(95)00460-2.

[158] T.B. Lindemer, F.A. Washburn, C.S. MacDougall, Study of phase behavior in the YBa2Cu307-x__BaCuO2+y__CuO-Ag system, Phys. C Supercond. 196 (1992) 390–398. doi:10.1016/0921-4534(92)90462-l.

[159] F. Taïr, L. Carreras, J. Camps, J. Farjas, P. Roura, A. Calleja, T. Puig, X. Obradors, Melting temperature of YBa2Cu3O7−x and GdBa2Cu3O7−x at subatmospheric partial pressure, J. Alloys Compd. 692 (2017) 787–792. doi:10.1016/j.jallcom.2016.08.072.

[160] M. Ohring, The Materials Science of Thin Films, Elsevier, 1992.

[161] H.J.T. Ellingham, Transactions and communications, J. Soc. Chem. Ind. 63 (1944) 125–160. doi:10.1002/jctb.5000630501.

[162] B.E. Deal, A.S. Grove, General relationship for the thermal oxidation of silicon, J. Appl. Phys. 36 (1965) 3770–3778. doi:10.1063/1.1713945.